

NUCLEAR STRUCTURE BELOW  $^{132}\text{Sn}$ : AN INVESTIGATION OF  
NEUTRON-RICH NUCLIDES VIA  $\beta$  AND ISOMERIC DECAY

By

Bryan Earl Tomlin

A DISSERTATION

Submitted to  
Michigan State University  
in partial fulfillment of the requirements  
for the degree of

DOCTOR OF PHILOSOPHY

Department of Chemistry

2006

# ABSTRACT

## NUCLEAR STRUCTURE BELOW $^{132}\text{Sn}$ : AN INVESTIGATION OF NEUTRON-RICH NUCLIDES VIA $\beta$ AND ISOMERIC DECAY

By

Bryan Earl Tomlin

Almost everything that is known about nuclear shell structure has been derived from experimental work on stable nuclides or nuclides very close to stability. This is largely a consequence of accessibility—historically the means did not exist to produce and study exotic nuclides very far from stability. The well-known magic proton and neutron numbers have been validated, in certain regions, as experiment has pushed further out, but it should not be assumed that the magic numbers will remain magic in nuclides with extreme ratios of neutrons to protons. In fact, the smaller neutron magic numbers (*i.e.* 8, 20) have already been observed to disappear in some neutron-rich nuclides [1–3].

The effect of the reduction, or quenching, of neutron shell gaps in neutron-rich nuclides has been known in theoretical calculations since the late 1970s [4]. The consequence of neutron shell quenching in neutron-rich nuclides in an astrophysical context has been used in attempts to understand the significant departures of calculated rapid neutron-capture process (*r*-process) yields from the observed solar *r*-process abundances. Since the theoretical phenomenon of quenching is strongly model-dependent, unambiguous experimental indicators of the shell structure of very neutron-rich nuclides are important. The results of recent experiments on the nuclide  $^{130}_{48}\text{Cd}_{82}$  [5, 6] have been interpreted as evidence of a weakening of the  $N = 82$  shell closure just below  $Z = 50$ .

This thesis describes an investigation of the experimental signatures for the

persistence of the  $N = 82$  shell closure, or alternatively the emergence of  $N = 82$  shell quenching, for neutron-rich  ${}_{46}\text{Pd}$ ,  ${}_{47}\text{Ag}$ , and  ${}_{48}\text{Cd}$  nuclides.

An experiment was performed at the National Superconducting Cyclotron Laboratory (NSCL) at Michigan State University to study the low-energy structure of neutron-rich transition-metal nuclides with  $44 < Z < 50$  and  $N < 82$  in the region near doubly-magic  ${}^{132}_{50}\text{Sn}_{82}$ . Exotic nuclides were produced by projectile fragmentation of a  ${}^{136}\text{Xe}^{49+}$  beam at 120 MeV/nucleon. The NSCL Beta Counting System (BCS), employing a double-sided Si strip detector, was used to identify secondary beam fragments and correlate implantation events with subsequent beta-decay events, on an event-by-event basis [7]. In addition to the BCS, twelve auxiliary HpGe gamma-ray detectors were employed to measure both beta-delayed gamma rays, as well as, prompt gamma rays emitted following isomeric decay.

New spectroscopic data were obtained for neutron-rich isotopes of  ${}_{44}\text{Ru}$ ,  ${}_{45}\text{Rh}$ ,  ${}_{46}\text{Pd}$ ,  ${}_{47}\text{Ag}$ ,  ${}_{48}\text{Cd}$ , and  ${}_{49}\text{In}$ . These new data include isomeric-transition and beta-decay half-lives and gamma-ray energies and relative intensities. Deduced level schemes were used to extend the systematics of Pd, Ag and Cd isotopes to higher mass numbers. In this work, the neutron-rich even-even  ${}_{46}\text{Pd}$   $E(2_1^+)$  and  $E(4_1^+)$  systematics were extended up to  ${}^{120}\text{Pd}_{74}$ , and no evidence of a reduced  $N = 82$  shell gap in this isotopic series was found. Additionally, the partial level schemes that were deduced for  ${}^{123,125}\text{Ag}$  and  ${}^{125-127}\text{Cd}$  have been interpreted as demonstrating single-particle character, indicative of intact  $Z = 50$  and  $N = 82$  shell gaps.

## ACKNOWLEDGMENTS

Without question, these acknowledgements must begin with thanks to my thesis advisor, Paul Mantica. This document would not exist without his guidance and patience. In most things that I do I'm about as slow as molasses in January, and I suspect that Paul often felt like a hare coaching a tortoise, yet he never once complained. Thanks Paul!

I also must thank Bill Walters for his valuable insight regarding the work herein. I owe a debt of gratitude to Bill for proposing the experiment that this work is based on and for mercifully allowing me to use it for my thesis after my own experiment was not approved.

This thesis would not have been possible without the assistance of a number of individuals. I would like to thank Colin Morton for his work in setting up and executing my experiment and for assistance in the earlier stages of the data analysis. I especially want to thank Sean Liddick for all of his help. Sean was always two steps ahead of me in his data analysis, and I benefitted greatly from the many things that he learned along the way. Thanks for answering, often repeatedly, my many questions regarding "Spe'Tcl" and C++ and ROOT and L<sup>A</sup>T<sub>E</sub>X. Thanks also to Fernando Montes, who had nearly the same data set, for many valuable conversations.

I thank David Morrissey, Hendrik Schatz, and Krzysztof Starosta for serving on my guidance committee.

Finally, I offer special thanks to Sean, Jeremy, Ivan, Michal, Mark and Chandana for the hours of interesting conversations and for keeping me distracted just enough to make graduate school enjoyable!

# Contents

<b>1</b>	<b>Introduction</b>	<b>1</b>
1.1	The Nuclear Shell Model . . . . .	1
1.1.1	Development of the Nuclear Shell Model . . . . .	1
1.1.2	Low-Lying Nuclear Excited States . . . . .	6
1.2	Nuclear Structure Near $^{132}\text{Sn}$ . . . . .	15
1.3	Proposed Experiment . . . . .	21
<b>2</b>	<b>Methods</b>	<b>24</b>
2.1	Populating Nuclear Excited States . . . . .	24
2.1.1	Beta Decay . . . . .	24
2.1.2	Isomeric Transitions . . . . .	27
2.2	Nuclear Excited-State Spectroscopy . . . . .	28
2.2.1	Gamma Decay . . . . .	29
2.2.2	Data Analysis Methods . . . . .	32
<b>3</b>	<b>Experimental Setup and Technique</b>	<b>36</b>
3.1	Radionuclide Production . . . . .	36
3.1.1	Projectile Fragmentation . . . . .	36
3.1.2	Primary Beam . . . . .	37
3.1.3	Fragment Separation and Identification . . . . .	40
3.1.4	Total Kinetic Energy Determination . . . . .	43
3.2	Beta Counting System . . . . .	51
3.2.1	Hardware and Electronics . . . . .	51
3.2.2	Implantation-Beta Decay Correlation . . . . .	57
3.2.3	Beta-Decay Half-life Determination . . . . .	62
3.3	HpGe Array . . . . .	65
3.3.1	Hardware and Electronics . . . . .	66
3.3.2	Prompt Gamma Radiation Measurement . . . . .	72
3.3.3	Beta-Delayed Gamma Radiation Measurement . . . . .	76
<b>4</b>	<b>Results</b>	<b>78</b>
4.1	Overview of Data Collected in Exp. 01015 . . . . .	78
4.2	Isomers . . . . .	80
4.2.1	$^{129}\text{Sn}$ . . . . .	86
4.2.2	$^{127}\text{In}$ . . . . .	91
4.2.3	$^{129}\text{In}$ . . . . .	97

4.2.4	$^{125}\text{Cd}$ . . . . .	103
4.2.5	$^{126}\text{Cd}$ . . . . .	108
4.2.6	$^{127}\text{Cd}$ . . . . .	113
4.2.7	$^{123}\text{Ag}$ . . . . .	118
4.2.8	$^{124}\text{Ag}$ . . . . .	123
4.2.9	$^{125}\text{Ag}$ . . . . .	127
4.2.10	$^{121}\text{Pd}$ . . . . .	131
4.2.11	$^{117}\text{Ru}$ . . . . .	133
4.3	Beta-Decay Parents . . . . .	137
4.3.1	$^{126}\text{Cd}$ . . . . .	141
4.3.2	$^{122}\text{Ag}$ . . . . .	145
4.3.3	$^{121}\text{Pd}$ . . . . .	153
4.3.4	$^{122}\text{Pd}$ . . . . .	157
4.3.5	$^{119}\text{Rh}$ . . . . .	163
4.3.6	$^{120}\text{Rh}$ . . . . .	166
<b>5</b>	<b>Interpretation of Results</b> . . . . .	<b>172</b>
5.1	Shell Quenching Near $^{132}\text{Sn}$ ? . . . . .	172
5.2	Systematics of Even-Even Pd Isotopes . . . . .	173
5.3	Neutron- and Proton-Hole Configurations in Odd-Even Ag Isotopes . . . . .	177
5.4	Systematics of Cd Isotopes . . . . .	180
5.5	Conclusion . . . . .	188
<b>6</b>	<b>Summary</b> . . . . .	<b>190</b>
	<i>Bibliography</i> . . . . .	<b>194</b>

# List of Figures

1.1	Atomic Ionization Energies . . . . .	2
1.2	Atomic and Nuclear Orbital Ordering . . . . .	3
1.3	Two-Neutron Separation Energies . . . . .	5
1.4	Shell Model Description of $^{17}\text{O}$ . . . . .	7
1.5	Nuclear Models Across Major Shells . . . . .	10
1.6	Evolution of Dy Excited States . . . . .	13
1.7	Dy $E(2_1^+)$ and $E(4_1^+)/E(2_1^+)$ . . . . .	15
1.8	Neutron-Rich Sn Region . . . . .	16
1.9	$E(2_1^+)$ Systematics of $_{52}\text{Te}$ , $_{54}\text{Xe}$ , and $_{56}\text{Ba}$ . . . . .	18
1.10	$E(2_1^+)$ Systematics of $_{44}\text{Ru}$ , $_{46}\text{Pd}$ , and $_{48}\text{Cd}$ . . . . .	18
1.11	Single-Particle Orbitals for Different Potentials . . . . .	19
1.12	Cd Isotope Masses . . . . .	21
1.13	Range of Nuclides Presently Studied . . . . .	23
2.1	Schematic Representation of Beta-Gamma Spectroscopy and Isomer Spectroscopy. . . . .	26
2.2	Schematic Representation of Gamma Decay. . . . .	30
2.3	Gamma-Ray Cascade. . . . .	33
2.4	Gamma-Ray Intensity Matching. . . . .	34
3.1	CCF and A1900 Layout . . . . .	39
3.2	A1900 Dispersive Plane . . . . .	42
3.3	Sample Particle Identification Plot . . . . .	44
3.4	Schematic Diagram of $\Delta E$ Detectors . . . . .	46
3.5	TKE Calibration Curves I . . . . .	47
3.6	TKE Calibration Curves II . . . . .	48
3.7	Representative Total Kinetic Energy Spectrum . . . . .	50
3.8	Schematic Diagram of Beta Counting System . . . . .	52
3.9	Electronics Diagram for Double-Sided Si Strip Detector . . . . .	56
3.10	Electronics Diagram for PIN Detectors . . . . .	58
3.11	DSSD Implantation Multiplicity Distributions . . . . .	59
3.12	DSSD High-Gain Energy Thresholds . . . . .	61
3.13	Implant- and Decay-Correlated PID Plots . . . . .	63
3.14	Electronics Diagram for HpGe Detectors . . . . .	67
3.15	Calibration Curve for SeGA-TAC . . . . .	68
3.16	SeGA-TAC Time Spectrum . . . . .	68
3.17	Schematic of HpGe-Detector Array . . . . .	70

3.18	Cross-Section of HpGe-Detector Array . . . . .	70
3.19	Photopeak Efficiency Curve of HpGe Array . . . . .	71
3.20	Gamma-Ray Energy Residual Plots for Each HpGe Detector . . . . .	73
3.21	Total Gamma-Ray Energy Residual Plot for All HpGe Detectors . . . . .	74
4.1	PID Plot for All Beam Fragments Incident on PIN01a . . . . .	79
4.2	PID Plot for All Implant-Correlated Fragments . . . . .	80
4.3	Representative Total Kinetic Energy Spectrum . . . . .	85
4.4	$^{129m}\text{Sn}$ Prompt Gamma Ray Spectrum . . . . .	87
4.5	$^{129m}\text{Sn}$ Prompt Fragment- $\gamma\gamma$ Spectra . . . . .	88
4.6	$^{129m}\text{Sn}$ Decay Curve . . . . .	89
4.7	Decay Scheme of $^{129}\text{Sn}$ Isomers . . . . .	92
4.8	$^{127m}\text{In}$ Prompt Gamma Ray Spectrum . . . . .	93
4.9	$^{127m}\text{In}$ Prompt Fragment- $\gamma\gamma$ Spectra . . . . .	94
4.10	$^{127m}\text{In}$ Decay Curve . . . . .	94
4.11	Decay Scheme of $^{127}\text{In}$ Isomer . . . . .	96
4.12	$^{129}\text{In}$ Total Kinetic Energy Spectrum . . . . .	98
4.13	$^{129m}\text{In}$ Prompt Gamma-Ray Spectrum . . . . .	99
4.14	$^{129m}\text{In}$ Prompt Fragment- $\gamma\gamma$ Spectra . . . . .	100
4.15	$^{129m}\text{In}$ Decay Curve . . . . .	101
4.16	Decay Scheme of $^{129}\text{In}$ Isomer . . . . .	103
4.17	$^{125}\text{Cd}$ Total Kinetic Energy Spectrum . . . . .	104
4.18	$^{125m}\text{Cd}$ Prompt Gamma-Ray Spectrum . . . . .	105
4.19	$^{125m}\text{Cd}$ Prompt Fragment- $\gamma\gamma$ Spectra . . . . .	106
4.20	$^{125m}\text{Cd}$ Decay Curve . . . . .	107
4.21	Proposed Decay Scheme for $^{125}\text{Cd}$ Isomer . . . . .	108
4.22	$^{126}\text{Cd}$ Total Kinetic Energy Spectrum . . . . .	109
4.23	$^{126m}\text{Cd}$ Prompt Gamma-Ray Spectrum . . . . .	110
4.24	$^{126m}\text{Cd}$ Prompt Fragment- $\gamma\gamma$ Coincidence Spectra . . . . .	111
4.25	$^{126m}\text{Cd}$ Decay Curve . . . . .	112
4.26	Proposed Decay Scheme for $^{126}\text{Cd}$ Isomer . . . . .	113
4.27	$^{127}\text{Cd}$ Total Kinetic Energy Spectrum . . . . .	114
4.28	$^{127m}\text{Cd}$ Prompt Gamma-Ray Spectrum . . . . .	115
4.29	$^{127m}\text{Cd}$ Prompt Fragment- $\gamma\gamma$ Spectra . . . . .	116
4.30	$^{127m}\text{Cd}$ Decay Curve . . . . .	116
4.31	Proposed Decay Scheme for $^{127}\text{Cd}$ Isomer . . . . .	117
4.32	$^{123}\text{Ag}$ Total Kinetic Energy Spectrum . . . . .	118
4.33	$^{123m}\text{Ag}$ Prompt Gamma Ray Spectrum . . . . .	119
4.34	$^{123m}\text{Ag}$ Prompt Fragment- $\gamma\gamma$ Spectra . . . . .	120
4.35	$^{123m}\text{Ag}$ Prompt Fragment- $\gamma\gamma$ Spectra . . . . .	121
4.36	$^{123m}\text{Ag}$ Decay Curve . . . . .	122
4.37	Proposed Decay Scheme for $^{123}\text{Ag}$ Isomer . . . . .	124
4.38	$^{124}\text{Ag}$ Total Kinetic Energy Spectrum . . . . .	125
4.39	$^{124m}\text{Ag}$ Prompt Gamma-Ray Spectrum . . . . .	125
4.40	$^{124m}\text{Ag}$ Prompt Fragment- $\gamma\gamma$ Spectra . . . . .	126
4.41	$^{124m}\text{Ag}$ Decay Curve . . . . .	126

4.42	$^{125}\text{Ag}$ Total Kinetic Energy Spectrum . . . . .	128
4.43	$^{125m}\text{Ag}$ Prompt Gamma-Ray Spectrum . . . . .	129
4.44	$^{125m}\text{Ag}$ Prompt Fragment- $\gamma\gamma$ Spectra . . . . .	129
4.45	$^{125m}\text{Ag}$ Decay Curve . . . . .	130
4.46	Proposed Decay Scheme for $^{125}\text{Ag}$ Isomer . . . . .	131
4.47	$^{121}\text{Pd}$ Total Kinetic Energy Spectrum . . . . .	132
4.48	$^{121m}\text{Pd}$ Prompt Gamma-Ray Spectrum . . . . .	133
4.49	$^{121m}\text{Pd}$ Decay Curve . . . . .	134
4.50	$^{117}\text{Ru}$ Total Kinetic Energy Spectrum . . . . .	135
4.51	$^{117m}\text{Ru}$ Prompt Gamma-Ray Spectrum . . . . .	135
4.52	$^{117m}\text{Ru}$ Decay Curve . . . . .	136
4.53	Decay Scheme of $^{113}\text{Ru}$ Isomer . . . . .	137
4.54	Comparison of $^{126}\text{Cd}$ TKE Spectra . . . . .	140
4.55	$^{126}\text{Cd}$ Beta-Delayed Gamma-Ray Spectrum . . . . .	142
4.56	Fragment- $\beta\gamma\gamma$ Coincidence Spectra for the Decay of $^{126}\text{Cd}$ . . . . .	142
4.57	$^{126}\text{Cd}$ Decay Curve . . . . .	143
4.58	Gamma-Gated $^{126}\text{Cd}$ Decay Curve . . . . .	144
4.59	Decay Scheme for $^{126}\text{Cd}$ . . . . .	145
4.60	$^{122}\text{Ag}$ Beta-Delayed Gamma-Ray Spectrum . . . . .	146
4.61	Fragment- $\beta\gamma\gamma$ Coincidence Spectra for the Decay of $^{122}\text{Ag}$ . . . . .	147
4.62	$^{122}\text{Ag}$ Decay Curve . . . . .	148
4.63	Gamma-Gated $^{122}\text{Ag}$ Decay Curve . . . . .	149
4.64	Partial Decay Scheme for $^{122}\text{Ag}$ . . . . .	150
4.65	Isomeric Beta-Decay Feeding of $^{122}\text{Cd}$ . . . . .	151
4.66	$^{121}\text{Pd}$ Beta-Delayed Gamma-Ray Spectrum . . . . .	154
4.67	Fragment- $\beta\gamma\gamma$ Coincidence Spectra for the Decay of $^{121}\text{Pd}$ . . . . .	156
4.68	$^{121}\text{Pd}$ Decay Curve . . . . .	157
4.69	Gamma-Gated $^{121}\text{Pd}$ Decay Curve . . . . .	158
4.70	$^{122}\text{Pd}$ Beta-Delayed Gamma-Ray Spectrum . . . . .	159
4.71	$^{122}\text{Pd}$ Decay Curve . . . . .	160
4.72	Gamma-Gated $^{122}\text{Pd}$ Decay Curve . . . . .	161
4.73	Decay Scheme for $^{122}\text{Pd}$ . . . . .	163
4.74	$^{119}\text{Rh}$ Beta-Delayed Gamma-Ray Spectrum . . . . .	164
4.75	Fragment- $\beta\gamma\gamma$ Coincidence Spectra for the Decay of $^{119}\text{Rh}$ . . . . .	165
4.76	$^{119}\text{Rh}$ Decay Curve . . . . .	166
4.77	Gamma-Gated $^{119}\text{Rh}$ Decay Curve . . . . .	167
4.78	Gamma-Gated $^{119}\text{Rh}$ Decay Curve . . . . .	168
4.79	$^{120}\text{Rh}$ Beta-Delayed Gamma-Ray Spectrum . . . . .	169
4.80	$^{120}\text{Rh}$ Decay Curve . . . . .	170
4.81	Gamma-Gated $^{120}\text{Rh}$ Decay Curve . . . . .	170
4.82	Decay Scheme for $^{120}\text{Rh}$ . . . . .	171
5.1	Even-Even Pd Excited-State Systematics . . . . .	174
5.2	$E(2_1^+)$ Systematics of Even-Even Pd from Experiment and IBM-2 . . . . .	175
5.3	$E(2_1^+)$ Systematics of Even-Even Pd and Xe . . . . .	176
5.4	Odd-A Ag Excited-State Systematics . . . . .	178

5.5	Comparisons of $^{123,125}\text{Ag}$ and $^{125,127}\text{In}$ . . . . .	179
5.6	$E(2_1^+)$ Systematics of Even-Even Cd, Te and Hg . . . . .	182
5.7	Proposed Decay Scheme for $^{126}\text{Cd}$ Isomer . . . . .	184
5.8	Even- $A$ Cd Excited-State Systematics . . . . .	185
5.9	R-value Systematics of Odd- $A$ Cd Isotopes . . . . .	185
5.10	Comparisons of $^{125,127}\text{Cd}$ and $^{127,129}\text{Sn}$ . . . . .	187
5.11	Odd- $A$ Cd Excited-State Systematics . . . . .	188

# List of Tables

2.1	Beta-Decay Selection Rules. . . . .	26
2.2	Angular Momentum and Parity Selection Rules. . . . .	30
3.1	$\Delta E$ Calibration Runs . . . . .	48
3.2	BCS Detectors. . . . .	53
3.3	Calibration Gamma Rays. . . . .	72
4.1	PID Inventory. . . . .	81
4.2	Summary of Isomer Results . . . . .	82
4.3	Summary of Isomer Results II . . . . .	83
4.4	Summary of TKE Results . . . . .	84
4.5	Sn-A PID Gate Counts. . . . .	87
4.6	$^{129}\text{Sn}$ Prompt Gamma Rays. . . . .	87
4.7	In-A+2 PID Gate Counts. . . . .	93
4.8	$^{127}\text{In}$ Prompt Gamma Rays. . . . .	94
4.9	In-A+1 PID Gate Counts. . . . .	98
4.10	$^{129}\text{In}$ Prompt Gamma Rays. . . . .	99
4.11	Cd-A PID Gate Counts. . . . .	104
4.12	$^{125}\text{Cd}$ Prompt Gamma Rays. . . . .	105
4.13	Cd-A+1 PID Gate Counts. . . . .	109
4.14	$^{126}\text{Cd}$ Prompt Gamma Rays. . . . .	110
4.15	Cd-A+2 PID Gate Counts. . . . .	114
4.16	$^{127}\text{Cd}$ Prompt Gamma Rays. . . . .	115
4.17	Ag-A+1 PID Gate Counts. . . . .	119
4.18	$^{123}\text{Ag}$ Prompt Gamma Rays. . . . .	120
4.19	Ag-A+2 PID Gate Counts. . . . .	123
4.20	$^{124}\text{Ag}$ Prompt Gamma Rays. . . . .	124
4.21	Ag-A+3 PID Gate Counts. . . . .	127
4.22	$^{125}\text{Ag}$ Prompt Gamma Rays. . . . .	128
4.23	Pd-A+1 PID Gate Counts. . . . .	132
4.24	$^{121}\text{Pd}$ Prompt Gamma Rays. . . . .	133
4.25	Ru-A+1 PID Gate Counts. . . . .	134
4.26	$^{117}\text{Ru}$ Prompt Gamma Rays. . . . .	136
4.27	Summary of Beta-Decay Results . . . . .	138
4.28	Summary of Beta-Decay Results II . . . . .	139
4.29	Gamma Transitions Observed for $^{126}\text{Cd}$ $\beta$ -Decay. . . . .	141
4.30	Gamma Transitions Observed in $^{122}\text{Ag}$ Decay. . . . .	146

4.31	Gamma Transitions Observed in $^{121}\text{Pd}$ Decay. . . . .	155
4.32	Gamma Transitions Observed in $^{122}\text{Pd}$ Decay. . . . .	159
4.33	Gamma Transitions Observed in $^{119}\text{Rh}$ Decay. . . . .	164
4.34	Gamma Transitions Observed in $^{120}\text{Rh}$ Decay. . . . .	169
5.1	$E(2_1^+)$ and $E(4_1^+)$ for $_{46}\text{Pd}$ and $_{54}\text{Xe}$ . . . . .	175
6.1	Summary of New Isomer Results . . . . .	191
6.2	Summary of New Beta-Decay Results . . . . .	192

# Chapter 1

## Introduction

### 1.1 The Nuclear Shell Model

#### 1.1.1 Development of the Nuclear Shell Model

The key development in understanding the periodicity of the reactivity of the chemical elements was the discovery that atomic electrons arrange themselves into discrete energy levels, referred to as orbitals. A cluster of these atomic orbitals with the same principal quantum number is known as an atomic shell. The presence of a large energy separation between neighboring orbitals indicates a shell closure, the effects of which are familiar to all in the electronic (and chemical) properties of the noble gases. The classic experimental signature of atomic shell structure is the periodic behaviour of the first ionization energies, which are plotted in Fig. 1.1. Certain numbers of electrons (2, 10, 18, *etc.*) have relatively large ionization potentials followed by steep drops in the next ionization potential. Such declines are the result of weaker binding of the next sequential electron. In other words, a single electron outside of a closed shell is easily removed from an atom. The quantum mechanically derived arrangement of electron orbitals shown schematically in Fig. 1.2a reproduces the numeric signatures seen in Fig. 1.1.

The atomic shell model was a triumph of early quantum mechanics in that it could

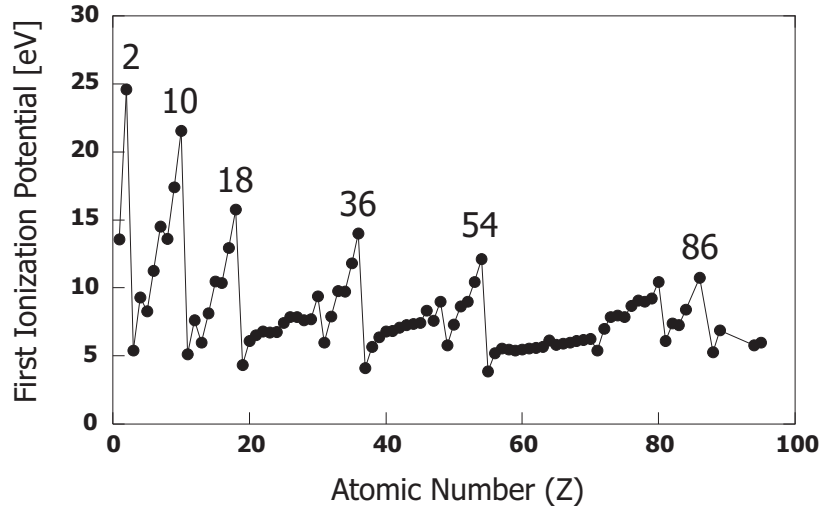


Figure 1.1: The atomic ionization energies up to  $Z \sim 93$ . The shell effects are clearly evident in the step decline of ionization potentials after certain values of  $Z$ .

explain properties known to chemists for many years such as discrete line spectra and chemical trends formally organized by Mendeleev in 1869. In the late 1940s the atomic shell model was adapted by nuclear physicists to describe the structure of the atomic nucleus. The nuclear shell model is based on the idea that protons and neutrons, independently, are arranged into characteristic orbitals. The attempt was in part motivated by the observation of periodic trends in experimental nuclear properties. Several nuclear properties suffice to illustrate this point, but the two-neutron separation energy ( $S_{2n}$ ) provides a particularly nice analogy. Simply stated, the  $S_{2n}$  is the energy required to remove two neutrons from a nucleus. One may regard  $S_{2n}$  as a nuclear ionization energy. Two-neutron rather than single-neutron separation is considered so as to avoid the odd-even zigzag effect caused by the energy associated with forming neutron pairs.

A plot of  $\Delta S_{2n}$  versus neutron number for several elements is shown in Fig. 1.3, where the quantity  $\Delta S_{2n}$  is given by

$$\Delta S_{2n} = S_{2n}^{exp} - S_{2n}^{semi} \quad (1.1)$$

in which  $S_{2n}^{exp}$  is the experimental two-neutron separation energy and  $S_{2n}^{semi}$  (given by

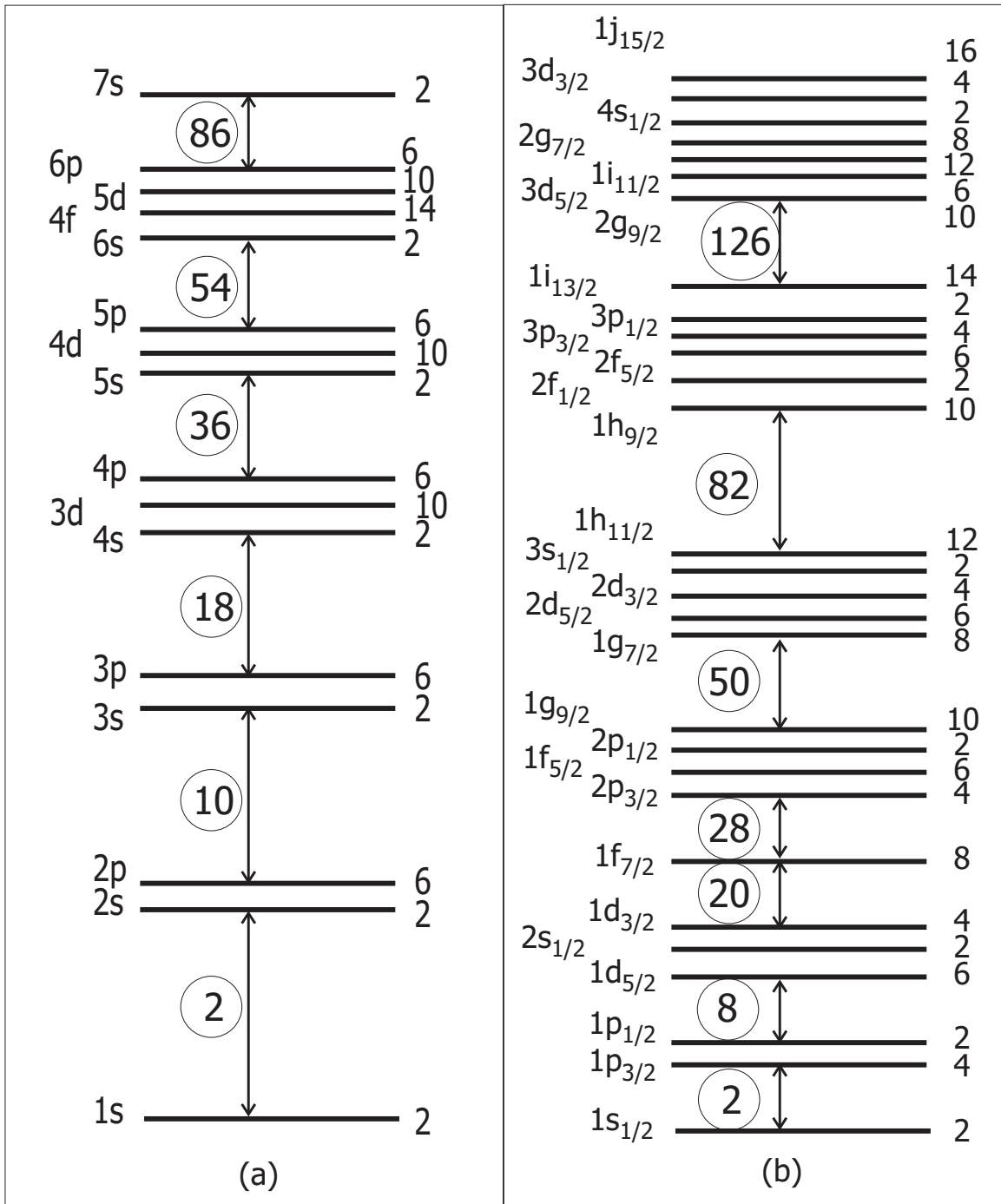


Figure 1.2: (a) Atomic orbital energy diagram. (b) Nuclear orbital energy diagram. The energies are not to scale in (a) or (b).

Eq. 1.2 where  $M_N$  is the mass of a neutron) is the two-neutron separation energy calculated from the semi-empirical mass equation [8].

$$S_{2n}^{semi} = M(Z, A - 2) - M(Z, A) + 2M_N \quad (1.2)$$

The semi-empirical mass equation may be expressed as

$$M(Z, A) = f_1(A)Z^2 + f_2(A)Z + f_3(A) - \delta \quad (1.3)$$

where  $\delta = 0$  for odd- $A$  nuclides,  $\delta = 11A^{-1/2}$  for even-even nuclides, and  $\delta = -11A^{-1/2}$  for odd-odd nuclides and where the coefficients  $f_1$ ,  $f_2$ , and  $f_3$  are given by

$$f_1(A) = 0.717A^{-1/3} + 111.036A^{-1} - 132.89A^{-4/3} \quad (1.4)$$

$$f_2(A) = 132.89A^{-1/3} - 113.029 \quad (1.5)$$

$$f_3(A) = 951.958A + 14.66A^{2/3} \quad (1.6)$$

The difference was considered in order to negate the overall variation of the nuclear binding energy. Comparison with the ionization potential plot (see Fig. 1.1) reveals analogous behaviour in the atomic and nuclear systems. For certain numbers of neutrons (2, 8, 20, 28, *etc.*) a steep decline in  $S_{2n}$  occurs on going to the next higher neutron number. In the nuclear shell model, the nucleon numbers where these rapid changes occur are called magic numbers. Following a magic number of neutrons, an extra pair of neutrons is more weakly bound than its predecessors, suggesting that the pair lies outside a closed neutron shell. A plot of two-proton separation energies as a function of atomic number ( $Z$ ) would reveal the same trends with the same magic numbers. Consequently, similar but independent shell structures can be applied to the two nucleons.

Mayer [9] and Haxel, Jensen and Suess [10] were the first to theoretically reproduce the observed nucleon magic numbers. Theoretical agreement with the magic numbers

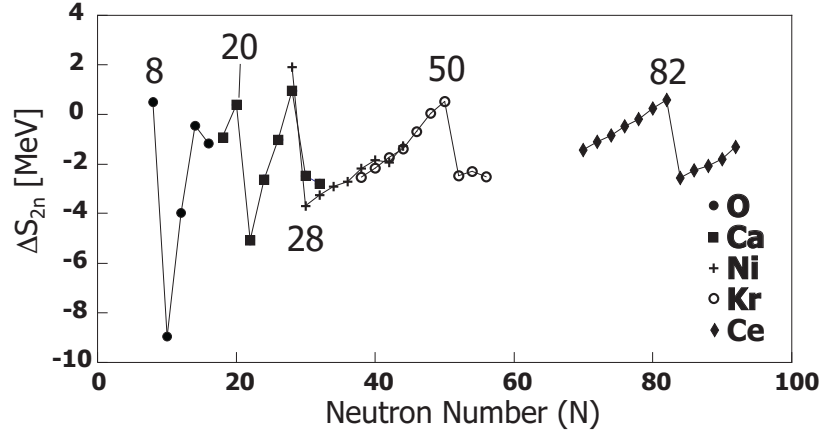


Figure 1.3: The  $\Delta S_{2n}$  values for several elements. The neutron-shell effects are clearly evident in the sharp drop in  $\Delta S_{2n}$  following the indicated neutron numbers.

was obtained by including a spin-orbit interaction in a nuclear potential with an appropriate shape. The underlying idea of the spin-orbit interaction is that a nucleon experiences different forces in the nucleus depending on whether its orbital angular momentum vector ( $\vec{\ell}$ ) is parallel or antiparallel to its intrinsic angular momentum vector ( $\vec{s}$ ). The potential energy term for this contribution may be written:

$$V_{SO} \propto V(r)\vec{\ell} \cdot \vec{s} \quad (1.7)$$

A central potential based on the spherical harmonic oscillator reproduces the first three magic numbers—2, 8, and 20—but fails to reproduce the higher magic numbers. Inclusion of the spin-orbit term in the potential exactly reproduces the empirical magic numbers, when the magnitude of the  $V(r)$  term in Eq. 1.7 is comparable to the spacing between the harmonic oscillator shells and the sign is negative. The nucleon orbital ordering is illustrated in Fig. 1.2b. The significant effect of the spin-orbit interaction is to drop higher-spin orbitals into the next lower oscillator shell. Consider for instance, the  $1h_{11/2}$  and  $1h_{9/2}$  orbitals, a spin-orbit pair that is part of the fifth harmonic-oscillator shell. The spin-orbit interaction lowers the energy of the  $1h_{11/2}$  orbital relative to the  $1h_{9/2}$  orbital, such that the former moves into the major shell below magic number 82, while the latter remains in the major shell above magic

number 82 (see Fig. 1.2b). The presence of these higher-spin orbitals just before a shell closure has a well known effect on nuclides near magic numbers of protons or neutrons that will be described later.

Despite the experimental similarities seen between the atomic and nuclear systems, the analogy is not perfect. Whereas in an atom the electrons are subject to an external potential from the nuclear charge, in a nucleus the protons and neutrons are subject to a potential created by the nucleons themselves. Furthermore, the exact form of the nuclear strong force is unknown, so the nuclear orbital ordering cannot be derived as in the case of the atomic orbital ordering. Nevertheless, using a variety of approximate nuclear potentials, nuclear theorists have been very successful in predicting nuclear shell structure and reproducing experimental observations over the last half-century (see Ref. [11]).

### 1.1.2 Low-Lying Nuclear Excited States

#### Single-Particle Nuclei

Once the fundamental properties of a nucleus such as half-life and decay modes are established, researchers in the field of nuclear structure turn to the arrangement and properties of nuclear excited states. In many cases the nuclear shell model provides a relatively simple explanation for the origin of nuclear excited states. In a first approximation, nuclear excited states arise from the properties of a few valence nucleons, *i.e.*, those nucleons that lie in unfilled shells. In an extreme approximation, the closed shell(s) beneath the valence shell may be thought of as an inert core. The model, in this regard, is once again analogous to the atomic shell model where chemical properties are due to the valence electrons and the inner shell electrons do not participate in chemical reactivity.

The valence-nucleon concept is illustrated in Figure 1.4, which shows the ground- and first five excited-state spins and parities of  $^{17}_8\text{O}_9$ . This nuclide has one neutron

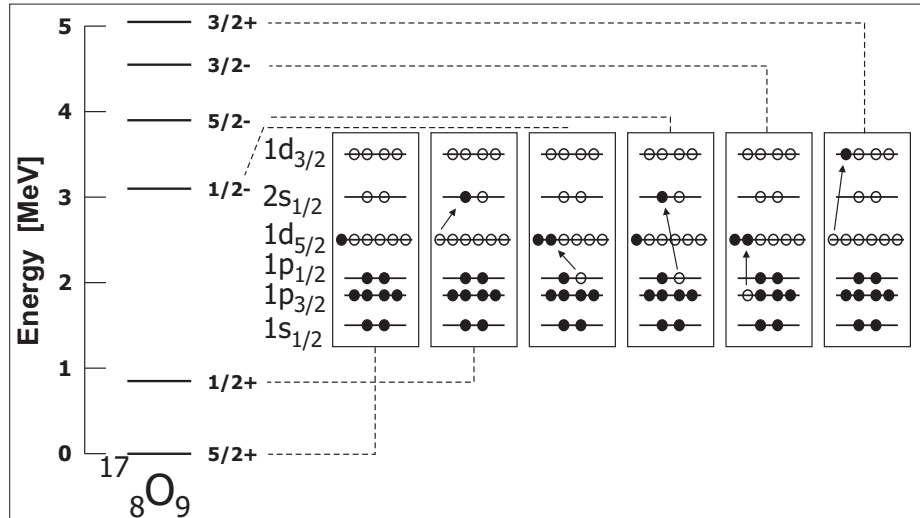


Figure 1.4: Within the shell model the first several excited states in  $^{17}\text{O}$  are explained by the valence neutron configurations. This figure is similar to Fig. 5.11 in Krane [12].

outside the doubly-magic  $^{16}_8\text{O}_8$  core. The spin and parity of  $5/2^+$  for the ground state is due entirely to the  $1d_{5/2}$  neutron since all other neutrons and all protons in this nucleus are inside closed shells. The ground-state spin comes directly from the total angular momentum of the odd neutron ( $J = 5/2$ ); the positive parity is given by  $(-1)^\ell$  where the orbital angular momentum value,  $\ell$ , is 2. The first excited state is explained by the promotion of this odd neutron to the  $2s_{1/2}$  orbital, and the spin and parity are explained in the same manner as the ground-state spin and parity. In general the term “extreme single-particle” model is used when referring to nuclei whose properties are determined solely by a single neutron or proton. Beyond the extreme single-particle picture, the third and fourth excited states of  $^{17}_8\text{O}_9$  are each produced by the coupling of two unpaired neutrons in separate orbitals; however, these odd-parity states actually result from the mixing of several of these configurations and are more complicated than suggested by the extreme single-particle model.

Simple application of the single-particle shell model, as detailed above, is quite useful in making first-order approximations, especially for ground-state spins and parities. Accurate shell-model descriptions of the ordering and spins and parities of nuclear excited states require sophisticated calculations and have used a variety of

available nuclear potentials that include effective interactions. Nevertheless, a number of nuclides close to closed shells have been studied and are well described by the single-particle shell model.

### **Few-Particle Nuclei**

The portrait that is painted above for the single-particle shell model is applicable to nuclei that have a single odd proton or odd neutron (or holes) outside of a closed shell. This is a relatively small set of nuclides, of course. For nuclei with several valence nucleons outside of closed shells (few-particle nuclei) the picture becomes more complicated. If an odd number of neutrons or protons are present, the single unpaired nucleon could be treated with the single-particle shell model and the other (paired) valence nucleons would be treated as part of the core of closed-shell nucleons. The paired valence nucleons are coupled to  $J = 0$ , just like the core. Configurations that involve splitting valence nucleon pairs are unlikely to contribute to low-energy excited states because the strong proton-proton (p-p) and neutron-neutron (n-n) pairing interactions make pair splitting energetically expensive. In general, a better overall description of the excited states is obtained by including all of the valence nucleons in a calculation. Nuclear properties are calculated in the shell model by assuming that nucleons are independent particles moving in a central potential with a residual nucleon-nucleon interaction strength that serves as an important fitted parameter. The presence of several valence nucleons in an incomplete shell leads to a large number of possible configurations of particles and holes, with the number of such configurations increasing to a maximum when the shell is half filled. Therefore, few-particle nuclides are computationally more complex than single-particle nuclides, but are nevertheless well described by the shell model [13].

## Collective Nuclei

The single-particle shell model represents one extreme picture of the atomic nucleus. At the other end of the spectrum the nucleus can be described in terms of the bulk properties of all nucleons. The description of nuclear properties based on the total behavior of all nucleons is known as the collective model. Nuclear properties are derived from macroscopic parameters such as mass, radius, and volume [14]. The collective model successfully accounts for the observed properties of many nuclides that have large numbers of valence nucleons that are found in between the magic numbers. The success of the collective model in describing low-lying states in terms of vibrations or rotations of the nucleus does not invalidate the shell model. Even in nuclei described macroscopically by the collective model, the shell model is still considered the appropriate microscopic model of the nucleus. In fact, it was theoretically demonstrated in the 1960s that collective properties do indeed arise within the shell model [15]. Thus, in principle the shell model is capable of describing nuclides with many valence particles; however, in practice, the computational complexity severely limits the number of nucleons that can be treated with the independent-particle assumption.

The applicability of the shell model and the collective model can be presented geographically on the nuclear landscape. The single-particle shell model is quite successful for nuclides within a few nucleons on either side of the proton and neutron magic numbers. Nuclides with proton and neutron numbers midway between magic numbers (midshell nuclides) are well described by the collective model. Figure 1.5 illustrates the distribution of shell-model versus collective nuclides for the  $Z = 50 - 82$  and  $N = 82 - 126$  shells. The regions in the figure marked “vibrational” and “rotational” represent collective nuclides. As this one shell illustrates, more nuclides are represented by the collective model than by the single-particle shell model [15], as there are more nuclides in the middle than on the edges of the diagram. The degree of collective behavior within a nucleus, known as “collectivity”, varies across a shell. In Figure 1.5, nuclides at the center of the circular region have the highest collectivity,

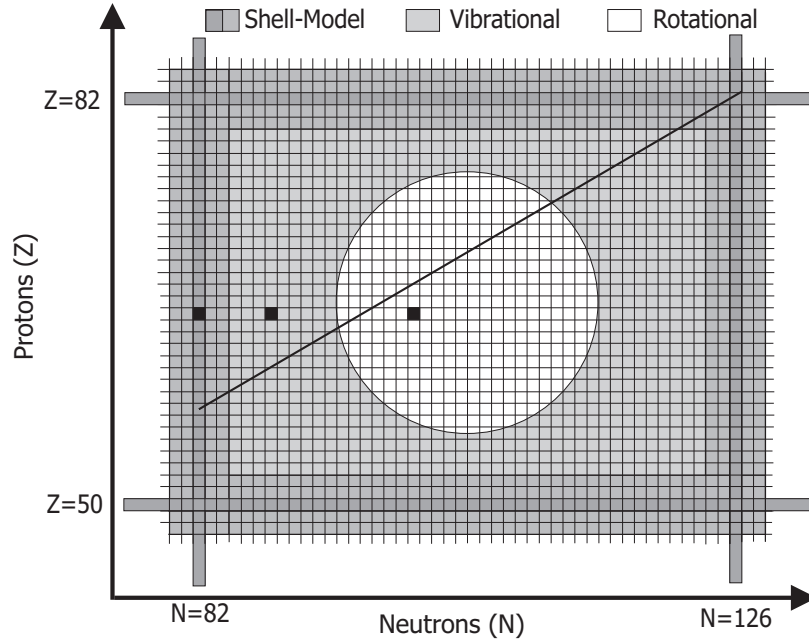


Figure 1.5: The regions of nuclides for which the shell model and collective model are applicable. Collective nuclides are located in the vibrational and rotational areas. The positions of  $^{148}\text{Dy}$ ,  $^{154}\text{Dy}$  and  $^{166}\text{Dy}$ , respectively, are marked by black boxes from left to right. The line of beta-stability is indicated by the solid line.

and the degree of collectivity decreases radially from the center.

Within the collective model nuclear excitations are generally explained in terms of the accumulating effect of residual interactions among the many valence nucleons [15]. A residual interaction is a small deviation from the approximate, average spherical potential felt by a nucleon, within the description of the shell model. The influence of the residual interactions on the spherical nuclear potential leads to changes in the static shape and dynamic shape (*i.e.* shape oscillations) [15]. The extent of the shape change depends upon the degree of collectivity in the nucleus. In certain nuclei, which have spherical equilibrium shapes, these excitations appear as shape vibrations. A convenient physical picture is that of a vibrating drop of liquid in which the excitation energy is described in terms of harmonic-oscillation phonons. Such nuclei are called spherical-vibrational and represent the lowest degree of collectivity. Nuclei with spherical equilibrium shapes are located near magic numbers of protons and neutrons; therefore, vibrational excitations occur in the region near, but not on,

the edges shown in Figure 1.5.

Moving deeper into a given shell, the number of valence nucleons increases further, leading to higher collectivity. The higher collectivity gives rise to nuclides with static deformations—as opposed to the dynamic deformations associated with nuclear vibrations. These nuclides have nonspherical equilibrium shapes that can undergo rotational excitation, much like molecules do. Deviation from sphericity in nuclei is quantified in terms of the axially-symmetric deformation parameter  $\beta$ . The definition of  $\beta$  is such that  $\beta < 0$  describes an oblate spheroid and  $\beta > 0$  describes a prolate spheroid. Asymmetric-rotational nuclei represent an intermediate degree of collectivity, and symmetric-rotational nuclei represent the highest degree of collectivity observed [15]. The region of rotational nuclides is indicated in the middle of the proton and neutron shells in Figure 1.5.

Collectivity increases smoothly up to the midpoint of the shell and decreases thereafter toward the next shell closure. The modes of excitations across the shell also vary smoothly, progressing from vibrational to rotational with mixed nuclides occurring throughout. The mixed nuclides display both vibrations and rotations in varying degrees.

### **Interacting Boson Model**

A successful model of collective nuclides, the interacting boson model (IBM), has been developed by Arima and Iachello [16–18]. The IBM is an algebraic (group theory) nuclear model that is based upon the dynamic symmetry of nuclides undergoing collective motion. It is an approximate model in that it assumes regular proton and neutron shell closures, and it is parameterized in terms of valence proton and neutron fermions that are paired up to form  $s$ - and  $d$ -wave bosons. The IBM also assumes that nuclear excitations arise only from these valence bosons and not the closed-shell core [19]. The IBM-2 is a more recent extension of the model that treats proton bosons and neutron bosons as separate entities.

## Systematics of the Energy of the First Excited $2^+$ State

The preceding paragraphs described broad classes of nuclides that ranged from single-particle shell model nuclides to collective vibrators and collective rotators. An experimental signature exists in nuclides that signals the onset of collectivity across a shell. Nuclear excited states are found, in certain nuclides, that are not easily explained by the single-particle shell model. The nuclides in this subset have even values of  $Z$  and even values of  $N$  (hence known as even-even nuclides) and, therefore, contain only paired nucleons. To apply the shell model to these nuclides, one must consider all excited states as arising either from the promotion of a pair of nucleons or from the breaking of at least one nucleon-nucleon pair. Since pair breaking requires approximately 2 MeV per pair, all states thus derived necessarily lie above 2 MeV of excitation. The promotion of a pair would generally require even more energy. However, many even-even nuclides have excited states far below this energy. The existence of the lower-energy excited states of even-even nuclides are, in fact, explained by the collective model. The first few excited states of two dysprosium isotopes,  $^{154}\text{Dy}$  and  $^{166}\text{Dy}$ , are given as examples in Figure 1.6 [20, 21].

A few similarities among the nuclear states of  $^{154}\text{Dy}$  and  $^{166}\text{Dy}$  should be noted. First, both of these nuclides have  $0^+$  ground states, a feature of all even-even nuclides, since all of the paired nucleons couple to  $J = 0$ . Second, the first excited states in both Dy isotopes have  $J^\pi = 2^+$ . This is also a feature of nearly all even-even nuclides—only a few exceptions have been found out of the hundreds of even-even nuclides that have been studied. Finally, in even-even nuclides a  $4^+$  excited state is always found somewhere above the first  $2^+$  state (written  $2_1^+$ ), and quite often it is the second excited state.

The excitation energies of  $2_1^+$ - and  $4_1^+$ -levels in even-even nuclides are commonly used as indicators of nuclear shape. Figure 1.6 shows the ground state and two excited states for three Dy isotopes and illustrates the fact that the energies of the  $2_1^+$ - and  $4_1^+$ -states both decrease relative to the ground state as the number of valence neutrons in

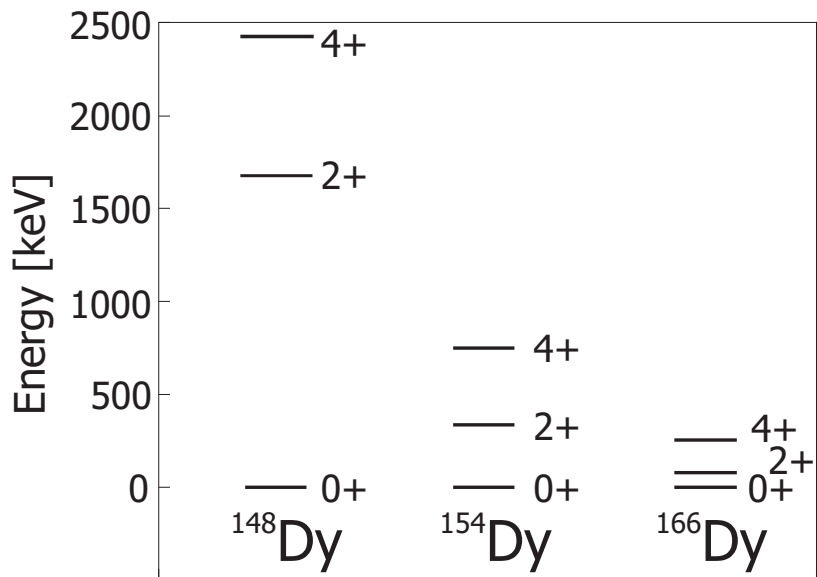


Figure 1.6: A comparison of the first excited  $2^+$  and  $4^+$  states of the even-even Dy isotopes indicated in Fig. 1.5.

these isotopes increases. (These three isotopes were chosen for their relative positions within the  $Z = 50 - 82$  and  $N = 82 - 126$  shells.) Referring to Figure 1.5,  $^{148}\text{Dy}$  with 82 neutrons lies within the range of shell-model nuclides;  $^{154}\text{Dy}$  with 88 neutrons lies in the range of vibrational nuclides with dynamic deformation; and  $^{166}\text{Dy}$  with 100 neutrons lies within the range of rotational nuclides with static deformation. The downward trend of the excited states observed in the Dy isotopes occurs smoothly towards midshell.

In particular, the energy of the first excited  $2^+$ -state, symbolized by  $E(2_1^+)$ , is an important systematic indicator of changes in nuclear structure. The variation of  $E(2_1^+)$  with neutron number for all known even-even Dy isotopes, shown in Figure 1.7, highlights the expected trend due to the onset of collectivity. Following the data from left to right,  $E(2_1^+)$  rises from the middle of the  $N = 50 - 82$  shell, peaks at magic  $N = 82$ , and decreases again toward the middle of the  $N = 82 - 126$  shell. Thus, the evolution from collective to single-particle and back to collective can be seen from the systematic variation of the energy of the  $2_1^+$  level. The element Dy was chosen as an example, but the analysis of  $E(2_1^+)$  values is applicable to even- $Z$  elements across the

chart of the nuclides. The inverse quantitative relationship between  $E(2_1^+)$  and the degree of collectivity in a nuclide is described in terms of the deformation parameter,  $\beta$ , by the empirical Grodzins' Rule [22, 23]:

$$E(2_1^+) = \frac{1225}{A^{7/3}\beta^2} \text{ MeV} \quad (1.8)$$

Earlier in this chapter the two-neutron separation energy was presented as an experimental quantity that can be used to indicate the presence of a shell closure (*i.e.* a magic number) among nucleon orbitals. The peak in the  $E(2_1^+)$  value at  $N = 82$  in Figure 1.7 also reveals the presence of a magic number. An increase in  $E(2_1^+)$  leading to a local maximum is thus another means of identifying a shell closure. A number of other experimentally derived quantities are also used to identify shell closures, including  $S_{2n}$  (from measured masses), the reduced transition probability  $[B(E2)]$  for the  $2_1^+ \rightarrow 0_{g.s.}^+$  transition, and the nuclear quadrupole moment. The use of  $E(2_1^+)$  for evaluating the  $N = 82$  shell closure was important to the present work, and will be discussed in a later section.

The systematic variation of the energy of the first  $2^+$  state can serve as one indicator of the transition from shell model to collective model. It also indicates the evolution within the collective model from spherical-vibrational to symmetric-rotational, based on the fact that rotational excitations are lower in energy than vibrational. However, another empirical parameter, the  $E(4_1^+)/E(2_1^+)$  ratio, can be used to distinguish amongst collective nuclides. As Figure 1.6 shows, both  $E(2_1^+)$  and  $E(4_1^+)$  track downward as collectivity increases, but they do not decrease with the same slope. The ratio of the energies is  $<2$  for shell-model nuclides and approximately 2.0 for spherical-vibrational nuclides just beyond a magic number (as expected for a harmonic oscillator). It increases to a value of 2.5 for asymmetric-rotational nuclides and rises to a limiting value of 3.33 for a perfect symmetric-rotational nucleus at midshell. The variation of  $E(4_1^+)/E(2_1^+)$  versus neutron number for the even-even Dy

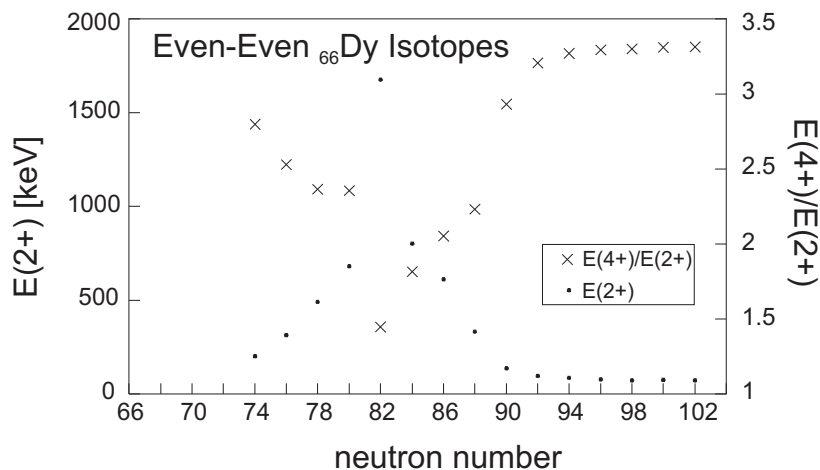


Figure 1.7: The  $E(2_1^+)$  and  $E(4_1^+)/E(2_1^+)$  values for all known even-even Dy isotopes.

isotopes is shown in Figure 1.7.

## 1.2 Nuclear Structure Near $^{132}\text{Sn}$

The study of the evolution of nuclear structure across the entire nuclear landscape is a large undertaking. The present work is concerned with the nuclear structure of neutron-rich nuclides very close to the  $Z = 50$  and  $N = 82$  magic numbers. The region of nuclides above  $Z = 50$  has been studied as far as, and beyond,  $N = 82$ ; however, below  $Z = 50$  only a few nuclides have been studied at  $N = 82$ , due to the difficulty of producing these extremely neutron-rich nuclides. Fortunately, new radioactive ion beam facilities are beginning to provide these  $Z < 50$ ,  $N \sim 82$  nuclides, but much remains to be learned about nuclear structure in this portion of the chart of the nuclides (see Fig. 1.8).

Much of what is known about nuclear shell structure has been derived from experimental work on stable nuclides or nuclides very close to stability. This is simply a consequence of accessibility—historically the means did not exist to produce exotic nuclides very far from stability. The well-known magic proton and neutron numbers have been validated in certain regions as experiment has pushed further out, but since the nature of the underlying nuclear force is not known it should not be assumed that



the magic numbers will remain magic in nuclides with extreme ratios of neutrons to protons. In fact, the smaller neutron magic numbers have already been observed to disappear in some neutron-rich nuclides [1–3].

Much is known about the  $N = 82$  nuclides above Sn, for example Figure 1.8 shows that just a few protons above  $Z = 50$ , stable nuclides appear at  $N = 82$ , so this region can hardly be called exotic. Figure 1.9 shows a plot of  $E(2_1^+)$  versus neutron number for  $_{52}\text{Te}$ ,  $_{54}\text{Xe}$ , and  $_{56}\text{Ba}$  isotopes. The peak in the  $E(2_1^+)$  values for the known isotopes of these three elements is evidence that, indeed,  $N = 82$  is observed to be a valid shell closure in this region.  $N = 82$  is known to be magic down to Sn, but it is not known how far below  $Z = 50$  this remains true. Recent experimental work along  $N = 82$  has been performed as far down as  $_{48}\text{Cd}$  [5,6]. However, the effect of the  $N = 82$  shell gap on  $E(2_1^+)$  values is also important in nuclides with  $N < 82$ . Similar to Figure 1.9, the  $E(2_1^+)$  systematics of three even- $Z$  elements below Sn are presented in Figure 1.10. The upward trend that is indicative of a shell closure is not yet apparent in the Ru isotopes (known only to midshell), may be beginning to be visible in the Pd isotopes, and appears to have flattened out in the Cd isotopes. Obviously more data need to be acquired for Pd and Ru in order to say anything about the goodness of the  $N = 82$  shell closure as far as  $Z = 46$  and  $Z = 44$ , respectively. Speculation regarding the quenching of the  $N = 82$  shell closure at  $Z = 48$  has led to some recent work on neutron-rich Cd up to  $N = 82$  [5,6].

Experimental interest in  $_{48}^{130}\text{Cd}_{82}$  over the past two decades has centered on its role as a classical neutron-magic waiting-point nuclide [24]. The path of the astrophysical rapid neutron-capture process ( $r$ -process) in the region near the  $Z = 50$  proton shell and the  $N = 82$  neutron shell is dependent on the nuclear structure properties of  $^{130}\text{Cd}$ . This strong interest from the nuclear astrophysics community has resulted in some recent experimental studies of  $^{130}\text{Cd}$ . Kautzsch *et al.* reported a single gamma ray at 957 keV correlated with  $^{130}\text{Cd}$  and postulated that it is the  $2_1^+ \rightarrow 0^+$  transition in this nuclide [6]. If this assignment is correct, then the  $E(2_1^+)$  of 957 keV, indicated

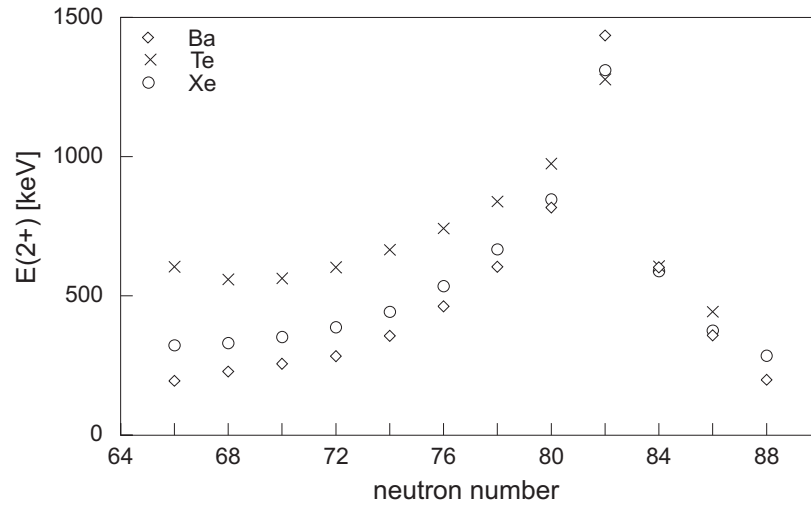


Figure 1.9:  $E(2_1^+)$  systematics of  $_{52}\text{Te}$ ,  $_{54}\text{Xe}$ , and  $_{56}\text{Ba}$  isotopes.

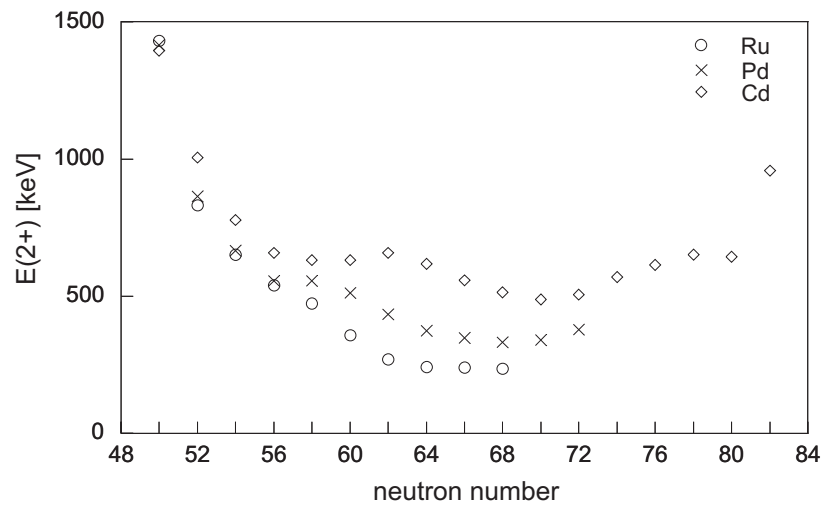


Figure 1.10:  $E(2_1^+)$  systematics of  $_{44}\text{Ru}$ ,  $_{46}\text{Pd}$ , and  $_{48}\text{Cd}$  isotopes.

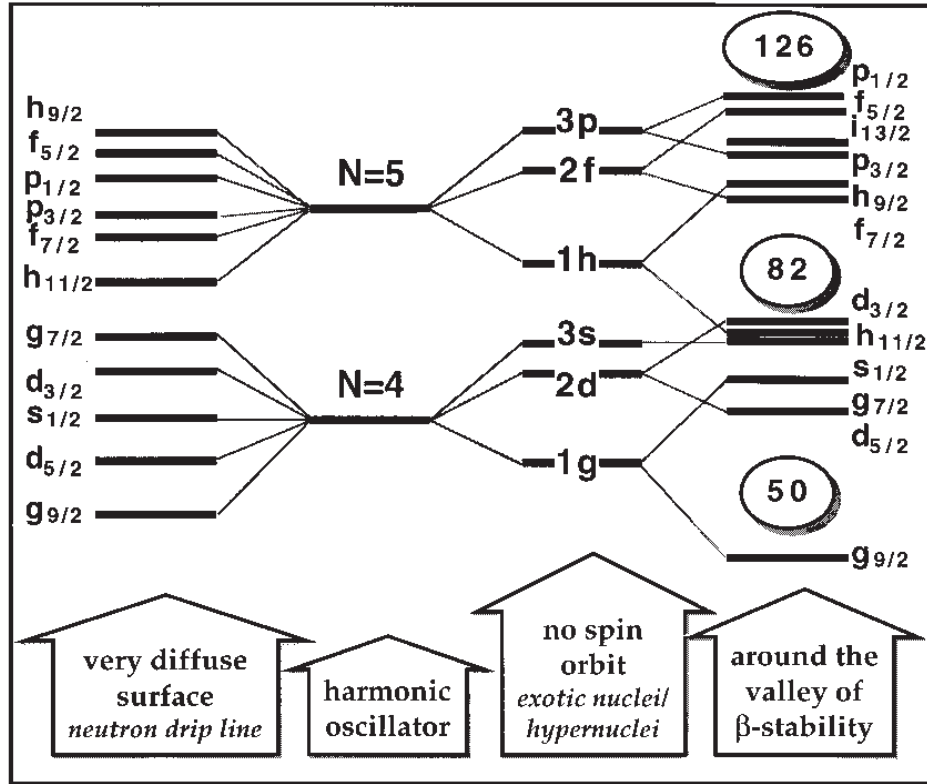


Figure 1.11: Single-particle orbitals for different potentials illustrating shell quenching near the neutron drip line. This figure is reproduced from Ref. [25].

in Fig. 1.10, is considerably lower than the  $\sim 1500$  keV that would be expected for a shell closure. The authors of Ref. [6] suggest that this is evidence of a reduction of the  $N = 82$  shell gap due to a reduction in neutron-neutron interaction strengths. Such a shell gap reduction, also known as shell quenching, would indicate that the magicity of  $N = 82$  is weakening and may completely disappear in elements further below  $Z = 48$ . The effect of shell quenching on the shell-model orbitals is illustrated in Figure 1.11, where the orbital sequence near stability is shown on the right and the new orbital sequence caused by a reduction of the neutron-neutron interaction strength is shown on the left. It should be noted that while Figure 1.11 illustrates single-particle orbital rearrangement near the neutron drip line, the region of nuclides being discussed here is quite far from the anticipated neutron drip line in the elements around Sn ( $N \sim 100$ ).

Concentrating on the Cd isotopes, the first measurement of the mass of  $^{130}\text{Cd}_{82}$

was reported by Dillmann *et al.* [5]. The mass, or  $Q_{\beta^-}$ , was measured by  $\beta$  end-point energy determination for the decay  $^{130}\text{Cd}_{82} \rightarrow ^{130}\text{In}_{81}$ . The authors noted that the experimental mass was larger than expected from some mass model calculations, such as the finite-range droplet macroscopic model (FRDM) [26], the extended Thomas-Fermi plus Strutinsky integral (ETFSI-1) [27], and the Duflo-Zucker mass formula [28], which all assumed a regular neutron shell closure at  $N = 82$ . In contrast, the Hartree-Fock-Bogolyubov (HFB) mean field model with SkP Skyrme effective interaction [25] and the ETFSI-Q model with SkSC4 interaction [29] both predict a mass for  $^{130}\text{Cd}$  that is closer to the new experimental value. The latter two models include neutron shell quenching at  $N = 82$ —the ETFSI-Q model includes quenching explicitly, albeit phenomenologically with an added  $N - Z$  term. The predictions of the mass models just described are illustrated in Figure 1.12. In the figure the reduced deviation of the mass from one of the models taken as a reference is plotted as a function of neutron number for the Cd isotopes. One can see that at larger neutron number ETFSI-Q follows the trend observed in the experimental and evaluated mass values [30, 31], whereas the non-quenching models (*i.e.* ETFSI-1) show the opposite trend. However, the calculated masses at  $N = 82$  are all rather close to the experimental data point, suggesting that this result is not definitive regarding the reduction of the  $N = 82$  shell gap in Cd isotopes.

The investigations of  $^{130}\text{Cd}$  described above are an important beginning to understanding the evolution of the  $N = 82$  shell closure below Sn, but more work must be done. Improved production yields of  $^{130}\text{Cd}$  at new radioactive beam facilities will enable future experiments to either confirm or refute these results. Just as important, however, are investigations in other neutron-rich nuclides in this region below Cd. Producing isotopes of these elements with 82 neutrons is extremely difficult, but much can be learned from the nuclides approaching  $N = 82$ .

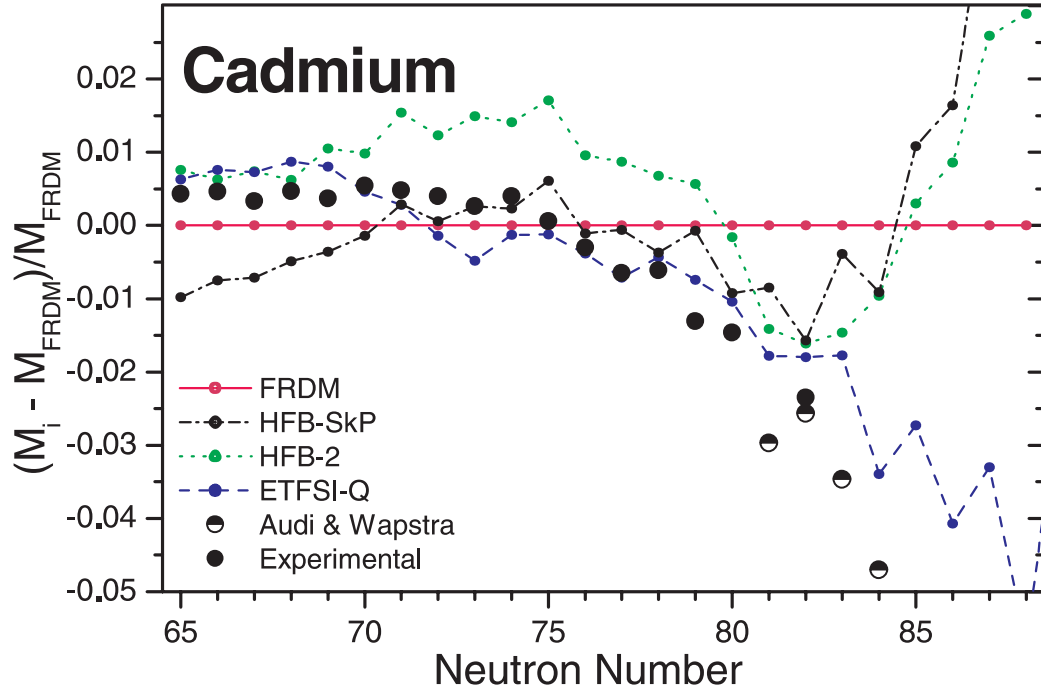


Figure 1.12: A comparison of experimental Cd masses and mass model predictions. Divergence of the mass models is evident at larger neutron numbers. This figure is reproduced from Ref. [5].

### 1.3 Proposed Experiment

The open question of  $N = 82$  shell quenching is certainly interesting and worthy of further investigation. The experimental work described in this document represents an attempt to further our understanding of the evolution of the  $N = 82$  shell in neutron-rich nuclides. In order to address the quenching of the  $N = 82$  shell below  $Z = 50$ , an experiment was performed at the National Superconducting Cyclotron Laboratory in 2003. In this experiment, neutron-rich nuclides in the region  $Z < 50$ ,  $N \sim 82$  (Fig. 1.13) were produced and studied by a combination of beta-gamma spectroscopy and isomer-decay spectroscopy. The use of both spectroscopies allowed a study of the quantum structure of beta-decay parent and daughter nuclides. The excited states, thus derived, were used to further the systematics of both odd- and even- $A$  isotopes of several elements and to understand the effect of the  $N = 82$  shell in the nuclides that were studied. The next chapter will provide a succinct review of the decay spectroscopies employed to study exotic neutron-rich nuclides. It

is not intended to be exhaustive, but merely to aid the reader in understanding the techniques employed. Subsequent chapters will describe the experimental methods, results and conclusions drawn from our results.



# Chapter 2

## Methods

The present work is concerned with determining the extent to which the  $N = 82$  shell gap is preserved for certain neutron-rich isotopes of Cd, Ag, Pd, Rh and Ru in the  $A \sim 120$  regime. The validity of this shell closure was tested by probing low-energy excited states of these nuclides. Two methods were employed to access quantum states of the nuclear systems. One of these methods, beta-gamma spectroscopy, provides information about the excited states of a daughter nucleus. The other method, isomer-decay spectroscopy, provides information about the excited states of a parent nucleus. These methods will be described in the following sections.

### 2.1 Populating Nuclear Excited States

#### 2.1.1 Beta Decay

One of the earliest observed radioactive decay modes was the emission of fast electrons from the atomic nucleus. The related processes of positron emission ( $\beta^+$ ) and orbital electron capture (EC) have been grouped with the former and are collectively known as beta decay. The basic process of beta decay involves the conversion of a neutron

into a proton (or a proton into a neutron in the case of  $\beta^+$  and EC):

$$n \longrightarrow p^+ + e^- + \bar{\nu} \quad (2.1)$$

$$p^+ \longrightarrow n + e^+ + \nu \quad (2.2)$$

$$p^+ + e^- \longrightarrow n + \nu \quad (2.3)$$

$\beta^-$  decay is the only mode that will be discussed in the present work. The process of  $\beta^-$  decay involves the emission of an electron and an electron anti-neutrino, each with a total angular momentum  $J$  (orbital plus intrinsic), from a parent nucleus (with a certain angular momentum) to a daughter nucleus (with its own angular momentum). Conservation of momentum requires that only certain combinations of the above momenta are possible in each case. Additionally, experimental observations reveal that emissions of the lowest angular momentum occur much more frequently than others. The wavefunctions of the parent and daughter nuclei and the wavefunctions of the emitted particles also have a quality known as parity ( $\pi$ ), related to the symmetry properties of the wavefunctions. Parity describes how the sign of the wavefunction changes with an inversion of all spatial coordinates and can take one of two values, even (+) or odd (-). Beta decay can produce a daughter state with the same parity or opposite parity to that of the parent state. The momentum and parity conditions lead to the division of beta decay phenomena into processes termed “allowed” decays and “forbidden” decays. The forbidden decays are further divided into increasing degrees of forbiddenness (*i.e.* first-forbidden, second-forbidden, *etc.*). Each subset of beta decay has a set of rules for the angular momentum and parity changes between the initial and final nuclear states. These are referred to as the selection rules (see Table 2.1).

The beta decay of a nucleus produces a daughter nucleus either in its ground state or in an excited state. The probability that a given state in the daughter is populated following beta decay is dependent on the degree of forbiddenness of the

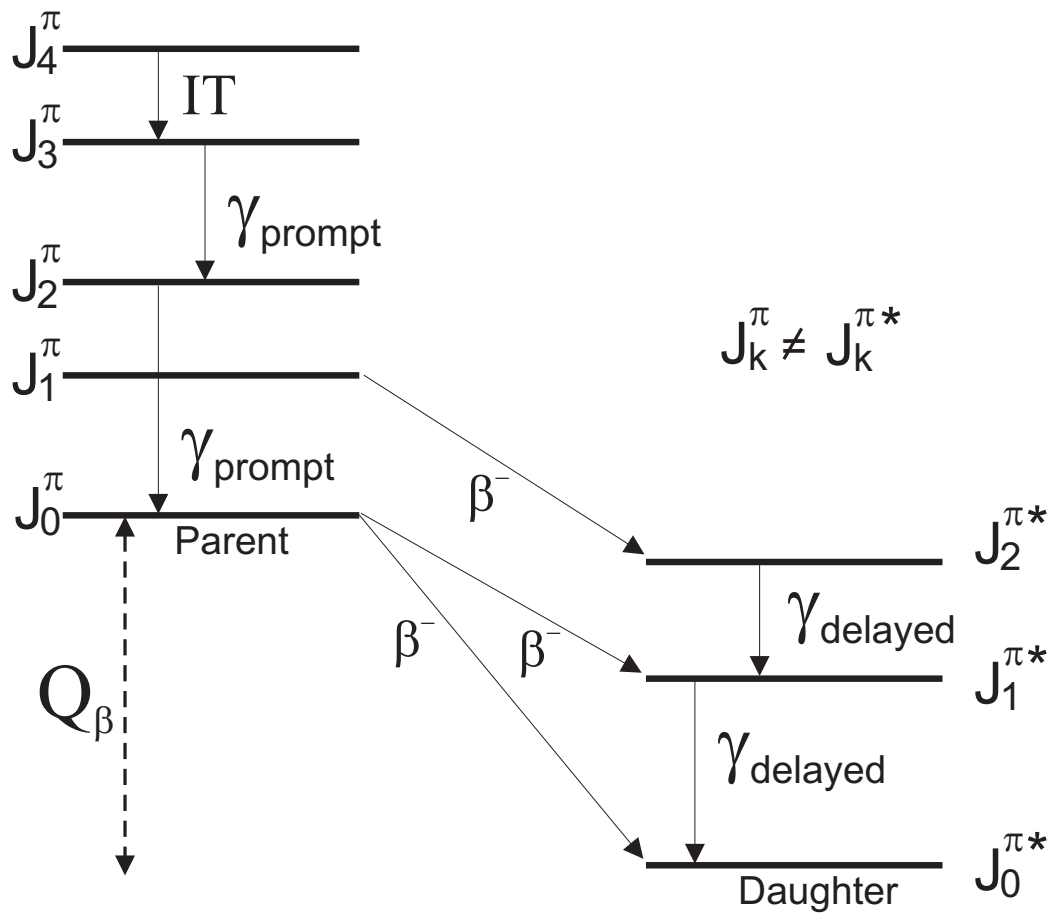


Figure 2.1: Schematic representation of beta-gamma spectroscopy and isomer spectroscopy.

Table 2.1: Beta-decay selection rules.

Decay Mode	$\Delta J$	$\Delta \pi$
superallowed ( $0^+ \rightarrow 0^+$ )	0,1	no
allowed	0,1	no
first-forbidden	0,1,2	yes
second-forbidden	2,3	no
third-forbidden	3,4	yes
fourth-forbidden	4,5	no

decay (weighted by the energy difference between the states to the fifth power). For example, beta decay from a  $1^+$  parent state to a  $0^+$  daughter state is accomplished with  $\Delta J = 1$  and no parity change. As Table 2.1 shows, this is classified as an allowed decay. Now suppose that the decay populates a  $3^+$  daughter state from the same parent state. A  $\Delta J = 2$  with no parity change indicates a second-forbidden decay. The  $1^+ \rightarrow 0^+$  transition has a higher probability of occurring in a given decay than does the  $1^+ \rightarrow 3^+$  transition, if all other factors are equal.

As discussed above, beta decay does not always lead to a daughter nucleus in the ground state. Frequently it is found that some higher-lying states can be populated in a daughter nucleus. While all energetically possible branches may be present, those that are less forbidden will dominate. The fraction of all beta decays that lead to a given state in the daughter is called the branching ratio to a state.

By taking advantage of the selectivity of the beta-decay process, spin and parity assignments in nuclei connected by beta decay can be made with some degree of confidence. More importantly, beta decay often provides a means of directly populating different quantum states of a daughter nucleus. Probing a nucleus by measuring the properties of these quantum states is a mechanism by which the nuclear structure of the daughter system can be elucidated. Beta decay was employed in the present work to populate excited states in isotopes of  $_{45}\text{Rh}$ ,  $_{46}\text{Pd}$ , and  $_{47}\text{Ag}$ .

### 2.1.2 Isomeric Transitions

In order to populate an excited state in a daughter nucleus the parent nucleus must first be produced. Notice that having one more neutron and one fewer proton, the parent nucleus is more exotic than the daughter and often harder to produce. To study a nuclide without first producing the even more exotic parent nuclide, excited states must be populated by other means. In the present work nuclear excited states in certain nuclides were observed by isomeric transitions.

An isomer is an excited state of a nucleus that has relatively long lifetime compared

to other nearby states in the same nucleus. In practice, a lifetime greater than  $10^{-9}$  s is usually considered isomeric when compared to the typical lifetime of a typical gamma-emitting excited state of less than  $10^{-12}$  s. This definition of isomerism is not rigorous, but rather is a working description based on the finite resolving times of nuclear detection systems. As the time resolution of a detection system becomes smaller, states with even shorter half-lives could be considered isomeric.

In general, isomerism is explained by the poor quantum-mechanical overlap of the wavefunction of the isomeric state and wavefunctions of the states just below it in energy. This poor overlap is often associated with large angular momenta and significantly reduces the probability that a gamma transition will occur between the isomeric state and the ground- or other lower-lying states. The reduced transition probability is manifest as a longer half-life for the isomeric state. The decay of an isomer by emission of a gamma ray is known as an isomeric transition (IT). An IT may populate a series of excited states with lower energy than the isomeric state via a cascade of gamma decay. The example on the left-hand side of Figure 2.1 illustrates how an IT populates excited states in a sequential process. In this work isomers with microsecond lifetimes, produced in the projectile-fragmentation process (described in Section 3.1), were used to learn about nuclides not populated by beta decay.

## 2.2 Nuclear Excited-State Spectroscopy

The previous section discussed two means of populating excited states in a nucleus—beta decay and isomeric transitions. The following section will describe the method, gamma-ray spectroscopy, that was used to study nuclear excited states. A general explanation of gamma decay and the techniques used to translate gamma-ray spectral observations into a description of nuclear excited states will be given.

### 2.2.1 Gamma Decay

A nucleus in an excited state typically returns to its ground state by the emission of one or more photons in a process known as gamma decay. The excited daughter states that are produced via beta decay usually undergo gamma decay. Gamma rays emitted following beta decay are said to be emitted in coincidence with the beta particle and are referred to as beta-delayed gamma rays (see Fig. 2.1 for transitions labeled  $\gamma_{delayed}$ ). Nuclear excited states can also be populated by processes other than beta decay, such as fission or nucleus-nucleus collisions. Gamma rays emitted from these excited states or following an IT are referred to as prompt gamma rays (see Fig. 2.1 for transition labeled  $\gamma_{prompt}$ ). Prompt and beta-delayed gamma-ray energies range from tens of keV to several MeV.

In addition to removing energy from the excited state, gamma-ray photons also carry angular momentum. This angular momentum is manifest in the multipole order of the photons. Each photon carries  $L\hbar$  units of angular momentum, where  $L$  is the order of the multipole (*i.e.*  $L = 2$  is quadrupole,  $L = 3$  is octupole, *etc.*). The electromagnetic character of the radiation (electric versus magnetic) is determined by the change of parity between the states connected by the gamma decay. In analogy with beta decay, a set of selection rules for gamma decay has been formulated to describe the type of gamma ray expected for a given transition. The possible multipolarities for a gamma transition are given by the following expression relating the angular momenta:

$$|J_i - J_f| \leq L \leq (J_i + J_f) \quad (2.4)$$

where  $J_i$  and  $J_f$  are the spins of the initial and final nuclear excited states, respectively. The parity selection rules are given in Table 2.2.

The above selection rules allow for several types of gamma rays, symbolized as either  $EL$  or  $ML$ , for a given transition between nuclear states. For instance, the radiation field of a given gamma ray could be electric quadrupole whereas another could

Table 2.2: Parity selection rules for gamma-ray emission.

	$L = \text{even}$	$L = \text{odd}$
$\Delta\pi = \text{no}$	electric	magnetic
$\Delta\pi = \text{yes}$	magnetic	electric

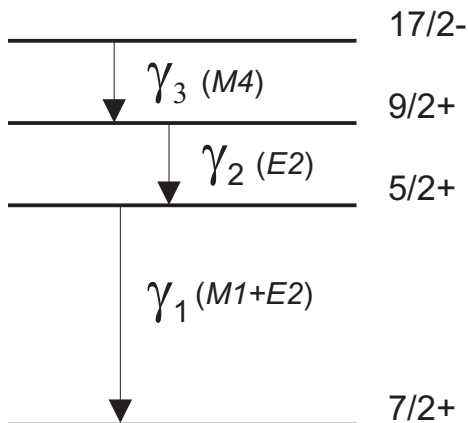


Figure 2.2: Schematic representation of gamma decay.

be magnetic octupole, written as  $E2$  and  $M3$ , respectively. Application of Eq. 2.4 when  $J_i$  and  $J_f$  are both nonzero results in several possible values of  $L$ . This point is illustrated with the help of Figure 2.2. The transition  $\gamma_1$  shown in the figure yields  $L = \{1, 2, 3, 4, 5, 6\}$ . All six of these values are possible, but the probability that an emitted gamma ray will have a given multipolarity varies considerably with the value of  $L$ . The transition associated with each of the possible  $L$  values has a partial decay constant [ $\lambda(EL)$  or  $\lambda(ML)$ ] that describes the probability for such a transition to occur. A useful set of equations, known as the Weisskopf estimates [32], has been derived for approximating transition probabilities as functions of  $A$  and the gamma-ray energy  $\mathcal{E}$ . The Weisskopf estimates are based on a quantum mechanical treatment of the  $2^L$ -pole radiating nucleus, where the transition of a single proton from one shell-model orbital to another is solely responsible for the radiation [33]. The Weisskopf estimates,

taken from Ref. [33], for the lowest four multipoles are given in Eqs. 2.5-2.12

$$\lambda(E1) = 1.0 \times 10^{14} A^{2/3} \mathcal{E}^3 \quad (2.5)$$

$$\lambda(E2) = 7.3 \times 10^7 A^{4/3} \mathcal{E}^5 \quad (2.6)$$

$$\lambda(E3) = 3.4 \times 10^1 A^2 \mathcal{E}^7 \quad (2.7)$$

$$\lambda(E4) = 1.1 \times 10^{-5} A^{8/3} \mathcal{E}^9 \quad (2.8)$$

$$\lambda(M1) = 5.6 \times 10^{13} \mathcal{E}^3 \quad (2.9)$$

$$\lambda(M2) = 3.5 \times 10^7 A^{2/3} \mathcal{E}^5 \quad (2.10)$$

$$\lambda(M3) = 1.6 \times 10^1 A^{4/3} \mathcal{E}^7 \quad (2.11)$$

$$\lambda(M4) = 4.5 \times 10^{-6} A^2 \mathcal{E}^9 \quad (2.12)$$

where  $\lambda$  has units of  $\text{s}^{-1}$  and  $\mathcal{E}$  is in MeV.

For a given transition type ( $E$  or  $M$ ) in a given nucleus, the lowest possible multipolarity is the most probable. In the example of Figure 2.2, the  $5/2^+ \rightarrow 7/2^+$  transition most likely radiates an  $M1$  gamma ray; however, for certain values of  $A$  and  $\mathcal{E}$ , an  $E2$  gamma ray has a comparable transition probability. In some collective nuclides an  $E2$  can actually be more probable than an  $M1$  [33]. It should be noted that mixed  $M1 + E2$  gamma transitions are commonly found in nuclei, meaning that both types of electromagnetic radiation will be observed. The origin of the  $M1 + E2$  transition can be understood based on their comparable gamma transition probabilities.

A different scenario may be seen in the other transition of Figure 2.2. The  $\gamma_2$  transition yields  $L = \{2, 3, 4, 5, 6, 7\}$ , with the lowest-order transitions being  $E2$  and  $M3$ , respectively. Based on the Weisskopf estimates for  $E2$  and  $M3$ , this transition would be expected to produce an  $E2$  gamma ray since the  $M3$  is less probable by many orders of magnitude. Thus, in practice only one type of electromagnetic radiation would be observed for this transition, even though several types are possible in principle.

It should be stressed that the  $\lambda$  values obtained from the Equations 2.5—2.12 represent estimates based on the single-nucleon assumption and deviations from experimental values are frequently observed. Contrary to what is expected from the Weisskopf estimates, higher multipolarity gamma rays ( $L = 3, 4$ ) are observed with significant intensity in some nuclides, which indicate that the transition is carried out by more than a single nucleon. Gamma transitions arising from the movement of several valence nucleons among shell-model orbitals would not be expected to agree well with Weisskopf estimates due to the nature of the underlying assumption. In this regard, experimental deviations give hints as to the nature of the interaction that gives rise to the gamma transition.

The above paragraphs were intended to provide a succinct description of gamma ray characteristics. The next section describes how these gamma ray properties were used to elucidate the quantum structure of the nuclides of interest.

## 2.2.2 Data Analysis Methods

The exotic nuclides that were investigated in the present work were studied by means of gamma-ray spectroscopy, a technique of elucidating nuclear structure by observing the gamma rays emitted from nuclear excited states. The level structure of a nuclide can be well described by the application of information obtained from gamma-ray spectroscopy, since a number of observables give direct structural information. In a typical experiment the energy and intensity of each observed gamma ray is measured. The gamma-ray energy reveals the energy separation between two states. For a transition that feeds into the ground state (zero excitation energy), the gamma-ray energy is the excitation energy of the decaying state. Excited states may be depopulated by a cascade of gamma rays rather than a transition directly to ground state. The excitation energies of states like these can be deduced by calculating the sums of the observed gamma-ray energies. For instance, excited states are frequently depopulated by multiple paths, and the sums of the gamma energies along each path should add

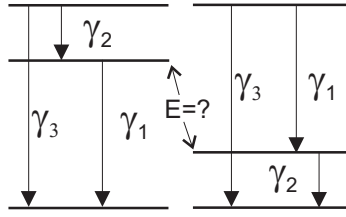


Figure 2.3: Schematic representation of gamma cascade. Energies are insufficient to determine the first excited state.

up to the excitation energy of the state ( $E_{\gamma_3} = E_{\gamma_1} + E_{\gamma_2}$  Fig. 2.3). The appearance of the same energy value from the sums of different gamma rays is a strong indicator that a level probably exists at that energy.

Calculating gamma-energy sums is an easy means to identify level energies, but gamma-gamma coincidences provide reliable information about the relationships between gamma transitions. The nuclear states that connect gamma transitions in a cascade normally have very short lifetimes ( $< 10^{-12}$  s), such that these gamma rays are emitted in rapid succession. The time resolution of current gamma-ray detectors is significantly longer than these lifetimes, and as a consequence, successive gamma rays are often detected coincidentally. Depending upon the interrelationships of transitions in a nucleus, multiple gamma rays may be detected in coincidence with a given transition. A gamma-ray spectrum of all gamma rays detected in time coincidence with the given transition is called a gamma-gamma coincidence spectrum. Gamma-gamma coincidence spectra indicate the component transitions of gamma cascades. Knowledge of the cascade determines the energy of the level at the top of the cascade but sometimes several possibilities exist for the intermediate levels. This is illustrated in Figure 2.3, where the order of gamma transitions 1 and 2 is needed to assign the energy-order of the states.

Gamma-ray energies do not necessarily reveal transition order. Gamma-ray intensities help in this regard. The intensity of a gamma ray leading out of a level should equal the sum of the intensities of all gamma rays that feed that level (see Fig. 2.4), assuming that the level in question is not fed directly by beta decay. Fre-

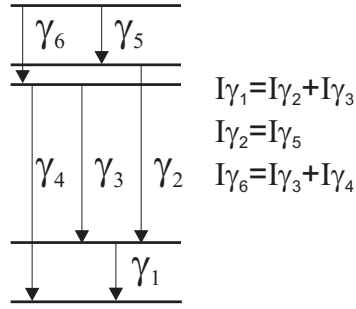


Figure 2.4: Schematic representation of gamma cascade. The interrelated intensities ( $I_{\gamma}$ ) clarify the order of gamma transitions.

quently gamma-ray intensity helps to identify the lowest transition where several cascades merge, since all of the gamma strength from above feeds into that one transition. Thus, an ordering of gamma transitions can be made in some cases based on intensities.

Spins and parities of nuclear excited states can also be obtained from the spectroscopic measurements. As just discussed, the multipole order of the gamma ray is dependent on the angular momentum of the photon, which in turn is dependent on the spins of the connected states. If angular-correlation measurements are performed, then the  $J^{\pi}$  value of the initial or final state can be assigned, assuming that the other is already known; however, in the absence of angular correlation measurements, some assumptions can be made regarding the initial and final state spins and parities. Gamma rays of the  $M1$ ,  $E1$  and  $E2$  types are much more common than other multipole orders, and these gamma photons are identified with  $\Delta J=1$  or  $2$ . In experiments like the present work, the most intense gamma rays are more likely to be seen. Thus, transitions between states that differ in spin by one or two units should predominate. In practice,  $J^{\pi}$  assignments are rarely made without reference to neighboring isotopes. Even in exotic nuclides, the systematics of excited states for isotopes closer to stability provide strong indications of what the level spins probably are.

In experiments, such as the one presented in the current work, the strongest beta-decay branches into the daughter nuclide are observed. As already mentioned this tends to select allowed or first-forbidden branches that most likely have  $\Delta J=0,1$ .

Assuming that the parent  $J^\pi$  is known then the  $J^\pi$  of populated daughter states can be tentatively assigned or at least narrowed to two or three possible values.

In summary, gamma-transition energies are measured experimentally, and the energies of nuclear excited states are determined using a combination of gamma energy sums and gamma-gamma coincidence relationships. Gamma-ray intensities are also measured and are used to order gamma transitions within cascades. Based on the predominance  $\Delta J=1,2$  gamma transitions and the information provided by excited-state systematics, tentative  $J^\pi$  assignments can be made for nuclear excited states.

Two broad categories of gamma rays were mentioned earlier—beta-delayed gamma rays and prompt gamma rays. Nuclear structure details about the exotic nuclides of interest were obtained by both beta-delayed gamma-ray spectroscopy and prompt gamma-ray spectroscopy. Whereas beta-gamma spectroscopy reveals information about the daughter nucleus, prompt gamma-ray spectroscopy provides information about the parent nucleus. Much of what was described above regarding beta-gamma spectroscopy also holds true for the application of prompt gamma spectroscopy. The measurement of prompt gamma-ray energies, intensities and gamma-gamma coincidence relationships aids in the construction of level structures. Assignments of  $J^\pi$  to excited states are, once again, made based on systematics and the predominance of  $\Delta J=1,2$  gamma-ray transitions.

The preceding sections described a number of beta- and gamma-decay observables that are used to understand nuclear structure. In the present work the following were recorded: beta-decay half-lives, beta-delayed gamma-ray energies, relative intensities and coincidence relationships; isomeric half-lives; prompt gamma-ray energies, relative intensities and coincidence relationships. The next chapter will describe the experimental techniques that were employed to measure the aforementioned observables as a means toward understanding the influence of  $N = 82$  in neutron-rich isotopes of Cd, Ag, Pd, Rh, and Ru.

# Chapter 3

## Experimental Setup and Technique

### 3.1 Radionuclide Production

The neutron-rich nuclides that were investigated in the present work were produced using the National Superconducting Cyclotron Laboratory (NSCL) Coupled-Cyclotron Facility at Michigan State University as part of experiment number 01015. A schematic of the facility layout is shown in Fig. 3.1. The linking of the existing K500 and K1200 cyclotrons, completed in 2001, created a facility capable of producing radioactive ion beams via projectile fragmentation of intense, intermediate-energy primary beams of relatively heavy ions. The A1900 projectile-fragment separator [34] was concurrently constructed to provide a means of selecting nuclides of interest from the distribution of fragmentation products. A description of the cyclotron-separator system, in the context of how it was employed in Experiment 01015, is given in the next several paragraphs.

#### 3.1.1 Projectile Fragmentation

Radioactive ion beams are produced at the NSCL via the process of projectile fragmentation, which takes advantage of the relatively high-energy beams that can be obtained with the coupled superconducting cyclotrons. Projectile fragmentation [35],

as employed in the present work, is the process whereby a projectile ion makes an inelastic collision with a target ion. The interaction effectively shears off a number of nucleons from the projectile ion in a step referred to as abrasion. The remnant of the projectile ion (*i.e.* the fragment), which continues moving in the forward direction due to the kinematics, is usually left in an excited state. Cooling of the fragment may subsequently occur as a few nucleons evaporate in a process known as ablation. The net result of an ion beam undergoing the abrasion-ablation processes is a wide distribution of fragments with masses ( $A$ ) and atomic numbers ( $Z$ ) below that of the original projectile ion. These fragmentation products make up a secondary beam that also contains energy-degraded primary beam ions that passed through the target without reacting.

A primary ion beam of  $^{136}_{54}\text{Xe}_{82}$  and a target of  $^9_4\text{Be}$  were used in the present work. These choices were made to maximize the production yield of  $^{120}_{45}\text{Rh}_{75}$ , within the range of available beam-target combinations. Production yields were calculated using the computer program LISE [36]. The reaction parameters that were optimized included the primary beam energy, beam current, target material (*e.g.*  $^9\text{Be}$  versus  $^{nat}\text{Ni}$ ), and target thickness. A suitable production rate for  $^{120}\text{Rh}$  was found using a primary beam of  $\leq 10$  pnA at an energy of 120 MeV/nucleon with a 188 mg/cm<sup>2</sup> Be target. The calculated yield of  $^{120}\text{Rh}$  was 183 particles/hour/pnA of primary beam, representing approximately two percent of the mixed secondary beam after the separator.

### 3.1.2 Primary Beam

The primary ion beam begins at the ion source, where the stable isotope of choice is volatilized and partially ionized in an electron-cyclotron resonance (ECR) ion source. The gas-phase ions are emitted from the source into the K500 cyclotron with energies on the order of 100 keV. Primary acceleration of the beam then occurs in the K500 cyclotron. The ion beam is extracted from the K500 and passes via an evacuated beamline into the K1200 cyclotron where further electron stripping increases the ionic

charge. Secondary acceleration of the beam in the K1200 results in the final beam energy. Primary beam energies up to 200 MeV/A can be obtained with the coupled cyclotrons. The fully accelerated beam emerges from the K1200 and travels down a short segment of beamline to the target box where it is impinged on the production target.

In order to produce neutron-rich nuclides in the  $A \sim 120$  region, a primary beam of  $^{136}\text{Xe}$  was chosen. The choice of primary beam was essentially constrained to a list of previously developed beams. Within the list of available beams, the choice was based on the proximity of the primary-ion mass to the masses of the desired nuclides, as the probability for producing a given nuclide is greater the closer that nuclide's mass is to the primary-ion mass. For our purposes  $^{136}_{54}\text{Xe}$  provided the best available choice to access the neutron-rich nuclides around  $A \sim 120$ ,  $Z < 50$ .

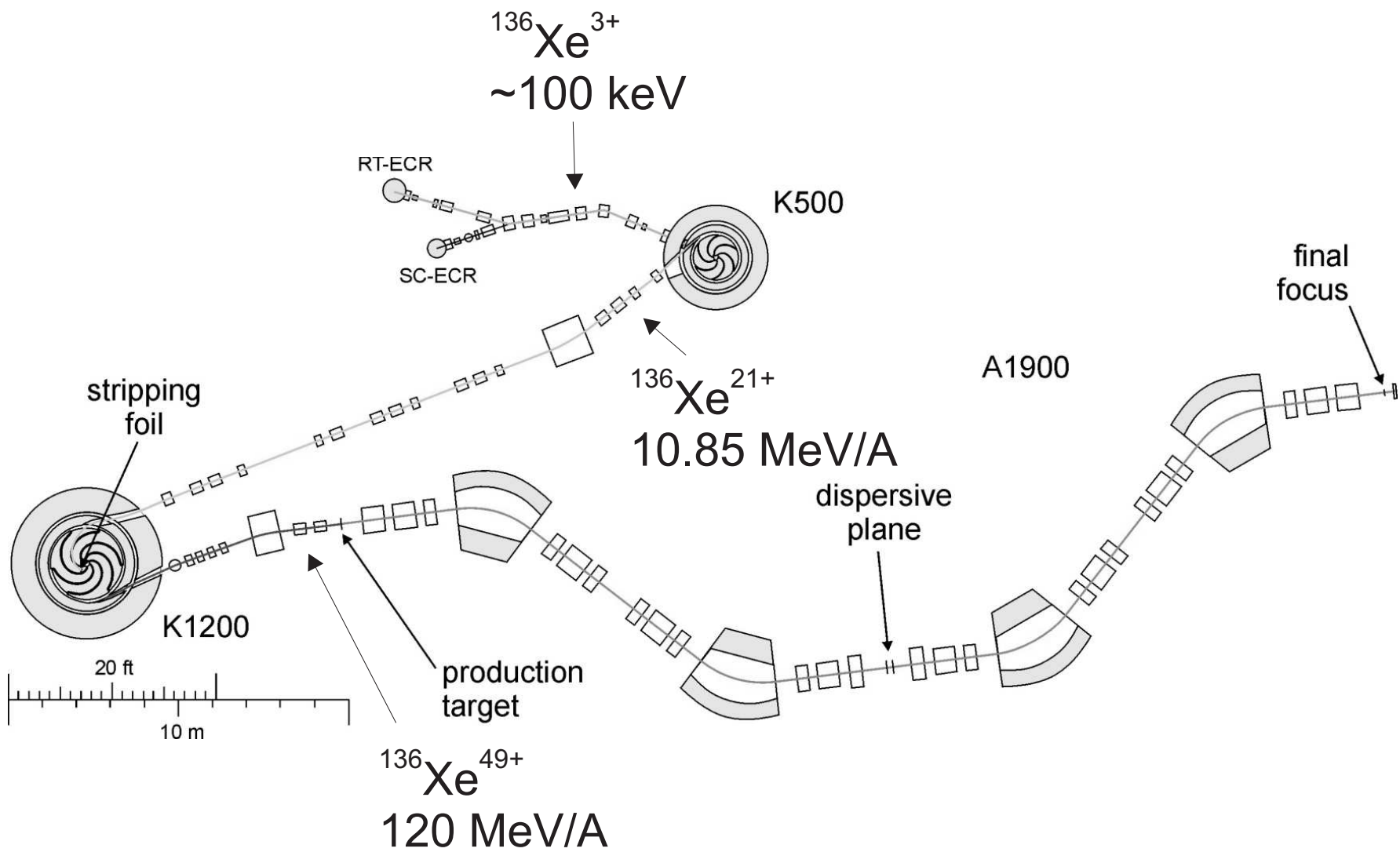


Figure 3.1: Schematic of the NSCL Coupled Cyclotron Facility and A1900 spectrometer.

The  $^{136}\text{Xe}^{49+}$  primary beam was extracted from the K1200 cyclotron at an energy of 120 MeV/nucleon. The beam was made incident on a 188 mg/cm<sup>2</sup> Be foil in the target box located along the beamline between the K1200 and the A1900 (see Figure 3.1). Products of the fragmentation of  $^{136}\text{Xe}$  with a magnetic rigidity of 3.9597 T·m continued moving forward along the beamline into the A1900 spectrometer.

### 3.1.3 Fragment Separation and Identification

#### A1900 Tuning

As stated in the previous section, the secondary ion beam, immediately after the target, is a mixture of many species including the fragmentation reaction products and unreacted primary beam. If the secondary beam were to be used in this condition, the exotic nuclides of interest would be very difficult to detect and study amongst the overwhelming number of other species. In order to separate the interesting nuclides from the rest of the secondary beam the A1900 spectrometer was used. The A1900 is a large magnetic spectrometer capable of resolving the components of fast exotic beams produced using the Coupled Cyclotron facility. The device consists of four 45° dipole magnets and twenty-four superconducting quadrupole magnets, sixteen of which have coaxial superconducting hexapole and octupole magnets for higher-order corrections. Technical details regarding the A1900 can be found in Ref. [34].

Isotopic separation is achieved in three stages. First, the impure beam passes through a dispersive element (*i.e.* the first two dipoles) with a user-defined magnetic rigidity. This section of the A1900 selects for a narrow range of momentum-to-charge ratio, described in terms of the momentum acceptance (maximum  $\Delta p/p \sim 5\%$ ). Those ions that satisfy the condition go through the aperture. Following this first stage, the beam should, in principle, be largely free of unreacted primary beam; however, in the present work a significant amount of primary beam in various charge states (mostly 51+ to 54+) was present after the aperture. In the next stage, the

transmitted ions pass through a thin wedge of material to effect a differential energy loss. This achromatic wedge, typically made of plastic or aluminum, causes ions of different charge to exit with different momenta. Finally, a second dispersive element selects for a narrow range of momentum-to-charge ratio.

In NSCL Experiment 01015, the A1900 was tuned to optimize the passage of  $^{120}_{45}\text{Rh}^{45+}$  and simultaneously eliminate as many interfering species as possible. The magnetic rigidities of the first and second dispersive elements were set to  $B\rho_{1,2} = mv/q = 3.9597 \text{ T}\cdot\text{m}$  and  $B\rho_{3,4} = 3.8397 \text{ T}\cdot\text{m}$ , respectively. A combination of a 28-mg/cm<sup>2</sup> foil of BC400 fast scintillator plastic (polyvinyltoluene) and a curved 120- $\mu\text{m}$  thick Kapton (polyimide) foil, with a total effective thickness of 62.276 mg/cm<sup>2</sup> of aluminum, in a standard A1900 achromatic wedge mount was used as a degrader at the intermediate dispersive plane. The momentum acceptance of the A1900, which has a maximum value of 5.5%, was restricted to 1.1% in order to avoid charge states of the  $^{136}\text{Xe}$  primary beam (*i.e.*,  $^{136}\text{Xe}^{54+}$ ,  $^{136}\text{Xe}^{53+}$ ,  $^{136}\text{Xe}^{52+}$ ,  $^{136}\text{Xe}^{51+}$ , predominantly). The 1.1% momentum acceptance was achieved by means of two 13-mm thick Al bars that were positioned with a 65-mm gap between them at the dispersive plane upstream of the plastic degrader, as shown in Figure 3.2.

### Fragment Identification

Identification of the post-A1900 secondary beam fragments was accomplished using a particle-identification (PID) plot based on time-of-flight and energy loss in a silicon PIN detector located at the experimental endstation, downstream of the A1900 exit. The fragment times-of-flight were measured between the dispersive image plane of the A1900 and a plastic scintillator (“N3 scintillator”) at the endstation. The timing signal at the A1900 was obtained using the “Image-2 North” (I2N) scintillator in the beam path, as diagrammed in Figure 3.2. The scintillator, with fast timing characteristics, supplied the time-of-flight (ToF) stop signal and the N3 scintillator supplied the start signal. A 500- $\mu\text{m}$  Si PIN detector provided an energy-loss signal ( $\Delta E$ ) for the

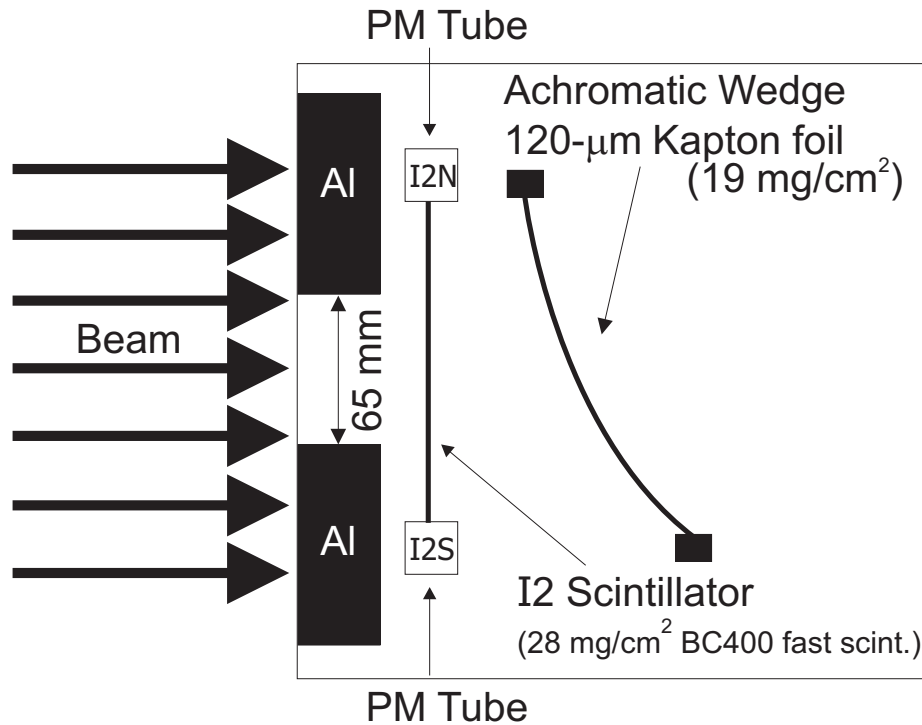


Figure 3.2: The arrangement of the Al bars and plastic wedge at the dispersive image plane. This figure is not to scale.

secondary beam fragments that traversed its thickness.

A typical PID plot of  $\Delta E$  versus ToF is shown in Figure 3.3. This plot represents all secondary beam ions that were incident upon the most upstream Si PIN detector at the experimental endstation. In principle each approximately hexagonal region (commonly called a “blob”) within the PID plot represents a different isotope. This isotopic separation is accomplished in two parts. First, the  $\Delta E$  values provide elemental separation since ion energy loss is a function of  $Z^2$ ; thus, each row of blobs represents isotopes of one element. Secondly, ToF values provide separation in mass number  $A$ , since a heavier ion has a lower velocity for a constant magnetic rigidity and, hence, a longer time-of-flight. The various spectra associated with a given isotope were obtained by gating on a contour drawn around the blob.

The identity of the PID blobs was determined by systematically proceeding from known fragments, identified by prompt gamma rays from  $\mu s$  isomers, to the region of new nuclides. The initial A1900 settings were centered on  $^{134}_{52}\text{Te}$ , a nuclide with well-

known gamma transitions that were observed with HpGe gamma-ray detectors in both the A1900 focal plane and at the experimental endstation. The  $B\rho$  of the second half of the A1900 ( $B\rho_{3,4}$ ) was adjusted to yield a PID containing both  $_{52}\text{Te}$  and  $_{51}\text{Sb}$  blobs. In the next bootstrapping step, the  $B\rho$  was again adjusted to give a PID containing  $_{51}\text{Sb}$  and  $_{50}\text{Sn}$  blobs. In the third step, the A1900 settings were centered on  $_{50}\text{Sn}$  only. At each stage the fragments were identified by unique gamma transitions. Finally, the  $B\rho$  settings were moved to center on  $^{120}_{45}\text{Rh}$ . The final setting still included Sn isotopes for identification by prompt isomeric gamma rays and yielded the range of nuclides indicated in Figure 3.3.

### 3.1.4 Total Kinetic Energy Determination

#### Charge-State Contaminants

The primary beam used in the present work was composed of  $^{136}\text{Xe}^{49+}$  ions. A very large fraction of the beam ions did not undergo projectile fragmentation in the target and thus passed through unreacted. These unreacted primary beam ions experienced charge-exchange interactions with the atomic electrons of the Be target, yielding a distribution of  $^{136}\text{Xe}$  ionic charges in the secondary beam. Likewise, the ions produced by fragmentation also underwent charge-exchange interactions in the target. Consequently, several different charge states of a given product nuclide were present in the secondary beam. Many of these contaminating species were filtered out of the beam by the A1900; however, the similarity of  $A/q$  values (proportional to the momentum-to-charge ratio and thus  $B\rho$ ) for certain species made separation in the A1900 impossible. For instance, the  $A/q$  values of  $^{120}\text{Rh}^{45+}$  and  $^{117}\text{Rh}^{44+}$ , 2.67 and 2.66, respectively, are close enough that both ions fall within the A1900 acceptance. Also, the velocities of each ion are close enough to give nearly identical ToF and  $\Delta E$  values in the PID plot. Thus, within a given PID blob more than one species may be present. This was indeed born out in the present work, and as a consequence the PID

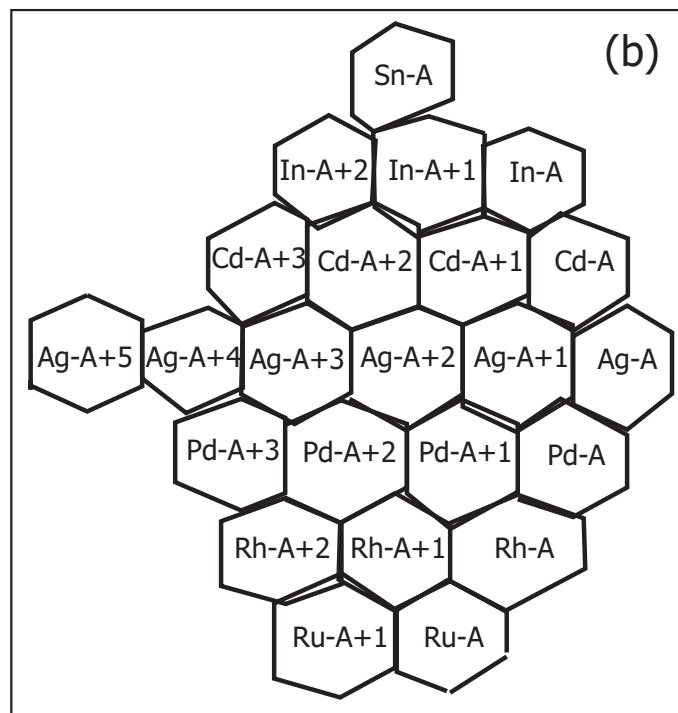
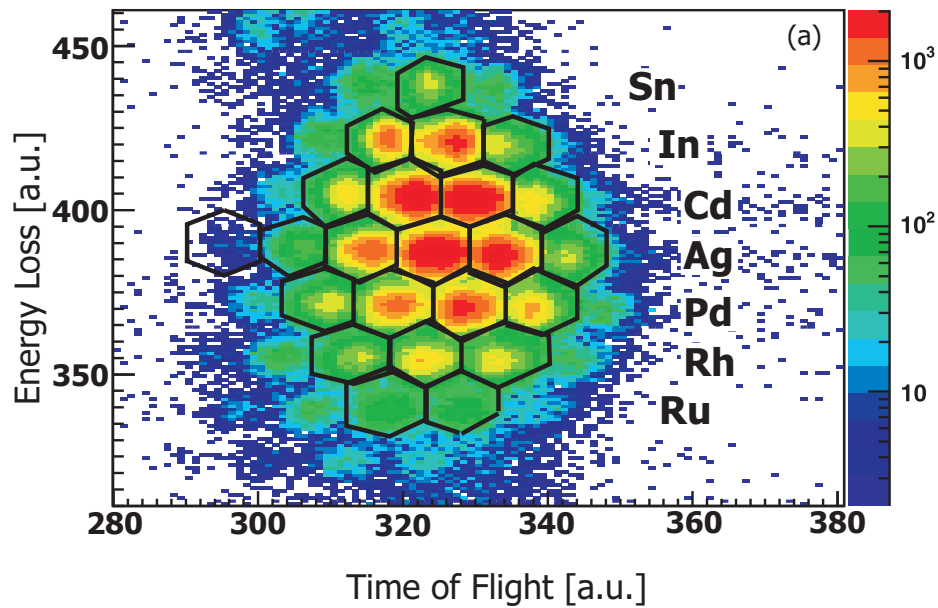


Figure 3.3: (a) A representative particle identification plot for all beam fragments incident on the first upstream PIN detector (PIN01a). Each row of blobs represents one element, and the software contour gates are superimposed. (b) The key for the notation used to designate the blobs and gates is provided.

plot of Experiment 01015 did not provide unambiguous identification of individual isotopes.

### **TKE Reconstruction**

A remedy to the problem of charge-state contamination can be found in the determination of fragment total kinetic energies (TKE). Energetic ions are commonly identified with TKE by means of the  $\Delta E/E$  ratio. In principle, if the total kinetic energies are measured with sufficient resolution, then the species within a given PID region can be resolved in a TKE spectrum. Since the presence of charge-state contaminants in the secondary beam was anticipated during the planning for Experiment 01015, Si PIN  $\Delta E$  detectors with sufficient resolution and thicknesses were included in the experimental setup to enable the measurement of fragment kinetic energies, and no passive energy degraders were incorporated into the setup. The relative positions of the three energy-loss detectors, labeled PIN1a, PIN2 and PIN2a, are illustrated in Figure 3.4 with the beam passing into the DSSD from the left. As the beam ions pass through each  $\Delta E$  detector, they lose a certain amount of energy depending upon their individual mass, nuclear charge, and kinetic energy. The ions then deposit the remainder of their energy upon coming to rest in the thick Double-Sided Silicon Strip Detector (DSSD). As opposed to the true total kinetic energy of each ion, the quantity measured (TKE\*) is given by the sum of the energy-loss values:

$$TKE^*(MeV) = \Delta E_{PIN1a} + \Delta E_{PIN2} + \Delta E_{PIN2a} + \Delta E_{DSSD} \quad (3.1)$$

The true total kinetic energy of each ion is then given by

$$TKE(MeV) = TKE^* + \Delta E_{scint} \quad (3.2)$$

where the energy loss in a thin, upstream plastic scintillator (equivalent to 17 mg/cm<sup>2</sup> of Al) was calculated using LISE++. TKE\*, rather than the true TKE, was measured

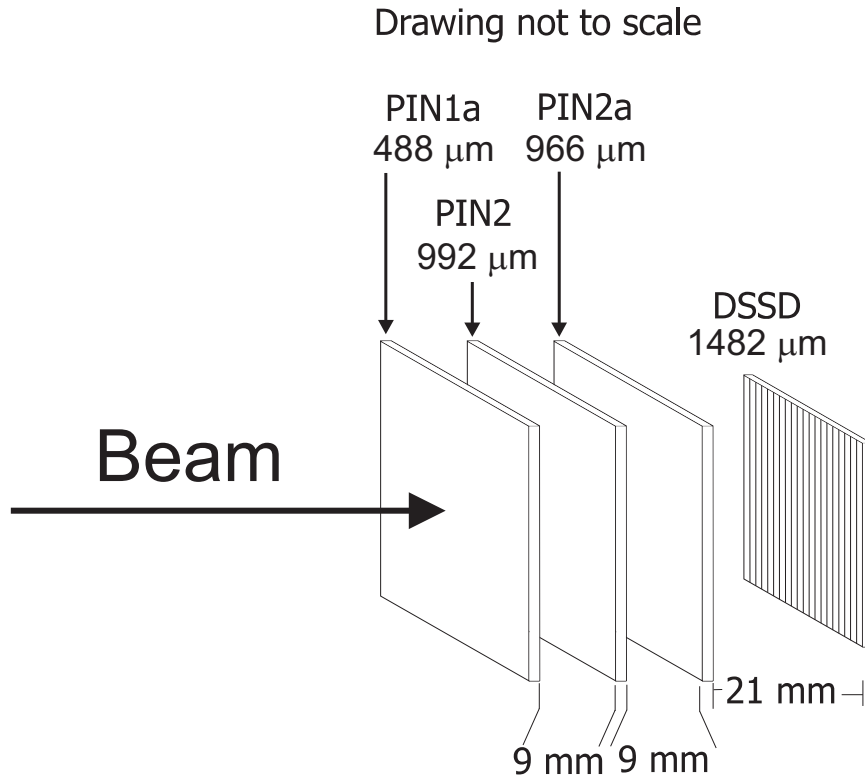


Figure 3.4: Schematic showing the relative positions of the  $\Delta E$  PIN detectors of the BCS.

because the energy resolution of the plastic scintillator was not sufficient for this purpose.

### TKE Calibration

The magnitude of the energy loss in the Si detectors was related to the electrical signal by the calibration curves shown in Figures 3.5 and 3.6. Five separate energy calibration runs were recorded during the experiment. Energy-degraded primary beam ( $^{136}\text{Xe}^{54+}$ ) was passed through the A1900 with five different  $B\rho$  settings and was incident upon the  $\Delta E$  detectors at the experimental endstation. The energy loss of the  $^{136}\text{Xe}$  ions in each detector was obtained by fitting the peak in the energy-loss spectrum with a Gaussian function using the program DAMM (Display, Analysis and Manipulation Module) [37]. The centroids of the  $\Delta E$  peaks for each detector were plotted against the theoretically calculated energy losses to obtain calibration curves

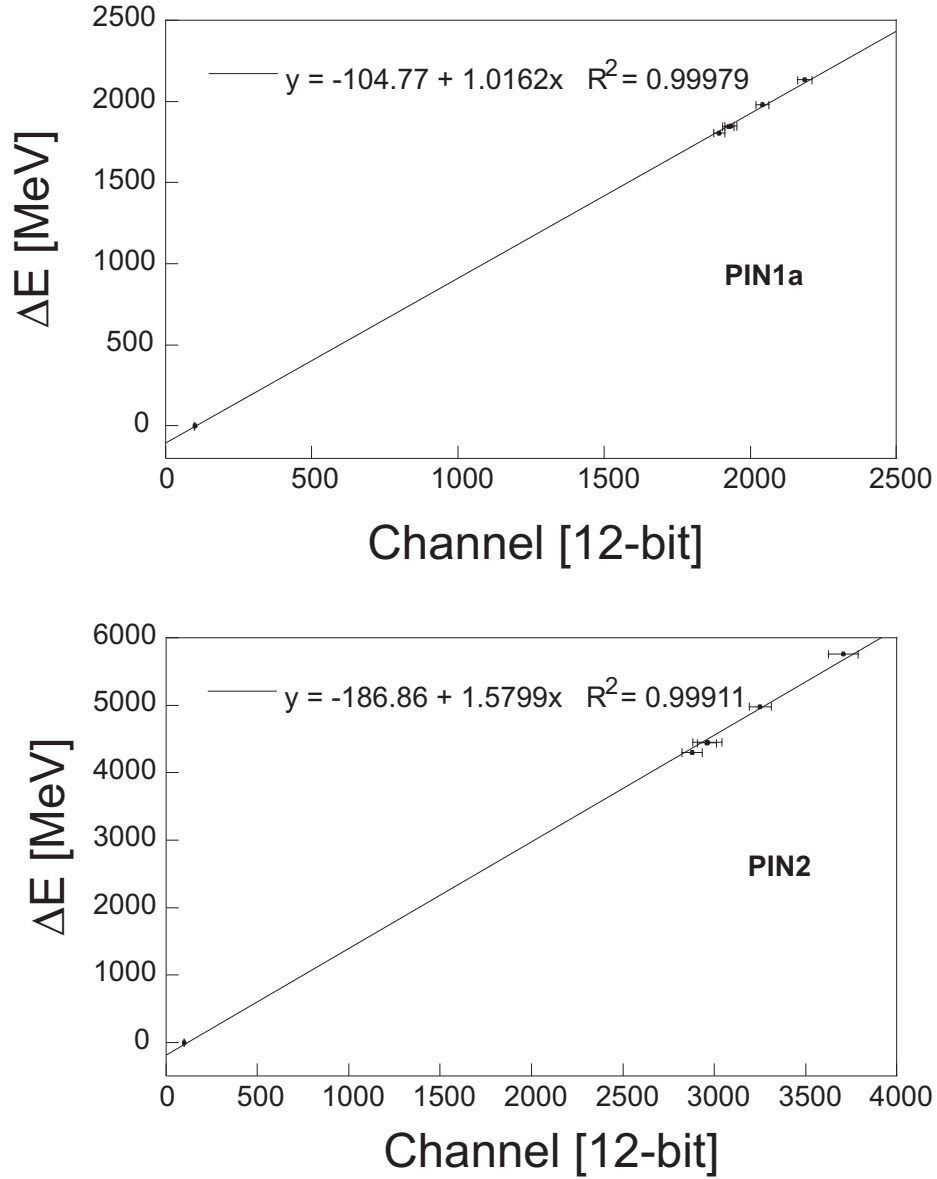


Figure 3.5: Energy calibration plots for the Si detectors PIN1a and PIN2.

for each detector. The theoretical energy losses in each Si detector were calculated using the computer program LISE++ [36]. Information regarding the five calibration runs is provided in Table 3.1. The individual components of the TKE were each calibrated independently for each particle and the linear adjustments were applied in software, with the result being stored as a software parameter. The total kinetic energies were obtained by summing the calibrated energy-loss parameters and storing the result as another parameter, again, event-by-event for each particle.

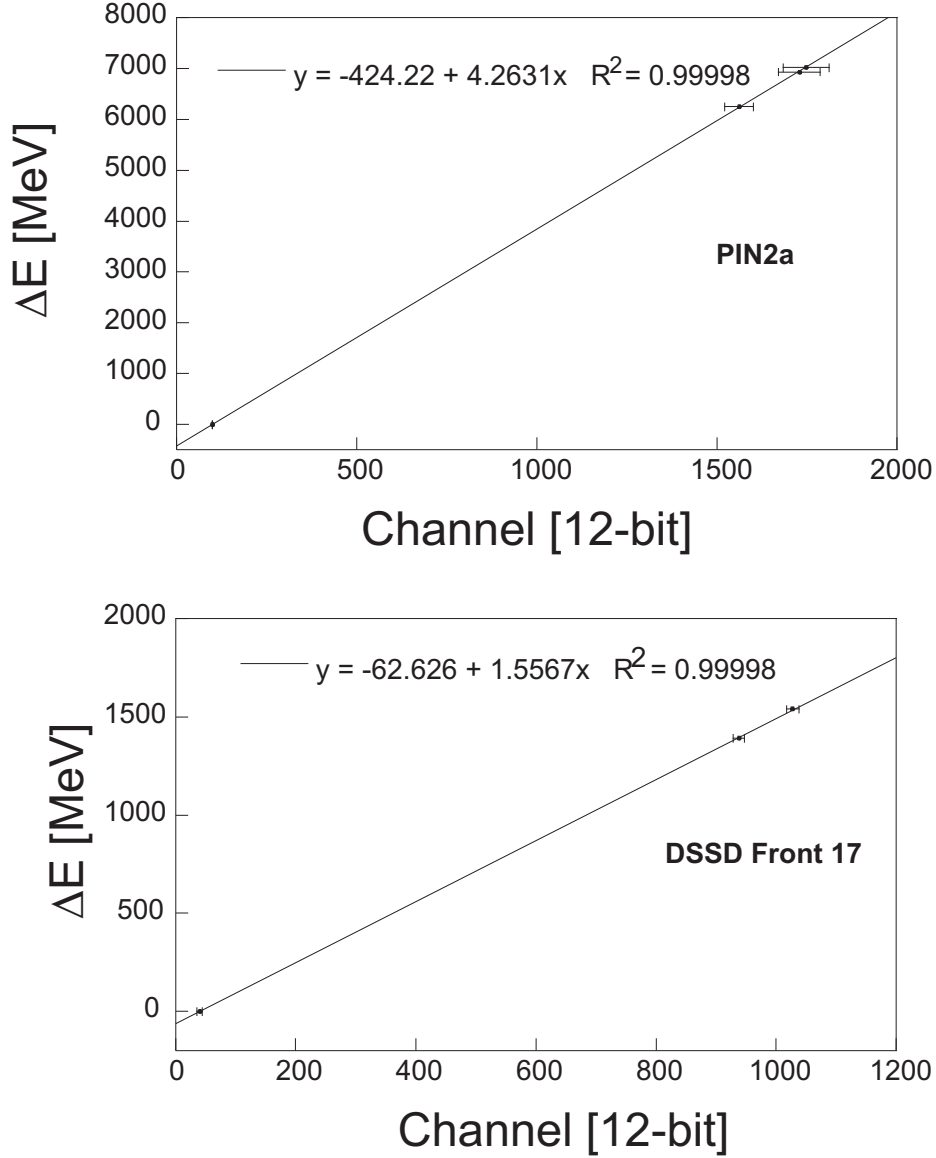


Figure 3.6: Energy calibration plots for the Si detectors PIN2a and a representative plot for one DSSD strip.

Table 3.1: Settings for the five  $\Delta E$  calibration runs. The N3 scintillator was not in the beam for runs 1003 and 1004. For runs 1086, 1087, and 1088, 17 mg/cm<sup>2</sup> of Al was included in the LISE++ calculations to simulate the scintillator.

Run No.	Ion	Beam Energy [MeV/u]	$B\rho$ [T·m]
1003	$^{136}\text{Xe}^{54+}$	108.619	3.8850
1004	$^{136}\text{Xe}^{54+}$	98.698	3.6940
1086	$^{136}\text{Xe}^{54+}$	91.3908	3.5480
1087	$^{136}\text{Xe}^{54+}$	110.176	3.9143
1088	$^{136}\text{Xe}^{54+}$	113.665	3.9793

## TKE Gating Procedure

The following section describes the procedure that was employed for producing TKE gates. TKE spectra were constructed in the data-analysis program SpecTcl [38]. A TKE spectrum for all beam ions was obtained as a one-dimensional spectrum of the 16-bit TKE parameter, mentioned in the preceding paragraph. A spectrum for each PID region was made by gating the overall TKE spectrum with each PID contour. The TKE spectrum gated on the Ag-A+2 contour (the PID region associated with  $^{124}\text{Ag}$ ) is given in Figure 3.7 as a representative example. Two distinct peaks can be seen in this example—one due to the fully-stripped ion ( $^{124}\text{Ag}^{47+}$ ) and the other due to the charge-state contaminant ion ( $^{121}\text{Ag}^{46+}$ ). In the present work, TKE distributions were assumed to be approximately Gaussian functions. In order to deconvolute the overlapping distributions, a two-component Gaussian-function fit with background component was applied to each spectrum. The fitting was performed in the peak-fitting program DAMM. The spectra were exported from SpecTcl as ASCII files and converted to a DAMM-readable format (.spk) using the conversion program asc2spk. Centroids, FWHM values and peak areas were recorded for both peaks in each fragment-gated TKE spectrum. The results of the TKE-fitting procedure are presented in Chapter 4.

One-dimensional TKE gates were constructed for use in preparing single nuclide-gated gamma-ray spectra (prompt and beta-delayed) in the present work. Gates were chosen to balance the desire to eliminate charge-state interference with the need to preserve as many counts of the fully-stripped exotic nuclides as possible. This was accomplished by testing several different TKE gate ranges for each TKE spectrum. The tested ranges usually included a very restrictive cut that included only the high-energy side of the fully-stripped peak; several liberal cuts that included the full baseline width of the fully-stripped peak and varying amounts of the charge-state peak; and a cut that excluded the fully-stripped peak but incorporated much of the lower charge-state peak. In each case an “AND” gate of the TKE cut and the corresponding

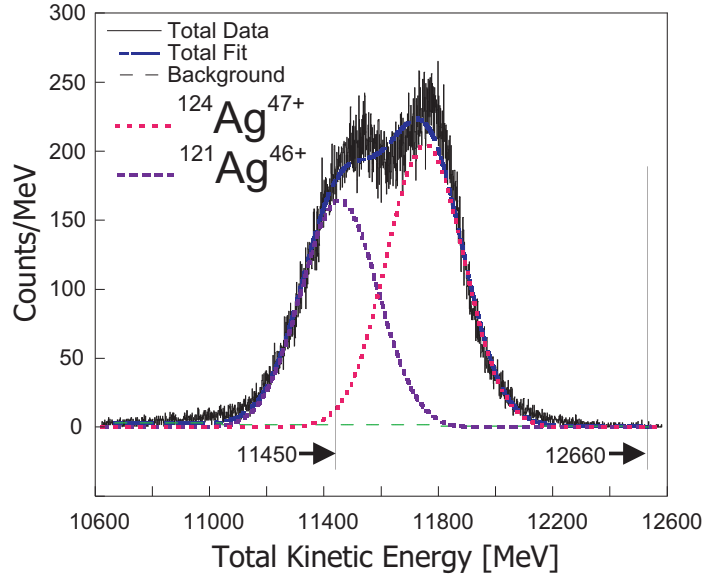


Figure 3.7: A representative TKE spectrum. The larger peak is attributed to  $^{124}\text{Ag}^{47+}$  and the smaller peak to  $^{121}\text{Ag}^{46+}$ . The vertical lines indicate the range of the  $^{124}\text{Ag}$  TKE gate.

PID contour was formed in SpecTcl to select for events within a given PID blob that fall within a given range of kinetic energy. The effect of these compound gates on prompt and beta-delayed gamma-ray spectra was observed. The extreme TKE cuts, charge-state only and fully-stripped only, were compared to confirm the identity of the ions under each peak using known gamma rays. The set of intermediate compound gates developed for a given PID region were applied to gamma-ray spectra and compared on two characteristics—peak areas and background counts. Comparison of background levels was performed by visual inspection; the peak intensities were usually checked quickly in SpecTcl by integrating the range of channels encompassed by the full-baseline width. The goal of maintaining gamma-peak intensities for the fully-stripped species was given precedence over eliminating background; therefore, relatively liberal TKE gates were used in most cases. In all cases the contaminant gamma-ray peaks were easily identified and distinguished from the gamma-ray peaks attributed to the fully-stripped species. Furthermore, no direct gamma peak interferences were observed. The values used to create the TKE gates are given in Table 4.2 on page 82.

## 3.2 Beta Counting System

The previous section (3.1) described how exotic neutron-rich nuclides were produced, separated and identified. The hardware and data-analysis techniques that were used to study the nuclides of interest are described in the following section.

### 3.2.1 Hardware and Electronics

The NSCL Beta Counting System (BCS) [7] was employed in the present work to stop the fast fragments of the secondary beam and to observe their subsequent beta decay. The BCS was designed with a number of capabilities related to observing beta decay, including a set of detectors for beta-decay endpoint measurement and electron tracking. Neither of these uses were pursued in the present analysis, although experimental data were recorded from this set of “calorimeter” detectors. A schematic diagram of the BCS is presented in Figure 3.8. The heart of the BCS, as used in Experiment 01015, was a double-sided silicon strip detector (DSSD—Micron Semiconductor, Ltd. Type BB1) with the approximate active dimensions of  $40\text{ mm}\times 40\text{ mm}\times 1.5\text{ mm}$ . The entrance and exit faces of the DSSD was electrically segmented into forty approximately 1-mm wide strips. The strips on one face were aligned perpendicular to the strips on the opposite face, effectively dividing the active area of the detector into 1600  $1\text{-mm}\times 1\text{-mm}$  pixels.

In addition to the DSSD, the BCS contained six single-sided silicon strip detectors (SSSD) with active volumes of  $50\text{ mm}\times 50\text{ mm}\times 1\text{ mm}$ . The active area on one face of each detector was electrically segmented into 16 strips. The SSSD’s were positioned with their faces parallel and strips alternately perpendicular to each other. The stack of SSSD’s was placed 7 mm downstream of the DSSD with the separation between each of the SSSD’s of approximately 1 mm.

The third component of the BCS was comprised of three unsegmented silicon PIN detectors, which were positioned upstream of the DSSD, and two Si PIN detectors that

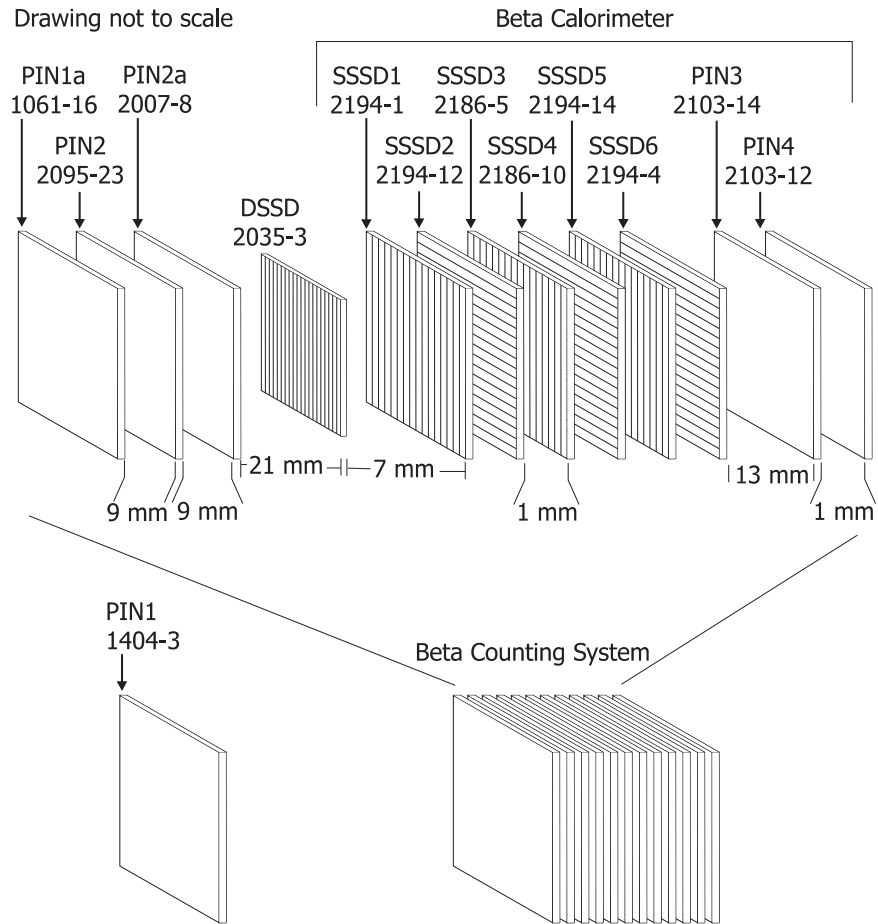


Figure 3.8: Schematic showing the relative positions of all the component detectors of the BCS. This figure was reproduced with modifications from Ref. [39].

Table 3.2: A list of the detectors comprising the BCS in Exp. 01015 and their attributes are given.

Detector	Serial No.	Active Area [mm×mm]	Thickness [ $\mu\text{m}$ ]
PIN1a	1061-16	50×50	488
PIN2	2095-23	50×50	992
PIN2a	2007-8	50×50	966
DSSD	2035-3	40×40	1482
SSSD1	2194-1	50×50	990
SSSD2	2194-12	50×50	977
SSSD3	2186-5	50×50	981
SSSD4	2186-10	50×50	975
SSSD5	2194-14	50×50	989
SSSD6	2194-4	50×50	988
PIN3	2103-14	50×50	993
PIN4	2103-12	50×50	998

were placed downstream of the last SSSD (please see Fig. 3.8 for spacing information). The three upstream PIN detectors were previously described in Section 3.1 in relation to their use as  $\Delta E$  detectors. The two downstream PIN detectors, along with the six SSSD's, were originally incorporated for beta-decay electron tracking and calorimetry; however, neither of those uses was pursued in the present work. The first upstream SSSD (labeled SSSD1) was employed to reject false beta-decay events caused by low-mass beam particles. The remainder of the SSSD's, PIN3, and PIN4 were not used for any other purposes, and these detectors will not be discussed further. The attributes of the BCS Si detectors are summarized in Table 3.2.

The DSSD served a dual role in the Beta Counting System, acting as an implantation detector and as a beta-decay detector. Secondary-beam ions, whose energies were attenuated by the three  $\Delta E$  detectors, were stopped in the active volume of the DSSD. The total thickness of  $\Delta E$  detectors was chosen to ensure that the fragments were stopped in the thickness of the DSSD, closer to the upstream face. Sometime after implantation these radioactive ions underwent beta decay with the resultant emission of an electron. Detection of both implantation events and beta-decay events are quite disparate duties. The energy deposited by a fast beam fragment coming to

rest within the detector volume is several GeV, whereas the energy deposited by a beta-decay electron within the same volume is only on the order of 100 keV. Electronic modules capable of processing signals from both types of events were developed for use with the BCS [7].

A schematic diagram of the DSSD electronics, used in the present work, is shown in Figure 3.9. The DSSD signals are read off of two 50-pin connectors, where 40 pins on each connector carry signal and the other ten are at ground. As shown in the schematic, a grounding board, which split the signals from each 50-channel ribbon cable into three 34-channel twisted-pair ribbon cables, was included between the DSSD and preamplifiers, such each signal wire had a corresponding ground. In order to process signals in the high- and low-energy ranges, six 16-channel dual-gain analog preamplifiers (model CPA16) supplied by MultiChannel Systems were used. The implantation energy signals were processed through the low-gain side (0.03 V/pC) of the preamplifier and sent directly to CAEN V785 VME ADCs for digitization. The beta-decay energy signals were processed through the high-gain side (2 V/pC) of the preamplifier and directed to Pico Systems 16-channel shaper/discriminator CAMAC modules for further processing. The energy signals from the shaper output were then sent to CAEN V785 VME ADCs for digitization.

The half of the electronics dedicated to processing time signals is shown in Figure 3.9. Beta-decay signals from the high-gain preamplifier were processed through the Pico Systems discriminators, and the fast output signals were used in forming the master trigger. The discriminator outputs for all 40 strips of the front of the DSSD were combined with a logical OR gate; likewise, the outputs for all 40 strips of the back of the DSSD were also combined with a logical OR gate. The condition for a master trigger was determined by a logical AND gate of the DSSD front signal and DSSD back signal, *i. e.*, if any front strip *and* any back strip had a signal above discriminator threshold then a master gate was generated. Such a master trigger was then checked against a data-acquisition computer not-busy signal using a second logical

AND gate. If the computer was not busy, a master-live trigger was generated. The master-live trigger defined an event. This event logic is summarized in the flow chart of Figure 3.9.

The applications of the Si PIN detectors were touched upon in Sections 3.1.3 and 3.1.4. To reiterate, PIN1a, PIN2 and PIN2a functioned as energy-loss detectors needed for the determination of the total kinetic energies of the fragments. PIN1a also provided the  $\Delta E$  signal used in preparing the particle-identification plot. The energies lost by secondary-beam ions as they traversed the thickness of these silicon detectors were on the order of 1 GeV; consequently, low-gain amplification was sufficient for generation of energy signals. As indicated in Figure 3.10, energy-loss signals in all PIN's were processed by Tennelec preamplifiers and shaping amplifiers (TC178 and TC241S, respectively) and digitized by CAEN 785 ADC's. PIN2a was also used in defining beta-decay events by detecting beta-decay electrons emitted from the DSSD in the upstream direction. In order to identify these  $\sim 100$ -keV electrons and fast beam fragments, the raw PIN2a output was split into high-gain and low-gain amplification stages, with both signals finally digitized by CAEN 785 ADC's.

Fast signals from the Si PIN detectors were used in timing logic. As shown in Figure 3.10, a fast timing output from PIN1a was used as a start for the prompt gamma-ray TAC (SeGA-TAC).

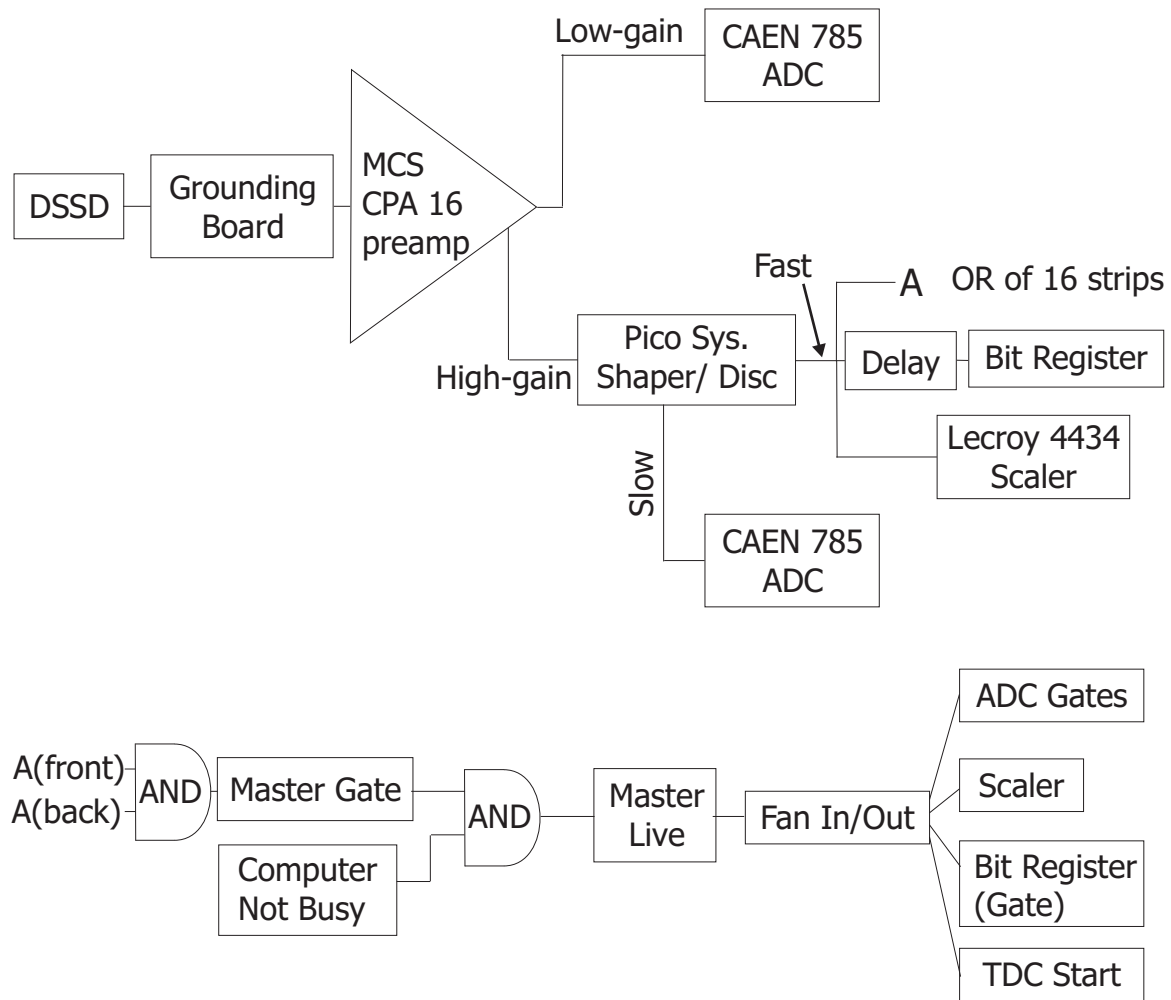


Figure 3.9: Electronics diagram for double-sided Si strip detector. Figure reproduced from Ref. [39].

### 3.2.2 Implantation-Beta Decay Correlation

The essential function of the Beta Counting System in the present work was to associate the implantation of radioactive beam ions with subsequent beta-decay events one atom at a time. In principle, when a single ion is implanted in the DSSD a signal is produced in one of the forty strips on the front of the DSSD and in one of the forty strips on the back of the DSSD. The intersection of these two strips defines a silicon pixel. Such an event yields a total-energy signal for the implantation that is time-stamped and stored offline. After a period of time dependent upon the half-life of the implanted ion, a beta-decay electron will be emitted. Before escaping from the pixel where it was created the electron will deposit a portion of its energy in that pixel. This event also yields an energy signal that is time-stamped and stored offline. The detected beta decay is then correlated in software with the implantation that occurred in the same pixel at an earlier time. In general, the identity of the implanted ion is known from the PID plot and TKE spectrum; therefore, the identity of the beta-decaying nucleus can also be known, and information about the decay can be obtained. For instance, the beta-decay half-life may be deduced from the difference between the absolute times of a correlated implantation and decay. Also, auxiliary detectors can be used with the BCS to measure beta-delayed gamma rays and neutrons from correlated implants. In practice several considerations were taken to assure that reliable correlations were made. Allowances were necessary for the spatial and temporal distributions of implantation and decay events.

The assumption that only one pixel is associated with each implant event is an oversimplification. When a beam fragment is stopped in the DSSD a signal is induced in several strips on each face of the detector, meaning that one of several pixels could contain the implanted ion. The number of strips that are activated by a fragment is referred to as the multiplicity. The multiplicity distribution for implant events in the present work is given in Figure 3.11. Integer numbers in  $x$  and  $y$ , specifying the position of the implant event, are assigned in software according to the front and

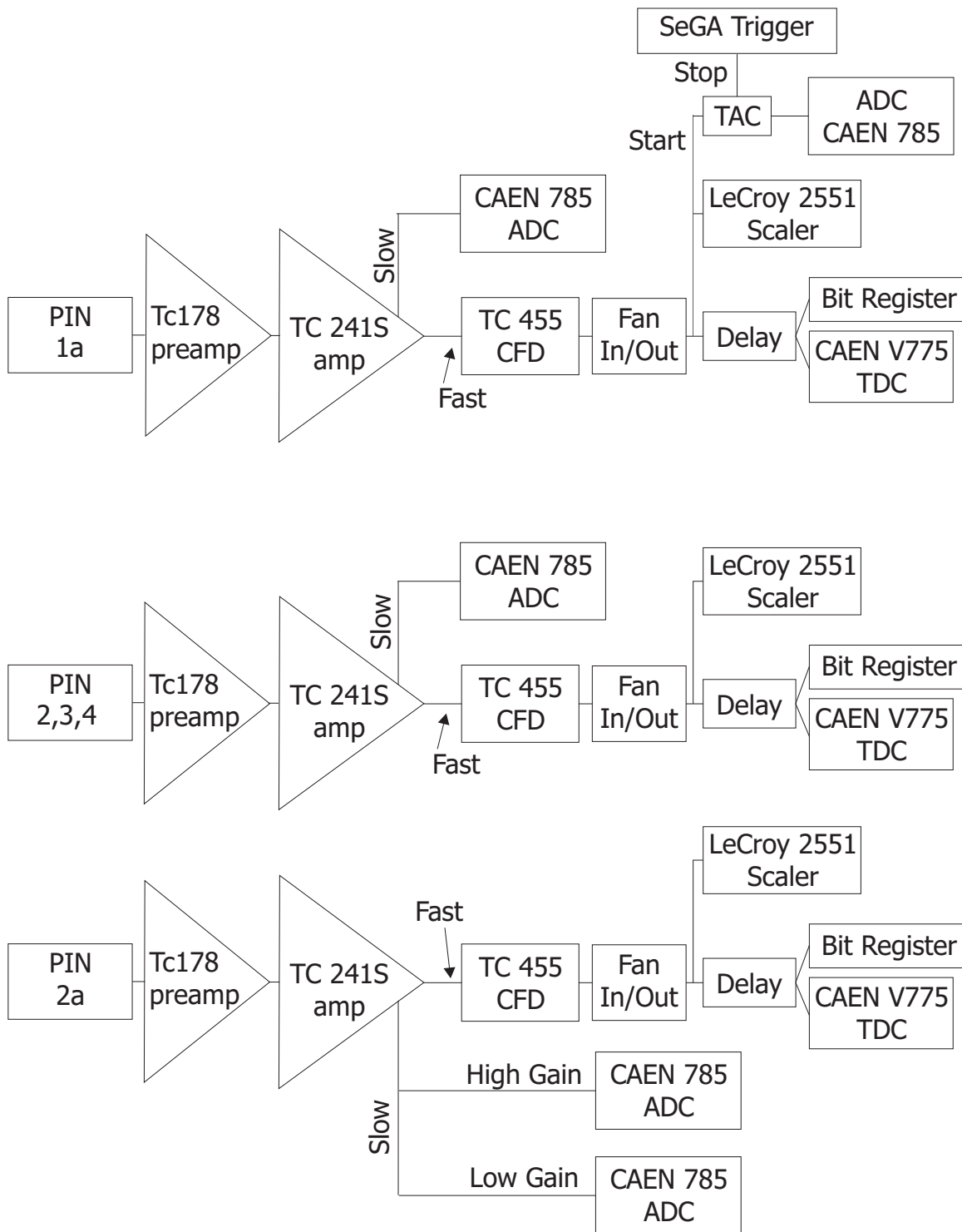


Figure 3.10: Electronics diagram for the Si PIN detectors. This figure was reproduced with modifications from Ref. [39].

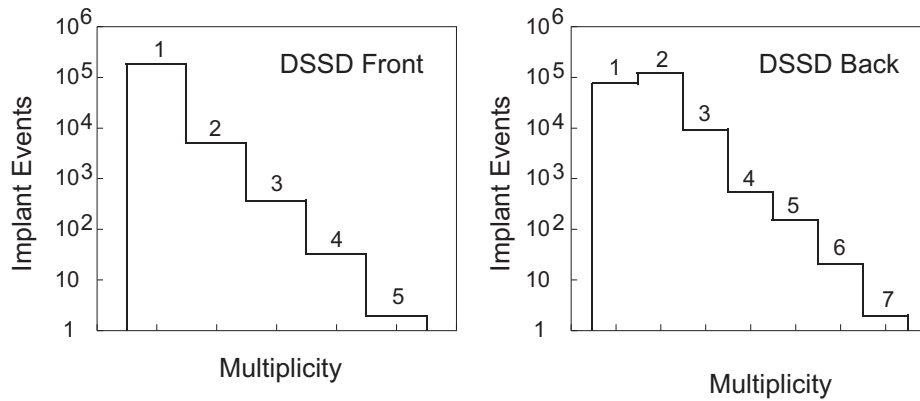


Figure 3.11: Implant-event multiplicity distributions for the front and back faces of the DSSD.

back strips that had the largest energy signals. The fact that implant multiplicities may be greater than unity results in some degree of ambiguity regarding the true implantation location, since the strip with the largest energy signal may not contain the implanted ion. In the present work an expanded 9-pixel correlation field was used to recover associated events that would normally be lost by a one-pixel field. A 9-pixel correlation field consists of a given pixel and the eight surrounding nearest-neighbor pixels. In software, a beta-decay event was correlated with a previous implant in the same pixel or any one of the eight surrounding pixels. Thus, if a beta decay occurs in a pixel containing an implanted ion but the implantation maximum-energy signal was recorded for one of the adjacent pixels, then a proper correlation of the two events can be obtained.

Obviously, if two ions are implanted in the same pixel in quick succession then the source of a subsequent beta decay is uncertain. To minimize this problem, the rate of implantation is normally kept below 100 Hz; for Experiment 01015 the implantation rate was only  $\sim 1$  Hz. Also, the beam was defocussed to spread the implantations over as much of the surface area of the detector as possible, thus reducing the likelihood that two successive implants would be within the same pixel. The combined effect of these two precautions was such that the average time between successive implants in the same pixel was about 100 seconds. Additionally, a minimum time between

implants of 5.0 seconds was required in software. Successive implants that occurred within this time were discarded from the analysis.

In addition to the spatial correlation just described, a temporal correlation was also required in software. A beta decay was only associated with a previous implant event if the implant event occurred no more than 5.0 seconds before the decay. The value of 5.0 seconds is referred to as the correlation cut-off time.

In contrast to the massive, highly-charged fragments associated with implants, the electrons emitted by beta decay are light and have unit charge; consequently, a beta-decay electron will deposit a small amount of energy that is often below the threshold of detection before escaping from the pixel where it was created. Such subthreshold energy deposition limits the beta-decay detection efficiency. An effort was made to cool the DSSD to  $\sim 0^\circ\text{C}$ , using an ethylene glycol chiller, in order to lower the noise threshold in each strip and to minimize the number of lost events.

The beta-decay energy thresholds for all DSSD strips were set before Experiment 01015. Two levels of thresholds were used on the high-gain electronics channels—hardware thresholds and software thresholds. The hardware thresholds of the shaper-discriminator modules were set on a channel-by-channel basis for all eighty DSSD strips by inspection of the shaper output signals on an oscilloscope triggered on the discriminator signals. The software thresholds were determined using a  $1.108\text{-}\mu\text{Ci } ^{90}\text{Sr}$  beta-emitting source. A beta-decay energy spectrum was recorded for each DSSD strip (see Fig. 3.12), and the thresholds were set in the “notch” between the noise peak and the beta-decay spectrum, as shown in the examples. The average high-gain threshold of the front forty strips was  $\sim 100$  keV, and the average threshold of the back forty strips was  $\sim 120$  keV. (In post-experiment analysis it was determined that these thresholds were above the signals that would be generated by conversion electrons, thus accounting for the non-observation of these events.) Software thresholds for the low-gain channels were set online above the noise peak generated by high-gain triggers. The average low-gain thresholds for the front and back strips were 500 keV and  $\sim 800$

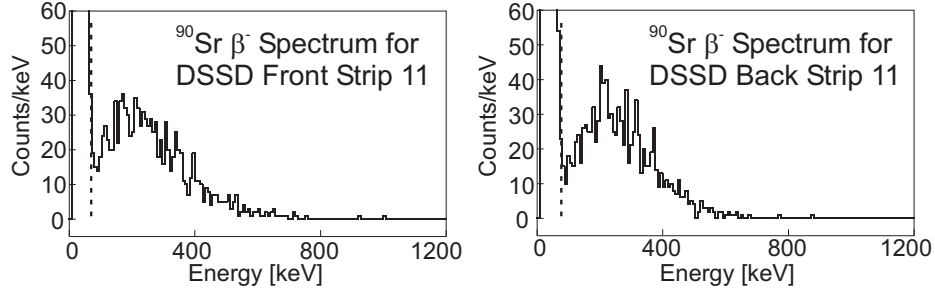


Figure 3.12: Representative beta-decay energy spectra used for the threshold calibration of two DSSD strips. The dashed line indicates the position of the software thresholds.

keV, respectively.

The gain-matching of the DSSD strips was performed using a  $^{228}\text{Th}$  alpha-emitting source. The alpha-particle energy spectrum of the  $^{228}\text{Th}$  decay chain was recorded for all eighty DSSD strips, and gain-matching was performed on the 5.4-MeV peak.

One further source of uncertainty in the correlation was the effect of light particles in the beam. As a result of the projectile-fragmentation process the secondary beam contained small, energetic ions, such as  $^4\text{He}$  and  $^2\text{H}$ , which penetrated all detectors in the BCS. The passage of light particles through the DSSD can produce energy signals above the beta-decay (high-gain) thresholds but below the low-gain thresholds. Since the master trigger is determined by events above the high-gain threshold, the presence of light particles can cause false triggers and, as a result, erroneous implant-decay correlations. However, these particles could be identified by (large) signals in the other detectors. The implant and decay conditions were defined to minimize events caused by light particles. The Boolean relations applied in software that differentiated true (1) events from false (0) events are given in Eqs. 3.3 and 3.4,

$$Implant = PIN1a + DSSD_{front} + DSSD_{back} + \overline{SSSD1} \quad (3.3)$$

$$Decay = \overline{PIN1a} + DSSD_{front} + DSSD_{back} + (\overline{SSSD1} \text{ OR } \overline{PIN2a_{high}}) \quad (3.4)$$

where the value of the detector name indicates the presence (1) or absence (0) of an energy signal and a “+” indicates a logical AND. The implant condition required

that a fragment travel through PIN1a but not SSSD1; the highly-penetrating light particles pass through both. The decay condition required that PIN1a did not fire in coincidence with the high-gain DSSD channels—this obviously eliminated incoming light fragments. The decay condition also required that only SSSD1 or the PIN2a high-gain channel had a signal; such a signal would be generated by the decay electron emitted from the DSSD in the downstream or upstream direction, respectively.

To summarize, the BCS had the capability of stopping fast secondary beam fragments in a double-sided Si strip detector and associating these implants with subsequent beta decay on an event-by-events basis. The beam spot was made large and the beam rate was kept at  $\sim 1$  Hz to reduce the likelihood of back-to-back implants in the same pixel. The maximum time between implants and the correlation time were both set to 5.0 seconds during data analysis. Also, a nine-pixel correlation field was used to improve correlation efficiency. The software implantation and decay conditions were determined to reduce the interference of light beam fragments.

The PID plot that was shown in Figure 3.3 contains all fragments incident upon PIN1a, without regard to the implantation and decay conditions. For the purposes of constructing implant/decay correlated fragment gates, implant- and decay-correlated PID plots were prepared in software, as shown in Figure 3.13. These PID plots contain only those fragments, incident upon PIN1a, that satisfied the implantation and decay conditions, respectively. Contour gates drawn around blobs in the decay-correlated PID were used to select for specific fragments in all work related to beta-decaying species. The uncorrelated PID plot was used for the spectroscopy of isomers in this work.

### **3.2.3 Beta-Decay Half-life Determination**

One of the important goals of the present work was to extract beta-decay half-lives using the Beta Counting System, from the data for the various isotopes implanted in the detector. The following section will describe how implant/decay-event data were

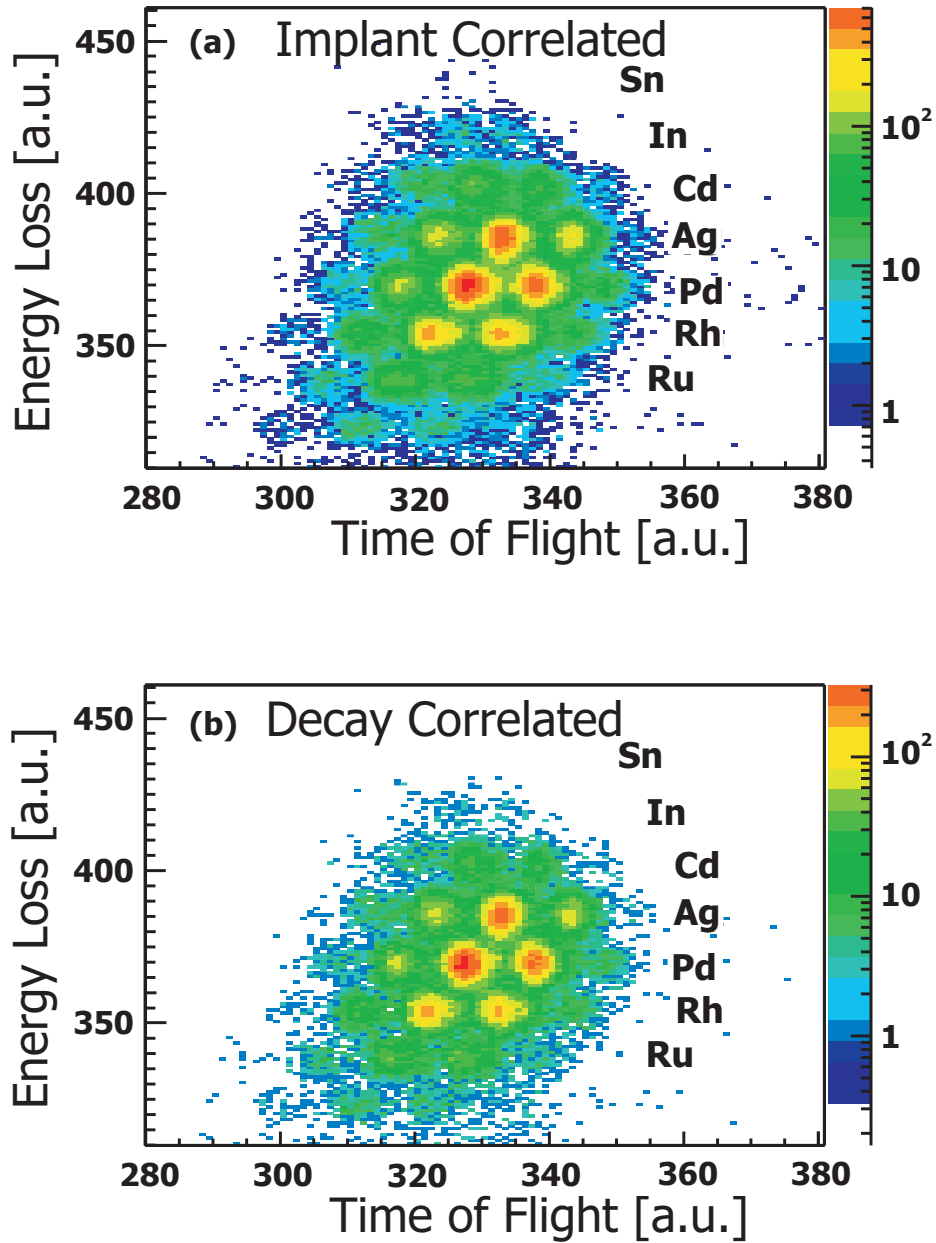


Figure 3.13: (a) The PID plot for all fragments correlated with a valid implantation event in this analysis. (b) The PID plot for all fragments correlated with a valid beta-decay event in this analysis.

processed to deduce half-lives.

During the experiment, valid implant and decay events were correlated with the absolute value of a free-running clock, and these values were stored electronically with each event. The real-time clock with a resolution of  $30.5 \mu\text{s}$  consisted of two Ortec RC014 modules in CAMAC. These modules were operated in series fast/slow mode. The first clock, *i.e.* the fast clock, counted internal pulses at a rate of  $8^5 \text{ Hz}$  (*i.e.*,  $2^{15}$  counts per second). This module contained a 16-bit register, so after two seconds  $2^{16}$  pulses filled the register and the module generated an overflow output signal. The second clock, *i.e.* the slow clock, counted the number of overflow signals from the fast clock. Thus, each count in the slow clock corresponded to a 2-s interval, and each tick in the fast clock corresponded to a  $30.5\text{-}\mu\text{s}$  interval. These clocks were reset at the beginning of each run.

The time distribution of all correlated beta-decay events, or simply the beta-decay curve, was constructed in the data analysis program SpecTcl as the difference in absolute implant- and decay-event times for all measured fragments, histogrammed into 10-ms bins. In order to obtain the decay curves for each implanted nuclide, the total decay curve was gated with the correlated PID plot contours. Text files, containing bin numbers and counts per bin, were generated from the fragment-gated decay curves and were read into a ROOT-based curve-fitting program [39]. The curve-fitting program incorporated a rebinning algorithm and performed a multi-component least-squares fit. The number of decay components that could be fit was adjustable: parent, daughter and granddaughter components, and constant or exponential background components were available. In most cases the granddaughter generation was not used. An exponentially decaying background has been observed in previous experiments employing the BCS [40]. Exponential backgrounds were tested in a few cases in the present measurement but were found to give poor overall fits; therefore, all fits in the present work included constant backgrounds. The appropriateness of using a constant background is not surprising given the fact that the rate of implantation ( $\sim 1 \text{ Hz}$ ) is

comparable to the decay constants ( $\lambda \sim 1s^{-1}$ ) of the secondary-beam daughter and granddaughter activity.

Necessary input parameters for decay-curve fitting included the desired bin size; start values for the parent decay constant, activity, and background level; and daughter and granddaughter decay constants. Outputs from the fitting program included the parent decay constant with calculated uncertainty from the fit, the fitted initial activity value with its uncertainty, and background level with uncertainty. A graphic output of the plotted data and component fits was also produced. The beta-decay half-life curves from this analysis are presented in Chapter 4.

The half-life values reported in the present work were checked by comparing fits obtained using differing input parameters. Most of the “final” fits were performed on decay curves that were compressed to 40 or 50 ms per bin. These bins sizes are smaller than the  $\geq 120$ -ms half-lives in the range of nuclides studied, so no deleterious effects were observed from using overly large bins. A daughter growth and decay component was included for each nuclide studied; in a few cases the granddaughter growth and decay was incorporated if the daughter half-life was short relative to the correlation time. Fits were performed on decay curves obtained with 5.0-second correlation cut-off times. All beta-decay half-lives obtained from the above procedure are presented in Section 4.3.

### **3.3 HpGe Array**

The previous section detailed the NSCL Beta Counting System, which was used to stop fast fragments from the secondary beam in a silicon implantation detector and correlate implanted ions with their subsequent beta decay on an event-by-event basis. An auxiliary detector array of twelve high-purity germanium (HpGe) gamma-ray detectors was used in conjunction with the BCS to observe gamma radiation emitted from the implanted nuclides and their decay products. This section will describe the

HpGe array hardware and the data analysis techniques that were used to study the excited states of the nuclides of interest.

### 3.3.1 Hardware and Electronics

An array of high-purity germanium gamma-ray detectors, known as the Segmented Germanium Array (SeGA), is available at the NSCL to observe gamma rays emitted from fast exotic beam fragments [41]. Twelve identical HpGe detectors from eighteen in the SeGA were employed in Experiment 01015 for the purpose of gamma-ray spectrometry. Each detector (from Eurisys) contains a cylindrical (80 mm×70 mm dia.) n-type germanium crystal electrically segmented into 32 regions. This high level of segmentation is necessary for in-beam spectroscopy of fast ions. In the present work, the segmentation was not necessary since the gamma radiation was emitted from stopped beam fragments; therefore, only signals from the central, axial contact were processed. Each detector contained an integrated room-temperature FET preamplifier. Energy signals from the preamplifiers were processed by Ortec 572 amplifier modules and digitized using Ortec AD413 8k ADC's. Fast timing signals from each preamplifier were processed and digitized as shown in Figure 3.14. HpGe energy signals were read out in singles mode, *i.e.*, every gamma ray observed by a detector was recorded electronically whenever a master-live trigger occurred.

Approximately halfway through the beamtime of Experiment 01015 it was realized that if an additional timing circuit were put in place, decay curves could be obtained for the large number of microsecond isomers being observed. Consequently, an additional TAC module was included in the HpGe electronics. A fast signal from PIN1a was used as the start and a signal from any one of the twelve HpGe detectors provided the stop. The time range was limited to 20  $\mu$ s, such that a secondary beam fragment incident upon PIN1a would open a 20- $\mu$ s gate on an Ortec 413A ADC to observe the prompt gamma decay of implanted isomers. A diagram of the SeGA-TAC electronics is given in Figure 3.14. This TAC was calibrated after the experiment us-

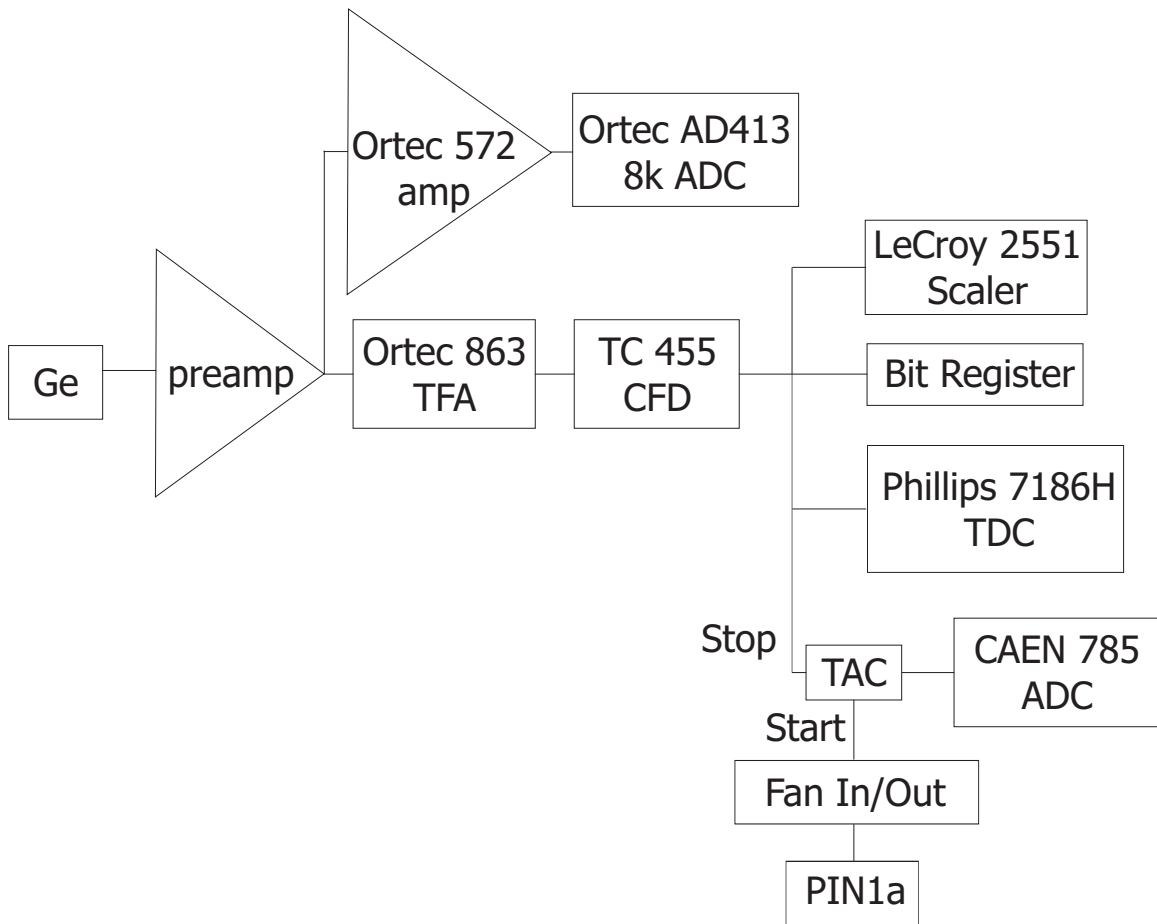


Figure 3.14: Electronics Diagram for HpGe Detectors.

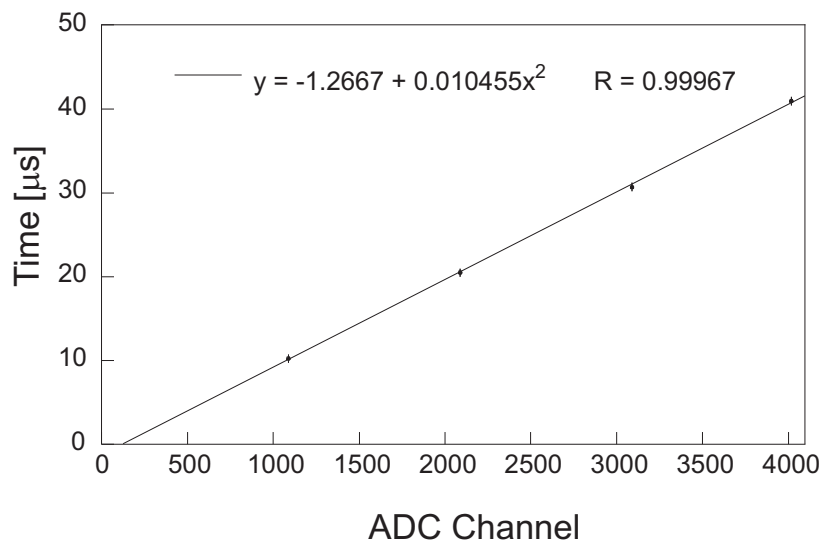


Figure 3.15: Calibration Curve for SeGA-TAC.

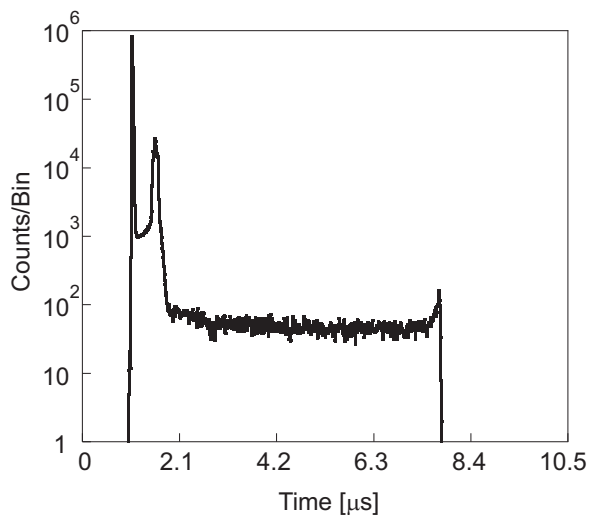


Figure 3.16: SeGA-TAC time spectrum for prompt gamma ray events.

ing an ORTEC 462 time calibrator module that provided start and stop pulses at selected periods. Four periods were chosen from 10.24 to 40.96  $\mu\text{s}$ . The four peaks in the resulting time spectrum were fitted using DAMM, and the centroids were used to prepare a calibration curve (see Fig. 3.15). A resolution of 10.5 ns/channel was determined. The time spectrum for all of the available data is shown in Figure 3.16. The structure at small time (below  $\sim 2.1 \mu\text{s}$ ) is attributed to prompt X-ray and low-energy gamma-ray flash caused by beam fragments interacting with the silicon of PIN1a.

The geometry of the HpGe array relative to the BCS is shown in Figures 3.17

and 3.18. The central axes of the cylindrical HpGe detectors were positioned parallel to the beam axis. The detectors were placed as close to the DSSD as was physically possible in order to maximize the overall detection efficiency. A standard gamma-ray source (SRM-4275-C69) [42] was used to determine the absolute efficiency of each detector at the end of the experiment. The source was placed at the DSSD position in the detector chamber at atmospheric pressure, and a 100-Hz signal from a pulser module was connected to the test input of each HpGe detector. The pulse-height spectrum of each detector was recorded in turn for  $\sim 1800$  seconds with a PC-based multichannel analyzer and with the NSCL data-acquisition system. Additionally, a  $^{56}\text{Co}$  gamma source (prepared at Florida State University) was placed at the DSSD position, and the pulse spectrum of all twelve detectors was recorded simultaneously for  $\sim 1$  hour using both acquisition systems. The  $^{56}\text{Co}$  calibration yielded relative efficiencies for high-energy gamma rays. The full-energy peak efficiency curve for the total 12-detector array is given in Figure 3.19. The data were plotted as  $\log(\text{efficiency})$  versus  $\log(\text{energy})$  and fitted with a fifth-order polynomial. The calibration equation was compared to the results of an MCNP [43] efficiency simulation, and the overall agreement between 150 keV and 3.5 MeV is excellent. The calculated peak efficiency of the entire array was determined to be 5.1% for a 1-MeV gamma ray.

The HpGe energy calibrations were performed before, during and immediately after Experiment 01015. The final energy calibrations used throughout this manuscript were based on the post-experiment data set. Calibration spectra for all twelve detectors were obtained using the mixed gamma source (SRM-4275-C69) and the FSU  $^{56}\text{Co}$  source, simultaneously. The data were collected using the NSCL data-acquisition system. A number of gamma peaks were fitted with DAMM, and a calibration curve for each detector was produced from the resulting centroids. The gamma-ray energies used in the energy calibration are given in Table 3.3.

Initially, one calibration was produced for each detector. These calibrations covered the entire range of energy from 123 keV to 3253 keV. It was subsequently noted

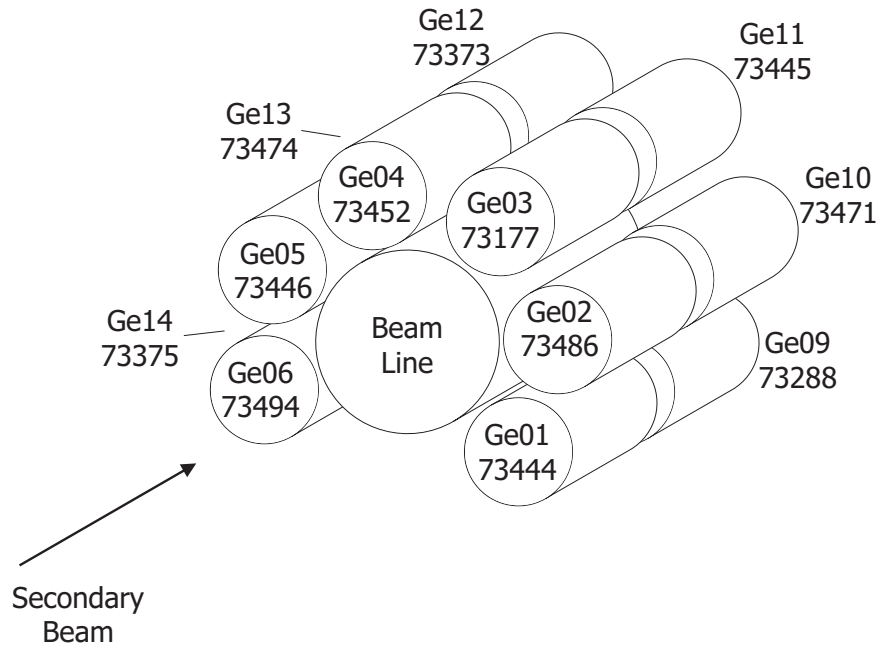
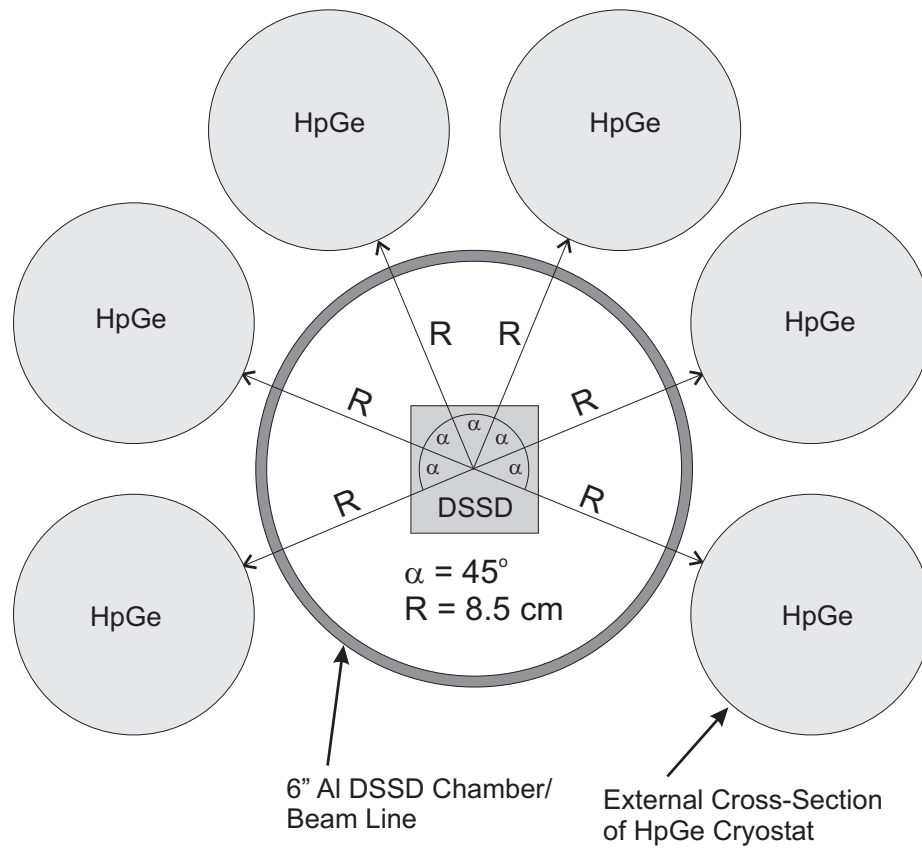


Figure 3.17: Schematic of HpGe detector positions relative to the beam line.



Note: Figure not to scale.

Figure 3.18: Cross-sectional view of HpGe detector positions relative to the DSSD.

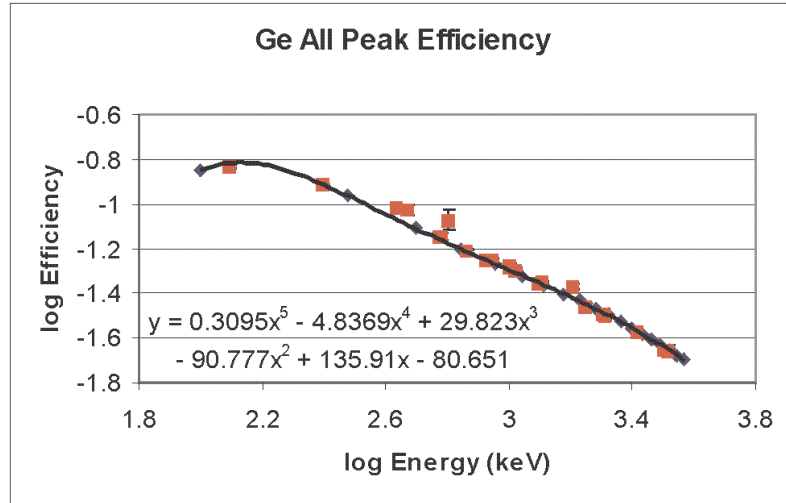


Figure 3.19: A plot of the  $\log(\text{efficiency})$  versus  $\log(\text{energy})$  for the total HpGe array. The data were fitted with a fifth-order polynomial. The squares represent the measured values and the diamonds represent the results of an MCNP [43] efficiency simulation.

that the cluster of high-energy points reduced the quality of the fit for the lower-energy calibration points; therefore, the somewhat broad calibration points at 2615, 3202 and 3253 keV were dropped, and two calibrations were prepared for each detector—one for energies of 123-1596 keV and another for 1596-3253 keV. A logic switch that would choose the appropriate calibration based on peak energy ( $<1500$  keV and  $\geq 1500$ ) was included in the data-analysis software. This split calibration turned out to be of no real significance to the analysis, since no gamma-ray peaks were observed above approximately 1100 keV due to the low statistics.

The calibration data were fitted in a spreadsheet using second-order polynomial functions. The resulting calibration curves above and below 1500 keV were found to be quite linear, with the nonlinear term typically being of the order  $10^{-7}$ . The fit parameters were included in a file that is read into SpecTcl before sorting data. The calibration data were then re-analyzed. The newly calibrated gamma-ray spectra were prepared, and the peaks were refitted in DAMM. The residual, that is, the difference of the “true” gamma energy (provided in a certificate with the source [42]) and the calibrated peak centroid, was calculated for all gamma rays in each detector. Plots of

Table 3.3: The gamma lines [42] that were used in calibrating the HpGe detectors.

Calibration Peak [keV]	Origin
123.071(1)	$^{154}\text{Eu}$
247.930(8)	$^{154}\text{Eu}$
591.763(5)	$^{154}\text{Eu}$
723.305(5)	$^{154}\text{Eu}$
873.190(5)	$^{154}\text{Eu}$
1274.536(6)	$^{154}\text{Eu}$
1596.495(18)	$^{154}\text{Eu}$
2034.755(13)	$^{56}\text{Co}$
2598.459(13)	$^{56}\text{Co}$
3253.416(15)	$^{56}\text{Co}$

the residuals as a function of gamma energy for all detectors are given in Figure 3.20, where the data points appear evenly distributed about zero. The standard deviation of the residuals about zero was used as an estimate of the systematic uncertainty of the measured gamma-ray energies.

As a final note, the final HpGe energy calibration was compared against the calibration data that was recorded mid-experiment, and excellent agreement was found across all gamma-ray energies.

### 3.3.2 Prompt Gamma Radiation Measurement

Chapter 2 described two types of gamma rays, prompt and beta-delayed, which reveal information about nuclear structure. Both were observed in the present work. This section will discuss the measurement and analysis of prompt gamma radiation emitted by excited secondary-beam fragments.

#### Fragment-Gated Prompt Gamma-Ray Spectra

In the present work, a prompt gamma ray was functionally defined as a gamma ray emitted from a secondary-beam fragment no more than 20  $\mu\text{s}$  after the fragment-generated  $\Delta E$  signal. Implantation in the DSSD was not a required condition; in fact some of the fragments that emitted prompt gamma radiation were likely stopped in

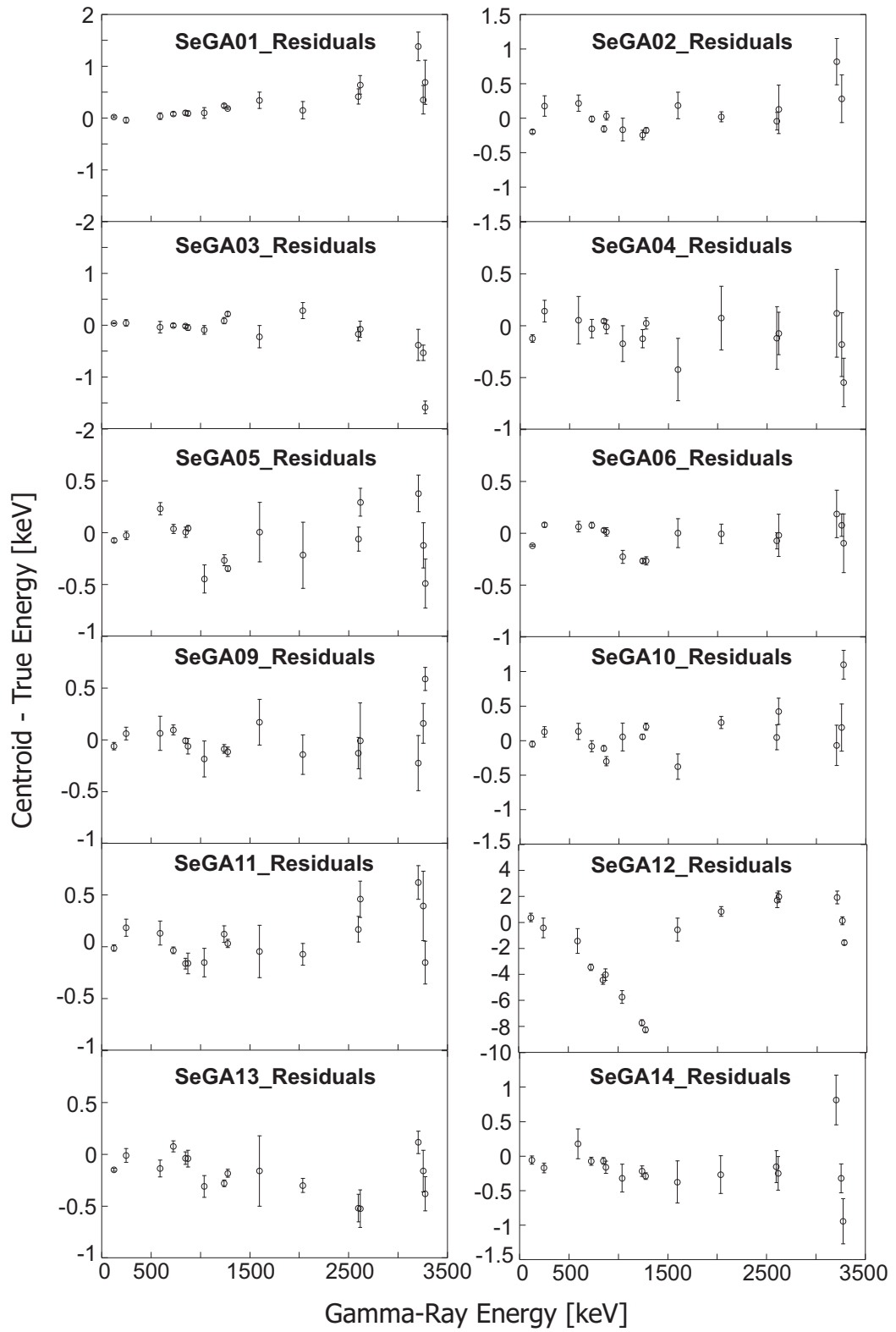


Figure 3.20: Gamma-ray energy residual plots for each HpGe detectors.

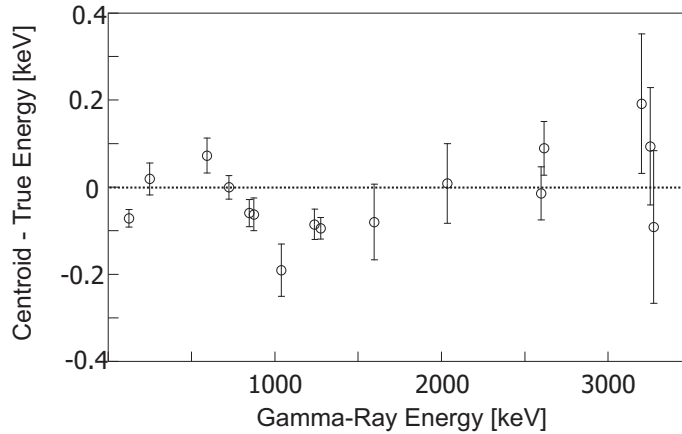


Figure 3.21: Total gamma-ray energy residual plot for all HpGe detectors.

PIN2 or PIN2a.

A total prompt gamma-ray energy spectrum was constructed in SpecTcl, by combining the energy-calibrated gamma spectra for all twelve HpGe detectors. A prompt gamma spectrum for each PID region was prepared from the prompt gamma spectrum by gating with the PID contours. As described in section 3.1.4, a variety of TKE gates were tested for every nuclide in the PID plot. In each case a compound gate of the final TKE cut and the PID contour was applied to the prompt gamma-ray spectrum to obtain a fragment-gated prompt gamma-ray spectrum.

The fragment-gated prompt gamma-ray spectra were exported from SpecTcl into the peak-fitting program DAMM. Gamma-ray peaks were fitted with Gaussian functions, and the resulting centroids, FWHM values, and peak areas were recorded. Peak areas were corrected for the relative detector efficiency and normalized to 100 for the most intense peak in each nuclide to obtain the relative intensities.

### Fragment-Gated Prompt $\gamma - \gamma$ Coincidence Spectra

The coincidence relationships between prompt gamma rays were examined. A two-dimensional matrix of prompt-gamma energy versus prompt-gamma energy for two-fold events was constructed in SpecTcl. Fragment gates (PID+TKE) were applied to the gamma-gamma matrix, and projections were then made using the individual

fragment-gated matrices. A gate was made on each gamma-ray peak along the abscissa, and the coincident energy spectrum was projected onto the ordinate; likewise, a gate was made on each gamma-ray peak along the ordinate, and the coincident energy spectrum was projected onto the abscissa. Each pair of x- and y-projections was summed in DAMM. No peaks were fitted, however, since the statistics in all cases were too weak (*i.e.* a typical peak was three counts in two adjacent channels). However, it should be stressed that the fragment- $\gamma\gamma$  triple coincidence produced very clean spectra with near-zero average backgrounds.

### **Isomer Half-Life Determination**

Half-lives of gamma-decaying isomers were deduced for some nuclides in the present work from the time spectrum of prompt gamma-ray emissions recorded using the SeGA-TAC. As previously mentioned, the SeGA-TAC was implemented at roughly the midpoint of the experiment; therefore, fewer data were available for determining half-lives than were available for determining gamma-ray energies.

A two-dimensional matrix of total prompt gamma-ray energy versus the SeGA-TAC time spectrum was prepared in software. Fragment gates were applied to the gamma-time matrix, and projections were then made using the individual gated matrices. A gate was made on each gamma-ray peak along the energy axis, and the coincident time spectrum was projected onto the time axis. The time projections were written to text files, and all of the time spectra for a given nuclide were summed in a spreadsheet. Individual fragment- $\gamma$ -gated time spectra contained so few counts that none were treated alone. Due to the double-peak structure at low times in the SeGA-TAC spectrum (see Fig. 3.16), all of the fragment- $\gamma$ -gated time spectra were truncated such that only the data beyond 2  $\mu\text{s}$  was used to determine half-lives. Single-component, unweighted exponential least-squares fits were applied to all of the fragment- $\gamma$ -gated time spectra using the computer program Kaleidagraph.

### 3.3.3 Beta-Delayed Gamma Radiation Measurement

Chapter 2 described two classes of gamma rays, prompt and beta-delayed, which reveal information about nuclear structure. Both were observed in the present work. This section will discuss the measurement and analysis of beta-delayed (delayed) gamma radiation emitted following the beta decay of implanted secondary-beam fragments.

#### Fragment-Gated Beta-Delayed Gamma-Ray Spectra

In the present work, a delayed gamma ray was functionally defined as a gamma ray emitted from an implanted ion in coincidence with a beta-decay signal in the DSSD. Correlation of a gamma ray with a beta-decay event was executed in software. A total delayed gamma-ray energy spectrum was constructed in SpecTcl, by combining the energy-calibrated delayed gamma spectra for all twelve HpGe detectors. A fragment-gated delayed gamma-ray spectrum for each PID region was prepared from the total delayed gamma spectrum by gating with the decay-correlated PID contours.

The fragment-gated beta-delayed gamma spectra were exported into the peak-fitting program DAMM. Gamma-ray peaks were fitted with Gaussian functions, and the resulting centroids, FWHM values, and peak areas were recorded in a spreadsheet. Peak areas were corrected for the relative detector efficiency and normalized to 100 for the most intense peak in each nuclide to obtain the relative intensities.

#### Fragment-Gated Beta-Delayed $\gamma - \gamma$ Coincidences

Coincidence relationships between delayed gamma rays were also examined. A two-dimensional matrix of delayed-gamma energy versus delayed-gamma energy for two-fold events was constructed in SpecTcl. The decay-correlated PID gates were applied to the gamma-gamma matrix, and projections were then made using the individual fragment-gated matrices. A gate was made on each gamma-ray peak along the abscissa, and the coincident energy spectrum was projected onto the ordinate; likewise,

a gate was made on each gamma-ray peak along the ordinate, and the coincident energy spectrum was projected onto the abscissa. Each pair of x- and y-projections was summed in DAMM. Low-background four-fold fragment- $\beta\gamma\gamma$  coincidence spectra were obtained.

### **Fragment- $\gamma$ -Gated Beta-Decay Half-Life Determination**

Gamma-gated beta-decay half-lives were deduced for some nuclides in the present work. The time spectrum of beta-decay events was obtained as described in section 3.2.3. In software, a two-dimensional matrix of total delayed gamma energy versus the beta-decay time spectrum was prepared, and the decay-correlated PID gates were applied to the gamma-time matrix. Projections were then made using the individual fragment-gated matrices. A gate was made on each gamma-ray peak along the energy axis, and the decay curve was projected on the time axis. The time projections were written to text files, and single-component, unweighted exponential least-squares fits were applied to all of the time spectra using the computer program Kaleidagraph. All of the time spectra for a given nuclide were also summed in a spreadsheet, and total fragment- $\gamma$ -gated time spectra were prepared.

The general explanation of the data-analysis techniques is now complete. The next chapter presents the results obtained in this work—the first section describes the results of the isomer studies and the second section describes the results for beta-delayed gamma-ray studies.

# Chapter 4

## Results

### 4.1 Overview of Data Collected in Exp. 01015

A large number of exotic nuclides were available for study amongst the ions in the cocktail secondary beam of NSCL Experiment 01015. The broadest view of the variety of nuclides in the secondary beam is revealed by the range of fragments that were incident on the first upstream PIN detector (*i.e.* PIN01a). In all, twenty-two nuclidic regions (blobs) were distinguished in the PIN01a PID plot. These regions correspond to seven elements from Ru ( $Z = 44$ ) to Sn ( $Z = 50$ ) with varying numbers of isotopes of each element. The PID blobs were labeled relative to the lightest isotope in each elemental series; for example, the lowest-mass Ag region was designated Ag-A, the next Ag-A+1, and so forth. “A” does not correspond to the same number in different elements, however. These labels were used for the sake of clarity, since each blob does not represent a specific mass or nuclide given the problem of charge-state contamination already discussed. The PIN01a PID plot is presented in Figure 4.1, along with a key for the labels used.

All of the fragments present in the secondary beam struck the first upstream PIN. Fewer fragments were actually implanted in the DSSD. The highest- $Z$  fragments lacked sufficient energy to reach the DSSD, due to their greater energy loss

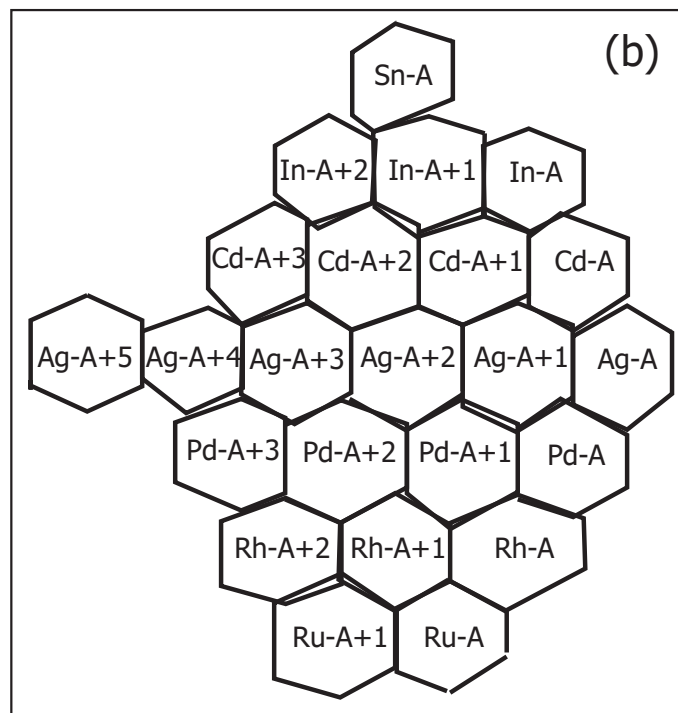
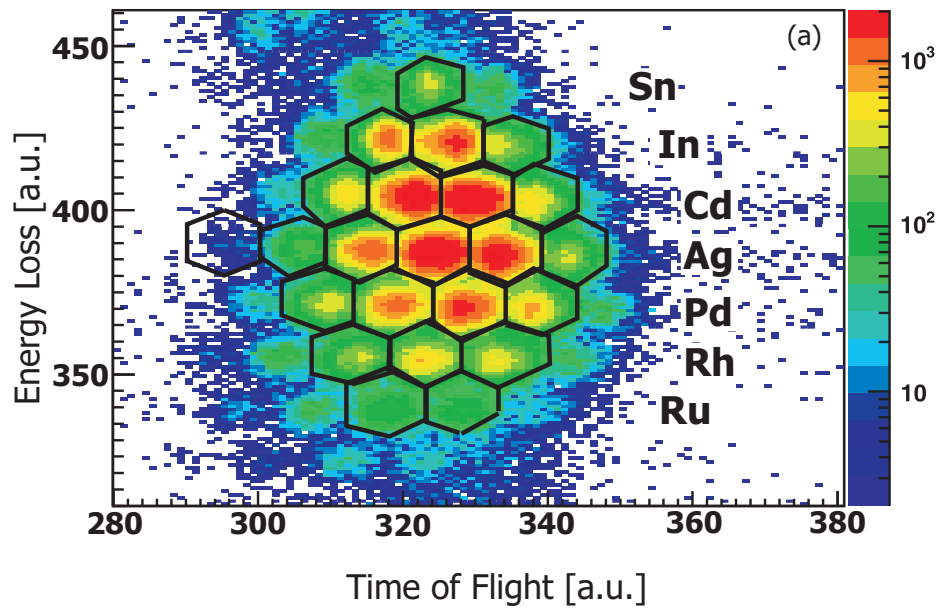


Figure 4.1: Similar to Figure 3.3. (a) The particle identification plot for all beam fragments incident on the first upstream PIN detector (PIN01a). Each row of blobs is labeled by element, and the software contour gates are superimposed. (b) A key for the notation used to designate the blobs and gates is provided.

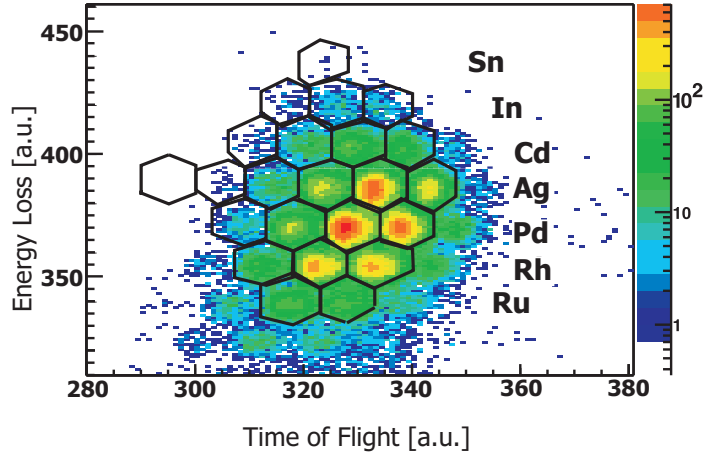


Figure 4.2: The particle identification plot for all beam fragments satisfying the DSSD implant condition. Each row of blobs is labeled by element, and the software contour gates are superimposed.

in each of the three  $\Delta E$  detectors. The fragments lose energy in the silicon detectors in proportion to  $Z^2$ . Consequently, the highest- $Z$  fragments generally stopped short of the DSSD while the lighter fragments were successfully implanted. The effective filtering by the  $\Delta E$  detectors is clearly seen in the implant-correlated PID plot, shown in Figure 4.2. Obviously any fragment, and collectively any nuclide, not implanted in the DSSD could not be correlated with a beta decay; thus, the range of beta-decaying nuclides that were studied was smaller than the range of nuclides that were studied via prompt gamma-ray emission. Table 4.1 presents the statistics for and summarizes the observed decay modes for the fragments in each PID blob.

## 4.2 Isomers

In the following sections (4.2.1-4.2.11) the results obtained for eleven nuclides that were observed to emit prompt gamma radiation are presented. The information given includes: fragment/TKE-gated gamma-ray energy spectra, fragment- $\gamma\gamma$  coincidence spectra, isomeric half-lives, and level structures in some instances. A summary of the the results obtained for the isomers observed is given in Tables 4.2 and 4.3. A general description of the analysis procedure used to study isomers in this work is presented

Table 4.1: The integrated number of events within each PID gate is given for all beam fragments incident on PIN01a and for beam fragments correlated with a DSSD implant.

PID Blob Gate	Fragments on PIN01a	Fragments in DSSD	$\beta$ -decay Correlated Fragments	Prompt $\gamma$ decay Observed	$\beta$ decay Observed
Sn-A	12200(110)	9(3)	0	✓	
In-A	15283(124)	248(16)	47(7)		
In-A+1	72997(270)	397(20)	92(10)	✓	
In-A+2	37376(193)	68(8)	18(4)	✓	
Cd-A	23183(152)	2392(49)	764(28)	✓	
Cd-A+1	134237(366)	4187(65)	1339(37)	✓	✓
Cd-A+2	121740(349)	1348(37)	433(21)	✓	
Cd-A+3	21188(146)	84(9)	35(6)		
Ag-A	13562(116)	7974(89)	2836(53)		✓
Ag-A+1	108657(330)	26222(162)	9978(100)	✓	✓
Ag-A+2	147982(385)	9079(95)	3685(61)	✓	✓
Ag-A+3	56013(237)	1230(35)	543(23)	✓	
Ag-A+4	6627(81)	51(7)	18(4)		
Ag-A+5	278(17)	0	0		
Pd-A	32584(181)	23883(155)	9261(96)		✓
Pd-A+1	85783(293)	38022(195)	15646(125)	✓	✓
Pd-A+2	60437(246)	8148(90)	3637(60)		✓
Pd-A+3	16495(128)	515(23)	234(15)		
Pd-A+4	959(31)	10(3)	5(2)		
Rh-A	24333(156)	19109(138)	7549(87)		✓
Rh-A+1	29177(171)	17729(133)	7824(88)	✓	✓
Rh-A+2	13993(118)	2927(54)	1390(37)	✓	✓
Rh-A+3	2369(49)	141(12)	66(8)		
Rh-A+4	204(14)	5(2)	1(1)		
Ru-A	6317(79)	4907(70)	2174(47)		✓
Ru-A+1	7744(88)	4904(70)	2348(48)	✓	✓
Ru-A+2	2028(45)	652(26)	349(19)		
Ru-A+3	378(19)	43(7)	26(5)		

Table 4.2: A summary of the TKE gating ranges and the observed number of counts in each TKE gate from the isomer analysis. The nuclide counts in the fourth column refer to the nuclides in the first column.

PID Blob Gate	Nuclide	TKE Gate Range [MeV]	Total Counts in TKE Gate Range	Nuclide Counts in TKE Gate Range	Isomer Fraction (%)
Sn-A	$^{129}\text{Sn}^{49+}$	11226, 12511	8981	8359	
In-A+1	$^{126}\text{In}^{48+}$	11200, 12000	52998	38110	
In-A+2	$^{127}\text{In}^{48+}$	10948, 12685	28997	19285	
In-A+1	$^{129}\text{In}^{49+}$	11607, 12691	37149	25692	
Cd-A	$^{125}\text{Cd}^{48+}$	11608, 13267	18296	15521	
Cd-A+1	$^{126}\text{Cd}^{48+}$	11582, 12808	91824	72659	
Cd-A+2	$^{127}\text{Cd}^{48+}$	11270, 12727	95369	30583	
Ag-A+1	$^{123}\text{Ag}^{47+}$	11194, 12398	97125	73995	
Ag-A+2	$^{124}\text{Ag}^{47+}$	11450, 12660	130826	72524	4.0(6)
Ag-A+3	$^{125}\text{Ag}^{47+}$	11325, 12100	35069	16653	
Pd-A+1	$^{121}\text{Pd}^{46+}$	11278, 12444	65136	35620	34.2(7)
Rh-A+2	$^{120}\text{Rh}^{45+}$	10516, 12403	12176	3056	6(2)
Ru-A+1	$^{117}\text{Ru}^{44+}$	10371, 12631	6154	2054	22(2)

in the next several paragraphs.

The analysis procedure began with the designation of a fragment gate to select an individual component of the secondary ion beam. The data-analysis program SpecTcl was used for software gating to select events associated with each fragment blob. The fragment energy loss and time-of-flight of the events located within a given PID blob correspond with values expected for a fully-stripped ion. However, for reasons discussed earlier, hydrogen-like charge-state contaminants were also present. The amount of charge-state contamination in a PID blob was addressed by inspection of the fragment-gated TKE spectrum. A representative fragment-gated TKE spectrum for In-A+1, which includes  $^{129}\text{In}^{49+}$  and  $^{126}\text{In}^{48+}$ , is shown in Figure 4.3. This TKE spectrum has two components—a main peak with small shoulder on the high-energy side of the distribution—due to the presence of both fully-stripped and hydrogen-like ions in the fragment gate. The entire distribution was fitted with two Gaussian components and a background contribution using the peak-fitting program DAMM. Each component of the fit is indicated in Figure 4.3. The hydrogen-like contaminant ions

Table 4.3: A summary of prompt  $\gamma$  rays and deduced  $T_{1/2}$  for nuclides implanted into PIN01a.

Nuclide	Gamma Rays [keV]	$T_{1/2}$ [ $\mu$ s]
$^{129}\text{Sn}$	382, 571, 1136, 1324	2.4(15)
$^{126}\text{In}$	244, 266, 279, 615 836, 864	5(7)
$^{127}\text{In}$	221, 233	3.5(3)
$^{129}\text{In}$	334, 359, 996, 1354	2.2(3)
$^{125}\text{Cd}$	409, 720, 743, 786 868, 923	1.7(8)
$^{126}\text{Cd}$	220, 248, 402, 405 653, 807, 815, 857	2.0(7)
$^{127}\text{Cd}$	739, 771, 822, 909	1.9(6)
$^{123}\text{Ag}$	350, 384, 391, 630 686, 714, 733, 770 1049, 1077, 1134	0.32(3)
$^{124}\text{Ag}$	156, 1133	1.9(2)
$^{125}\text{Ag}$	670, 685, 714, 729	0.44(9)
$^{121}\text{Pd}$	135	0.70(5)
$^{120}\text{Rh}$	211	not determined
$^{117}\text{Ru}$	185	1.4(6)

( $^{126}\text{In}^{48+}$ ) have slightly less kinetic energy than the fully-stripped ions; therefore, the higher-energy peak of a TKE spectrum was attributed to the fully-stripped fragment and the lower-energy peak was attributed to the hydrogen-like fragment.

In order to select for a specific isotope, a software cut on a TKE spectrum was made in SpecTcl. The range of this cut in the example of Figure 4.3 is indicated by the vertical lines. Several different TKE cut ranges were applied as software gates on the prompt-gamma ray spectrum. The effort was initially directed toward selecting the fully-stripped fragments as free of contamination as possible. However, in many cases a liberal TKE gate was used to include as many counts as possible of a given species, at the cost of a slightly higher gamma-ray background. The energy limits established for each TKE-spectrum gate are given in Table 4.2. A summary of TKE information from the isomer analysis is provided in Table 4.4. A final gamma-ray isomer spectrum for each nuclide was prepared in software by combining the fragment PID-blob gate and the TKE gate using a logical AND.

Table 4.4: A summary of the integrated number of counts in each TKE peak from the isomer analysis. The quantity TKE\* is described by Eq. 3.1 on page 45. The calculated TKE values were determined using the computer program LISE++. The difference between a calculated TKE and the measured TKE\* is simply the energy loss in the upstream plastic scintillator, which was not included in the measured value due to this detector's poor resolution.

PID Blob Gate	Fragment	Integrated Peak Counts	TKE* Peak Centroid [GeV]	TKE Peak $\sigma_{std}$ [GeV]	Calculated TKE [GeV]
Sn-A	$^{129}\text{Sn}^{49+}$	6914	11.62	0.59	12.36
	$^{132}\text{Sn}^{50+}$	515	11.91	0.59	12.58
In-A+1	$^{126}\text{In}^{48+}$	38260	11.59	0.73	12.14
	$^{129}\text{In}^{49+}$	18617	11.89	0.73	12.36
In-A+2	$^{127}\text{In}^{48+}$	23178	11.50	0.64	12.05
	$^{130}\text{In}^{49+}$	2982	11.80	0.64	12.27
Cd-A	$^{122}\text{Cd}^{47+}$	5155	11.61	0.64	12.02
	$^{125}\text{Cd}^{48+}$	13995	11.95	0.64	12.24
Cd-A+1	$^{123}\text{Cd}^{47+}$	43842	11.56	0.73	11.93
	$^{126}\text{Cd}^{48+}$	70922	11.88	0.73	12.15
Cd-A+2	$^{124}\text{Cd}^{47+}$	66592	11.49	0.79	11.83
	$^{127}\text{Cd}^{48+}$	29511	11.79	0.79	12.06
Ag-A+1	$^{120}\text{Ag}^{46+}$	71004	11.49	0.88	11.71
	$^{123}\text{Ag}^{47+}$	22951	11.78	0.88	11.93
Ag-A+2	$^{121}\text{Ag}^{46+}$	55478	11.45	0.74	11.62
	$^{124}\text{Ag}^{47+}$	69014	11.75	0.74	11.84
Ag-A+3	$^{122}\text{Ag}^{46+}$	27428	11.38	0.78	11.53
	$^{125}\text{Ag}^{47+}$	16147	11.68	0.78	11.75
Pd-A+1	$^{118}\text{Pd}^{45+}$	37131	11.40	0.93	11.40
	$^{121}\text{Pd}^{46+}$	33827	11.70	0.93	11.63
Rh-A+2	$^{117}\text{Rh}^{44+}$	7532	11.18	0.84	11.01
	$^{120}\text{Rh}^{45+}$	2524	11.49	0.84	11.23
Ru-A+1	$^{114}\text{Ru}^{43+}$	2712	11.11	0.99	10.79
	$^{117}\text{Ru}^{44+}$	1359	11.45	0.99	11.02

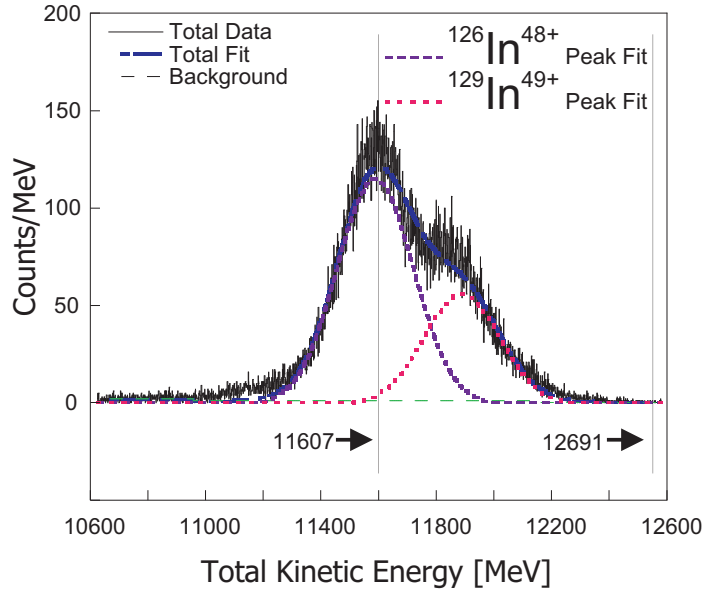


Figure 4.3: A sample TKE spectrum from the isomer analysis illustrating a software cut on the higher-energy  $^{129}\text{In}^{49+}$  peak. The vertical lines indicate the range of the  $^{129}\text{In}$  TKE gate.

### Prompt Gamma Radiation

The prompt gamma-ray spectrum for a given nuclide was obtained from the total prompt gamma-ray spectrum by gating on the corresponding fragment contour and TKE cut. The resulting peaks in each spectrum were fitted with Gaussian functions using DAMM. A background region of approximately 10 keV on each side of a peak was considered for each fit. Gamma-ray energies were obtained from the fitted peak centroids, and gamma-ray intensities were deduced from the peak areas. Coincidence relationships between the observed prompt gamma rays were also investigated. As described in Section 3.3.2, a two-dimensional gamma-gamma matrix was prepared for each nuclide by gating on a fragment PID-blob contour and appropriate TKE cut. One-dimensional gamma-ray spectra were projected from this fragment-gated two-dimensional matrix. The statistics in each fragment- $\gamma\gamma$  coincidence spectrum are extremely low, but the triple coincidence (frag- $\gamma\gamma$ ) provides a high degree of sensitivity due to low background. In many of these spectra a gamma “peak” with a single count was observed at an energy corresponding to a known gamma ray. Strictly speaking, a

gamma peak with a single count cannot be distinguished from a random coincidence. However, taking into consideration the near-zero average background and the fact that in several cases (*e.g.*  $^{129}\text{Sn}$ ) the single-count coincidences are corroborated by known gamma-ray coincidence relationships, it was concluded that the technique used to determine gamma-gamma coincidence relationships in this work was valid.

### Isomeric Half-Life

Fragment/TKE-gated prompt gamma-decay curves were obtained from the two-dimensional SeGA-TAC versus gamma singles matrix, as described in Section 3.3.2. Decay curves were rebinned with variable bin sizes for fitting. Half-life values were determined by single-component exponential least-squares fitting of the decay curves. The deduced half-life uncertainties reported in the subsequent sections are only representative of the least-squares fitting error and do not take the error bars into consideration; therefore, the reported uncertainties should be construed as significantly underestimating the true uncertainties.

#### 4.2.1 $^{129}\text{Sn}$

A single PID blob associated with Sn isotopes was identified and labeled as Sn-A (see Fig. 4.1). Fully-stripped  $^{132}\text{Sn}$  was expected to fall within the Sn-A PID region; however, the low production yield of  $^{132}\text{Sn}$  fragments was beneath the detection sensitivity of the experimental setup and no  $^{132}\text{Sn}$  prompt gamma rays were observed from the 2.03- $\mu\text{s}$  isomer [44]. Consequently, the hydrogen-like charge state of  $^{129}\text{Sn}$  was the only fragment found within this blob. The integrated events within the Sn-A PID contour for all experimental runs, as well as for the experimental runs that included the SeGA-TAC, are given in Table 4.5. Alongside these values are given the observed number of counts for  $^{129}\text{Sn}$  within the TKE cut.

The  $^{129}\text{Sn}$  prompt gamma-ray spectrum is shown in Figure 4.4. Four peaks were identified, and the deduced gamma-ray energies, peak areas, and relative intensi-

Table 4.5: The integrated number of events associated with the Sn-A PID gate.

Portion of Data	PID Contour	$^{129}\text{Sn}$ TKE Peak
All Runs	12200	8359
Runs w/SeGA TAC	6532	3719

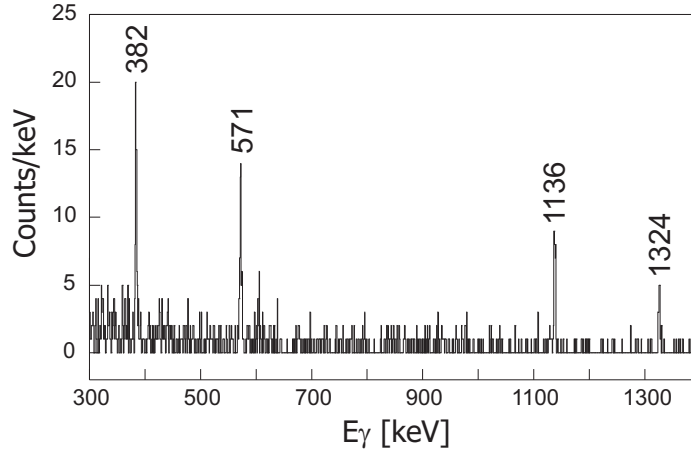


Figure 4.4: Prompt gamma-ray spectrum for  $^{129}\text{Sn}$ .

ties are displayed in Table 4.6. Coincidence relationships between the observed  $^{129}\text{Sn}$  prompt gamma rays were investigated, and the fragment- $\gamma\gamma$  coincidence spectra that were obtained in this work are shown in Figure 4.5. The fitted  $^{129}\text{Sn}$  prompt gamma-ray decay curve is shown in Figure 4.6. The half-life from the present work [ $T_{1/2} = 2.4(15)\mu\text{s}$ ] along with the literature values are included in the inset.

Table 4.6: The  $^{129}\text{Sn}$  prompt gamma-ray energies, integrated peak areas and relative intensities. Gamma-ray energies are compared with values from (a)Ref. [45] and (b)Ref. [46]. Literature values for the relative intensities were not available.

Gamma-Ray Energy [keV]			Fitted Peak Area	Relative Intensity	
This Work	Literature <sup>a,b</sup>			This Work	Literature
382.3(2)	382.2 <sup>a</sup>	382 <sup>b</sup>	43(8)	74(20)	-
570.4(3)	570.1 <sup>a</sup>	570 <sup>b</sup>	39(9)	87(27)	-
1136.3(3)	1136.0 <sup>a</sup>	1136 <sup>b</sup>	30(6)	100(28)	-
1324.0(2)	1323.8 <sup>a</sup>	1324 <sup>b</sup>	15(3)	55(16)	-

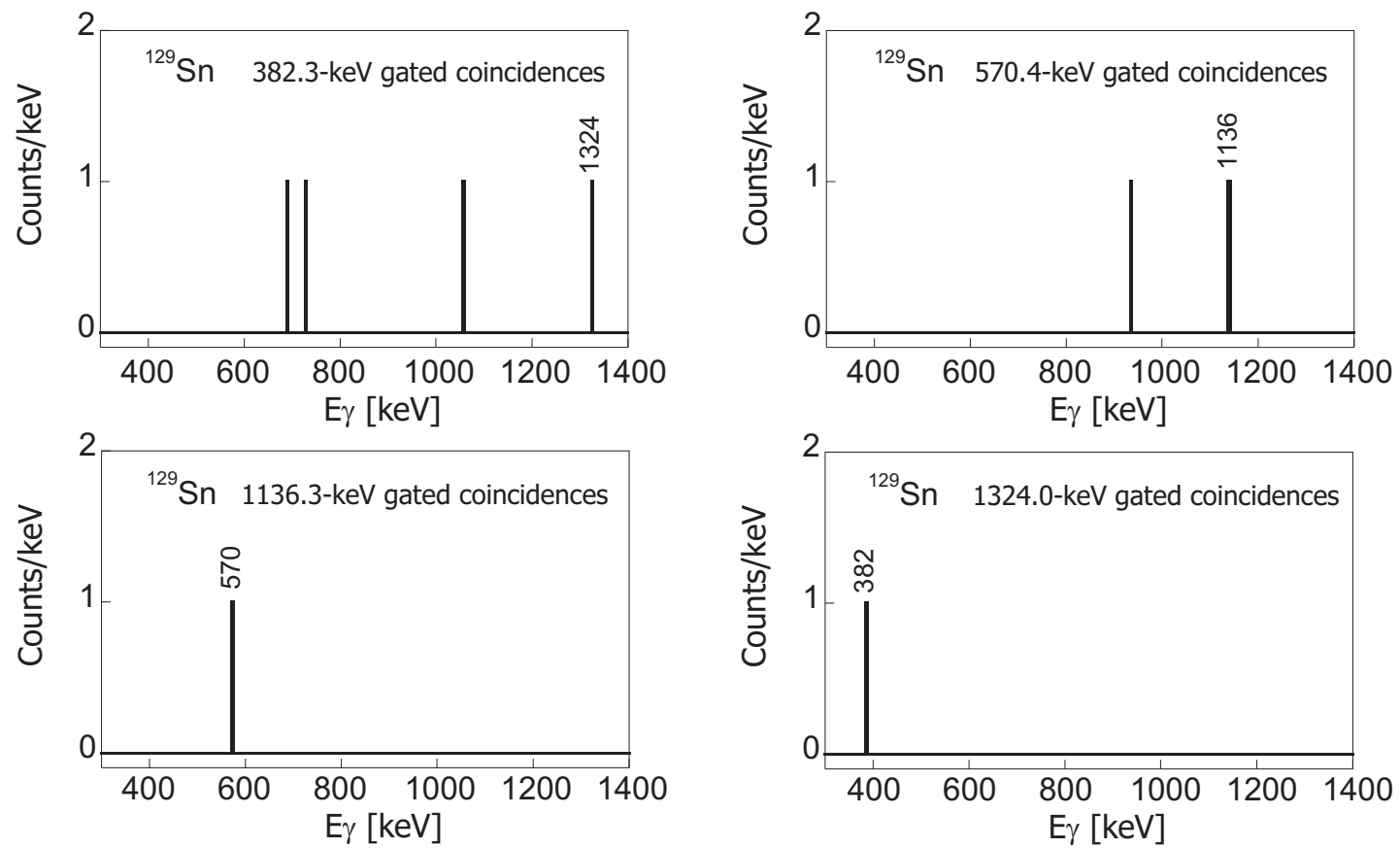


Figure 4.5: Prompt fragment- $\gamma\gamma$  coincidence spectra for  $^{129}\text{Sn}$ .

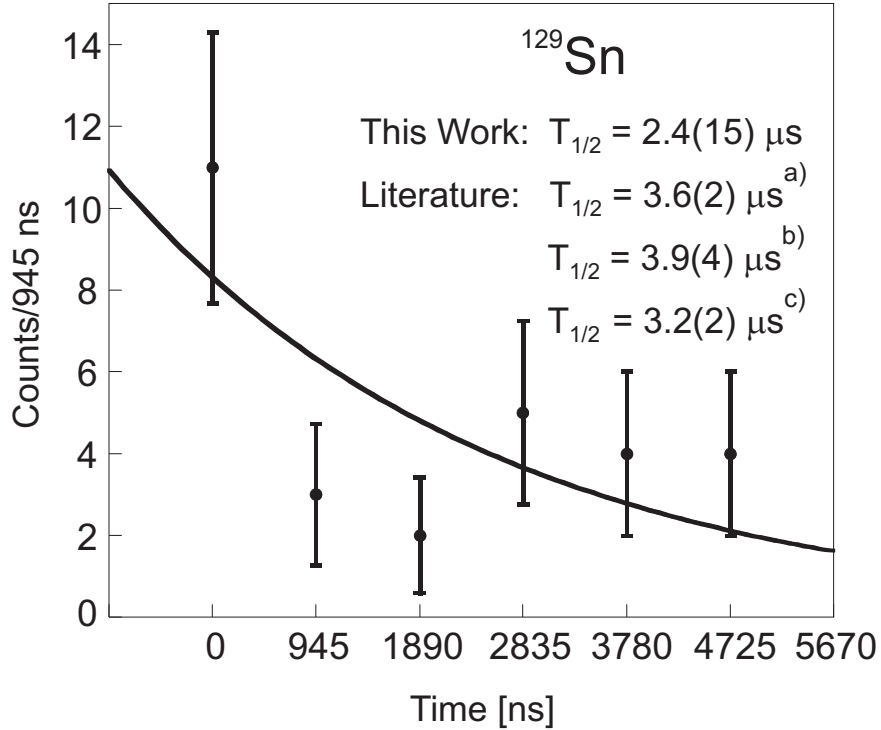


Figure 4.6: The fitted  $^{129}\text{Sn}$  isomer decay curve. The extracted half-life value is given in the inset along with the literature values reported by (a) Genevey *et al.* [45], (b) Hellström *et al.* [46], and (c) Gausemel *et al.* [47].

Two  $^{129}\text{Sn}$  isomers have been previously reported by Genevey *et al.* [45] and Gausemel *et al.* [47] and one of the isomers has also been reported by Hellström *et al.* [46]. The proposed isomer decay scheme is shown in Figure 4.7. The gamma-ray energies determined in the present work are in good agreement with those reported in the literature, as shown in Table 4.6. In the present work, the 382-keV transition and the 1324-keV transition were coincident, and these two gamma transitions are known to occur in a cascade from the  $15/2^+$  level. The 571- and 1136-keV gamma rays were found to be in coincidence with each other, and these two transitions also form a cascade from the  $15/2^+$  level in  $^{129}\text{Sn}$ . The  $15/2^+$  excited state at 1741 keV is believed to be populated by two sequential isomeric transitions—a 41.0-keV  $E2$  and a 19.7-keV  $E2$ , respectively. In principle, the two gamma-ray cascades observed in the present work should be seen in coincidence with these isomeric transitions; however, both of these ITs are below the gamma-ray detection threshold of Experiment 01015, so they

were not observed. Theoretically estimated total internal conversion coefficients for the 41.0- and 19.7-keV  $E2$  transitions are  $\sim 45$  and  $\sim 900$  [48], respectively, indicating that these are likely to be converted in  $^{129}\text{Sn}$ . No evidence of conversion-electron peaks was found in the recorded Si total energy spectrum taken in coincidence with  $^{129}\text{Sn}$  fragments.

The half-life for each of the two  $^{129}\text{Sn}$  isomers is indicated in the decay scheme, shown in Figure 4.7. The current experimental half-life value for  $^{129m}\text{Sn}$  is in agreement with the values reported by Genevey *et al.* [45] and Gausemel *et al.* [47] for the  $19/2^+$  isomer. Hellström *et al.* [46] reported a half-life value that is also in agreement with the present result, suggesting that the  $19/2^+$  isomer was observed in that work as well. Because the ITs were not measured in the present work, the half-lives of the two isomers were not determined individually. Both isomers may have been populated, but since the isomeric transitions were not observed there was no direct means of identifying the  $23/2^+$  isomer. The overall half-life for the cascade from the upper isomer is determined by the longer-lived  $3.6\text{-}\mu\text{s}$  level. In the work reported by Hellström, the upper isomer was not observed, and the author suggested that the upper isomer may not be strongly populated by the projectile fission used in that study. In a similar vein, perhaps, the projectile fragmentation used in the present work may not have strongly populated the  $23/2^+$  isomer.

In summary, the experimental observations of the  $^{129}\text{Sn}$  isomer in this work were found to be in good agreement with several published measurements. Such agreement has been interpreted as a validation of the data-analysis techniques employed in the present work.

The appearance of isomers in the neutron-rich isotopes of Sn has been known for a long time. Mayer [49] used deep inelastic nucleus-nucleus collisions to populate  $\mu\text{s}$  isomers in the odd-A nuclides  $^{119,121,123}\text{Sn}$ , and others [45–47, 50] have employed projectile fission to populate  $\mu\text{s}$  isomers in the more neutron-rich  $^{125,127,129}\text{Sn}$ . Thus, the current work demonstrates the feasibility of also populating these isomers via

projectile fragmentation.

From a theoretical standpoint, beyond the midpoint of the  $N=50-82$  shell the Sn isotopes can be treated by considering neutron holes as quasiparticles outside of the doubly-magic  $^{132}\text{Sn}$  core. The  $^{129}\text{Sn}$  nucleus is three neutron holes in the  $^{132}\text{Sn}$  core, with the  $3/2^+$  ground state coming from a  $\nu h_{11/2}^{-2} d_{3/2}^{-1}$  configuration. The low-lying, negative-parity states, shown in Figure 4.7, are believed to arise from the coupling of the odd  $h_{11/2}$  neutron hole to the  $^{130}\text{Sn}$ -core  $2^+$  excitation [47]. Based on a comparison of their data with OXBASH [51] shell-model calculations, Genevey *et al.* suggested that the  $\nu h_{11/2}^{-2} d_{3/2}^{-1}$  configuration is a major contributor to the  $19/2^+$  and  $23/2^+$  isomeric states in  $^{129}\text{Sn}$  [45]. Pinston *et al.* attributed the  $\nu h_{11/2} \otimes 5^-$  configuration as the major component of the isomeric states, with the  $5^-$  core excitation arising from a mixture of  $\nu h_{11/2} d_{3/2}$  and  $\nu h_{11/2} s_{1/2}$  configurations [50]. In general the presence of  $\mu\text{s}$  isomers in nuclides that are a few neutron holes outside of  $^{132}\text{Sn}$  has been attributed to the low-lying  $\nu h_{11/2}$  orbital [52]. The excited states produced by the  $h_{11/2}$  orbital tend to have significantly larger spins than the other excited states that come from  $d_{3/2}$  or  $s_{1/2}$  configurations. The large  $\Delta J$  value for a transition between two such states requires a higher multipolarity gamma ray with a consequently lower transition probability. This low transition probability is responsible for the characteristically longer-lived isomeric states. Also, the close spacing of excited states requires low-energy transitions, which are of lower probability as suggested by the Weisskopf estimates. In  $^{129}\text{Sn}$  low-energy  $E2$  transitions ( $<100$  keV) between the higher-spin, even-parity states lead to microsecond lifetimes of these isomers.

#### 4.2.2 $^{127}\text{In}$

Three PID regions associated with In isotopes were identified, and the heaviest-isotope blob, *i.e.* the blob furthest to the left in the PID plot, was labeled In-A+2, as shown in Figure 4.1. The fragment energy loss and time-of-flight of the events located within the In-A+2 PID blob correspond with ions of fully-stripped  $^{130}\text{In}^{49+}$ . However, the

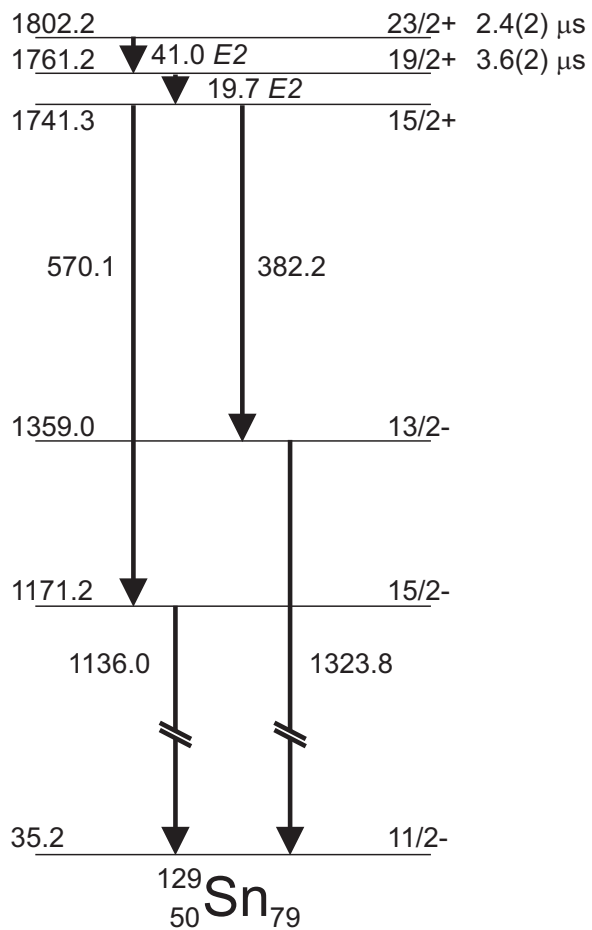


Figure 4.7: Decay scheme for  $^{129}\text{Sn}$  isomers from Ref. [45]. The quoted energies are in keV.

Table 4.7: The integrated number of events associated with the In-A+2 PID gate.

Portion of Data	PID Contour	$^{127}\text{In}$ TKE Peak
All Runs	37376	25692
Runs w/SeGA TAC	19756	13381

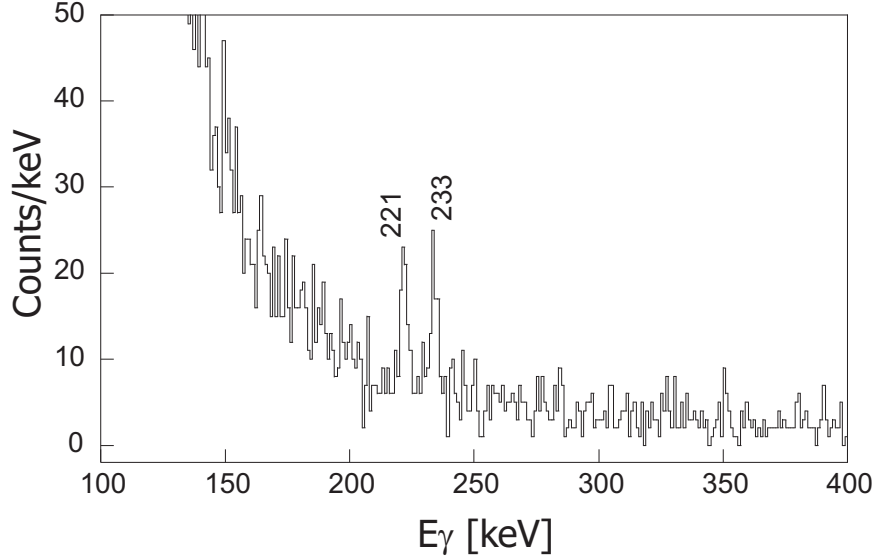


Figure 4.8: Prompt gamma-ray spectrum for  $^{127}\text{In}$ .

low level of  $^{130}\text{In}$  present in the secondary beam was beneath the detection sensitivity of the experimental setup, and no  $^{130}\text{In}$  prompt gamma rays were observed from the  $3.1\text{-}\mu\text{s}$  isomer reported in Ref. [53]. As a result, the hydrogen-like charge state of  $^{127}\text{In}$  was the only nuclide found within this blob. The integrated events within the In-A+2 PID contour for all experimental runs, as well as for the experimental runs that included the SeGA-TAC, are given in Table 4.7. Alongside these values are given the observed number of counts for the  $^{127}\text{In}$  within the TKE cut.

The  $^{127}\text{In}$  prompt gamma-ray spectrum is shown in Figure 4.8. Two peaks were identified, and the deduced gamma-ray energies, peak areas, and relative intensities are displayed in Table 4.8. Coincidence relationships between the observed  $^{127}\text{In}$  prompt gamma rays were investigated, and the fragment- $\gamma\gamma$  coincidence spectra that were obtained in this work are shown in Figure 4.9. The fitted  $^{127}\text{In}$  prompt gamma-ray decay curve is shown in Figure 4.10. The present half-life value of  $3.5(3)\ \mu\text{s}$  is significantly shorter than the literature values shown in the inset of Figure 4.10.

Table 4.8: The  $^{127}\text{In}$  prompt gamma-ray energies, integrated peak areas and relative intensities. Gamma-ray energies are compared with values from (a)Ref. [53]. Literature values for the relative intensities were not available.

Gamma-Ray Energy [keV]		Fitted Peak Area	Relative Intensity	
This Work	Literature <sup>a)</sup>		This Work	Literature
220.4(3)	221.3(5)	57(15)	100(37)	-
232.6(4)	233.4(5)	50(18)	90(40)	-

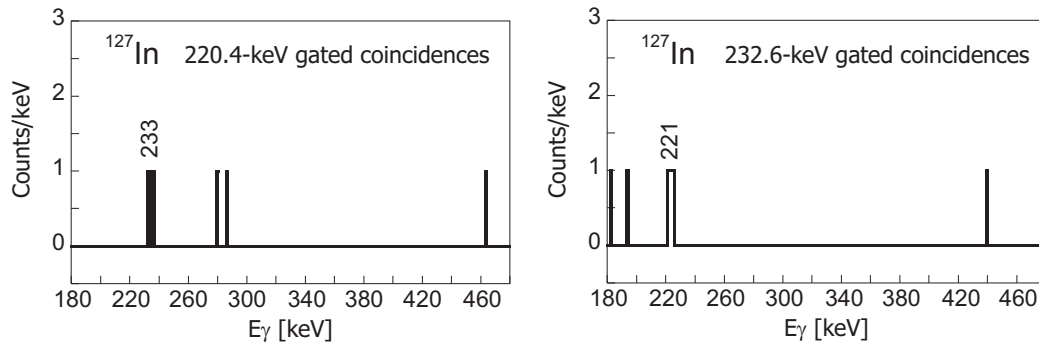


Figure 4.9: Prompt fragment- $\gamma\gamma$  spectra for  $^{127}\text{In}$ .

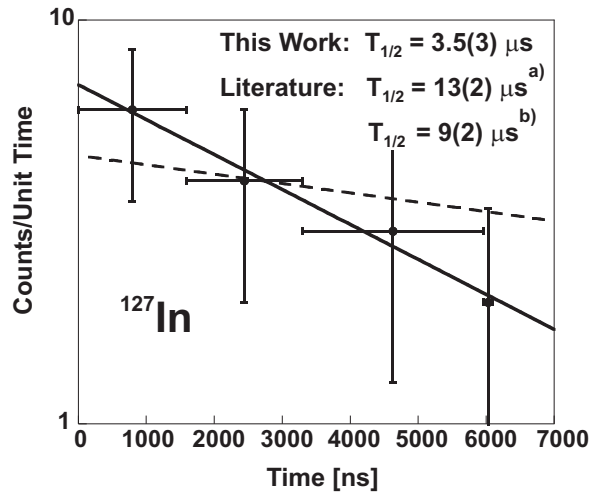


Figure 4.10: The fitted  $^{127}\text{In}$  isomer decay curve. The extracted half-life value is given in the inset along with the literature values reported by (a) Hellström *et al.* [46] and (b) Scherillo *et al.* [53]. The dashed line represents the fitted decay curve with a half-life constrained to  $13\ \mu\text{s}$ .

The  $^{127}\text{In}$  isomer has been previously reported by Hellström *et al.* [46] and Scherillo *et al.* [53]. The proposed level scheme [53] is given in Figure 4.11. The gamma-ray energies determined in the present work are in good agreement with those reported in the literature, as shown in 4.8. Although no gamma-ray relative intensity values are given, Hellström reported that the two gamma rays are of comparable intensities [46], which agrees well with the present observation. In the present work, the 221- and 233-keV transitions were coincident, in agreement with a previous observation [53]. These two gamma transitions are believed to occur in cascade from a  $25/2^+$  level, although the order of the transitions is not known. This  $25/2^+$  level is populated by a highly-converted 47.0-keV  $E2$  isomeric transition [53]. The IT was below the gamma-ray detection threshold and was not observed in this work, nor were the conversion electrons observed.

The current experimental half-life value for  $^{127m}\text{In}$  ( $3.5(3) \mu\text{s}$ ) does not agree with the values of  $13(2) \mu\text{s}$  and  $9(2) \mu\text{s}$  reported by Hellström and Scherillo, respectively. The  $^{127m}\text{In}$  decay curve shown in Figure 4.10 has rather low statistics, and considering the error bars, it could result from a longer half-life value. The decay curve with a half-life constrained to Hellström's value of  $13 \mu\text{s}$  is provided for illustration in Figure 4.10. It should be noted that the decay curve reported by Hellström *et al.* [46] shows an unexpectedly large number of counts in the first few hundred nanoseconds. Based on this observation, Scherillo *et al.* have suggested that a second isomer may be present, although they did not see evidence for it in their data and consequently estimate that such an isomer would have a half-life of less than  $\sim 500 \text{ ns}$  [53].

In summary, the experimentally observed  $^{127m}\text{In}$  prompt gamma-ray energies, relative intensities, and coincidence relationships, in this work, were found to be in good agreement with all of the published measurements. The rather poor agreement of the deduced half-life value is attributed to low statistics, however, the decay curve does suggest that half-life of several microseconds is likely.

The previous section described the odd- $A$   $^{129}\text{Sn}$  isomer, whose excited states are

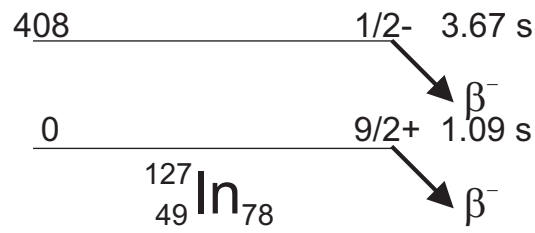
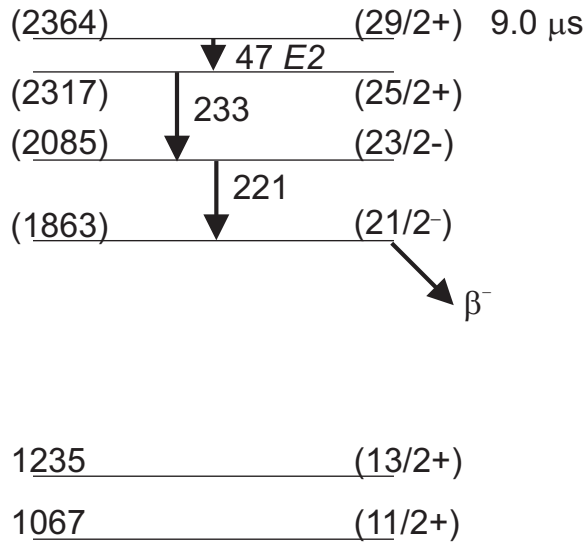


Figure 4.11: Decay scheme for the  $^{127}\text{In}$  isomers from Ref. [53]. The quoted energies are in keV.

determined by an odd number of neutron holes in the doubly-magic  $^{132}\text{Sn}$  core. In contrast to this,  $^{127}\text{In}$ , with an even number of neutrons ( $N=78$ ) and an odd number of protons ( $Z=49$ ), should be described as a proton hole inside the even-even, proton-magic  $^{128}_{50}\text{Sn}_{78}$  core. The single proton hole in the Sn core resides in the  $g_{9/2}$  orbital, and the even-parity excited states of  $^{127}\text{In}$  arise from the coupling of this proton hole to the  $^{128}\text{Sn} \nu h_{11/2}^{-4}$  configurations [53]. Thus, even-parity levels from the  $9/2^+$  ground state to the  $29/2^+$  isomeric state are produced by the  $\pi g_{9/2}^{-1} \otimes \nu h_{11/2}^{-4}$  configurations. The odd-parity states  $21/2^-$  and  $23/2^-$  are produced by the coupling of the  $\pi g_{9/2}$  hole to the  $7^-$   $^{128}\text{Sn}$  core excitation, which is equivalent to the configuration  $\pi g_{9/2}^{-1} \otimes \nu h_{11/2}^{-3} d_{3/2}^{-1}$  [53].

A low-lying (first excited state)  $1/2^-$  isomer is known to exist in all odd- $A$  In isotopes from  $^{103}\text{In}_{54}$  to  $^{131}\text{In}_{82}$ . The  $1/2^-$  isomer, which arises from the  $\pi p_{1/2}^{-1} \otimes \nu h_{11/2}^{-4}$  configuration, is usually depopulated by beta decay, but it can also be depopulated by an  $M4$  IT. The higher-spin  $29/2^+$   $^{127}\text{In}$  isomer observed in the present work has no known gamma transitions in common with the  $1/2^-$  isomer at  $\sim 420$  keV [53].

In addition to the  $1/2^-$  isomer, higher-energy isomers have also been observed in the odd- $A$  In isotopes  $^{123-129}\text{In}$  [53]. In contrast to the  $1/2^-$  isomer, which is attributable to the proton configuration, the  $29/2^+$   $^{127}\text{In}$  isomer is ascribed to the neutron  $h_{11/2}$  orbital that causes the energy compression of the  $25/2^+$  and  $29/2^+$  states [54].

### 4.2.3 $^{129}\text{In}$

Of the three PID blobs associated with In isotopes, the blob immediately to the right of In-A+2 in the PID plot was labeled In-A+1, as shown in Figure 4.1. The fragment energy loss and time-of-flight of the events located within the In-A+1 PID blob correspond with ions of fully-stripped  $^{129}\text{In}^{49+}$ . However, the In-A+1 gated TKE spectrum (Fig. 4.12) reveals the presence of two species:  $^{126}\text{In}^{48+}$  contaminant ions at the lower kinetic energy and  $^{129}\text{In}^{49+}$  ions at the higher kinetic energy. The upper and lower limits of the TKE gate are indicated in Figure 4.12 by the vertical lines.

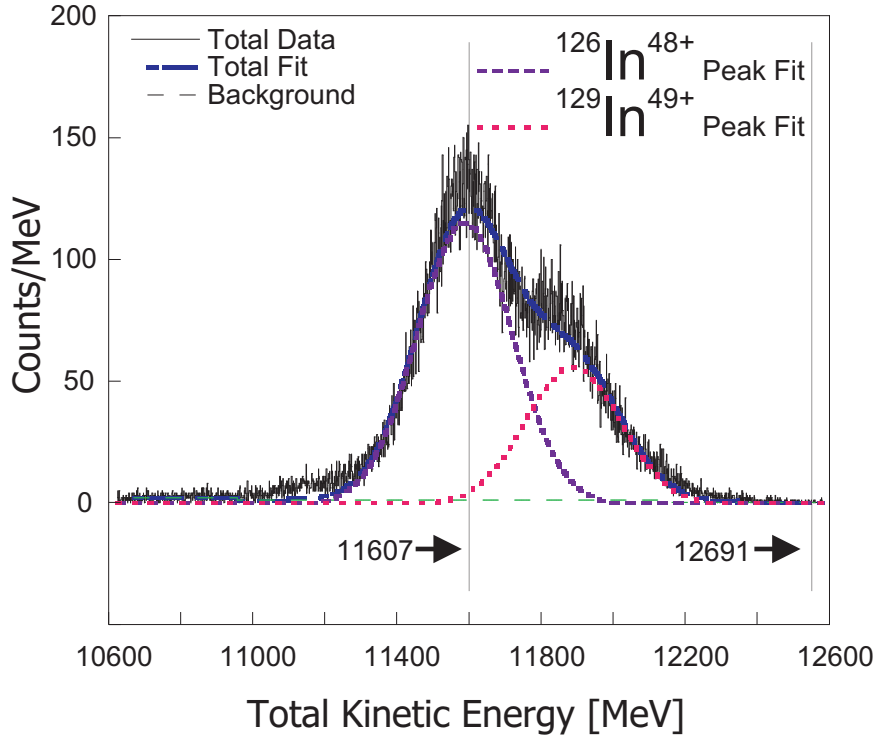


Figure 4.12: Two unequal distributions can be seen. The larger is attributed to  $^{126}\text{In}^{48+}$  and the smaller to  $^{129}\text{In}^{49+}$ . The vertical lines indicate the range of the  $^{129}\text{In}$  TKE gate.

Table 4.9: The integrated number of events associated with the In-A+1 PID gate.

Portion of Data	PID Contour	$^{129}\text{In}$ TKE Peak
All Runs	72997	19285
Runs w/SeGA TAC	35717	9427

The integrated events within the In-A+1 PID contour for all experimental runs, as well as for the experimental runs that included the SeGA-TAC, are given in Table 4.9 with the observed number of counts for  $^{129}\text{In}$  within the TKE cut.

The  $^{129}\text{In}$  prompt gamma-ray spectrum is shown in Figure 4.13. Four  $^{129}\text{In}$  peaks were identified, and the deduced gamma-ray energies, peak areas, and relative intensities are displayed in Table 4.10. Coincidence relationships between the observed  $^{129}\text{In}$  prompt gamma rays were also investigated, and the fragment- $\gamma\gamma$  coincidence spectra that were obtained in this work are shown in Figure 4.14. The fitted  $^{129}\text{In}$  prompt gamma-ray decay curve is shown in Figure 4.15. The half-life from the present work [2.2(3)  $\mu\text{s}$ ] along with the literature value are included in the inset.

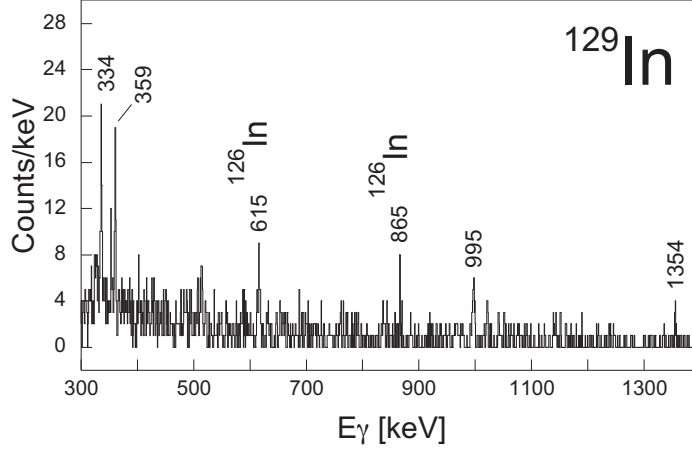


Figure 4.13: Prompt gamma-ray spectrum for  $^{129}\text{In}$ .

Table 4.10: The  $^{129}\text{In}$  prompt gamma-ray energies, integrated peak areas and relative intensities. Gamma-ray energies and relative intensities are compared with values from (a)Ref. [55].

Peak Energy [keV]		Fitted Peak Area	Relative Intensity	
This Work	Literature <sup>a)</sup>		This Work	Literature
334.3(2)	333.8	33(8)	70(21)	100
359.0(2)	359.0	29(5)	65(16)	83
995.5(3)	995.2	24(4)	100(24)	82
1353.6(3)	1354.1	6(3)	30(16)	28

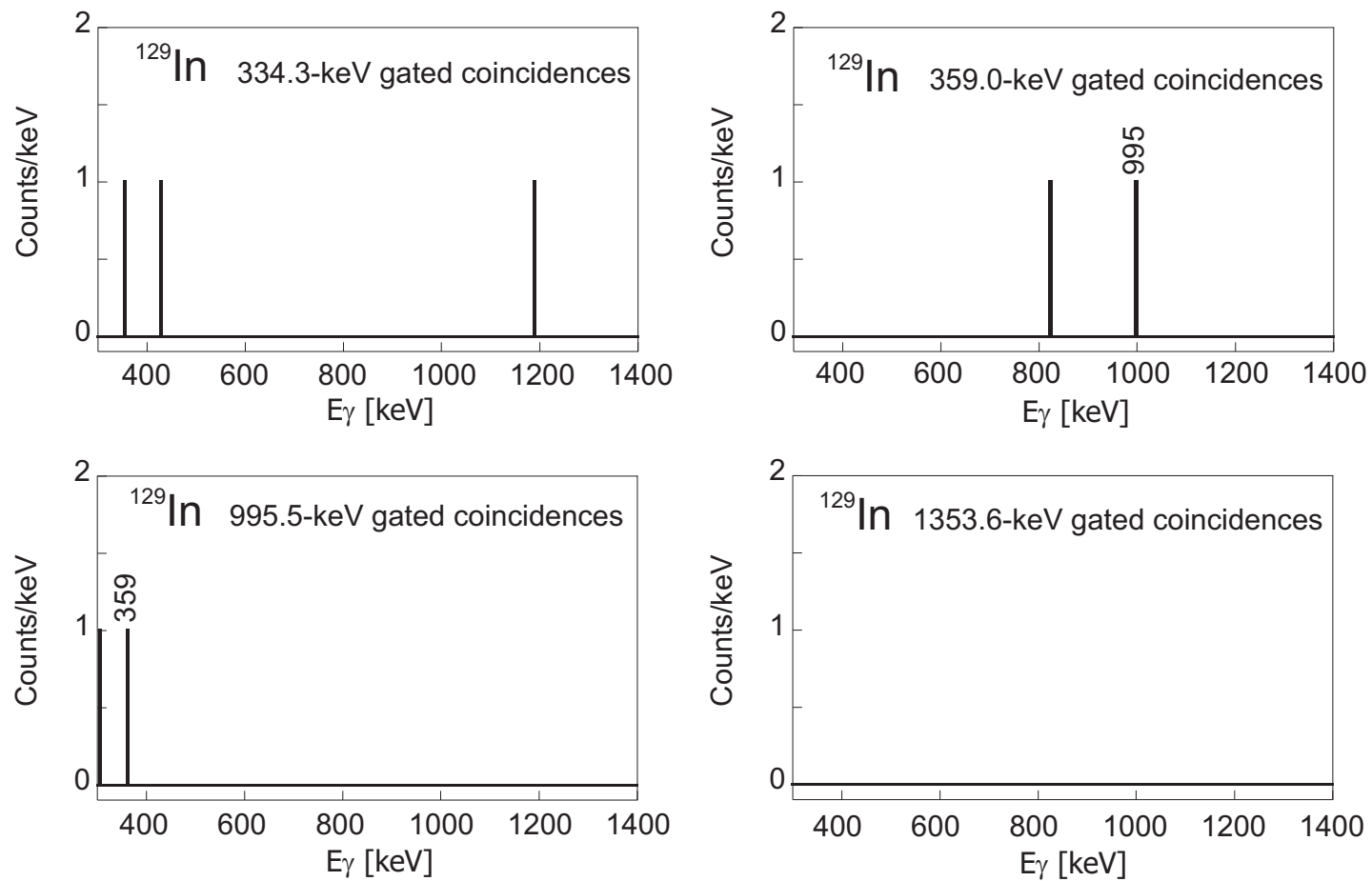


Figure 4.14: Prompt fragment- $\gamma\gamma$  spectra for  $^{129}\text{In}$ .

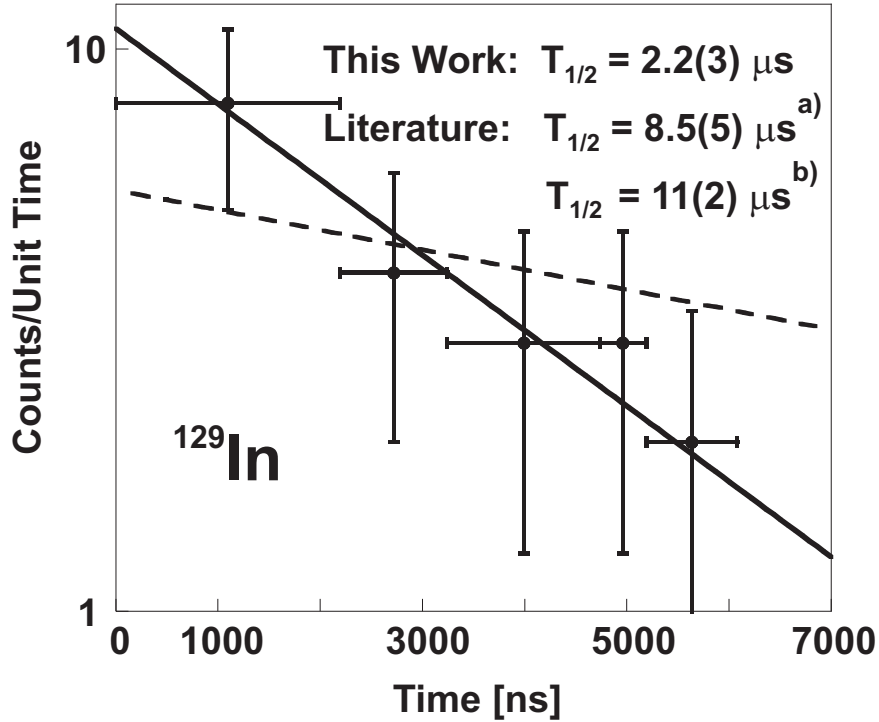


Figure 4.15: The fitted  $^{129}\text{In}$  isomer decay curve (solid line). The extracted half-life value is given in the inset along with the literature values reported by (a) Genevey *et al.* [55] and (b) Hellström *et al.* [46]. The dashed line represents the fitted decay curve with a half-life constrained to  $8.5 \mu\text{s}$ .

Four isomeric states are known in  $^{129}\text{In}$ , as shown in Figure 4.16. The  $17/2^-$  isomer observed in the present work has no known gamma transitions in common with the  $29/2^+$ ,  $23/2^-$ , or  $1/2^-$  isomers [53]. The  $^{129}\text{In}$   $17/2^-$  isomer has been previously reported by Hellström *et al.* [46] and Genevey *et al.* [45]. The proposed level scheme [53] is given in Figure 4.16. The gamma-ray energies determined in the present work are in good agreement with those reported in the literature, as shown in Table 4.10. The gamma-ray relative intensity values given by Genevey *et al.* [45] agree well with the present observation. In the present work, the 359- and 996-keV transitions were coincident, in agreement with a previous observation [55]. These two gamma transitions are believed to occur in cascade, where the 359-keV gamma ray is the  $13/2^+ \rightarrow 11/2^+$  transition and the 996-keV gamma ray is the  $11/2^+ \rightarrow 9/2^+$  transition. The  $13/2^+$  level is populated by a 333.8-keV  $M2$  isomeric transition from the  $17/2^-$  level [45]. This IT was observed in the present work.

The current experimental half-life value for this  $^{129}\text{In}$  isomer [2.2(3)  $\mu\text{s}$ ] does not agree well with the values of 11(2)  $\mu\text{s}$  and 8.5(5)  $\mu\text{s}$  reported by Hellström and Genevey, respectively. The  $^{129}\text{In}$  isomer decay curve shown in Figure 4.10 has rather low statistics, and considering error bars, the decay curve does appear to be rather flat, suggesting that the half-life is likely to be longer than the deduced value. The decay curve with a half-life constrained to Genevey's value of 8.5  $\mu\text{s}$  is provided for illustration in Figure 4.10.

In summary, the experimentally observed  $^{129}\text{In}$  isomeric prompt gamma-ray energies, relative intensities, and coincidence relationships, in this work, were found to be in good agreement with all of the published measurements for the  $17/2^-$  isomer. The rather poor agreement of the deduced half-life value is attributed to low statistics, however, the decay curve does suggest that half-life of several microseconds may be possible.

Analogous to  $^{127}\text{In}$ , the nuclide  $^{129}\text{In}$ , with an even number of neutrons ( $N=80$ ) and an odd number of protons ( $Z=49$ ), is well described as a proton hole inside the even-even, proton-magic  $^{130}\text{Sn}_{80}$  core. The single proton hole in the Sn core resides in the  $g_{9/2}$  orbital, and the even-parity excited states of  $^{129}\text{In}$  arise from the coupling of this proton hole to the  $^{130}\text{Sn}$   $\nu h_{11/2}^{-2}$  configurations [53]. Thus, even-parity levels from the  $9/2^+$  ground state to the  $29/2^+$  isomeric state are produced by the  $\pi g_{9/2}^{-1} \otimes \nu h_{11/2}^{-2}$  configurations. The odd-parity isomeric states  $17/2^-$  and  $23/2^-$  are produced by the coupling of the  $\pi g_{9/2}$  hole to the  $7^-$   $^{130}\text{Sn}$  core excitation, which is equivalent to the configuration  $\pi g_{9/2}^{-1} \otimes \nu h_{11/2}^{-3} d_{3/2}^{-1}$  [53].

The  $7^-$  level is observed to migrate to lower energies in the Sn isotopes (as well as in Cd isotopes) as the neutron number increases toward  $N = 82$ . The lowering of the  $7^-$ , and consequently the  $^{129}\text{In}$   $17/2^-$  level, brings the latter into the energy range where shell-model calculations by Genevey *et al.* predict the presence of three excited states above  $13/2^+$ , all with spin  $\leq 9/2$  [55]. The presence of these levels would explain the isomeric nature of the  $17/2^-$  level, since any transitions from the

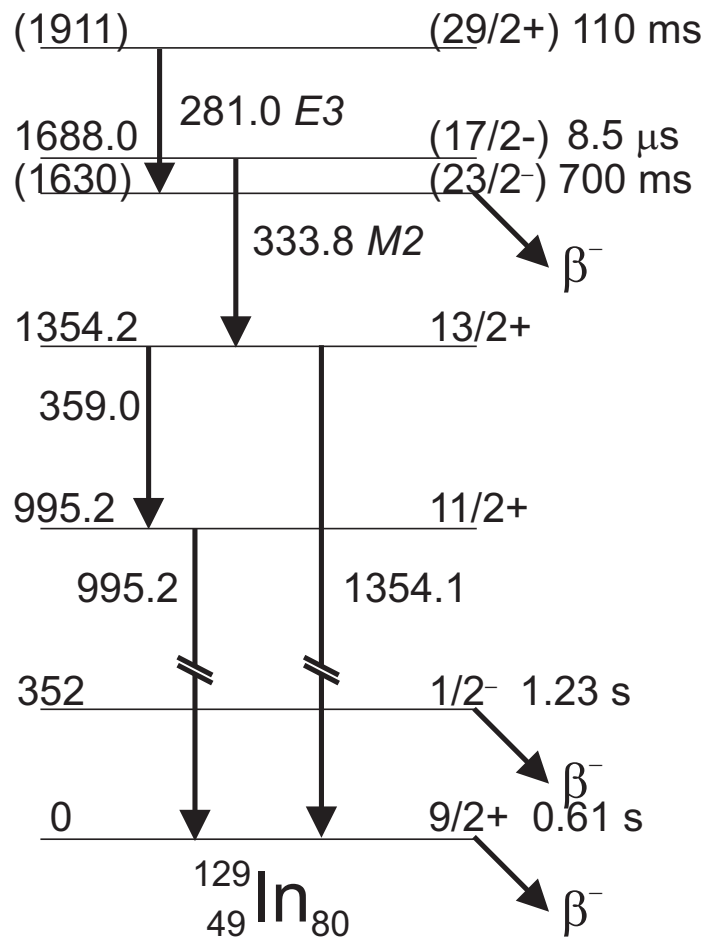


Figure 4.16: Decay scheme for the  $^{129}\text{In}$  isomers from Ref. [53]. The quoted energies are in keV.

17/2<sup>-</sup> level to these levels would be strongly hindered.

#### 4.2.4 $^{125}\text{Cd}$

Three PID regions associated with Cd isotopes were identified and labeled as Cd-A, Cd-A+1, and Cd-A+2, in order of increasing mass number. The Cd isotope blob furthest to the right in the PID plot was labeled Cd-A, as shown in Figure 4.1. The fragment energy loss and time-of-flight of the events located within the Cd-A PID blob correspond to fully-stripped  $^{125}\text{Cd}^{48+}$  ions. The Cd-A gated TKE spectrum (see Fig. 4.17) has two components— $^{122}\text{Cd}^{47+}$  contaminant ions, at lower kinetic energy, and  $^{125}\text{Cd}^{48+}$  ions. No prompt gamma rays from  $^{122}\text{Cd}$  were detected, in accordance with the non-observation of an isomer in that nuclide in previous work. The range of

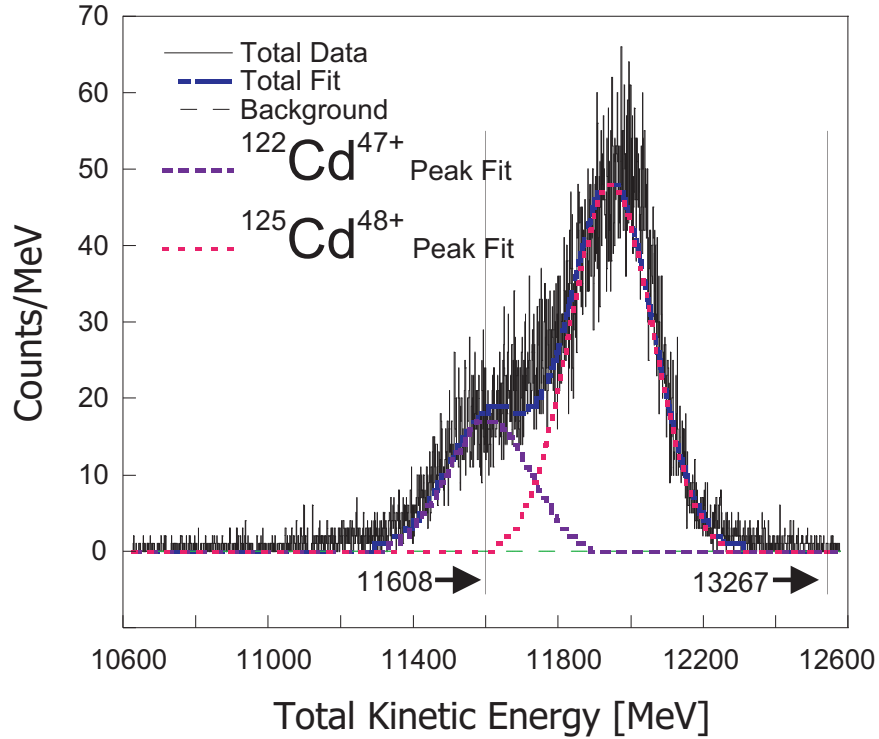


Figure 4.17: Two unequal distributions can be seen. The larger is attributed to  $^{125}\text{Cd}^{48+}$  and the smaller to  $^{122}\text{Cd}^{47+}$ . The vertical lines indicate the range of the  $^{125}\text{Cd}$  TKE gate.

Table 4.11: The integrated number of events associated with the Cd-A PID gate.

Portion of Data	PID Contour	$^{125}\text{Cd}$ TKE Peak
All Runs	23183	15521
Runs w/SeGA TAC	9640	6524

the  $^{125}\text{Cd}$  TKE gate is indicated in Figure 4.17 by the vertical lines. The integrated events within the Cd-A PID contour for all experimental runs, as well as for the experimental runs that included the SeGA-TAC, are given in Table 4.11. The observed number of counts for  $^{125}\text{Cd}$  within the TKE cut are give alongside these values.

The  $^{125}\text{Cd}$  prompt gamma-ray spectrum is shown in Figure 4.18. Six peaks were observed, and the deduced gamma-ray energies, peak areas, and relative intensities are displayed in Table 4.12. Coincidence relationships between the observed  $^{125}\text{Cd}$  prompt gamma rays were also investigated, and the fragment- $\gamma\gamma$  coincidence spectra that were obtained in this work are shown in Figure 4.19. The fitted  $^{125}\text{Cd}$  prompt gamma-ray decay curve is shown in Figure 4.20. The half-life from the present work

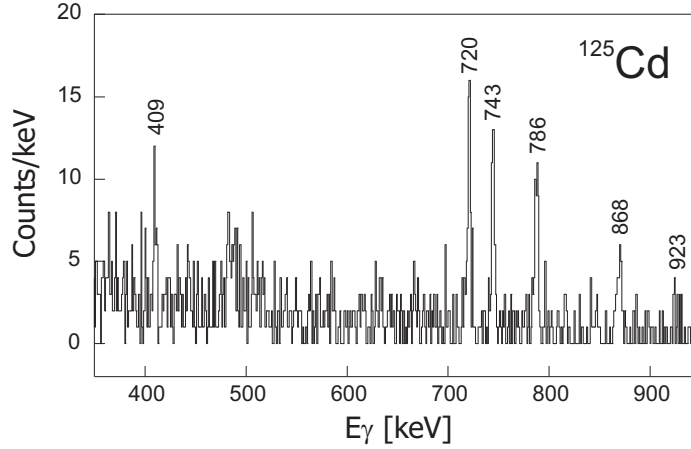


Figure 4.18: Prompt gamma-ray spectrum for  $^{125}\text{Cd}$ .

Table 4.12: The  $^{125}\text{Cd}$  prompt gamma-ray energies, integrated peak areas and relative intensities. Gamma-ray energies are compared with values from Hellström *et al.* [46]. Literature values for the relative intensities are not available.

Peak Energy [keV]		Fitted Peak Area	Relative Intensity	
This Work	Literature		This Work	Literature
408.7(5)	-	29(10)	42(17)	-
719.7(2)	720	48(9)	100(27)	-
743.3(2)	743	45(6)	96(22)	-
786.2(3)	-	42(7)	92(23)	-
867.7(5)	-	27(7)	63(20)	-
922.5(1)	-	8(8)	19(20)	-

(1.7(8)  $\mu\text{s}$ ) along with the literature value are included in the inset.

A  $^{125}\text{Cd}$  isomer was identified by Hellström *et al.* [46], but only the 720- and 743-keV gamma rays were reported. These two gamma-ray energies, as determined in the present work, are in good agreement with those reported in the literature. A proposed level scheme based on the present work is given in Figure 4.21, where the four most intense transitions have been placed in a cascade, in analogy to the lighter odd- $A$  Cd isotopes. The order of the transitions is not known, however, the most intense transition has been placed at the bottom. The proposed cascade is shown feeding into the known  $11/2^-$  beta-decaying isomer. No coincidence relationships were reported by Hellström for the  $^{125m}\text{Cd}$  gamma rays. In this work, the 720- and 743-keV transitions were observed to be coincident. Also, the 409- and 786-keV gamma rays were found

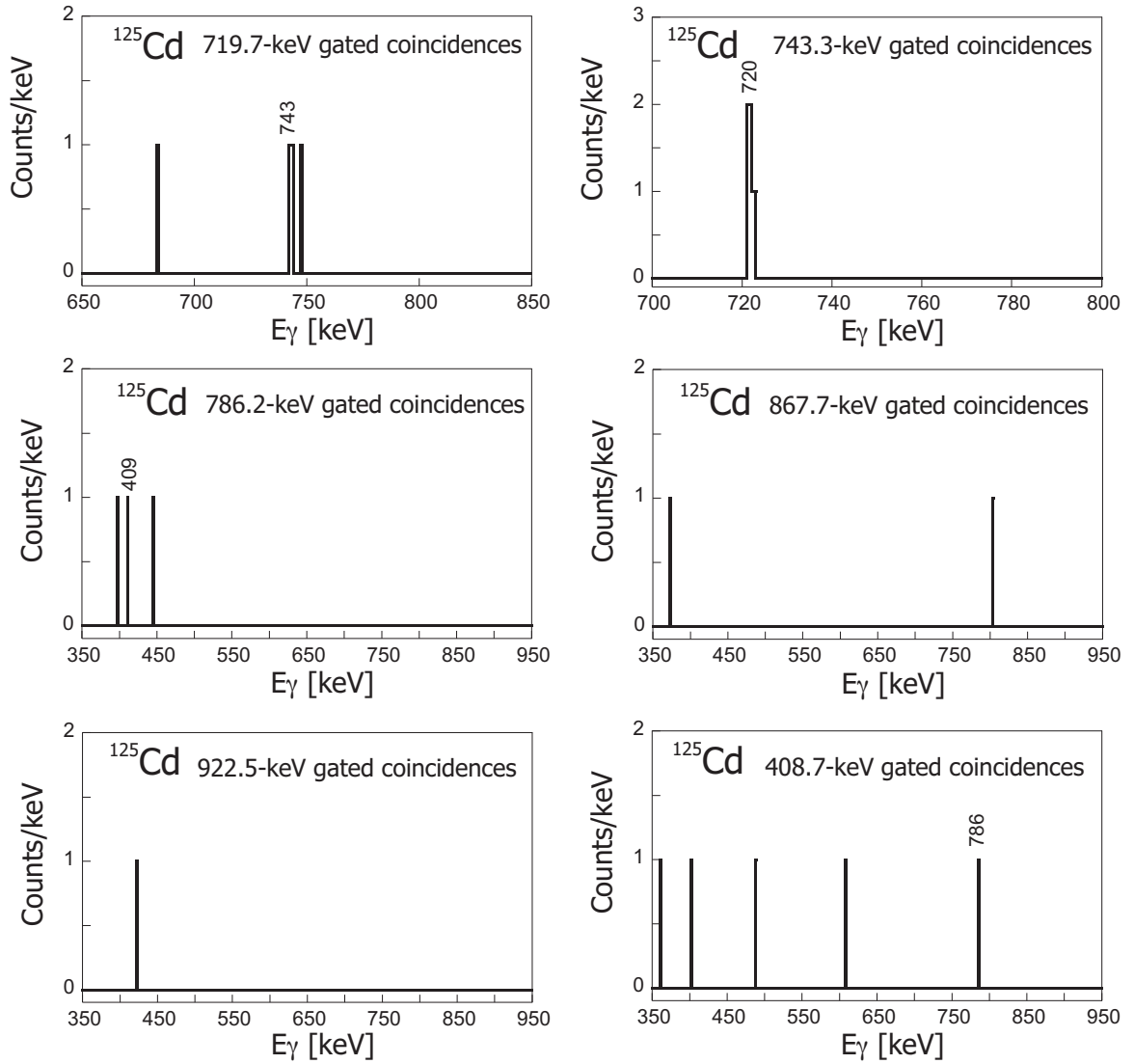


Figure 4.19: Prompt fragment- $\gamma$  spectra for  $^{125}\text{Cd}$ .

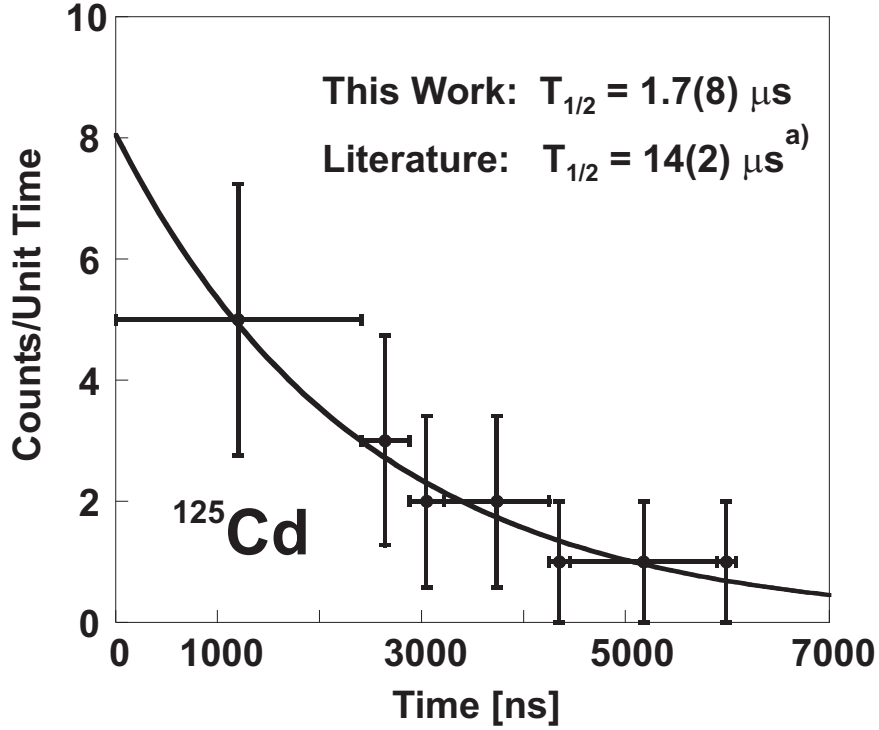


Figure 4.20: The fitted  $^{125}\text{Cd}$  isomer decay curve. The extracted half-life value is given in the inset along with the literature value reported by Hellström *et al.* [46].

to be in coincidence with each other, however, the 409-keV transition has not been placed in the level scheme. The current experimental  $^{125m}\text{Cd}$  half-life value of  $1.7(8)\ \mu\text{s}$  is within one standard deviation of the  $14(2)\text{-}\mu\text{s}$  value reported by Hellström *et al.* [46]. However, the rather flat decay curve shown in Figure 4.20 suggests that a half-life longer than the deduced value may be possible.

The nuclide  $^{125}_{48}\text{Cd}_{77}$  may be described as an odd neutron particle coupled to an even-even  $^{124}\text{Cd}$  core. The  $1/2^+$  ground state is based on an odd  $s_{1/2}$  neutron coupled to the  $(\pi g_{9/2}^{-2})_{0+}$  core. The  $11/2^-$  first excited state, which is a beta-decaying isomer, arises from the coupling of the  $(\pi g_{9/2}^{-2})_{0+}$  core to the same odd neutron in the  $h_{11/2}$  orbital. The  $15/2^-$  to  $31/2^-$  excited states shown in the level scheme are built upon the  $(\pi g_{9/2}^{-2}) \otimes (\nu h_{11/2}^1 d_{3/2}^1)$  core configurations coupled to the  $s_{1/2}$  neutron. The isomer is tentatively attributed to a  $31/2^-$  level of  $(\pi g_{9/2}^{-2})_{8+} \otimes (\nu h_{11/2}^1 d_{3/2}^1)_{7-} \otimes \nu s_{1/2}^1$  configuration, located near 3600 keV. A comparison of deduced half-life and the Weisskopf single-particle estimate for an  $E2$  transition suggests that the unobserved

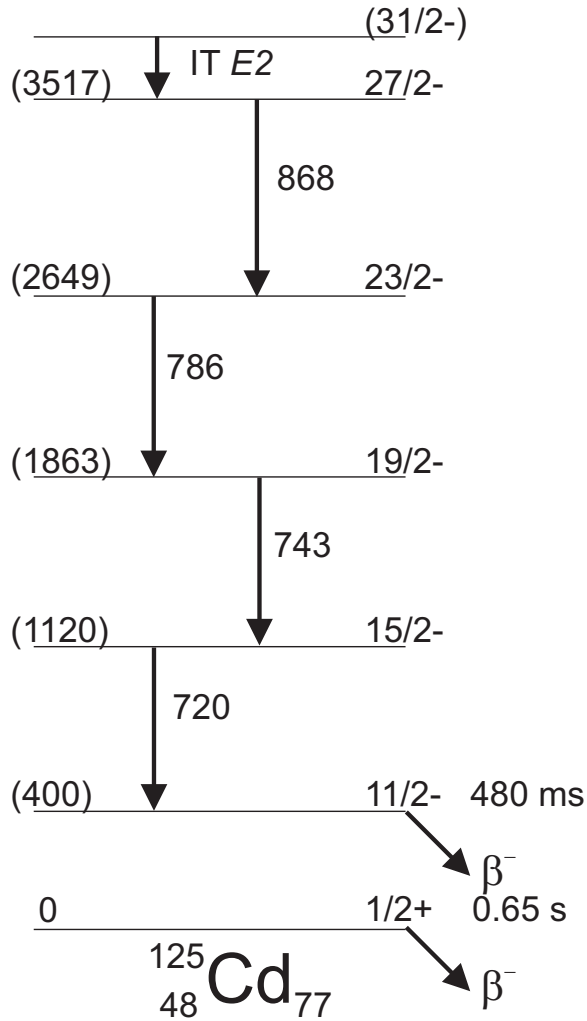


Figure 4.21: Proposed decay scheme for the  $^{125}\text{Cd}$  isomers. The quoted energies are in keV. The excitation energy of the  $11/2^-$  level is estimated from Cd systematics.

IT is approximately 100 keV in magnitude, which was below the threshold of detection in this work.

#### 4.2.5 $^{126}\text{Cd}$

The next heavier Cd isotopic blob was labeled Cd-A+1 (see Figure 4.1). The fragment energy loss and time-of-flight of the events located within the Cd-A+1 PID blob correspond to fully-stripped  $^{126}\text{Cd}^{48+}$  ions. However, a fraction of the Cd-A+1 fragments were  $^{123}\text{Cd}^{47+}$  ions, as illustrated by the two-component structure of the Cd-A+1 gated TKE spectrum in Figure 4.22. The range of the TKE cut is indicated

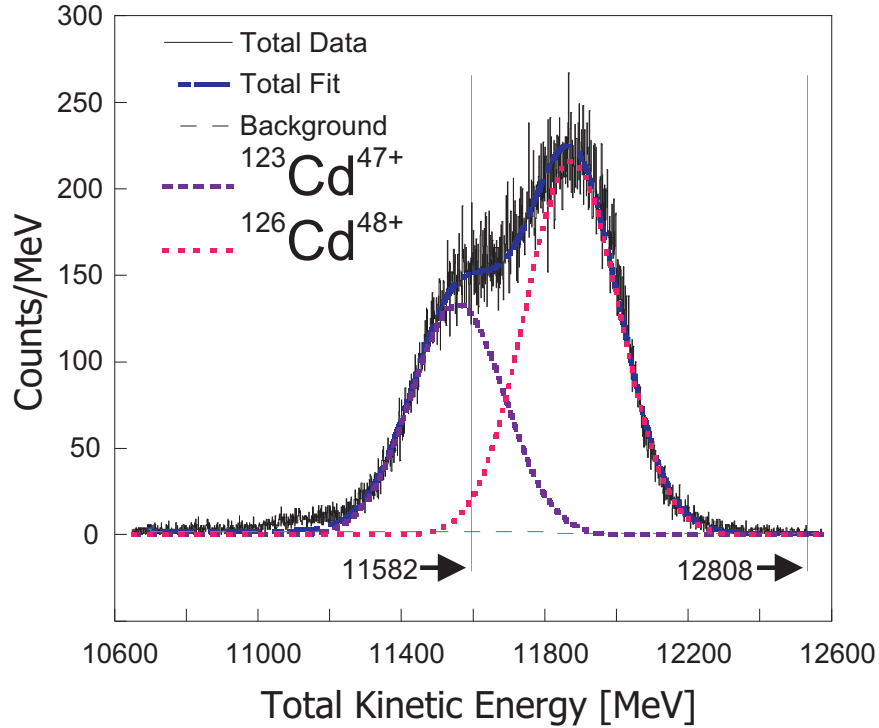


Figure 4.22: Two unequal distributions can be seen. The larger is attributed to  $^{126}\text{Cd}^{48+}$  and the smaller to  $^{123}\text{Cd}^{47+}$ . The vertical lines indicate the range of the  $^{126}\text{Cd}$  TKE gate.

Table 4.13: The integrated number of events associated with the Cd-A+1 PID gate.

Portion of Data	PID Contour	$^{126}\text{Cd}$ TKE Peak
All Runs	134237	72659
Runs w/SeGA TAC	61111	32232

in Figure 4.22 by the vertical lines. The integrated events within the Cd-A+1 PID contour for all experimental runs, as well as for the experimental runs that included the SeGA-TAC, are given in Table 4.13. Alongside these values are given the observed number of counts for  $^{126}\text{Cd}$  within the TKE cut.

The  $^{126}\text{Cd}$  prompt gamma-ray spectrum is shown in Figure 4.23. Eight peaks were identified, and the deduced gamma-ray energies, peak areas, and relative intensities are displayed in Table 4.14. Coincidence relationships between the observed  $^{126}\text{Cd}$  prompt gamma rays were also investigated, and the fragment- $\gamma\gamma$  coincidence spectra that were obtained in this work are shown in Figure 4.24. The fitted  $^{126}\text{Cd}$  prompt gamma-ray decay curve is shown in Figure 4.25. The half-life value from the present

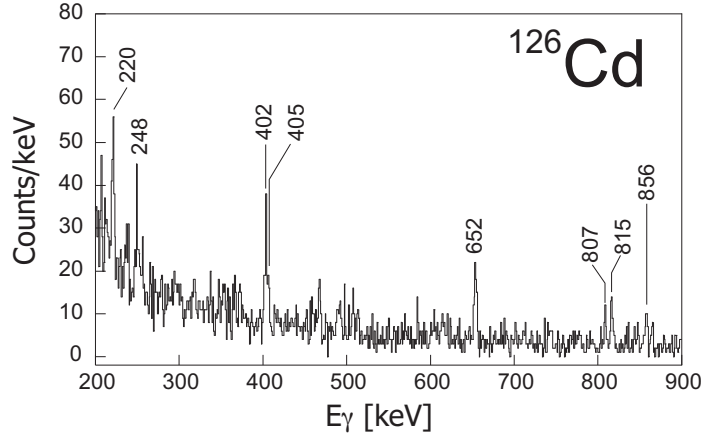


Figure 4.23: Prompt gamma-ray spectrum for  $^{126}\text{Cd}$ .

Table 4.14: The  $^{126}\text{Cd}$  prompt gamma-ray energies, integrated peak areas and relative intensities. Gamma-ray energies from Ref. [56] are  $^{126}\text{Ag}$   $\beta$ -delayed gamma rays.

Peak Energy [keV]		Fitted Peak Area	Relative Intensity	
This Work	Literature [56]		This Work	Literature
219.7(2)	-	97(22)	58(15)	-
248.2(2)	-	22(9)	14(6)	-
401.5(4)	401.6	76(19)	67(19)	-
405.1(7)	-	41(15)	36(14)	-
652.4(2)	651.8	84(10)	100(17)	-
807.0(2)	-	21(4)	28(7)	-
814.8(2)	814.8	40(6)	54(11)	-
856.4(4)	856.1	26(12)	36(17)	-

work (2.0(7)  $\mu\text{s}$ ) is included in the inset.

No observation of the  $^{126}\text{Cd}$  isomer has been reported in the literature. Scherillo *et al.* estimated that no  $\mu\text{s}$  isomer with a half-life longer than 0.5  $\mu\text{s}$  exists in  $^{126}\text{Cd}$  [53]. It should also be noted that no isomers have been observed in any other even-even Cd isotopes. Kautzsch identified several beta-delayed gamma rays from the decay of  $^{126}\text{Ag}$  (the beta-decay parent) and proposed the 652-keV gamma ray as the  $2^+ \rightarrow 0^+$  transition and the 815-keV gamma ray as the  $4^+ \rightarrow 2^+$  transition [56]. The gamma rays from Ref. [56] that overlap with the present work are listed in Table 4.14. A proposed decay scheme for the  $^{126}\text{Cd}$  isomer is given in Figure 4.26. This level scheme is based on systematics of even-even Cd isotopes and the beta-decay work of Kautzsch *et al.*. In the present work, gamma rays in the 248-keV to 652-keV

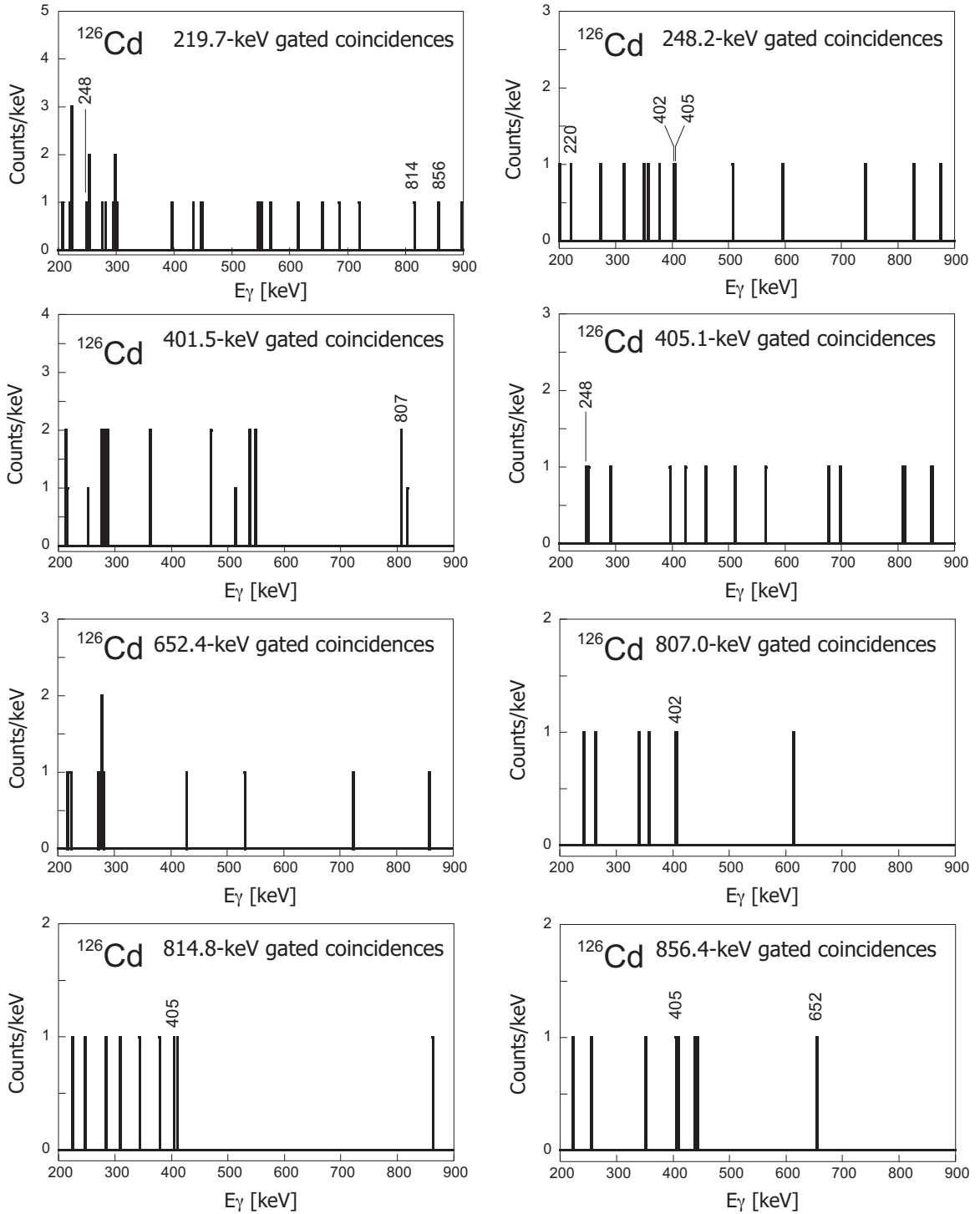


Figure 4.24: Prompt fragment- $\gamma\gamma$  coincidence spectra for  $^{126}\text{Cd}$ .

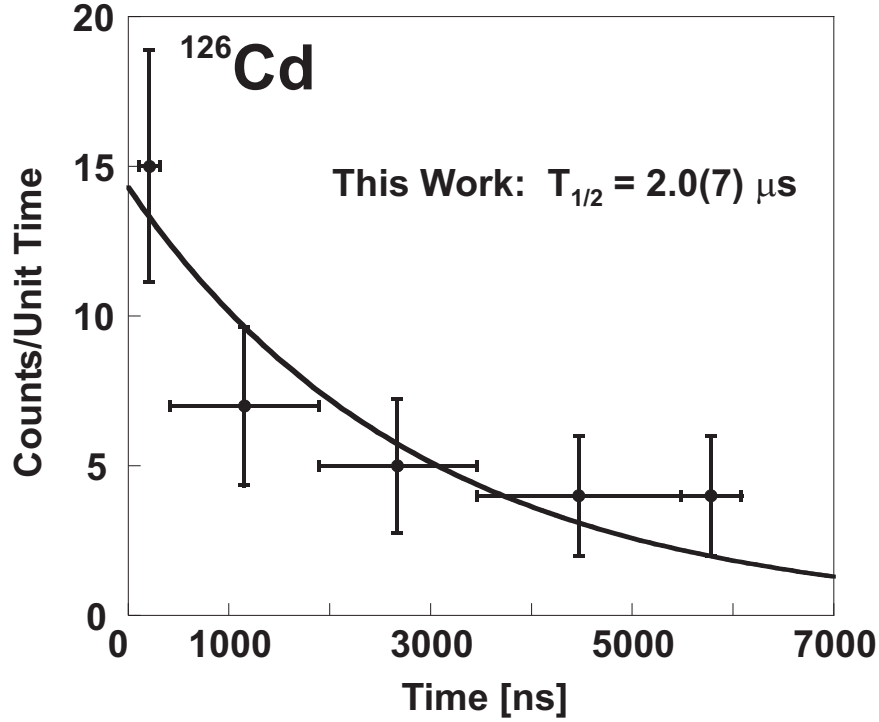


Figure 4.25: The fitted  $^{126}\text{Cd}$  prompt gamma-ray decay curve. The deduced half-life value is given in the inset.

cascade (see Fig. 4.26) were coincident, and the 402- and 807-keV transitions in the negative-parity cascade were coincident. These cascades were deduced from the coincidences. The 82-keV transition shown in the level scheme was not observed, as this energy was below the gamma-ray detection threshold. The deduced  $^{126m}\text{Cd}$  half-life [ $2.0(7) \mu\text{s}$ ] is not in agreement with the estimated half-life ( $<0.5 \mu\text{s}$ ) of Scherillo.

Considering the proximity to  $N = 82$ , the even-even nuclide  $^{126}_{48}\text{Cd}_{78}$  would be expected to show a relatively low degree of collectivity. Calculation of the  $E(4_1^+)/E(2_1^+)$  ratio yields a value of 2.25, in agreement with this expectation. The shell model describes two sets of even-parity states in  $^{126}\text{Cd}$ — $0^+$ ,  $2^+$ ,  $4^+$ ,  $6^+$ , and  $8^+$  levels arising from the splitting of the pair of  $\pi g_{9/2}$  holes; and  $0^+$ ,  $2^+$ ,  $4^+$ ,  $6^+$ ,  $8^+$ , and  $10^+$  levels arising from the splitting of a pair of  $\nu h_{11/2}$  holes. Likewise, the negative-parity levels are also generated by both proton and neutron configurations. The  $5^-$  level is produced by both the  $\pi(g_{9/2}^1 p_{1/2}^1)$  configuration and the  $\nu(h_{11/2}^1 d_{3/2}^1)$  configuration. The  $7^-$  level can also be produced by the  $\nu(h_{11/2}^1 d_{3/2}^1)$  configuration, and this neu-

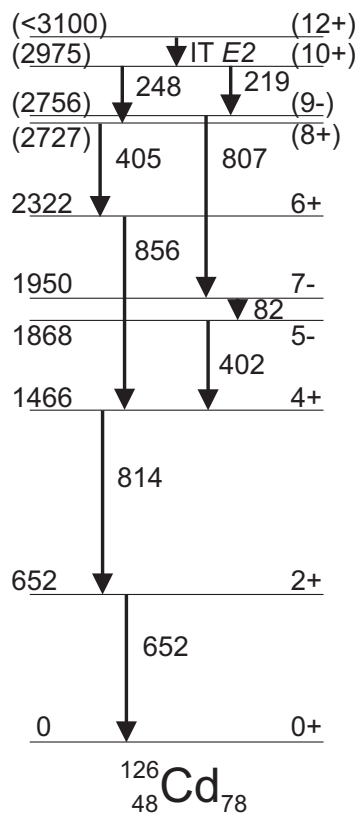


Figure 4.26: Proposed decay scheme for the  $^{126}\text{Cd}$  isomer. The quoted energies are in keV.

tron configuration coupled to the  $(\pi g_{9/2}^{-2})_{2+}$  excitation gives rise to the  $9^-$  level. The proposed isomeric  $12^+$  state at around 3100 keV is attributed to the four-particle  $(\pi g_{9/2}^1 p_{1/2}^1)_{5-} \otimes (\nu h_{11/2}^1 d_{3/2}^1)_{7-}$  configuration [57]. A comparison of deduced half-life and the Weisskopf single-particle estimate for an  $E2$  transition suggests that the unobserved IT is approximately 100–200 keV in magnitude.

#### 4.2.6 $^{127}\text{Cd}$

The fragment energy loss and time-of-flight of the events located within the Cd-A+2 PID blob (see Fig. 4.1) correspond to fully-stripped  $^{127}\text{Cd}^{48+}$  ions. The range of the Cd-A+2 TKE gate is indicated in Figure 4.27 by the vertical lines. The integrated events within the Cd-A+2 PID contour for all experimental runs, as well as for the experimental runs that included the SeGA-TAC, are given in Table 4.15. The number of observed counts for  $^{127}\text{Cd}$  within the TKE cut are given alongside these values.

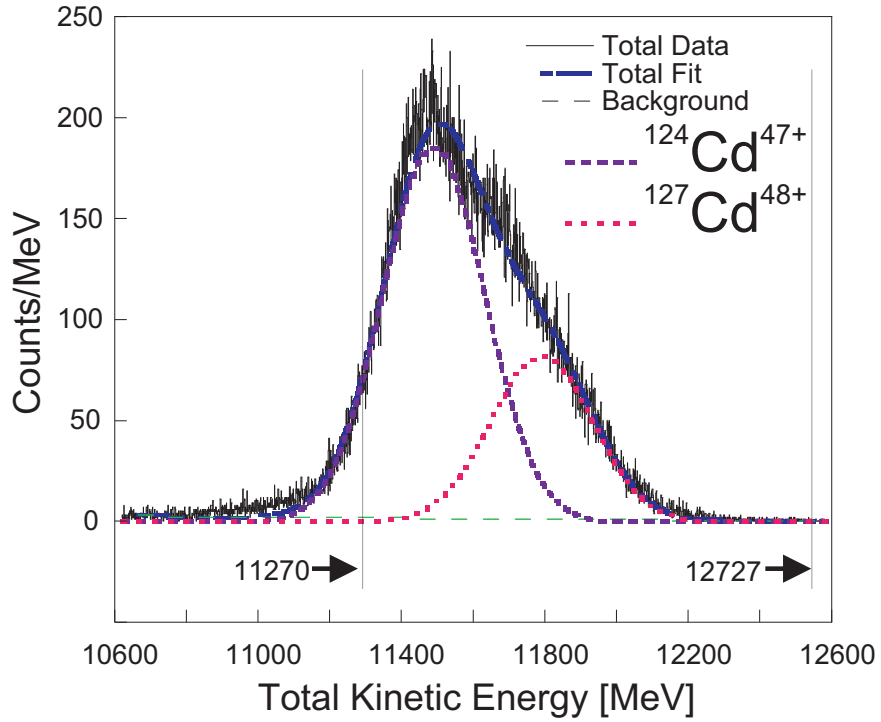


Figure 4.27: TKE spectrum for the Cd-A+2 PID blob. Two unequal distributions can be seen. The smaller is attributed to  $^{127}\text{Cd}^{48+}$  and the larger to  $^{124}\text{Cd}^{47+}$ . The vertical lines indicate the range of the  $^{127}\text{Cd}$  TKE gate.

Table 4.15: The integrated number of events associated with the Cd-A+2 PID gate.

Portion of Data	PID Contour	$^{127}\text{Cd}$ TKE Peak
All Runs	121740	30583
Runs w/SeGA TAC	60085	15492

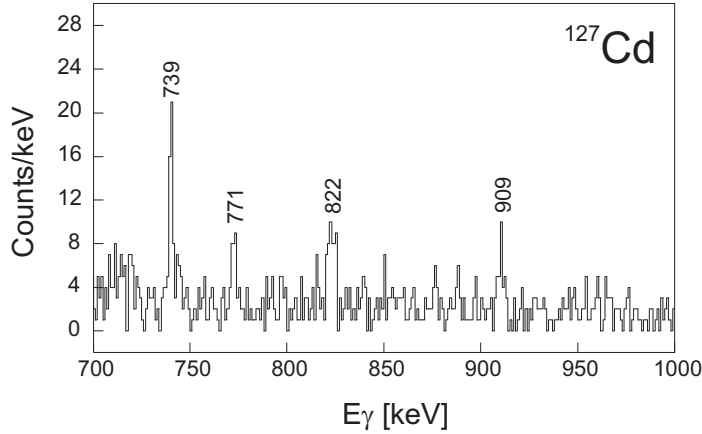


Figure 4.28: Prompt gamma-ray spectrum for  $^{127}\text{Cd}$ .

Table 4.16: The  $^{127}\text{Cd}$  prompt gamma-ray energies, integrated peak areas and relative intensities.

Peak Energy [keV]	Fitted Peak Area	Relative Intensity
738.7(2)	34(6)	80(50)
770.9(4)	23(7)	56(37)
821.4(7)	40(24)	100(85)
908.9(6)	28(13)	74(56)

The  $^{127}\text{Cd}$  prompt gamma-ray spectrum is shown in Figure 4.28. Four peaks were observed, and the deduced gamma-ray energies, peak areas, and relative intensities are displayed in Table 4.16. Coincidence relationships between the observed  $^{127}\text{Cd}$  prompt gamma rays were also investigated, and the fragment- $\gamma\gamma$  coincidence spectra that were obtained in this work are shown in Figure 4.29. The fitted  $^{127}\text{Cd}$  prompt gamma-ray decay curve is shown in Figure 4.30. The half-life value (1.9(6)  $\mu\text{s}$ ) from the present work is included in the inset.

Aside from a beta-decay  $Q$ -value measurement by Spanier *et al.* [58], very little is known about  $^{127}\text{Cd}$ . Observation of the  $^{127}\text{Cd}$  isomer has not been reported in the literature. A proposed level scheme based on the present work is given in Figure 4.31, where the four observed gamma transitions have been placed in a cascade, in analogy to the lighter odd- $A$  Cd isotopes. The order of the transitions is not known, however. The proposed cascade is shown feeding into a possible  $11/2^-$  beta-decaying isomer. In this work, the 739- and 822-keV transitions were coincident.

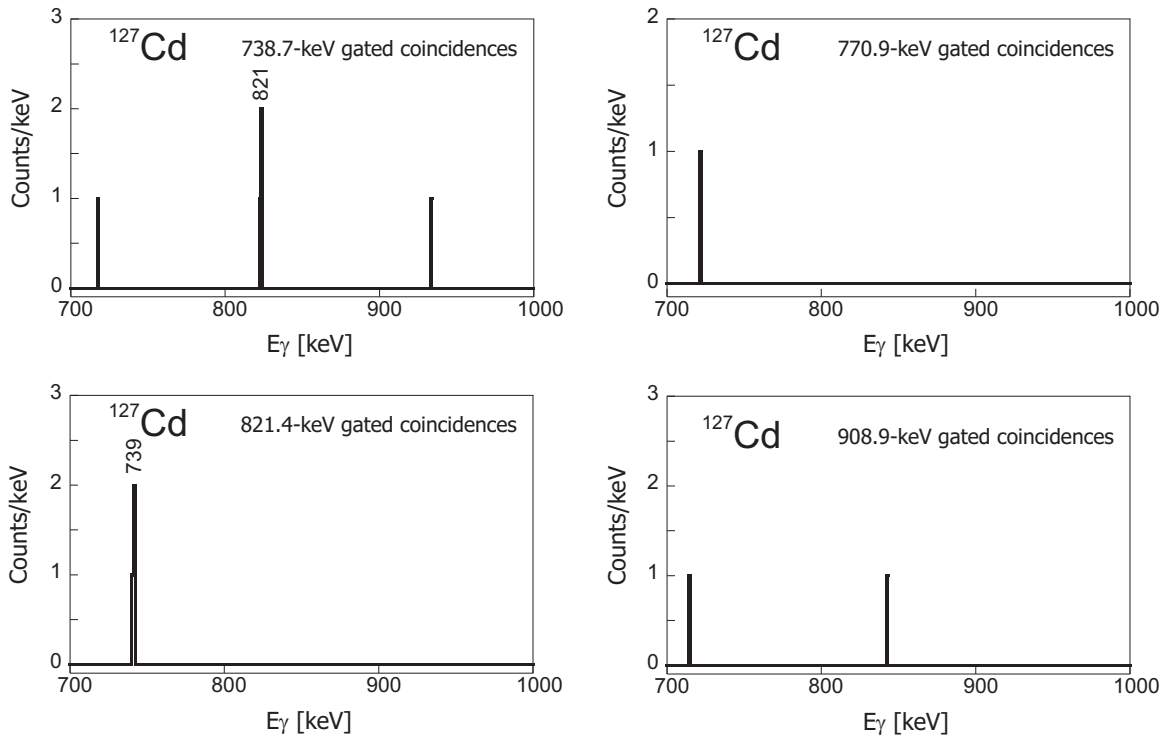


Figure 4.29: Prompt fragment- $\gamma\gamma$  spectra for  $^{127}\text{Cd}$ .

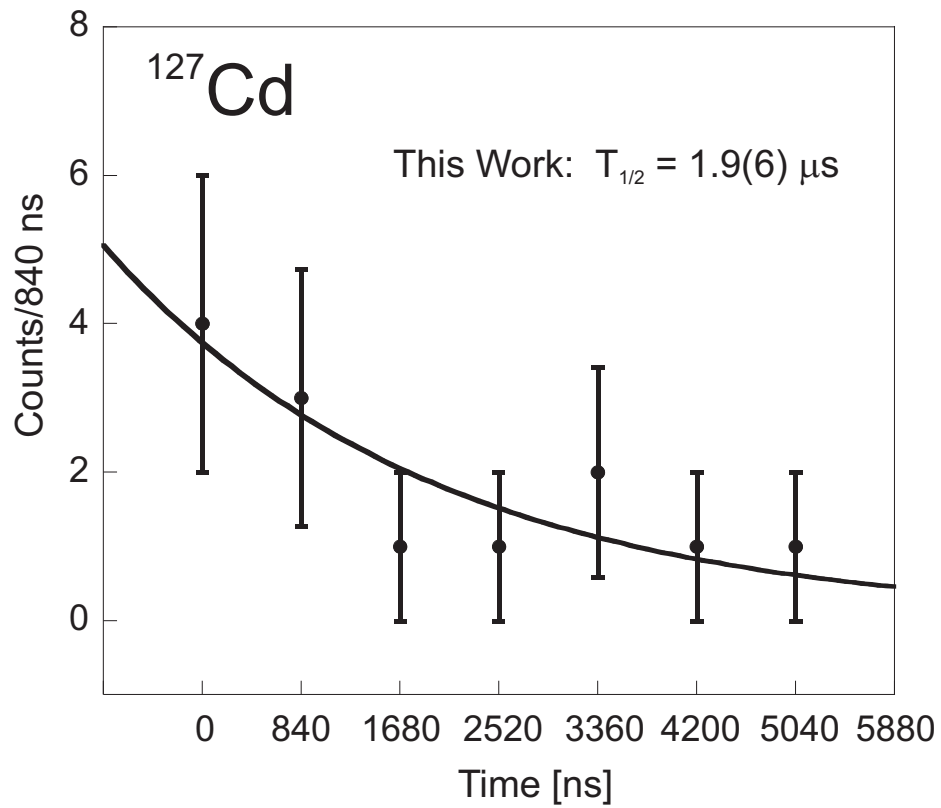


Figure 4.30: The fitted  $^{127}\text{Cd}$  isomer decay curve. The deduced half-life value is given in the inset.

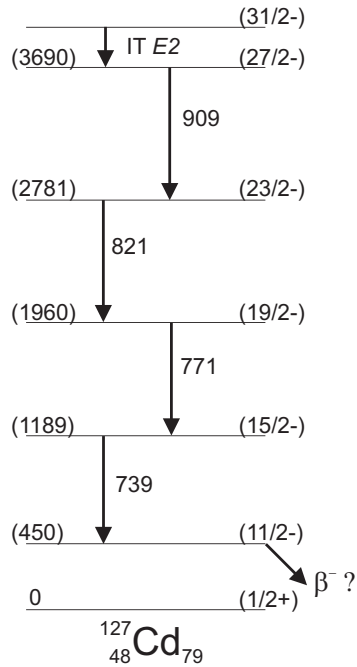


Figure 4.31: Proposed decay scheme for the  $^{127}\text{Cd}$  isomers. The quoted energies are in keV. The excitation energy of the  $11/2^-$  level is estimated from Cd systematics.

As the next heavier odd- $A$  isotope of Cd, the excited states of  $^{127}\text{Cd}$  are expected to be very similar to those of  $^{125}\text{Cd}$ . The spins and parities of the  $^{127}\text{Cd}$  excited states, as given in Figure 4.31, are based upon the systematics of the odd- $A$  Cd isotopes. The nuclide  $^{127}_{48}\text{Cd}_{79}$  may be described as an odd neutron particle coupled to an even-even  $^{126}\text{Cd}$  core. The  $1/2^+$  ground state is based on an odd  $s_{1/2}$  neutron coupled to the  $(\pi g_{9/2}^{-2})_{0+}$  core excitation. The  $11/2^-$  first excited state, which is likely a beta-decaying isomer, arises from the coupling of the  $(\pi g_{9/2}^{-2})_{0+}$  core excitation to the same odd neutron in the  $h_{11/2}$  orbital. The  $15/2^-$  to  $31/2^-$  excited states shown in the level scheme are built upon the  $(\pi g_{9/2}^{-2}) \otimes (\nu h_{11/2}^1 d_{3/2}^1)$  core configurations coupled to the  $s_{1/2}$  neutron. The isomer is tentatively attributed to a  $31/2^-$  level of  $(\pi g_{9/2}^{-2})_{8+} \otimes (\nu h_{11/2}^1 d_{3/2}^1)_{7-} \otimes \nu s_{1/2}^1$  configuration, located near 3800 keV. A comparison of the deduced half-life value of  $1.9(6) \mu\text{s}$  and the Weisskopf single-particle estimate for an  $E2$  transition suggests that the unobserved IT is approximately 100–200 keV in magnitude.

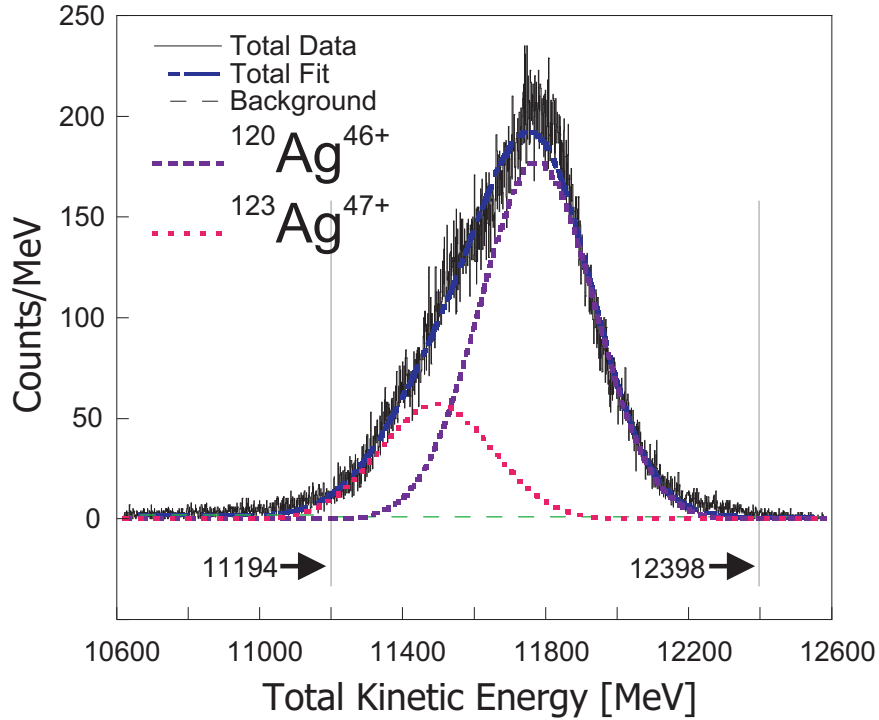


Figure 4.32: TKE spectrum for the Ag-A+1 PID blob. Two unequal distributions can be seen. The larger is attributed to  $^{123}\text{Ag}^{47+}$  and the smaller to  $^{120}\text{Ag}^{46+}$ . The vertical lines indicate the range of the  $^{123}\text{Ag}$  TKE gate.

#### 4.2.7 $^{123}\text{Ag}$

Five PID blobs associated with Ag isotopes were identified, and the second-lightest isotope blob (*i.e.* the isotope region second from the right in the PID plot) was labeled as Ag-A+1. The fragment energy loss and time-of-flight of the events located within the Ag-A+1 PID blob correspond with ions of fully-stripped  $^{123}\text{Ag}^{47+}$ . The Ag-A+1 gated TKE spectrum (see Fig. 4.32) has two components—a main peak, attributed to  $^{123}\text{Ag}^{47+}$ , with a small shoulder on the low-energy side of the distribution, attributed to  $^{120}\text{Ag}^{46+}$  contaminant ions. The range of the TKE gate is indicated in Figure 4.32 by the vertical lines. The integrated events within the Ag-A+1 PID contour for all experimental runs, as well as for the experimental runs that included the SeGA-TAC, are given in Table 4.17. The observed number of counts for  $^{123}\text{Ag}$  within the TKE cut are given alongside these values.

The  $^{123}\text{Ag}$  prompt gamma-ray spectrum is shown in Figure 4.33. Eleven peaks were

Table 4.17: The integrated number of events associated with the Ag-A+1 PID gate.

Portion of Data	PID Contour	$^{123}\text{Ag}$ TKE Peak
All Runs	108657	73995
Runs w/SeGA TAC	45601	31035

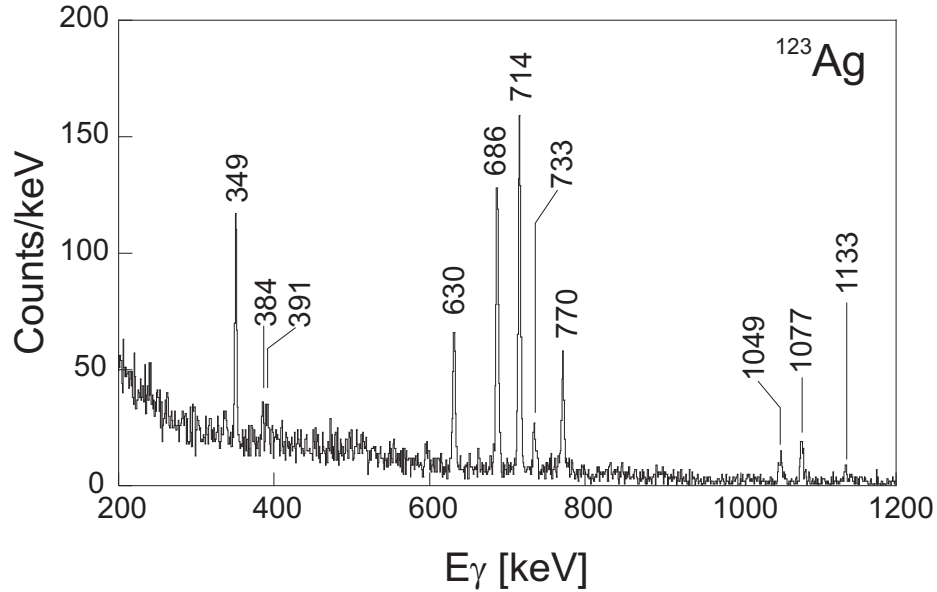


Figure 4.33: Prompt gamma-ray spectrum for  $^{123}\text{Ag}$ .

observed, and the deduced gamma-ray energies, peak areas, and relative intensities are displayed in Table 4.18. Coincidence relationships between the observed  $^{123}\text{Ag}$  prompt gamma rays were also investigated, and the fragment- $\gamma\gamma$  coincidence spectra that were obtained in this work are shown in Figure 4.34. The fitted  $^{123}\text{Ag}$  prompt gamma-ray decay curve is shown in Figure 4.36. The half-life from the present work [0.32(3)  $\mu\text{s}$ ] is included in the inset.

Observation of the  $^{123}\text{Ag}$  isomer has not been reported in the literature. A proposed level scheme based on the present work is given in Figure 4.37. The 384-, 391- and 1134-keV gamma rays have not been placed and may be part of a side band. In this work, the 630- and 770-keV transitions were coincident; the 686- and 714-keV transitions were coincident; and the 350-keV gamma ray was coincident with both the 1049- and 1077-keV gamma rays. Also these three pairs of gamma rays each sum to 1400 keV, supporting the arrangement of these gamma rays into three cascades

Table 4.18: The  $^{123}\text{Ag}$  prompt gamma-ray energies, integrated peak areas and relative intensities.

Peak Energy [keV]	Fitted Peak Area	Relative Intensity
349.5(1)	318(16)	37(2)
383.8(3)	45(16)	6(2)
390.8(3)	26(11)	3(2)
630.1(1)	196(15)	33(3)
685.6(1)	453(37)	80(7)
714.0(1)	553(14)	100(4)
732.9(3)	34(13)	6(3)
769.8(1)	138(10)	26(2)
1049.3(6)	50(23)	11(5)
1076.6(3)	68(14)	16(3)
1133.5(2)	19(4)	5(1)

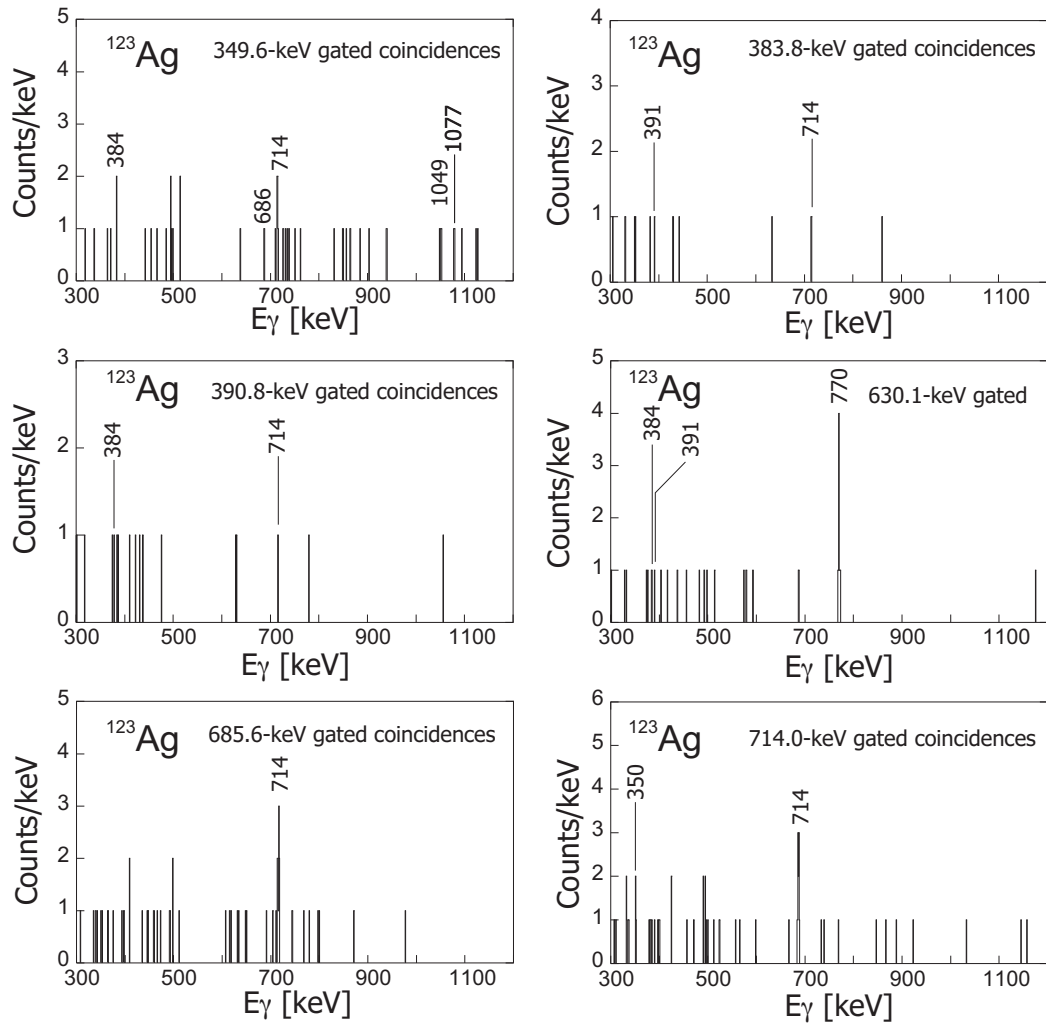


Figure 4.34: Prompt fragment- $\gamma\gamma$  spectra for  $^{123}\text{Ag}$ .

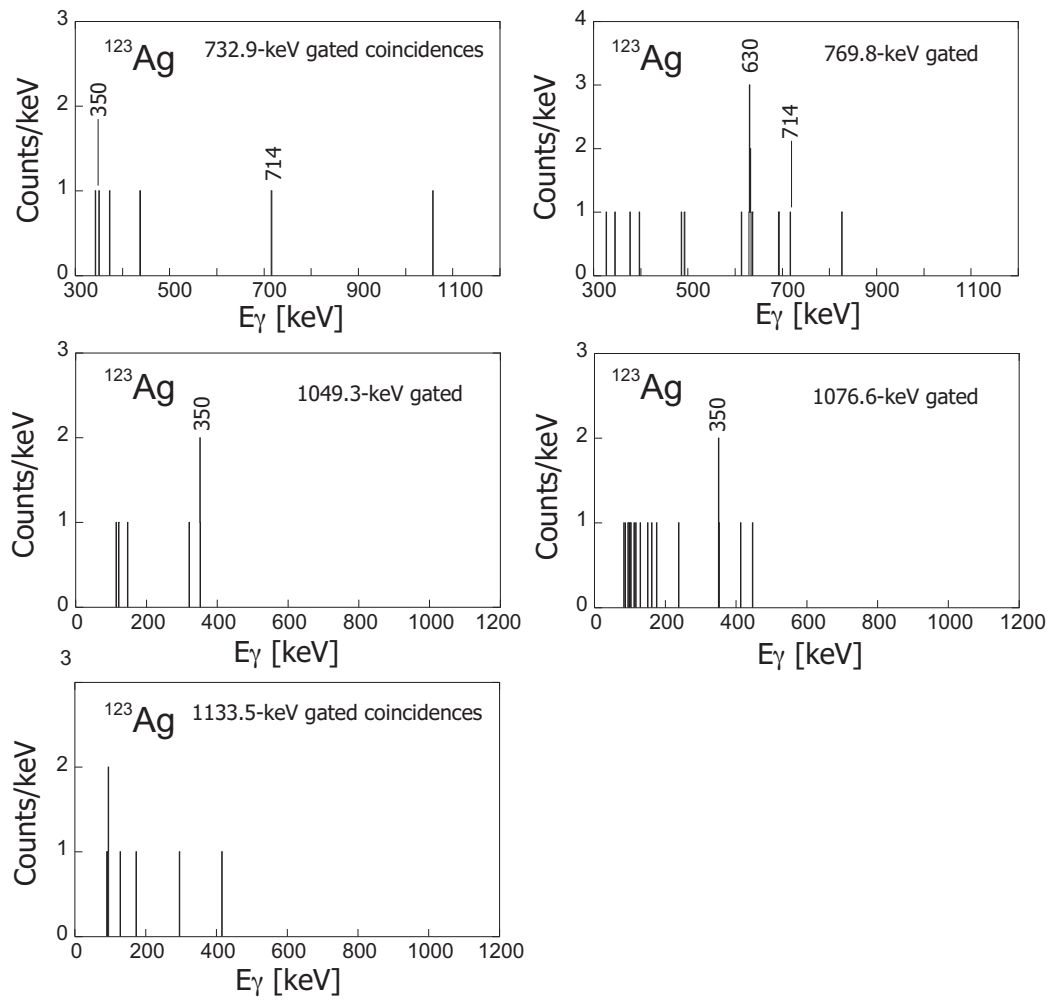


Figure 4.35: Prompt fragment- $\gamma\gamma$  spectra for  $^{123}\text{Ag}$ .

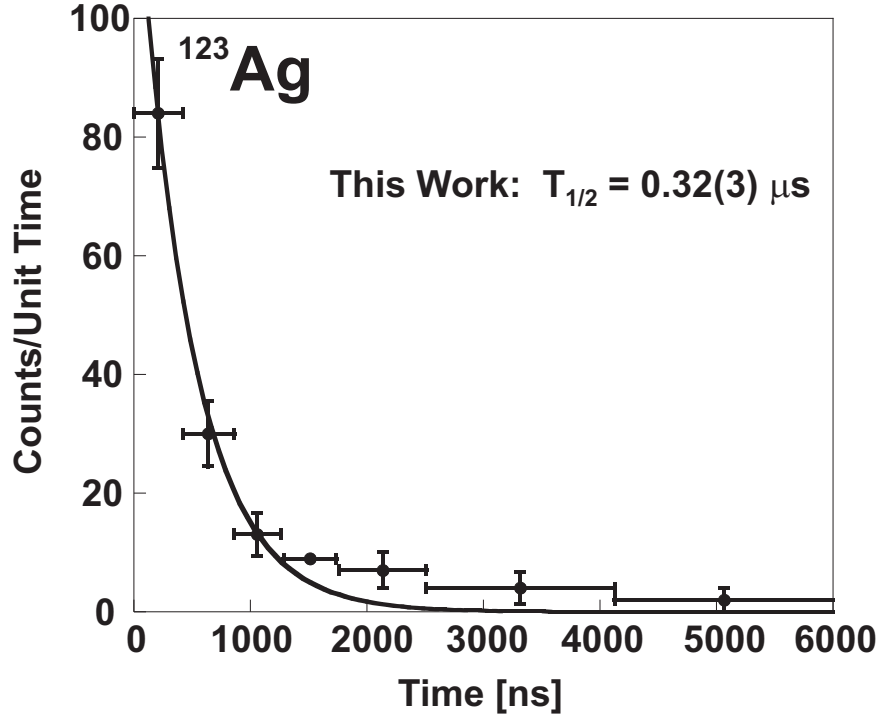


Figure 4.36: The fitted  $^{123}\text{Ag}$  isomer decay curve. The deduced half-life value is given in the inset.

from the possible  $15/2^+$  level at 1427 keV to the  $9/2^+$  level at 27 keV. The spin-parity assignments are based on systematics of the odd- $A$  Ag isotopes. The proposed level scheme suggests that the  $15/2^+$  level at 1427 keV is populated by two low-energy transitions that are in fed by the IT. These low-energy transitions, which may also be isomeric, and the slow  $E2$  IT indicated in the figure were likely below the gamma-ray detection threshold and were not observed. Comparison of the deduced half-life and Weisskopf estimates suggest that the  $E2$  IT is likely to be  $\leq 200$  keV in magnitude.

In analogy to the odd- $A$  In isotopes, the nuclide  $^{123}_{47}\text{Ag}_{76}$ , with an odd  $g_{9/2}$  proton, may be described in terms of the odd proton coupled to a pair of neutron holes. The  $^{123}\text{Ag}$  excited state spectrum can also be explained in terms of a three-proton hole in the even-even  $^{126}\text{Sn}$  core [57]. The  $7/2^+$  ground state and  $9/2^+$  first-excited state are produced by this three-proton cluster  $\pi g_{9/2}^{-3}$ . The  $11/2_1^+$ ,  $13/2^+$ ,  $15/2^+$ , and  $17/2^+$  excited states of  $^{123}\text{Ag}$  arise from the coupling of the odd proton to the  $\nu h_{11/2}^{-2}$  configurations. The second  $11/2^+$  level is produced by coupling the  $\pi g_{9/2}^{-3}$  and  $^{126}\text{Sn}$

Table 4.19: The integrated number of events associated with the Ag-A+2 PID gate.

Portion of Data	PID Contour	$^{124}\text{Ag}$ TKE Peak
All Runs	147982	68207
Runs w/SeGA TAC	66749	30711

$2^+$  configurations [57]. The odd-parity states  $17/2^-$  and  $21/2^-$  are produced by the  $\pi g_{9/2}^{-1} \otimes (\nu h_{11/2}^{-3} d_{3/2}^{-1})_{5^-}$  and  $\pi g_{9/2}^{-1} \otimes (\nu h_{11/2}^{-3} d_{3/2}^{-1})_{7^-}$  configurations, respectively. The  $21/2^-$  state is tentatively assigned as the isomer. The  $7^-$  level is observed to decrease significantly in the Sn and Cd isotopes between  $N = 76$  and  $N = 78$  [57]. The lowering of the  $7^-$ , and consequently the lowering of the  $21/2^-$  level relative to the  $17/2^-$  level could be the origin of the isomer in  $^{123}\text{Ag}$ .

#### 4.2.8 $^{124}\text{Ag}$

The fragment energy loss and time-of-flight of the events located within the Ag-A+2 PID blob correspond with ions of fully-stripped  $^{124}\text{Ag}^{47+}$ . The Ag-A+2 gated TKE spectrum has two components—roughly equal contributions of  $^{121}\text{Ag}^{46+}$  contaminant ions at lower energies and  $^{124}\text{Ag}^{47+}$  ions at the higher energies, as shown in Figure 4.38. The range of the TKE gate is indicated in Figure 4.38 by the vertical lines. The integrated events within the Ag-A+2 PID contour for all experimental runs, as well as for the experimental runs that included the SeGA-TAC, are given in Table 4.19. The observed number of counts for  $^{124}\text{Ag}$  within the TKE cut are given alongside these values.

The  $^{124}\text{Ag}$  prompt gamma-ray spectrum is shown in Figure 4.39. Two peaks were observed, and the deduced gamma-ray energies, peak areas, and relative intensities are displayed in Table 4.20. Coincidence relationships between the observed  $^{124}\text{Ag}$  prompt gamma rays were also investigated, and the fragment- $\gamma\gamma$  coincidence spectra that were obtained in this work are shown in Figure 4.40. The fitted  $^{124}\text{Ag}$  prompt gamma-ray decay curve is shown in Figure 4.41. The half-life from the present work [1.9(2)  $\mu\text{s}$ ] is included in the inset.

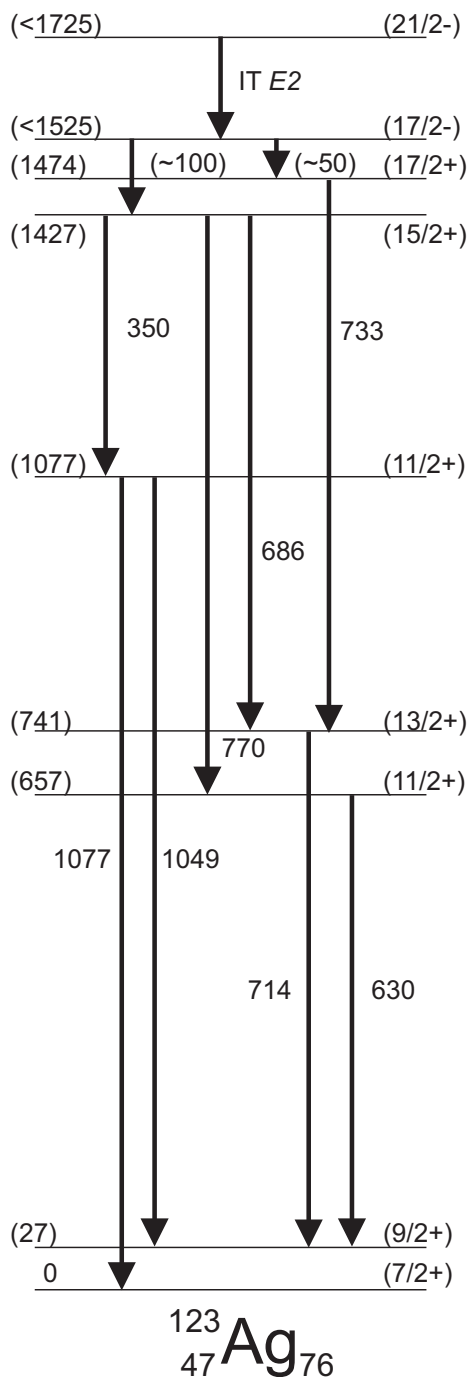


Figure 4.37: Proposed decay scheme for the  $^{123}\text{Ag}$  isomer. The quoted energies are in keV.

Table 4.20: The  $^{124}\text{Ag}$  prompt gamma-ray energies, integrated peak areas and relative intensities.

Peak Energy [keV]	Fitted Peak Area	Relative Intensity
155.5(2)	425(59)	100(20)
1132.2(7)	35(8)	26(7)

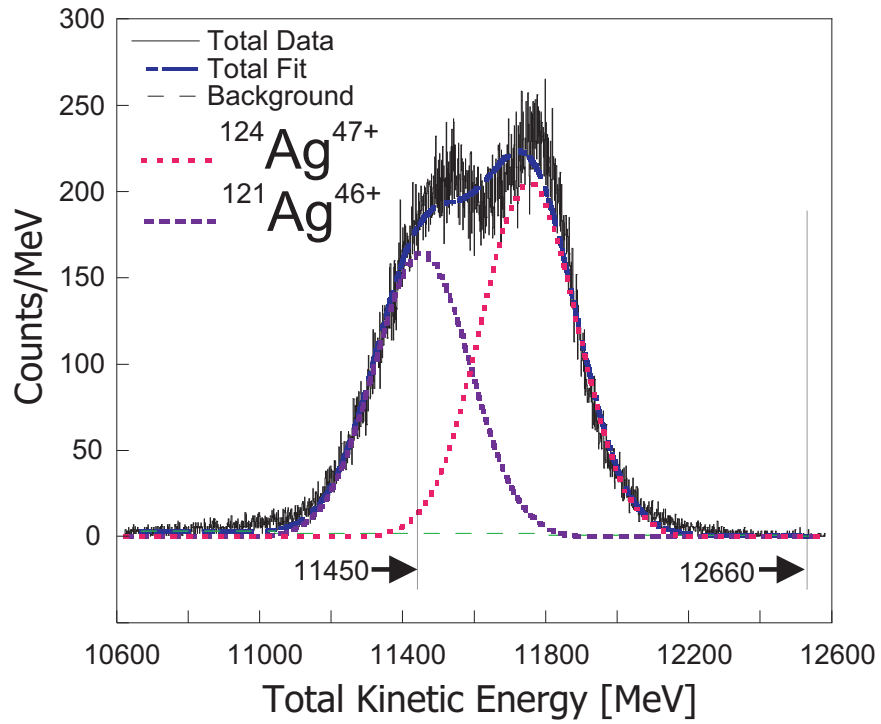


Figure 4.38: TKE spectrum for the Ag-A+2 PID blob. Two unequal distributions can be seen. The larger is attributed to  $^{124}\text{Ag}^{47+}$  and the smaller to  $^{121}\text{Ag}^{46+}$ . The vertical lines indicate the range of the  $^{124}\text{Ag}$  TKE gate.

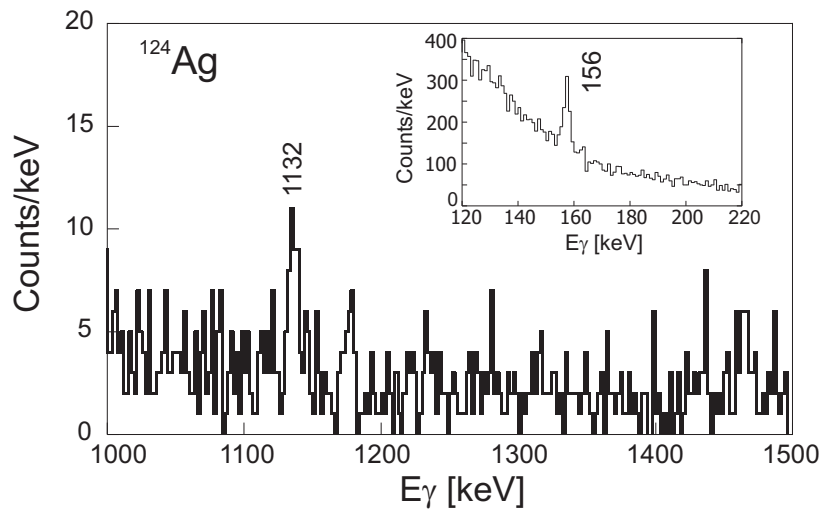


Figure 4.39: Prompt gamma-ray spectrum for  $^{124}\text{Ag}$ .

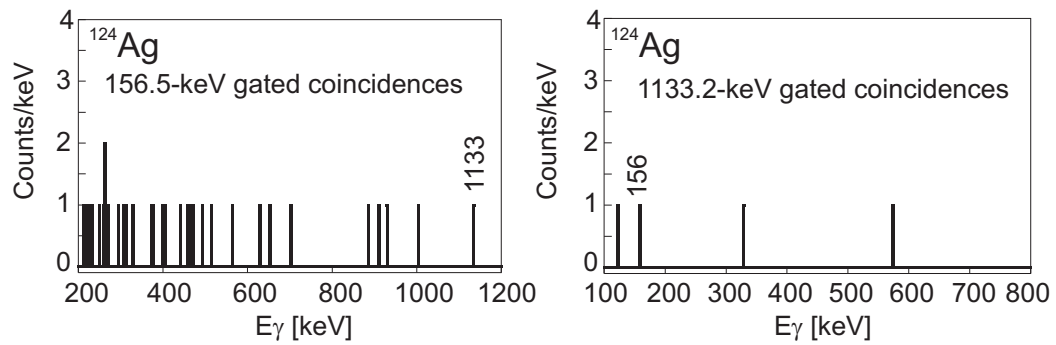


Figure 4.40: Prompt fragment- $\gamma\gamma$  spectra for  $^{124}\text{Ag}$ .

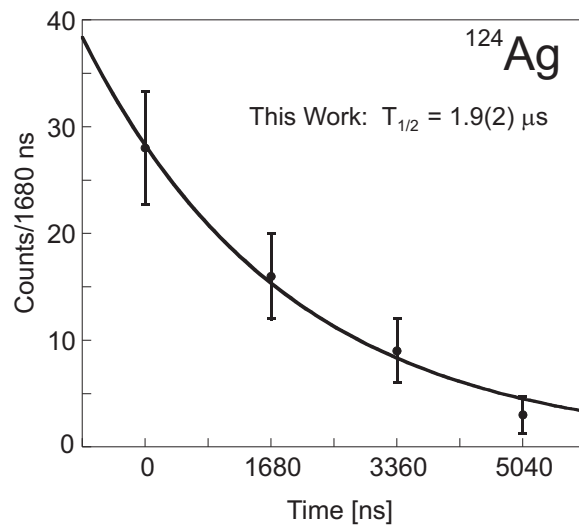


Figure 4.41: The fitted  $^{124}\text{Ag}$  isomer decay curve. The deduced half-life value is given in the inset.

Table 4.21: The integrated number of events associated with the Ag-A+3 PID gate.

Portion of Data	PID Contour	$^{125}\text{Ag}$ TKE Peak
All Runs	56013	16653
Runs w/SeGA TAC	27176	8177

No observation of the  $^{124}\text{Ag}$  isomer has been reported in the literature. Low-lying isomeric states near 100 keV are known in many odd-odd Ag isotopes up to  $^{120}\text{Ag}$ . These isomers are depopulated by beta decay and/or  $E3$  isomeric transitions. Unfortunately, almost nothing is known about the next lighter odd-odd Ag isotope,  $^{122}\text{Ag}$ . Based on the systematics of the lighter odd-odd Ag isotopes, the 156-keV gamma ray could be the IT from a low-lying state directly into the ground state, however, this would not explain the origin of the 1132-keV gamma ray. In this work, the 156- and 1132-keV gamma rays were coincident. Comparison of the deduced half-life and Weisskopf estimates suggest that a 156-keV IT is likely a slow  $E2$  gamma ray. A level scheme has not been proposed in the present work.

#### 4.2.9 $^{125}\text{Ag}$

The fragment energy loss and time-of-flight of the events located within the Ag-A+3 PID blob (see Fig. 4.1) correspond with ions of fully-stripped  $^{125}\text{Ag}^{47+}$ . The Ag-A+3 gated TKE spectrum contains  $^{125}\text{Ag}^{47+}$  ions, as well as,  $^{122}\text{Ag}^{46+}$  contaminant ions. The range of the TKE gate is indicated in Figure 4.42 by the vertical lines. The integrated events within the Ag-A+3 PID contour for all experimental runs, as well as for the experimental runs that included the SeGA-TAC, are given in Table 4.21. The observed number of counts for  $^{125}\text{Ag}$  within the TKE cut are given alongside these values.

The  $^{125}\text{Ag}$  prompt gamma-ray spectrum is shown in Figure 4.43. Four peaks were observed, and the deduced gamma-ray energies, peak areas, and relative intensities are displayed in Table 4.22. Coincidence relationships between the observed  $^{125}\text{Ag}$  prompt gamma rays were also investigated, and the fragment- $\gamma\gamma$  coincidence spectra

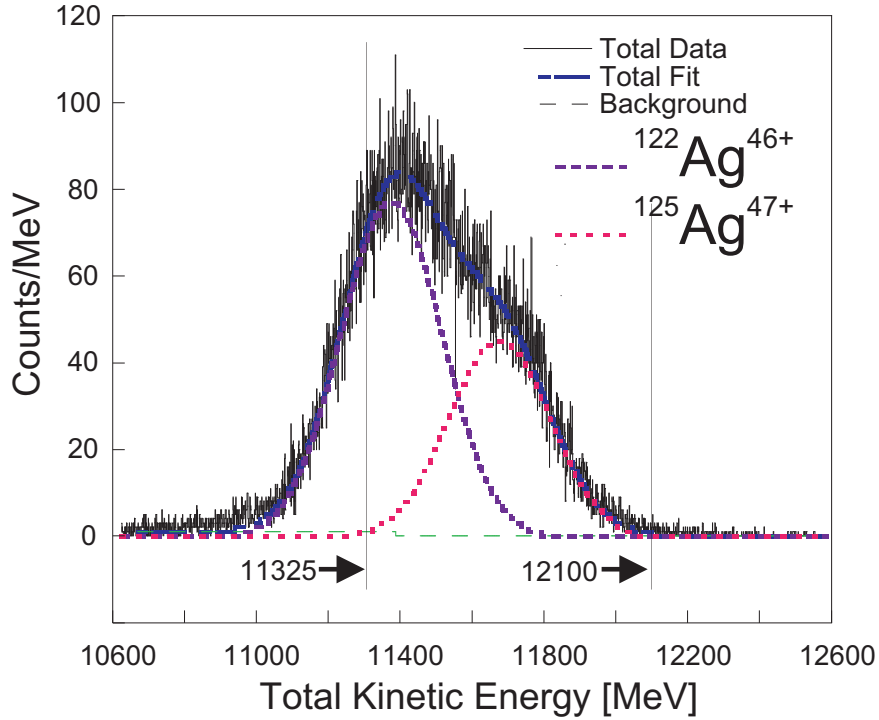


Figure 4.42: TKE spectrum for the Ag-A+3 PID blob. Two unequal distributions can be seen. The smaller is attributed to  $^{125}\text{Ag}^{47+}$  and the larger to  $^{122}\text{Ag}^{46+}$ . The vertical lines indicate the range of the  $^{125}\text{Ag}$  TKE gate.

Table 4.22: The  $^{125}\text{Ag}$  prompt gamma-ray energies, integrated peak areas and relative intensities.

Peak Energy [keV]	Fitted Peak Area	Relative Intensity
670.1(3)	50(11)	69(19)
684.4(3)	72(12)	100(24)
713.9(2)	34(7)	49(13)
729.1(2)	53(6)	77(16)

that were obtained in this work are shown in Figure 4.44. The fitted  $^{125}\text{Ag}$  prompt gamma-ray decay curve is shown in Figure 4.45. The half-life from the present work is included in the inset.

Observation of the  $^{125}\text{Ag}$  isomer has not been reported in the literature. A proposed level scheme based on the present work is given in Figure 4.46. The 671-keV and 729-keV gamma rays were coincident, and the 685- and 714-keV gamma rays were also coincident. The observed coincidences and the fact that these two pairs of gamma rays both sum to 1399 keV supports the arrangement of the four observed gamma

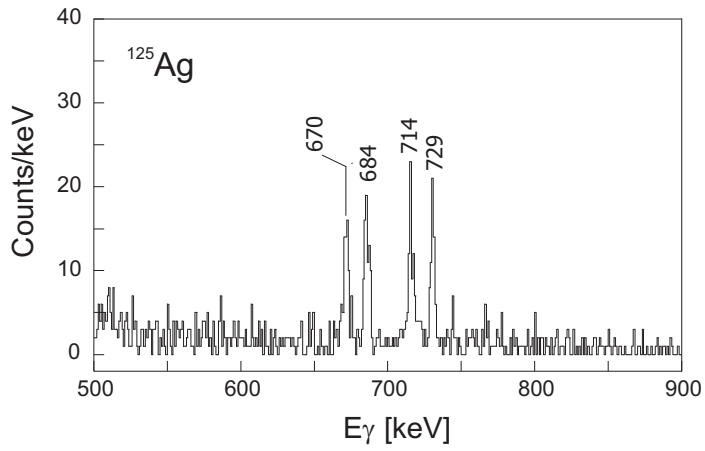


Figure 4.43: Prompt gamma-ray spectrum for  $^{125}\text{Ag}$ .

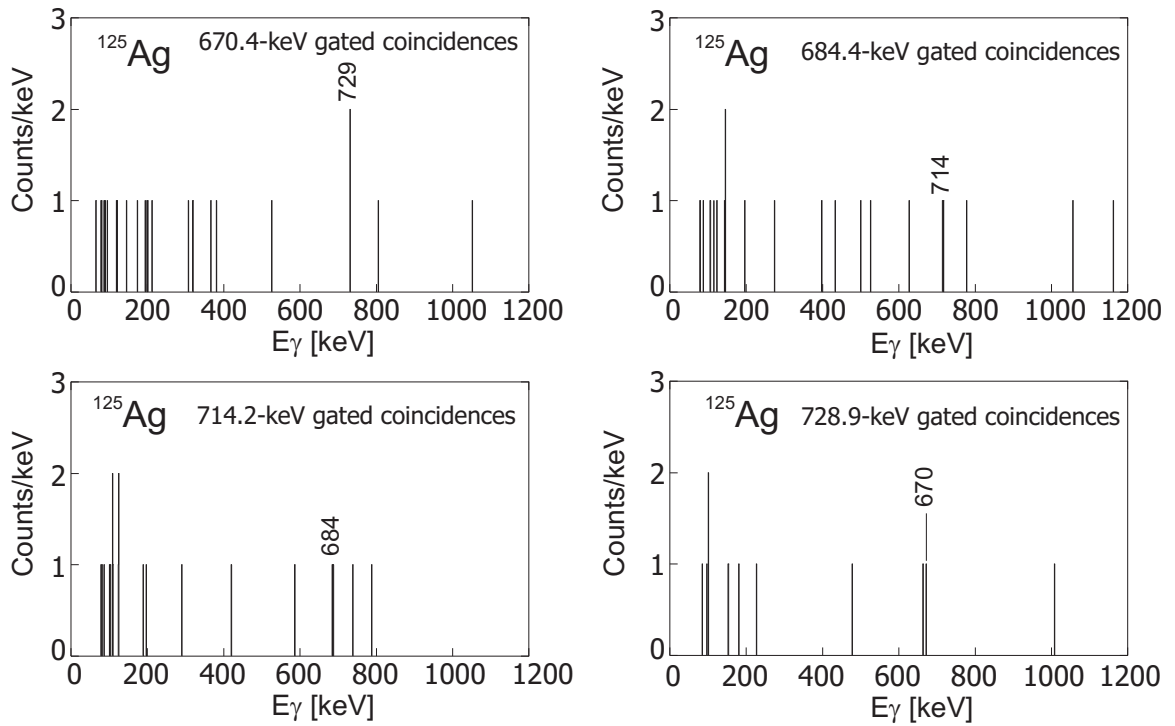


Figure 4.44: Prompt fragment- $\gamma\gamma$  spectra for  $^{125}\text{Ag}$ .

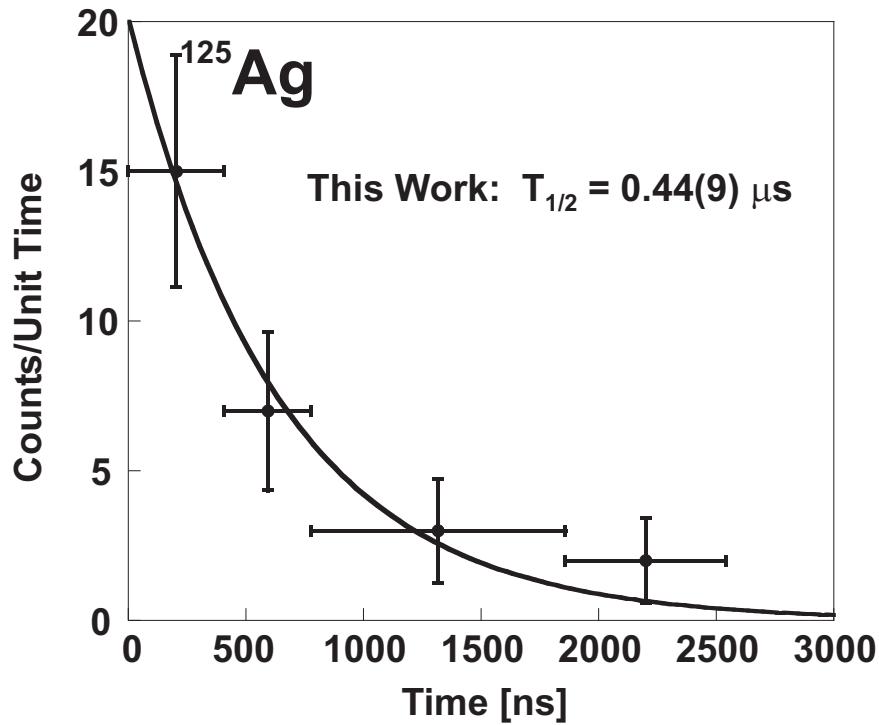


Figure 4.45: The fitted  $^{125}\text{Ag}$  isomer decay curve. The deduced half-life value is given in the inset.

rays into two cascades from the possible  $15/2^+$  level at 1399 keV to the ground state. It should be noted that the positions of the  $11/2^+$  and  $13/2^+$  levels, as shown in Figure 4.46, are uncertain since the orders of the two gamma-ray cascades could be different than those shown in the figure. The spin-parity assignments are based on systematics of the odd- $A$  Ag isotopes. The proposed level scheme suggests that the  $15/2^+$  level at 1399 keV is populated by the IT. The  $E2$  IT indicated in the figure was likely below the gamma-ray detection threshold and was not measured. Comparison of the deduced half-life and Weisskopf estimates suggest that the  $E2$  IT is likely to be  $\leq 100$  keV in magnitude.

Similar to  $^{123}\text{Ag}$ , the nuclide  $^{125}\text{Ag}$ , with an even number of neutrons ( $N=78$ ) and an odd number of protons ( $Z=47$ ), is well described by configurations of the odd proton coupled to a pair of  $\nu h_{11/2}$  holes. The odd proton resides in the  $g_{9/2}$  orbital, and the even-parity excited states of  $^{125}\text{Ag}$  arise from the coupling of this proton to the  $\nu h_{11/2}^{-2}$  configurations. Thus, even-parity levels from the  $9/2^+$  ground state to the

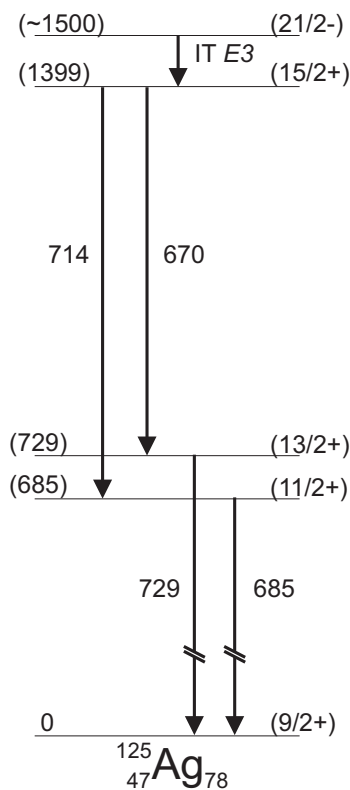


Figure 4.46: Proposed decay scheme for the  $^{125}\text{Ag}$  isomer. The quoted energies are in keV.

$17/2^+$  isomeric state are produced by the  $\pi g_{9/2}^1 \otimes \nu h_{11/2}^{-2}$  configurations.

#### 4.2.10 $^{121}\text{Pd}$

The fragment energy loss and time-of-flight of the events located within the Pd-A+1 PID blob (see Fig. 4.1) correspond with ions of fully-stripped  $^{121}\text{Pd}^{46+}$ . The Pd-A+1 gated TKE spectrum has two components—roughly equal contributions of  $^{118}\text{Pd}^{45+}$  contaminant ions at lower energies and  $^{121}\text{Pd}^{46+}$  at higher energies, as shown in Figure 4.47. The range of the TKE gate is indicated in Figure 4.47 by the vertical lines. The integrated events within the Pd-A+1 PID contour for all experimental runs, as well as for the experimental runs that included the SeGA-TAC, are given in Table 4.23. The observed number of counts for  $^{121}\text{Pd}^{46+}$  within the TKE cut are given alongside these values.

The  $^{121}\text{Pd}$  prompt gamma-ray spectrum is shown in Figure 4.48. One peak was

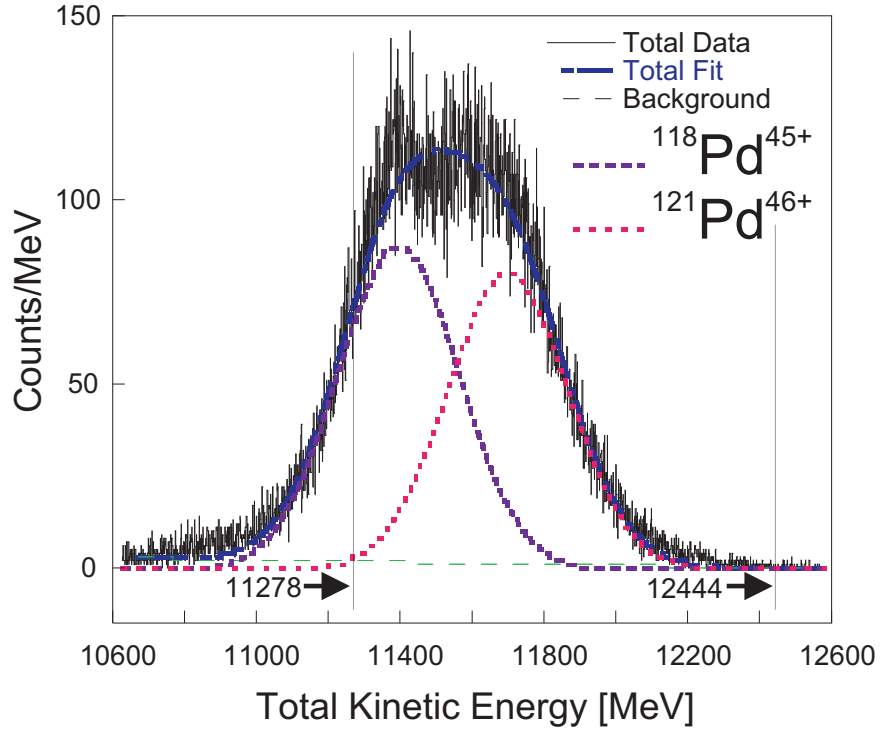


Figure 4.47: TKE spectrum for the Pd-A+1 PID blob. Two unequal distributions can be seen. The higher-energy peak is attributed to  $^{121}\text{Pd}^{46+}$  and the lower-energy peak is attributed to  $^{118}\text{Pd}^{45+}$ . The vertical lines indicate the range of the  $^{121}\text{Pd}$  TKE gate.

Table 4.23: The integrated number of events associated with the Pd-A+1 PID gate.

Portion of Data	PID Contour	$^{121}\text{Pd}$ TKE Peak
All Runs	85783	35620
Runs w/SeGA TAC	36104	15346

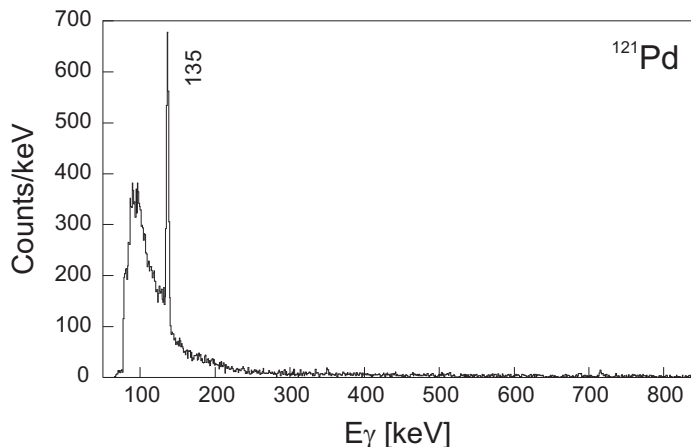


Figure 4.48: Prompt gamma-ray spectrum for  $^{121}\text{Pd}$ .

Table 4.24: The  $^{121}\text{Pd}$  prompt gamma-ray energy and integrated peak area.

Peak Energy [keV]	Fitted Peak Area
135.1(1)	1918(36)

observed, and the deduced gamma-ray energy and peak area are displayed in Table 4.24. The fitted  $^{121}\text{Pd}$  prompt gamma-ray decay curve is shown in Figure 4.49. The half-life from the present work [ $0.70(5) \mu\text{s}$ ] is included in the inset.

Observation of the  $^{121}\text{Pd}$  isomer has not been reported in the literature. Low-energy isomeric states near 100–200 keV are known in many odd- $A$  Pd isotopes up to  $^{117}\text{Pd}$  [59]. These isomers, which are odd-parity states produced by  $\nu h_{11/2}$  configurations [60], are generally depopulated by isomeric transitions rather than beta decay. Unfortunately, almost nothing is known about the next lighter odd- $A$  Pd isotope,  $^{119}\text{Pd}$ . Based on the systematics of the lighter odd- $A$  Pd isotopes, the 135-keV gamma ray could be the IT in  $^{121}\text{Pd}$ . Comparison of the deduced half-life and Weisskopf estimates suggest that a 135-keV IT is likely a slow  $E2$  gamma ray. A level scheme has not been proposed in the present work.

#### 4.2.11 $^{117}\text{Ru}$

The fragment energy loss and time-of-flight of the events located within the Ru-A+1 PID blob (see Fig. 4.1) correspond with ions of fully-stripped  $^{117}\text{Ru}^{44+}$ . The Ru-A+1

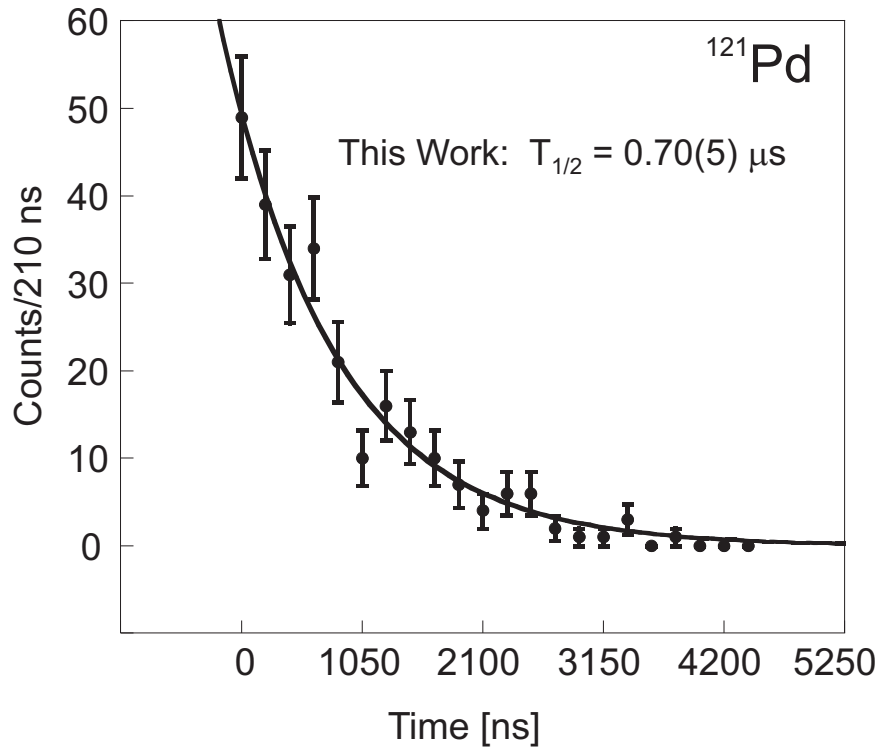


Figure 4.49: The fitted  $^{121}\text{Pd}$  isomer decay curve. The deduced half-life value is given in the inset.

Table 4.25: The integrated number of events associated with the Ru-A+1 PID gate.

Portion of Data	PID Contour	$^{117}\text{Ru}$ TKE Peak
All Runs	7744	2054
Runs w/SeGA TAC	3320	888

gated TKE spectrum is provided in Figure 4.50. The  $^{114}\text{Ru}^{43+}$  contaminant ions have slightly less kinetic energy than the  $^{117}\text{Ru}^{44+}$  ions; therefore, the smaller peak of the TKE spectrum was attributed to  $^{117}\text{Ru}$  with significant contribution from  $^{114}\text{Ru}$ . The range of the TKE gate is indicated in Figure 4.50 by the vertical lines. The integrated events within the Ru-A+1 PID contour for all experimental runs, as well as for the experimental runs that included the SeGA-TAC, are given in Table 4.25. The observed number of counts for  $^{117}\text{Ru}$  within the TKE cut are given alongside these values.

The  $^{117}\text{Ru}$  prompt gamma-ray spectrum is shown in Figure 4.51. One peak was observed and the deduced gamma-ray energy and peak area are displayed in Table 4.26. The fitted  $^{117}\text{Ru}$  prompt gamma-ray decay curve is shown in Figure 4.52. The half-life

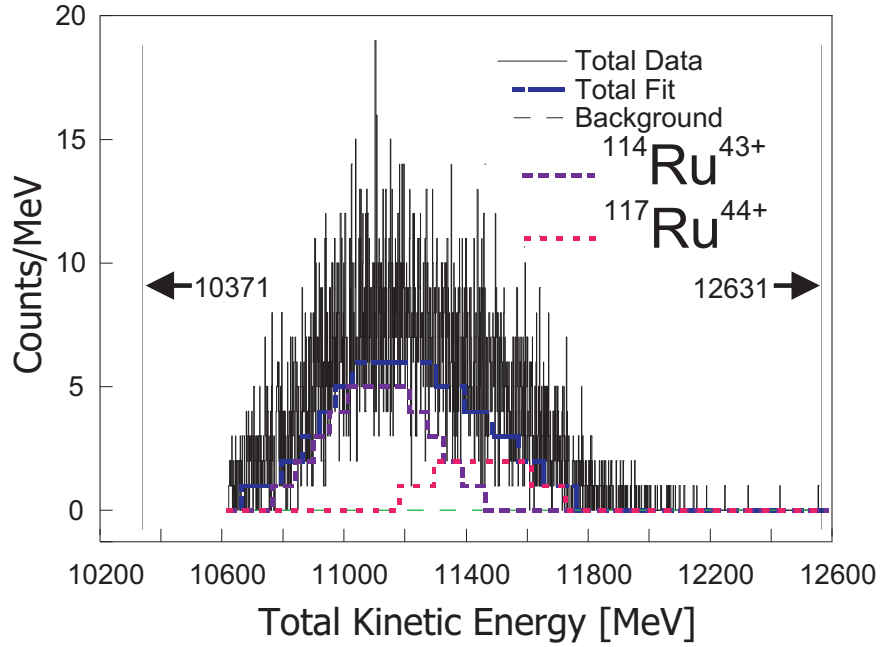


Figure 4.50: TKE spectrum for the Ru-A+1 PID blob. Two unequal distributions can be seen. The smaller is attributed to  $^{117}\text{Ru}^{44+}$  and the larger to  $^{114}\text{Ru}^{43+}$ . The vertical lines indicate the range of the  $^{117}\text{Ru}$  TKE gate.

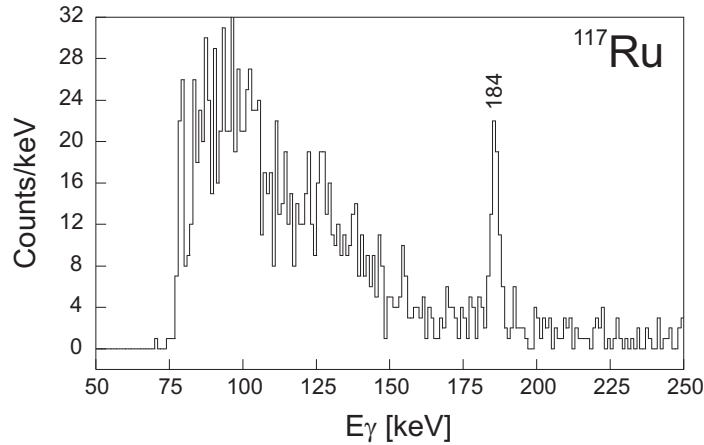


Figure 4.51: Prompt gamma-ray spectrum for  $^{117}\text{Ru}$ .

from the present work is included in the inset.

Observation of the  $^{117}\text{Ru}$  isomer has not been reported in the literature. Only one neutron-rich odd- $A$  isotope of Ru has been observed to have an isomer. A beta-decaying  $11/2^-$  130-keV isomer has been reported in  $^{113}_{44}\text{Ru}_{69}$  [61]. The decay scheme of the  $^{113}\text{Ru}$  isomer is given in Figure 4.53. The structure of the odd-parity isomer, built upon a  $\nu h_{11/2}$  configuration, is very similar to that observed in the odd- $A$  Pd

Table 4.26: The  $^{117}\text{Ru}$  prompt gamma-ray energy and integrated peak area.

Peak Energy [keV]	Fitted Peak Area
184.4(2)	67(7)

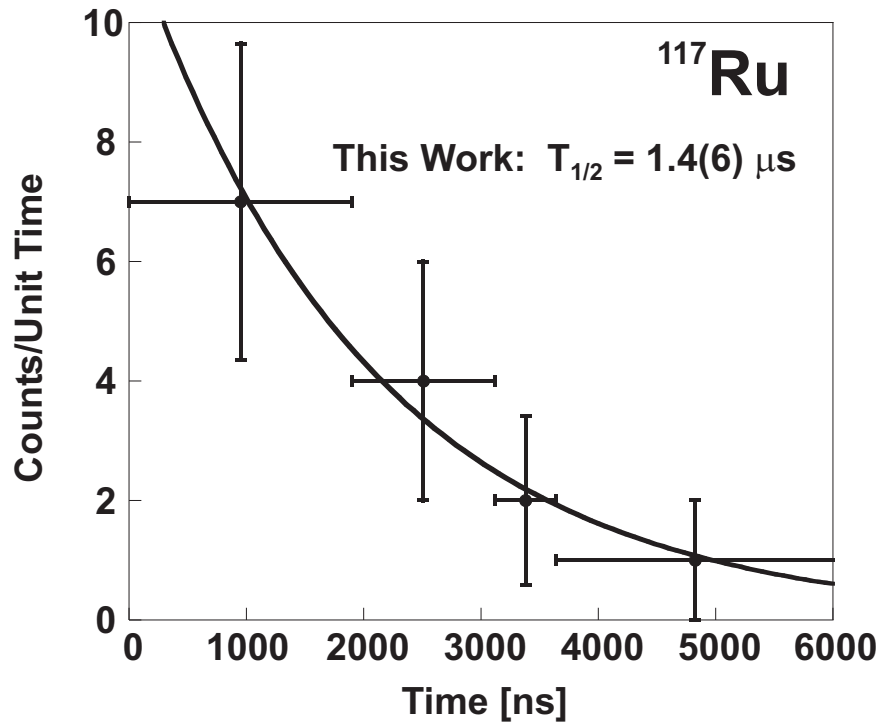


Figure 4.52: The fitted  $^{117}\text{Ru}$  isomer decay curve. The deduced half-life value is given in the inset.

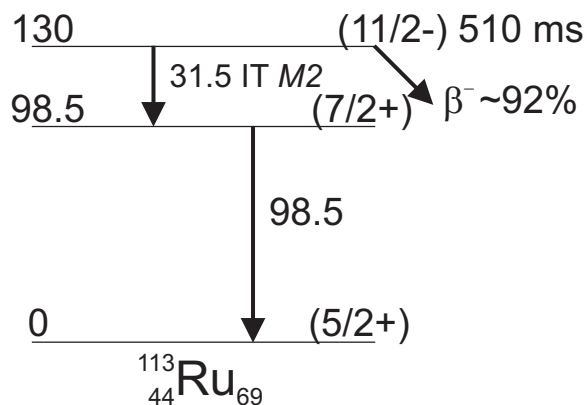


Figure 4.53: Decay scheme for the  $^{113}\text{Ru}$  isomer from Ref. [61]. The quoted energies are in keV.

isotopes [61]. By analogy with  $^{113}\text{Ru}$ , the 185-keV gamma ray could be the IT in  $^{117}\text{Ru}$ , but it may also be the  $7/2^+ \rightarrow 5/2^+$  transition with the IT being a low-energy gamma ray that was below the detection threshold in this work. Comparison of the deduced half-life and Weisskopf estimates suggest that a 185-keV IT is likely an  $E2$  gamma ray. A level scheme for  $^{117}\text{Ru}$  has not been proposed in the present work.

### 4.3 Beta-Decay Parents

In the following sections (4.3.1-4.3.6) the results obtained for the observed beta-decaying nuclides are presented. The information given includes: fragment-gated beta-delayed gamma-ray spectra, fragment- $\beta\gamma\gamma$  coincidence spectra, beta-decay half-lives, and level structures in some instances. A summary of the the beta-decay results is given in Tables 4.27 and 4.28. A general description of the analysis procedure used to study beta-decaying nuclides in this work was presented in Chapter 3, and some additional details are given in the next several paragraphs.

The PID gates, presented earlier for the isomer analysis, were used to select different components of the secondary ion beam. The charge-state contaminant ions, which caused ambiguity in the identification of fragments based on the PID plot alone, were not of concern in the analysis of beta-decay correlated events, because of a filtering effect based on the range of the fragments in the  $\Delta E$  detectors. This

Table 4.27: PID-gate statistics for Experiment 01015. The numbers presented here are the integrated counts of all fragments (fully-stripped *and* charge-state) within the indicated PID gate. The “Implanted Fraction” refers to the ratio of all fragments implanted in the DSSD (column 3) to all fragments incident on PIN1a (column 2) for the indicated PID gate. The righthand column refers to the ratio decay-correlated fragments (column 4) to implanted fragments (column 3).

PID Gate	Fragments Incident on PIN1a	Fragments Implanted in DSSD	$\beta$ -decay Correlated Fragments	Implanted Fraction (%)	$\beta$ -decay Correlated Fraction (%)
Cd-A+1	134237	4187	1339	3	32
Ag-A	13562	7974	2836	59	36
Ag-A+1	108657	26222	9978	24	38
Ag-A+2	147982	9079	3685	6	41
Pd-A	32584	23883	9261	73	39
Pd-A+1	85783	38022	15646	44	41
Pd-A+2	60437	8148	3637	14	45
Rh-A	24333	19109	7549	79	31
Rh-A+1	29177	17729	7824	61	44
Rh-A+2	13993	2927	1390	21	48
Ru-A	6317	4907	2174	78	44
Ru-A+1	7744	4904	2348	63	48

effect is illustrated in the TKE spectra of Cd-A+1 fragments, shown in Figure 4.54. Approximately 40% of the Cd-A+1 fragments were  $^{123}\text{Cd}^{47+}$  contaminant ions, as may be seen in the uncorrelated Cd-A+1 TKE spectrum on the lefthand side of the figure. These contaminant ions were largely stopped in the  $\Delta E$  detectors between PIN01a and the DSSD. Thus, the Cd-A+1 fragments implanted in the DSSD were predominantly  $^{126}\text{Cd}^{48+}$ . Inspection of the TKE spectrum for fragments that satisfied the DSSD implant condition reveals the filtering effect of the  $\Delta E$  detectors. Whereas in the TKE spectrum for all Cd-A+1 fragments incident upon PIN01a (see Fig. 4.54) two peaks are clearly visible, in the TKE spectrum for implanted fragments only one peak is observed centered at the energy expected for  $^{126}\text{Cd}^{48+}$ . The actual number of Cd-A+1 fragments that yielded data was finally determined by the decay condition. The decay-correlated Cd-A+1 TKE spectrum (see Fig. 4.54) looks the same as the implant-correlated TKE spectrum, albeit with reduced counts due to a correlation efficiency of less than unity ( $\lesssim 50\%$ ), and is free of charge-state contaminant ions.

Table 4.28: A summary of  $\beta$ -delayed  $\gamma$  rays, deduced fragment-gated  $\beta$ -decay half-lives and fragment- $\gamma$ -gated  $\beta$ -decay half-lives for nuclides implanted into the DSSD. The superscripts in the righthand column indicate the  $\gamma$  ray used for gating.

PID	Nuclide	Gamma Rays [keV]	$T_{1/2}$ [s]	$\gamma$ -gated $T_{1/2}$ [s]
Cd-A+1	$^{126}\text{Cd}^{48+}$	260, 428	0.48(4)	0.55(5) <sup>[260]</sup> , 0.36(2) <sup>[428]</sup> 0.46(3) <sup>[total]</sup>
Ag-A	$^{122}\text{Ag}^{47+}$	325, 570, 651, 668 760, 800, 849	0.39(2)	0.68(9) <sup>[325]</sup> , 0.34(4) <sup>[570]</sup> 0.35(5) <sup>[651]</sup> , 0.29(5) <sup>[760]</sup> 1.2(8) <sup>[800]</sup> , 0.42(8) <sup>[849]</sup> 0.35(2) <sup>[total]</sup>
Ag-A+1	$^{123}\text{Ag}^{47+}$	115, 123, 134, 263 346, 365, 409, 435 439, 591, 1248	0.26(1)	0.21(2) <sup>[263]</sup> , 0.39(5) <sup>[346]</sup> 0.31(3) <sup>[409]</sup> , 0.33(5) <sup>[439]</sup> 0.25(4) <sup>[591]</sup> , 0.27(2) <sup>[total]</sup>
Ag-A+2	$^{124}\text{Ag}^{47+}$	461, 540, 614, 773 838	0.18(1)	0.31(8) <sup>[461]</sup> , 0.18(2) <sup>[540]</sup> 0.16(1) <sup>[614]</sup> , 0.18(2) <sup>[773]</sup> 0.20(2) <sup>[total]</sup>
Pd-A	$^{120}\text{Pd}^{46+}$	159	0.46(1)	0.97(12) <sup>[159]</sup>
Pd-A+1	$^{121}\text{Pd}^{46+}$	135, 358, 626, 682 709, 1023, 1027 1369	0.248(5)	0.26(3) <sup>[135]</sup> , 0.5(1) <sup>[626]</sup> 0.40(7) <sup>[682]</sup> , 0.39(5) <sup>[709]</sup> 0.26(3) <sup>[1022+1026]</sup> , 0.33(2) <sup>[total]</sup>
Pd-A+2	$^{122}\text{Pd}^{46+}$	209, 241, 965	0.17(1)	0.40(3) <sup>[209]</sup> , 0.23(2) <sup>[965]</sup>
Rh-A	$^{118}\text{Rh}^{45+}$	370, 379, 433, 574 719, 814, 1035	0.31(1)	0.37(5) <sup>[370]</sup> , 0.32(3) <sup>[379]</sup> 0.52(6) <sup>[433]</sup> , 0.28(1) <sup>[574]</sup> 0.49(8) <sup>[719]</sup> , 0.17(1) <sup>[814]</sup> 0.23(2) <sup>[1035]</sup>
Rh-A+1	$^{119}\text{Rh}^{45+}$	247, 457, 585, 685 708	0.19(1)	0.28(2) <sup>[247]</sup> , 0.24(6) <sup>[457]</sup> 0.39(7) <sup>[585]</sup> , 0.8(3) <sup>[685]</sup> 0.43(9) <sup>[708]</sup> , 0.39(2) <sup>[total]</sup>
Rh-A+2	$^{120}\text{Rh}^{45+}$	436, 619, 901 1122, 1245	0.12(1)	0.16(2) <sup>[436]</sup> , 0.12(1) <sup>[total]</sup>
Ru-A	$^{116}\text{Ru}^{44+}$	246	0.18(1)	0.12(2) <sup>[246]</sup>
Ru-A+1	$^{117}\text{Ru}^{44+}$	583, 1276	0.16(2)	0.16(3) <sup>[583]</sup>

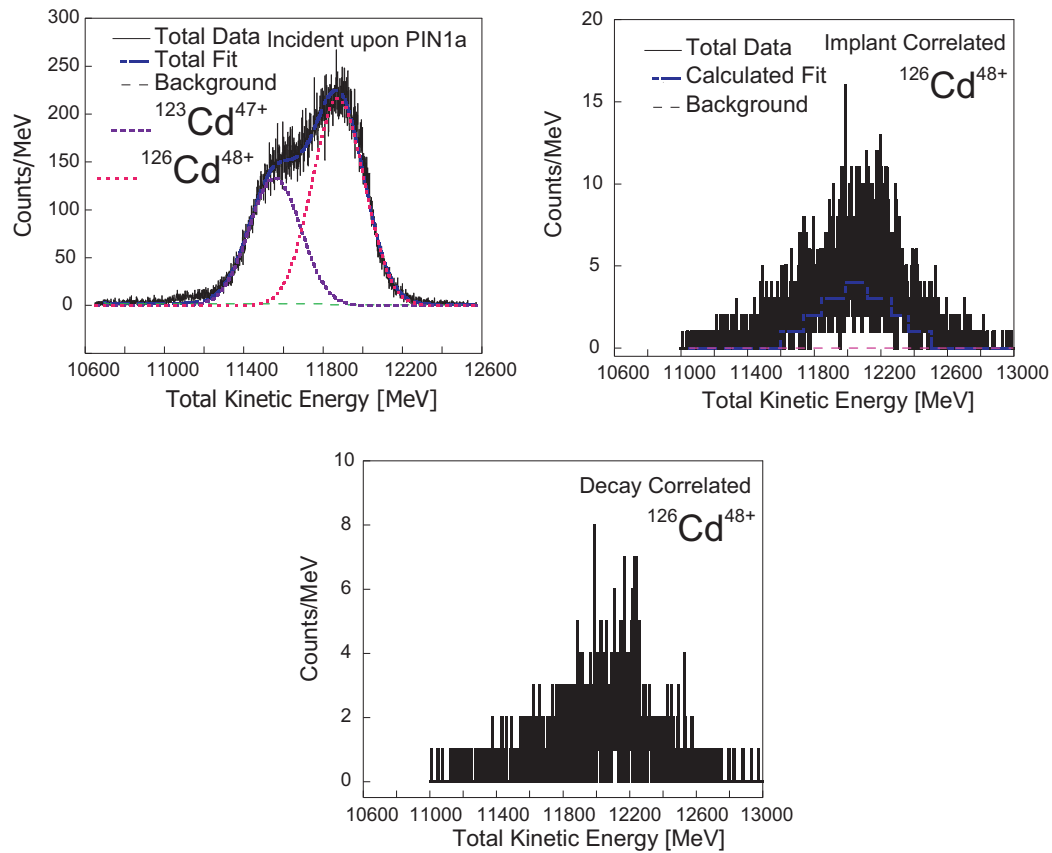


Figure 4.54: Uncorrelated, implant-correlated, and decay-correlated  $^{126}\text{Cd}$  TKE spectra.

Thus, fragment gates made with the decay-correlated PID were free of charge-state contaminant ions, and no TKE gating was applied in the beta-decay analysis.

### Beta-Delayed Gamma Radiation

The beta-delayed gamma-ray spectrum for a given nuclide was obtained from the total beta-delayed gamma-ray spectrum by gating on the corresponding decay-correlated PID contour. The gamma-ray peaks in each spectrum were fitted with Gaussian functions using DAMM. A background region of approximately 10 keV on each side of a peak was considered for each fit. Gamma-ray energies were obtained from the fitted peak centroids, and gamma-ray intensities were deduced from the peak areas. Coincidence relationships between the observed delayed gamma rays were also investigated, as described in Section 3.3.3.

Table 4.29: The  $^{126}\text{Cd}$  beta-delayed gamma-ray energies, integrated peak areas and relative intensities. The literature energies and relative intensities are from Ref. [62]. The values of absolute intensity per 100 decays are taken from Ref. [63].

Peak Energy [keV]		Fitted Peak Area	Relative Intensity		Absolute Intensity	
This Work	Lit.		This Work	Lit.	This Work	Lit.
259.4(2)	260.09(9)	47(7)	100(21)	100.0(40)	40(6)	79(20)
427.9(2)	428.11(6)	27(5)	79(19)	83.7(28)	31(5)	66(17)

### Beta-Decay Half-Life

Fragment-gated beta-decay curves were obtained as described in Section 3.3.3. These fragment- $\beta$  gated decay curves were rebinned by factors of four or five for fitting, and beta-decay half-lives were deduced from unweighted, exponential least-squares fits with constant backgrounds. The growth and decay of beta-decay daughter nuclides were included in the fit calculations in all cases, and the granddaughter generation was included in a few cases. Gamma-gated beta-decay half-life values were determined by single-component exponential least-squares fitting of the fragment- $\beta\gamma$  gated decay curves, also described in Section 3.3.3.

#### 4.3.1 $^{126}\text{Cd}$

Beta-decay data were obtained for one Cd isotope,  $^{126}\text{Cd}$ . As explained in Section 4.2.5 this isotope was identified within the Cd-A+1 PID region. The number of counts within the Cd-A+1 gate (total, implant-correlated, and decay-correlated) were given in Table 4.27.

The  $^{126}\text{Cd}$  beta-delayed gamma-ray spectrum is shown in Figure 4.55. Two peaks were observed, and the deduced gamma-ray energies, peak areas, relative intensities, and absolute intensities are displayed in Table 4.29. Coincidence relationships between the observed  $^{126}\text{Cd}$  delayed gamma rays were also investigated. The  $^{126}\text{Cd}$  fragment- $\beta\gamma\gamma$  coincidence spectra that were obtained in this work are shown in Figure 4.56.

The fitted  $^{126}\text{Cd}$  beta-decay curve is shown in Figure 4.57. The half-life from the present work [0.48(4) s] and the value reported by Gartner and Hill [0.506(15) s] are

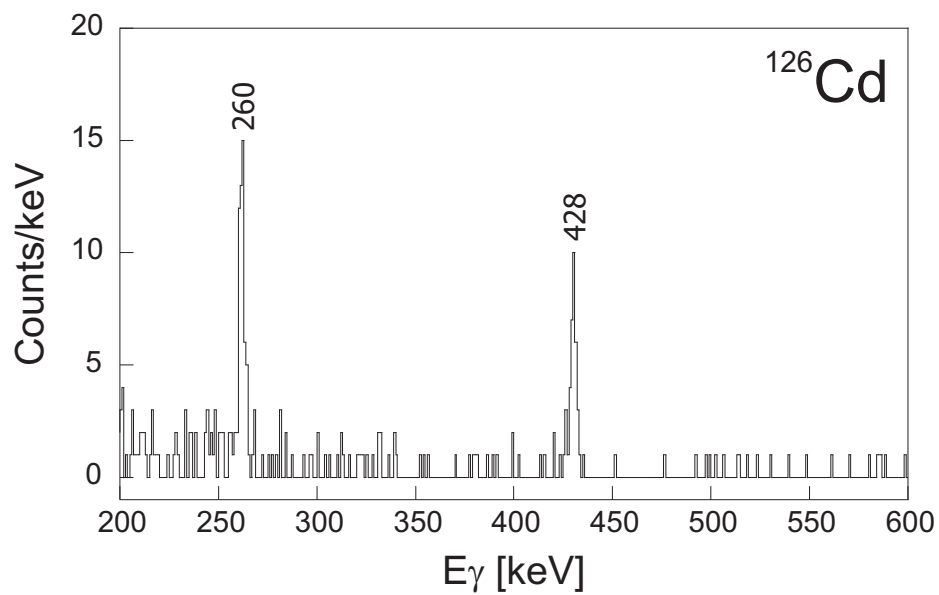


Figure 4.55: Beta-delayed gamma-ray spectrum for  $^{126}\text{Cd}$ .

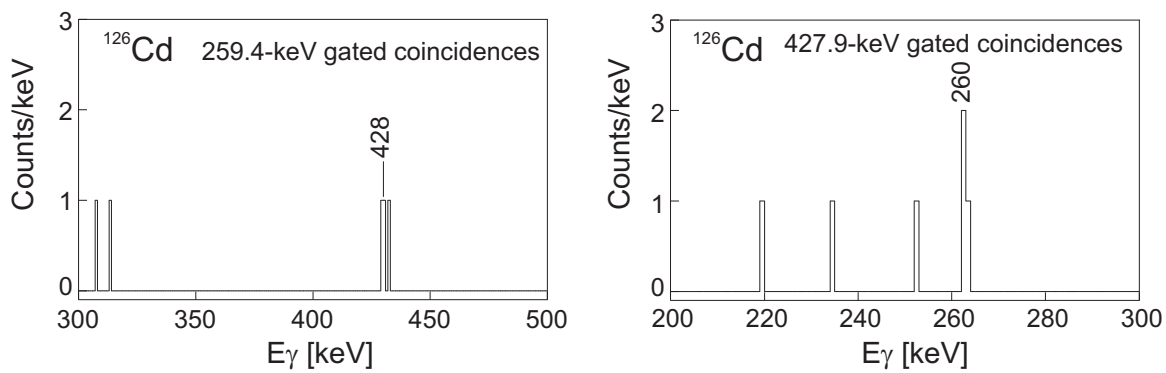


Figure 4.56: Fragment- $\beta\gamma\gamma$  coincidence spectra for the decay of  $^{126}\text{Cd}$ .

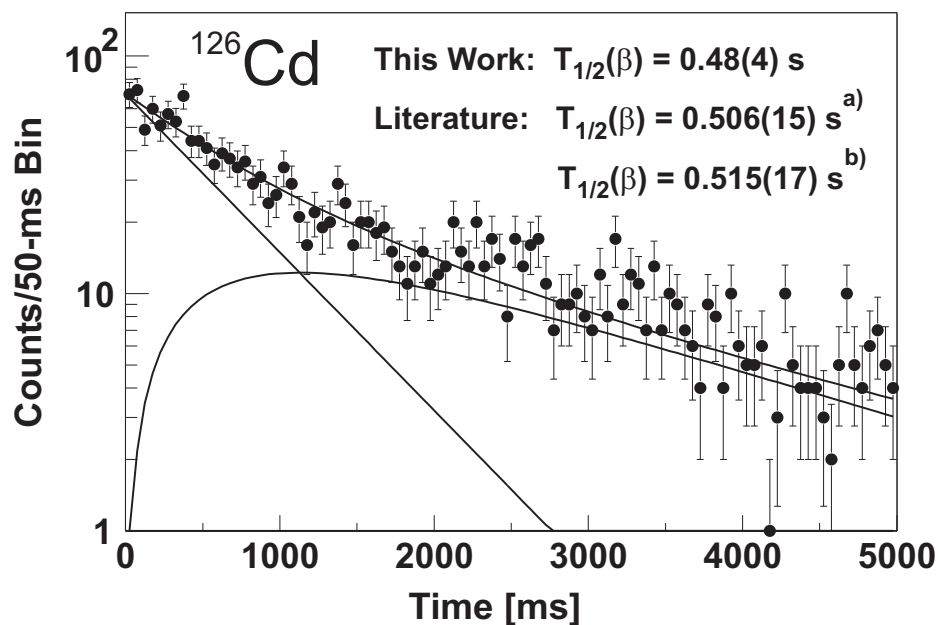


Figure 4.57: The fitted  $^{126}\text{Cd}$  beta-decay curve. The deduced half-life value and the literature values from (a) Ref. [62] and (b) Ref. [63] are given in the inset.

included in the inset. The evaluated half-life of  $0.515(17)$  s from the Nuclear Data Sheets [63] is also provided. Gamma-gated half-lives were also deduced in the present work. The fitted  $^{126}\text{Cd}$  gamma-gated decay curves are shown in Figure 4.58. The 260-keV gated half-life was determined to be  $0.55(5)$  s; the 428-keV gated half-life was determined to be  $0.36(2)$  s. The sum of the individual curves was also fitted and yielded a half-life value of  $0.46(3)$  s.

The beta-decay scheme for  $^{126}\text{Cd}$  was first reported by Gartner and Hill [62] and is well understood. The  $^{126}\text{Cd}$  beta-decay scheme is shown in Figure 4.59. The gamma-ray energies determined in the present work are in good agreement with those reported in the literature, as shown in Table 4.29. The 260- and 428-keV gamma rays that were observed in this work are also the most intense gamma transitions observed by Gartner and Hill. The third most intense transition previously observed (688 keV) had a relative intensity of  $5.9(4)\%$ . Such a gamma ray would only be seen at a level of about one count in the present work; therefore, it is clear that the statistics were insufficient to see any weaker gamma rays in  $^{126}\text{Cd}$ . In the present work, the 260- and 428-keV transitions were coincident and had similar relative intensities, suggesting a

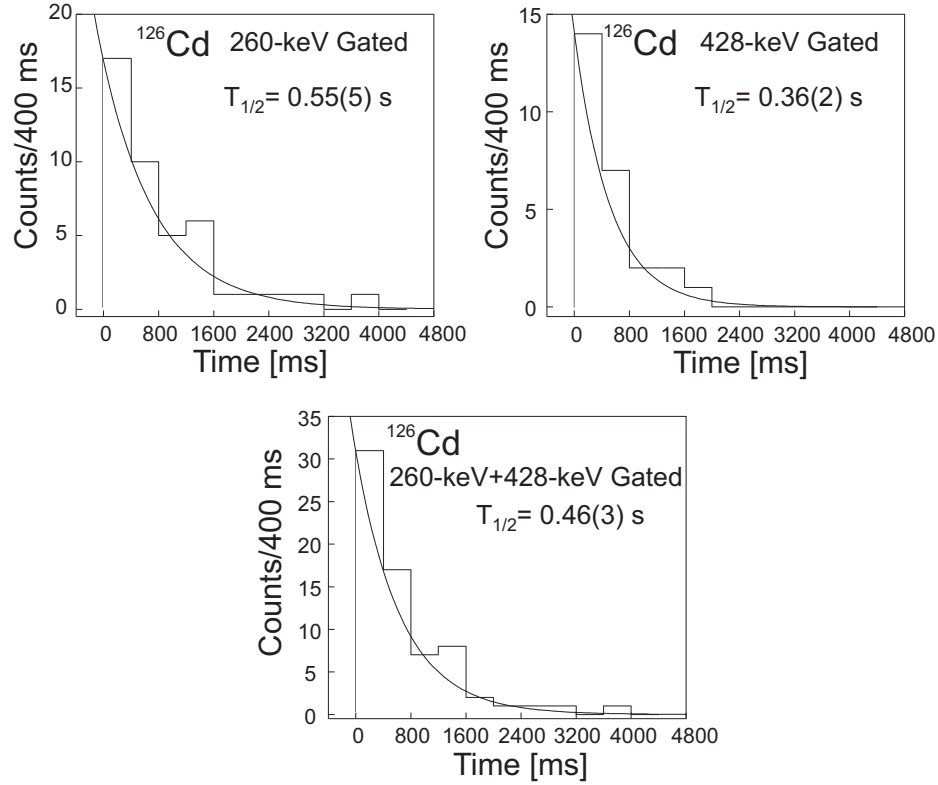


Figure 4.58: Gamma-ray gated  $^{126}\text{Cd}$  decay curves.

two-gamma cascade. Indeed, the 428-keV transition is believed to feed into the  $2^-$  level that is depopulated exclusively by the 260-keV gamma ray [62]. The absolute gamma-ray intensities (per 100 beta decays) are low by a factor of two compared to the published values. The source of this discrepancy has not been determined.

The  $^{126}\text{Cd}$  half-life value deduced by Gartner and Hill is a weighted average of the 260- and 428-keV gamma-gated half-lives, 0.509(1) s and 0.504(1) s, respectively [62]. Both the total beta-decay half-life and the 260-keV gated half-life deduced in the present work are in good agreement with those of Gartner and Hill; however, the current 428-keV gated half-life is lower than the published value by several standard deviations. The discrepancy has been attributed to the low gamma-ray statistics. A value of 0.48(4) s for the  $^{126}\text{Cd}$  beta-decay half-life was adopted in the present work.

The authors of Ref. [62] postulate that most of the  $^{126}\text{Cd}$  beta-decay strength populates the  $1^+$  level at 688 keV and that less than 1% goes to the  $3^+$  ground state. These  $J^\pi$  assignments are consistent with an allowed beta transition to the

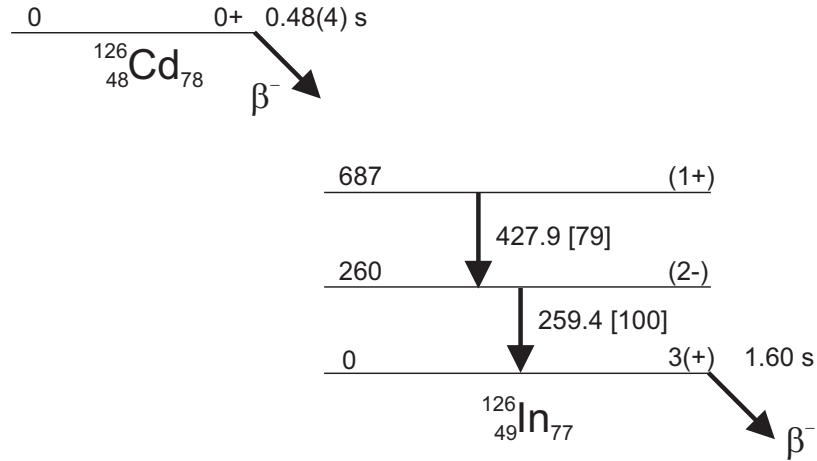


Figure 4.59: Partial decay scheme for  $^{126}\text{Cd}$  based on the present work. The  $J^\pi$  assignments and the  $^{126}\text{In}$   $\beta$ -decay half-life were obtained from Ref. [63]. The  $2^-$  spin assignment of the first excited state is attributed to Spanier [58]. The quoted energies are in keV.

688-keV level and a second-forbidden beta transition to the ground state. The beta decay possibly occurs by the conversion of a  $g_{7/2}$  neutron in  $^{126}\text{Cd}$  to a  $g_{9/2}$  proton in  $^{126}\text{In}$ . The  $3^+$  ground state and  $1^+$  excited state are attributed to the resulting  $(\pi g_{9/2}^{-1}) \otimes (\nu g_{7/2}^{-1})$  configurations [62]. The  $2^-$  level at 260 keV is attributed to the  $(\pi p_{1/2}^{-1}) \otimes (\nu g_{7/2}^{-1})$  configuration [58].

In summary, the experimental observations of  $^{126}\text{Cd}$  beta decay in the present work were found to be in good agreement with the published measurements, aside from the absolute gamma-ray intensity discrepancy. Such agreement has been interpreted as validation of the data-analysis techniques employed in the study of beta-decaying nuclides in the present work.

### 4.3.2 $^{122}\text{Ag}$

Beta-decay data were obtained for the nuclide  $^{122}\text{Ag}$ , which was identified within the Ag-A PID region. The number of counts within the Ag-A gate (total, implant-correlated, and decay-correlated) were given in Table 4.27. Approximately 59% of the Ag-A fragments incident upon PIN01a were implanted in the DSSD, and 36% of the implanted Ag-A fragments were correlated with beta-decay events.

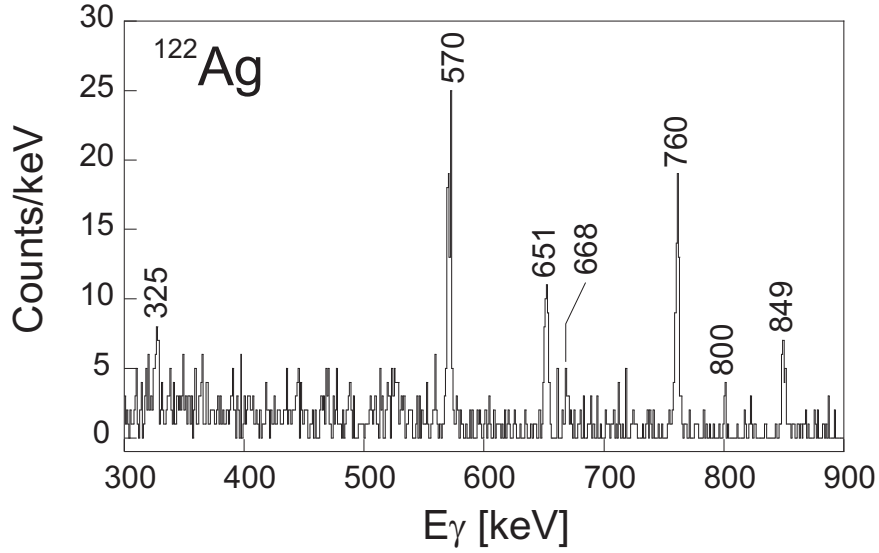


Figure 4.60: Beta-delayed gamma-ray spectrum for  $^{122}\text{Ag}$ .

Table 4.30: The  $^{122}\text{Ag}$  beta-delayed gamma-ray energies, integrated peak areas and relative intensities (normalized to 100 for the 570-keV  $\gamma$  ray). The published energies and relative intensities are taken from Ref. [64]. The absolute intensities are from Ref. [65].

Peak Energy [keV]		Fitted Peak Area	Relative Intensity		Absolute Intensity	
This Work	Lit. [64]		This Work	Lit. [64]	This Work	Lit. [65]
325.0(5)	324.6	22(8)	19(8)	4.0	9(3)	-
569.5(3)	569.5	81(13)	100(23)	100	49(8)	96(3)
650.6(2)	650.2	47(4)	63(12)	28.9	31(3)	20(3)
667.5(4)	667.6	14(4)	19(6)	7.9	9(3)	-
759.7(2)	759.7	56(6)	82(16)	43.5	40(4)	33(3)
799.6(2)	798.4	7(4)	11(6)	11.5	5(3)	13(5)
848.4(3)	848.8	20(4)	31(8)	15.2	15(3)	-

The  $^{122}\text{Ag}$  beta-delayed gamma-ray spectrum is shown in Figure 4.60. Seven peaks were observed, and the deduced gamma-ray energies, peak areas, relative intensities, and absolute intensities are displayed in Table 4.30. Coincidence relationships between the observed  $^{122}\text{Ag}$  delayed gamma rays were also investigated. The  $^{122}\text{Ag}$  fragment- $\beta\gamma\gamma$  coincidence spectra that were obtained in this work are shown in Figure 4.61.

The fitted  $^{122}\text{Ag}$  beta-decay curve is shown in Figure 4.62. The half-life from the present work [0.39(2) s] and the values reported by Shih *et al.* and Fogelberg *et al.* [66], 0.48(8) s and 1.5(5) s, respectively, are included in the inset. The presence of

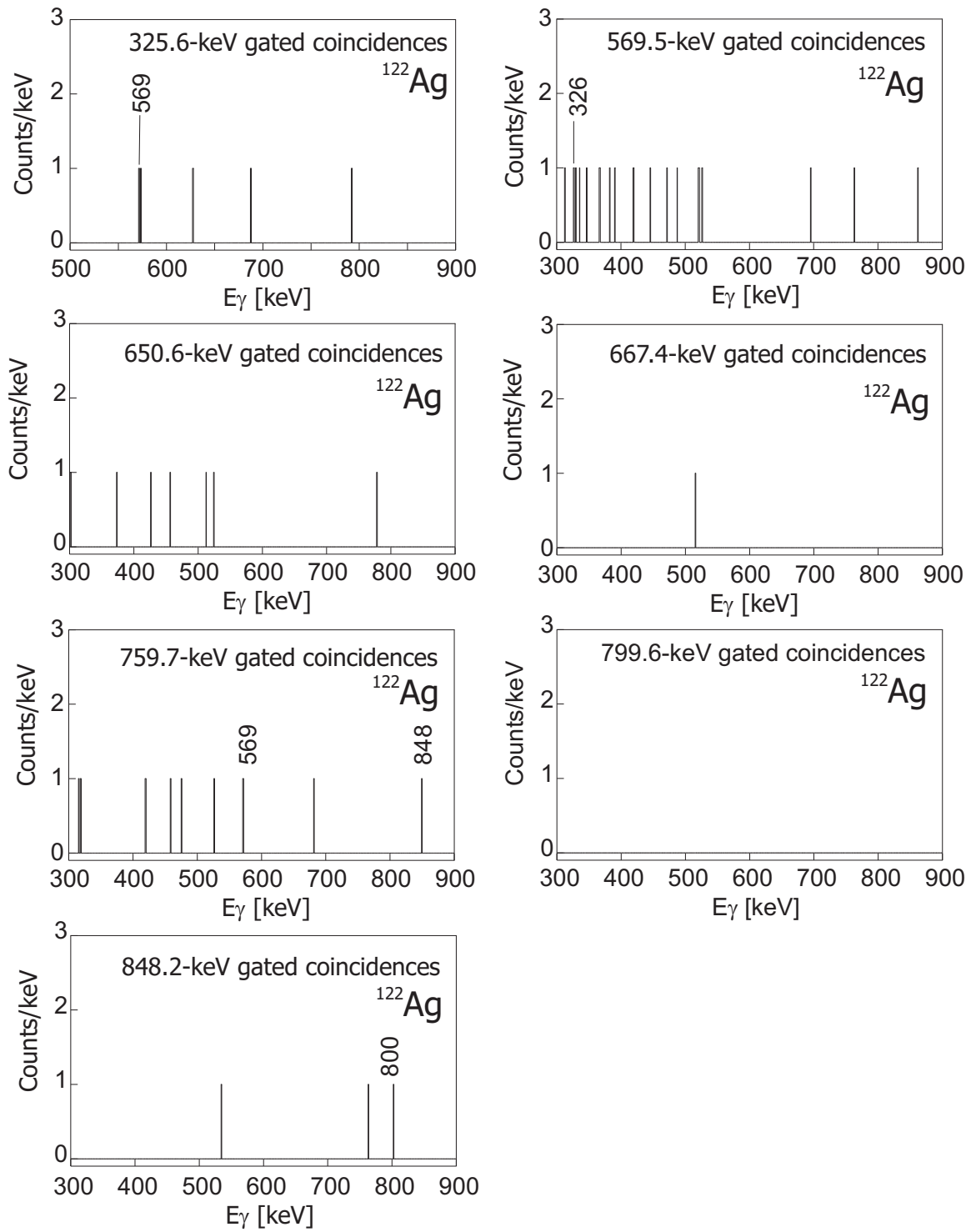


Figure 4.61: Fragment- $\beta\gamma\gamma$  coincidence spectra for the decay of  $^{122}\text{Ag}$ .

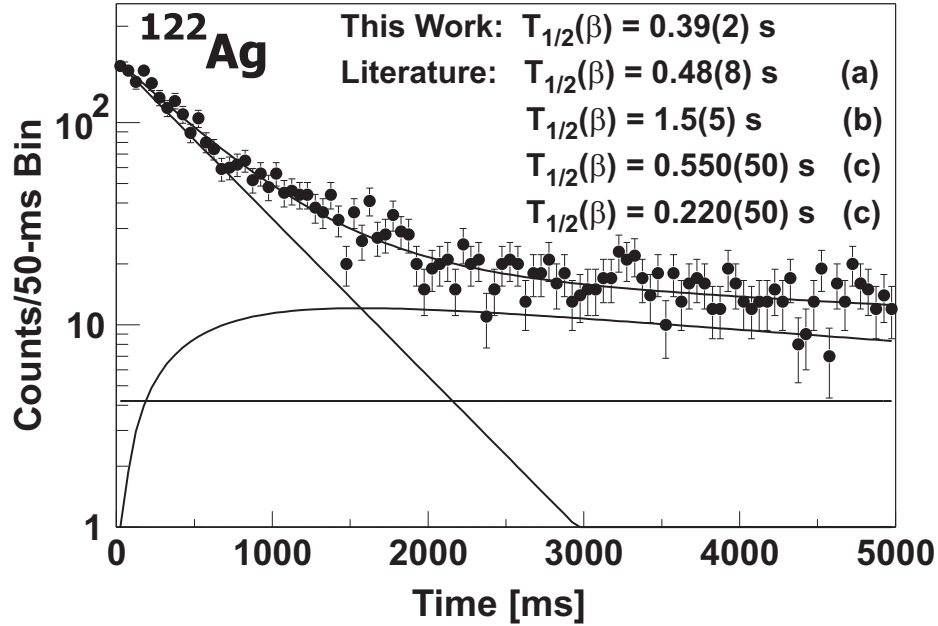


Figure 4.62: The fitted  $^{122}\text{Ag}$  beta-decay curve. The deduced half-life value and the literature values (a) Ref. [67], (b) Ref. [66], and (c) Ref. [24] are given in the inset. The values from Ref. [24] are for two different beta-decaying states.

a second beta-decaying state has been reported by Kratz *et al.* [24]. The measured half-life values of the two beta-decaying states [0.550(50) s and 0.200(50) s] are also provided in the inset.

Kratz *et al.* used laser resonance ionization to physically isolate two  $^{122}\text{Ag}$  isomers. In the present work it was not possible to separate these isomers. In order to differentiate the two beta-feeding states, gamma-gated half-lives were also deduced in the present work. The  $^{122}\text{Ag}$  gamma-gated decay curves are shown in Figure 4.63. The gamma-gated half-lives ranged in value between 0.29 s and 0.8 s. The sum of the individual curves was also fitted and yielded a half-life value of 0.38(2) s.

Fogelberg *et al.* [66] reported the observation of 1.5-second  $^{122}\text{Ag}$  beta decay, and Shih *et al.* [67] later identified 0.48-second  $^{122}\text{Ag}$  beta decay. The most extensive beta-decay scheme for  $^{122}\text{Ag}$ , without distinction between 0.48- and 1.5-second activity, was reported by Zamfir *et al.* [64]. Kratz *et al.* [24] have clearly identified the existence of two beta-decaying states in  $^{122}\text{Ag}$  by means of laser resonance ionization. Thus, at a minimum, two beta-decaying isomers have been observed in  $^{122}\text{Ag}$ , but the 1.5-s

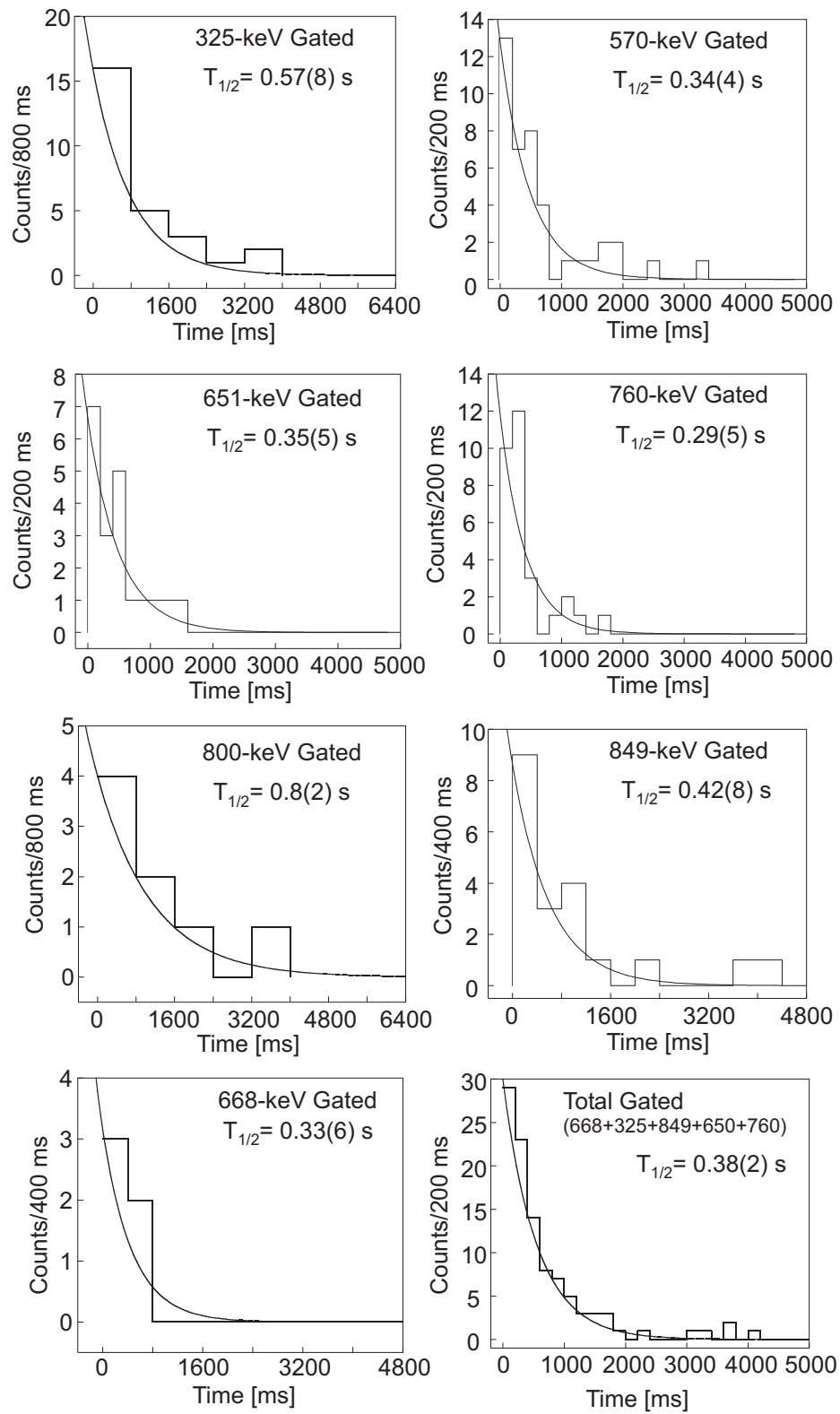


Figure 4.63: Gamma-ray gated  $^{122}\text{Ag}$  decay curves. The total gated decay curve is the sum of the individually gated decay curves.

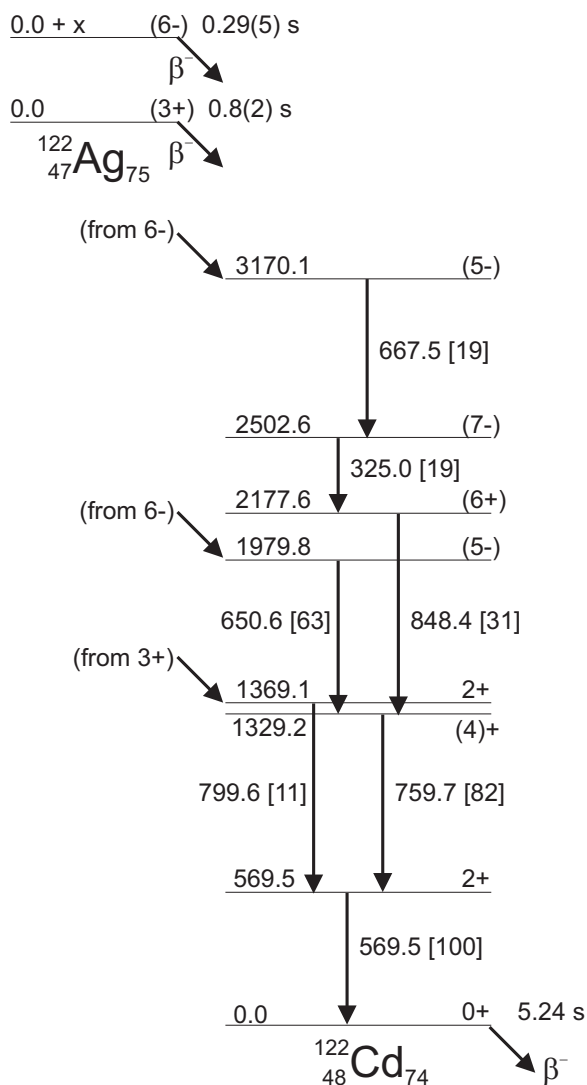


Figure 4.64: Partial decay scheme for  $^{122}\text{Ag}$  based on the present work. The level ordering and spin assignments are based on Refs. [57, 64]. The quoted energies are in keV.

activity seen by Fogelberg could be a third isomer in this nuclide. The beta-decay schemes of Shih and Kratz are given in Figure 4.65(a) and (b), respectively. The  $^{122}\text{Ag}$  beta-decay scheme based on the present work but using the level ordering of Ref. [64], is shown in Figure 4.64. The spin assignments were obtained from Refs. [57, 64].

Zamfir *et al.* reported 24 gamma transitions in the  $^{122}\text{Ag}$  decay. Seven of the strongest of these gamma rays were observed in the present work (see Table 4.30). The 570-keV gamma ray was the most intense, in agreement with the previous observations. The 760-keV gamma ray was coincident with the 849-keV and 570-keV

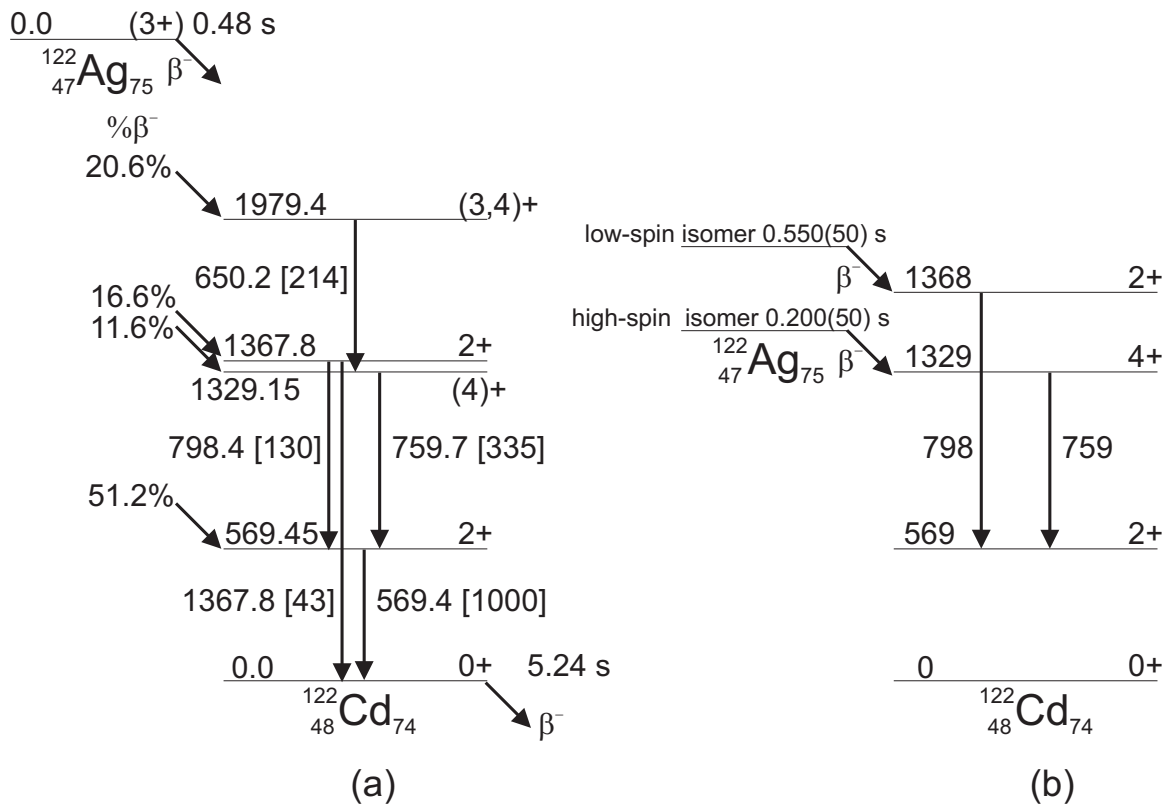


Figure 4.65: (a) Beta-decay feeding of levels in  $^{122}\text{Cd}$  deduced by Shih *et al.* [67]. (b) Beta-decay feeding of levels in  $^{122}\text{Cd}$  based on laser-resonance spectroscopy [24]. The quoted energies are in keV, and relative intensities are indicated in brackets.

gamma rays. The other expected coincidences were not observed due to the relatively low gamma-ray statistics.

A small degree of scatter is noted in the gamma-gated half-lives deduced presently, yet all are consistent with the  $\sim 0.5$  s literature values. The beta feeding deduced by Kratz [24], as shown in Figure 4.65, indicates that the 760-keV gamma ray is coincident with beta decay from the high-spin isomer in  $^{122}\text{Ag}$ . Our half-life value of 0.29(5) s for this transition is in agreement with the Kratz value of 0.200(50) s for the high-spin isomer. Based on the proposed beta-feeding, a half-life value of 0.29(5) s is adopted for the high-spin isomer, and the 0.8(2) s half-life obtained by gating on the 800-keV transition is adopted as the half-life of the low-spin isomer.

The distribution of  $^{122}\text{Ag}$  beta-decay strength, as deduced by Shih *et al.*, is given in Figure 4.65(a). These authors proposed that one-half of the beta transitions feed the first excited  $2^+$  state, and the rest is distributed amongst the next three excited states ( $4^+$ ,  $2_1^+$ , and  $5^-$ ). Shih *et al.* concluded that beta decay occurred from only one state in the parent. This conclusion is now known to be incorrect, since they observed both the 760- and 800-keV gamma rays. Zamfir *et al.* observed beta feeding to levels as high as 3170 keV but were not capable of discriminating between the two assumed beta-feeding states. Also, these authors did not report any beta-decay branching ratios. In the present work, three levels— $2_2^+$ ,  $5_1^-$ , and  $5_2^-$ —in  $^{122}\text{Cd}$  are clearly fed by beta decay since they are populated but not fed by gamma transitions. As shown in Figure 4.64, feeding of the levels at 1980 and 3170 keV is speculatively attributed to beta decay from the high-spin isomer. Feeding of the level at 1370 keV is known to occur from the low-spin isomer in  $^{122}\text{Ag}$  [24].

In the separate investigations by Shih and Zamfir, the  $^{122}\text{Ag}$  activity was obtained from mass-separated  $^{235}\text{U}$  fission products, and both used the TRISTAN mass separator [68,69]. Also, both investigations used 3-second counting periods on movable-tape apparatus. Given the similarity of these two experiments, one would expect the population of beta-decaying states in the parent nuclide would have been similar. The

present work used a different method of production, and thus it is possible that the beta-decaying states of  $^{122}\text{Ag}$  were populated with different relative yields. Relative to the 570- and 800-keV transitions, the 650- and 760-keV transitions each appeared with approximately twice the reported intensity. This discrepancy suggests that the 1980 and 3170 keV levels were more strongly populated by beta decay than was previously observed. Such a scenario is possible if the high-spin isomer were more heavily populated by projectile fragmentation than by fission.

The structure of  $^{122}\text{Cd}$  is quite similar to that of the other even-even Cd isotopes, such as  $^{126}\text{Cd}$  described in Section 4.2.5. The  $2_1^+$  and  $4^+$  excited states of the daughter are attributed to two-phonon collective vibrations [67]. The negative-parity levels arise from both proton and neutron configurations. The  $5^-$  levels are produced by both the  $\pi(g_{9/2}^1 p_{1/2}^1)$  configuration and the  $\nu(h_{11/2}^1 d_{3/2}^1)$  configuration [57]. The  $7^-$  level can also be produced by the  $\nu(h_{11/2}^1 d_{3/2}^1)$  configuration [57]. In the decay scheme of Figure 4.64, the  $3^+$  isomer in  $^{122}\text{Ag}$  is shown as the ground state based on the systematics of odd-odd Ag isotopes, but this assignment is not certain. The  $J^\pi$  of the high-spin isomer is not known, but could be  $6^-$  as in  $^{120}\text{Ag}$ , which would support the feeding of the  $5^-$  levels.

In summary, beta-decaying isomers are known in odd-odd Ag isotopes up to  $^{120}\text{Ag}$ . These nuclides, which are three proton holes inside of Sn, show structural systematics that are similar to the one proton-hole, odd-odd In isotopes. Kratz *et al.* [24] has demonstrated that the pattern of beta-decaying odd-odd Ag isotopes extends to  $^{122}\text{Ag}$ . The distribution of beta feeding into  $^{122}\text{Cd}$ , deduced in the present work, supports this observation.

### 4.3.3 $^{121}\text{Pd}$

Beta-decay data were obtained for  $^{121}\text{Pd}$ , which was identified within the Pd-A+1 PID region. The number of counts within the Pd-A+1 gate (total, implant-correlated, and decay-correlated) were given in Table 4.27. Approximately 44% of the Pd-A+1 frag-

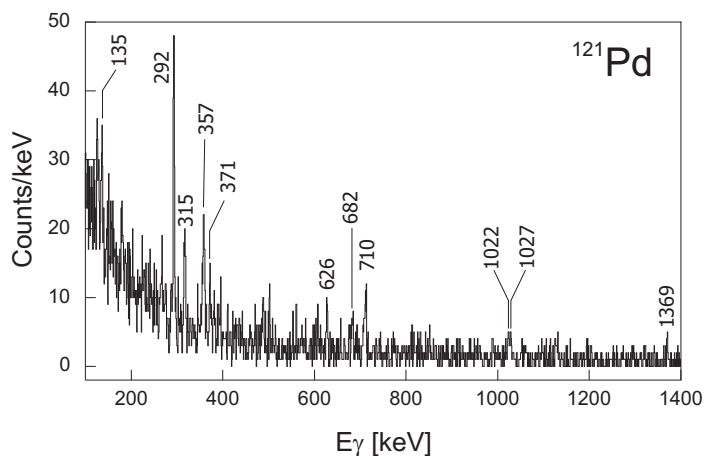


Figure 4.66: Beta-delayed gamma-ray spectrum for  $^{121}\text{Pd}$ .

ments incident upon PIN01a were implanted in the DSSD, and 41% of the implanted Pd-A+1 fragments were correlated with beta-decay events.

The  $^{121}\text{Pd}$  beta-delayed spectrum is shown in Figure 4.66. Twenty peaks were observed, and the assigned peak energies, peak areas, and relative intensities are displayed in Table 4.31. Coincidence relationships between the observed  $^{121}\text{Pd}$  delayed gamma rays were also investigated. The  $^{121}\text{Pd}$  fragment- $\beta\gamma\gamma$  coincidence spectra that were obtained in this work are shown in Figure 4.67.

Eight gamma rays are tentatively assigned to the decay of  $^{121}\text{Pd}$ . Six gamma transitions following the beta decay of the daughter nuclide  $^{121}\text{Ag}$  were observed. Five  $^{118}\text{Pd}$  beta-delayed gamma rays were also observed, revealing that a portion of the  $^{118}\text{Pd}^{45+}$  contaminant ions were implanted in the DSSD. Finally, one gamma ray from the decay of  $^{118}\text{Ag}$  (the  $^{118}\text{Pd}$  beta-decay daughter) was observed.

The fitted  $^{121}\text{Pd}$  beta-decay curve is shown in Figure 4.68. Gamma-gated half-lives were also deduced in the present work. The fitted curves are shown in Figure 4.69. The gamma-gated half-lives ranged in value between 0.26 s and 0.5 s, and the distribution of half-life values could be due to the presence of isomer(s). The sum of the individual curves was also fitted and yielded a half-life value of 0.33(2) s. A value of 0.248(5) s for the half-life of  $^{121}\text{Pd}$  was adopted in this work from the fragment- $\beta$  gated decay curve based on better statistics compared to the fragment- $\beta\gamma$  gated decay curves.

Table 4.31: The  $^{121}\text{Pd}$  beta-delayed gamma ray energies, integrated peak areas and relative intensities (normalized to 100 for the 709-keV  $\gamma$  ray). \*The bulk of the intensity of the 292-keV peak is attributed to  $^{121}\text{Pd}$ ; however, a small component is likely to come from the 293.47-keV  $^{121}\text{Ag}$  delayed gamma ray, which has only 7 units of intensity relative to 100 units of the 315-keV gamma ray.

Peak Energy [keV]	Fitted Peak Area	Relative Intensity	
		This Work	Literature
124.8(3) $^{118}\text{Pd}$	103(22)	-	-
134.5(5)	57(24)	53(27)	-
145.5(5) $^{118}\text{Pd}$	13(10)	-	-
150.3(5) $^{118}\text{Pd}$	18(12)	-	-
223.7(3) $^{118}\text{Pd}$	25(7)	-	-
292.0(1)*	103(7)	-	-
314.9(3) $^{121}\text{Ag}$	102(22)	-	-
351.3(7) $^{121}\text{Ag}$	38(11)	-	-
357.4(6)	55(31)	81(51)	-
362.8(13) $^{121}\text{Ag}$	16(9)	-	-
370.9(4) $^{121}\text{Ag}$	66(13)	-	-
379.8(9) $^{118}\text{Pd}$	21(10)	-	-
486.9(5) $^{118}\text{Ag}$	29(10)	-	-
500.9(4) $^{121}\text{Ag}$	25(9)	-	-
625.9(4)	32(9)	68(27)	-
681.5(5)	25(17)	56(41)	-
709.2(6)	44(12)	100(39)	-
1022.5(5)	14(4)	39(16)	-
1026.7(5)	14(3)	40(14)	-
1368.8(3)	9(3)	30(13)	-

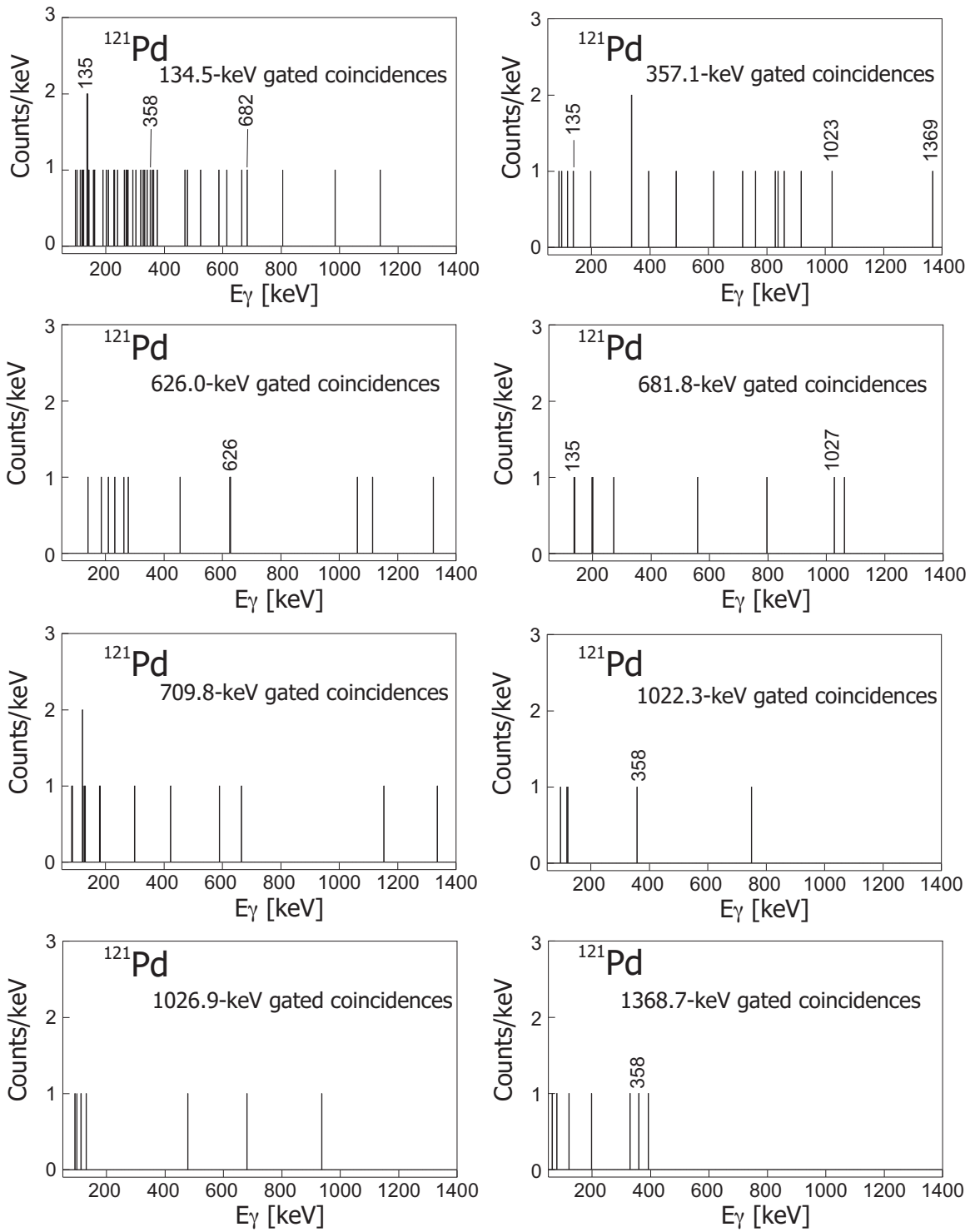


Figure 4.67: Fragment- $\beta\gamma$  coincidence spectra for the decay of  $^{121}\text{Pd}$ .

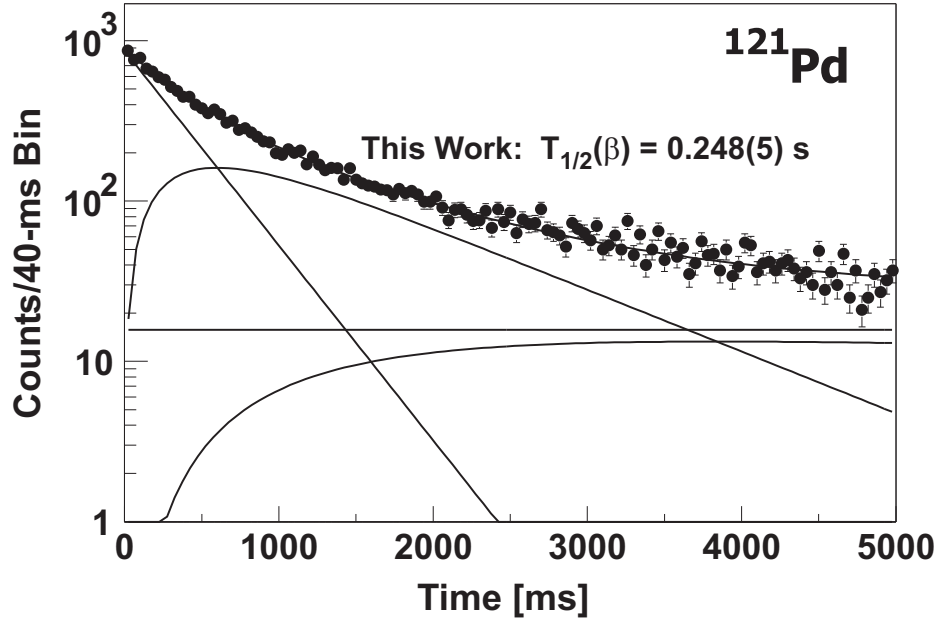


Figure 4.68: The fitted  $^{121}\text{Pd}$  beta-decay curve. The deduced half-life value is given in the inset. The daughter ( $^{121}\text{Ag}$ ) half-life was fixed at 0.78 s.

The present work is the first report of the new nuclide  $^{121}\text{Pd}$ . Based on the systematics of lighter odd- $A$  Pd isotopes, it is speculated that the beta decay occurs out of a  $7/2^+$  ground state into  $5/2^+$ ,  $7/2^+$  or  $9/2^+$  levels in  $^{121}\text{Ag}$ . Fragment- $\beta\gamma\gamma$  coincidences were not sufficient to determine the relationships of the individual gamma rays. A decay scheme for  $^{121}\text{Pd}$  has not been proposed in the present work.

#### 4.3.4 $^{122}\text{Pd}$

Beta-decay data were obtained for  $^{122}\text{Pd}$ , which was identified within the Pd-A+2 PID region. The number of counts within the Pd-A+2 gate (total, implant-correlated, and decay-correlated) were given in Table 4.27. Approximately 14% of the Pd-A+2 fragments incident upon PIN01a were implanted in the DSSD, and roughly one-half (45%) of the implanted Pd-A+2 fragments were correlated with beta-decay events.

The  $^{122}\text{Pd}$  beta-delayed gamma-ray spectrum is shown in Figure 4.70. Four peaks were observed, and the deduced gamma-ray energies, peak areas, and relative intensities are displayed in Table 4.32. Coincidence relationships between the observed  $^{122}\text{Pd}$  delayed gamma rays were also investigated. No coincidences were seen in the  $^{122}\text{Pd}$

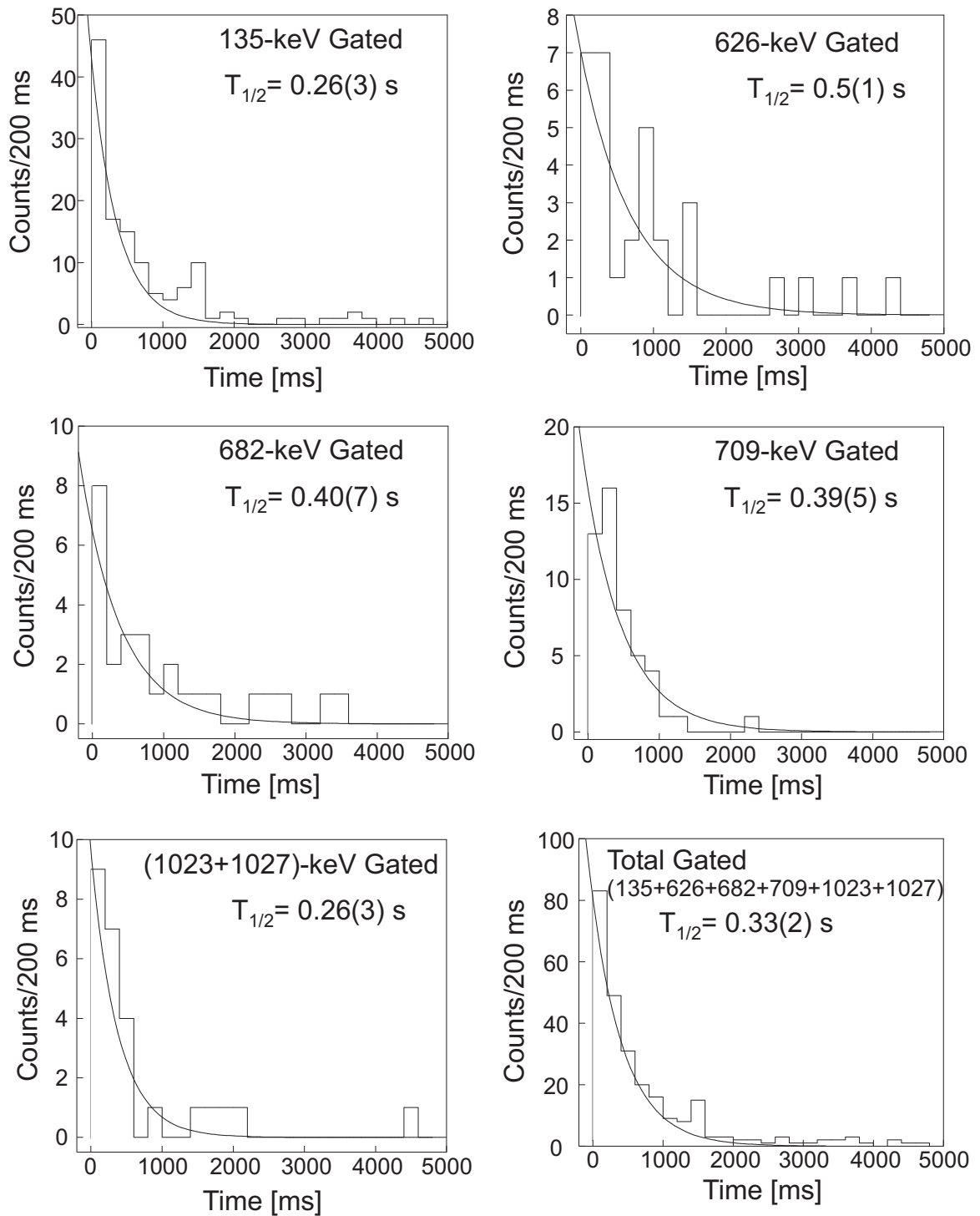


Figure 4.69: Gamma-ray gated  $^{121}\text{Pd}$  decay curves. The total gated decay curve is the sum of the individually gated decay curves.

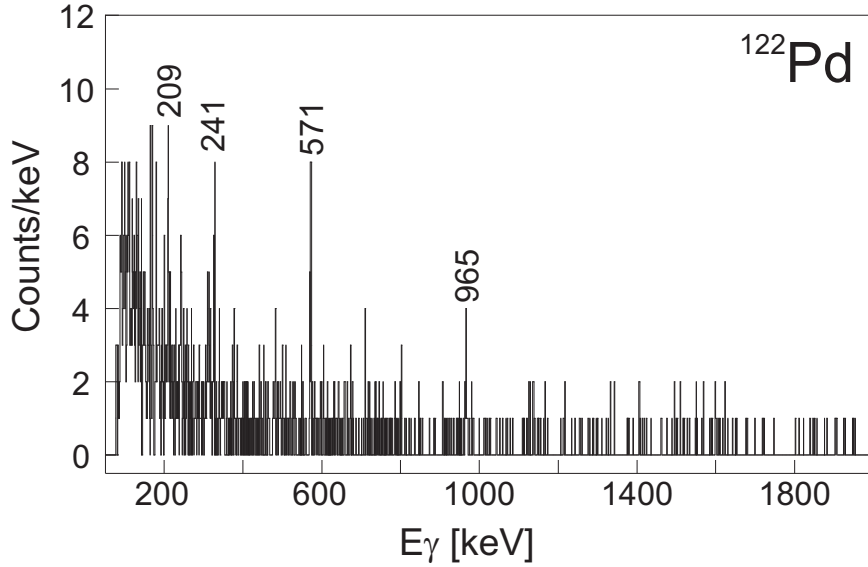


Figure 4.70: Beta-delayed gamma-ray spectrum for  $^{122}\text{Pd}$ .

Table 4.32: The  $^{122}\text{Pd}$  beta-delayed gamma-ray energies, integrated peak areas and relative intensities (normalized to 100 for the 209-keV  $\gamma$  ray). The italicized relative intensity is normalized to 100 for the  $^{122}\text{Ag}$  570-keV  $\gamma$  ray.

Peak Energy [keV]	Fitted Peak Area	Relative Intensity	
		This Work	Literature [67]
208.8(3)	18(5)	100(39)	-
241.2(3)	13(4)	78(33)	-
570.7(2) $^{122}\text{Ag}$	22(5)	<i>100(32)</i>	100.0
964.8(2)	5(2)	71(35)	-

fragment- $\beta\gamma\gamma$  coincidence spectra, due to the low gamma-ray statistics.

The fitted  $^{122}\text{Pd}$  beta-decay curve is shown in Figure 4.71. Gamma-gated half-lives were also deduced in the present work. The  $^{122}\text{Pd}$  gamma-gated decay curves are shown in Figure 4.72. The gamma-gated half-lives ranged in value between 0.23(2) s and 0.40(3) s, and it is possible that more than one beta-decaying state was observed. The sum of the individual curves was also fitted and yielded a half-life value of 0.34(2) s. A value of 0.17(1) s for the beta-decay half-life of  $^{122}\text{Pd}$  was adopted in this work from the fragment- $\beta$  gated decay curve, which had better statistics than the fragment- $\beta\gamma$  gated curves.

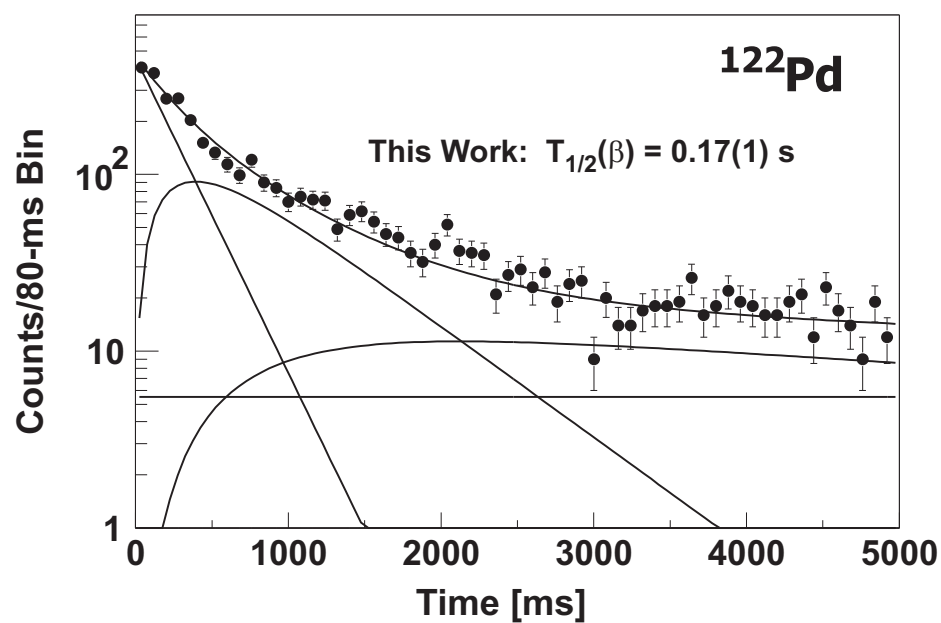


Figure 4.71: The fitted  $^{122}\text{Pd}$  beta-decay curve. The deduced half-life value is given in the inset. The daughter ( $^{122}\text{Ag}$ ) half-life was fixed at 0.5 s.

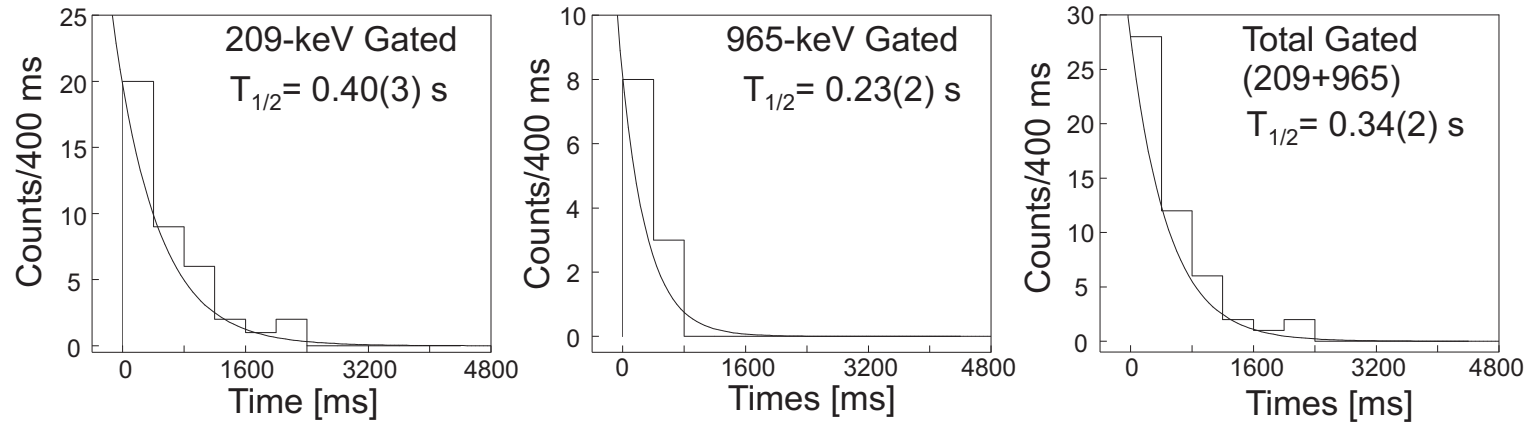


Figure 4.72: Gamma-ray gated  $^{122}\text{Pd}$  decay curves. The total gated decay curve is the sum of the individually gated decay curves.

The present work is the first report of the new nuclide  $^{122}\text{Pd}$ . Three gamma rays are tentatively assigned to the decay of  $^{122}\text{Pd}$ . One gamma transition (570 keV) following the beta decay of the daughter nuclide  $^{122}\text{Ag}$  was observed. The  $^{122}\text{Pd}$  beta-decay scheme is shown in Figure 4.64 and is based on similar structures in odd-odd Ag and In isotopes. The 209- and 241-keV transitions were ordered by intensity. As the arrows in the figure indicate, direct beta feeding into the two  $1^+$  levels is expected.

The appearance of the 570-keV gamma ray from the beta-decay daughter  $^{122}\text{Ag}$  provides a clue regarding the excited states populated in the beta decay of  $^{122}\text{Pd}$ . Based on the laser-resonance work of Kratz *et al.* [24], the  $4_1^+$  level in  $^{122}\text{Cd}$  is known to be fed by the high-spin beta-decaying isomer in  $^{122}\text{Ag}$ , and the  $2_2^+$  level is known to be fed by the low-spin isomer in  $^{122}\text{Ag}$ . These two levels are depopulated by 760- and 800-keV gamma rays, respectively, as shown in Figure 4.64 on page 150. The only daughter gamma ray observed in the  $^{122}\text{Pd}$  beta-delayed gamma spectrum is the 570-keV transition. In the  $^{122}\text{Ag}$  beta-delayed gamma-ray spectrum, which contained transitions fed by both the low-spin and high-spin isomers, the ratio of the intensities of the 760-keV transition and 570-keV transition was 1:1. The ratio of the 800-keV to 570-keV transition was 1:10. If the high-spin isomeric state of  $^{122}\text{Ag}$  were populated by the beta decay of  $^{122}\text{Pd}$ , then the 760-keV gamma ray should also be seen with intensity comparable to that of the 570-keV gamma ray. The fact that this gamma ray was not observed suggests that the levels of  $^{122}\text{Ag}$ , which are populated by beta feeding, bypass the high-spin isomer and decay into the  $3^+$  level (see Fig. 4.73).

In Section 4.3.2, several features of the odd-odd nuclide  $^{122}\text{Ag}$  were described, including the evidence for a low-lying isomeric state in this nuclide. Based on the first observation of the beta decay of  $^{122}\text{Pd}$ , it appears that this decay probably does not populate the high-spin isomer of  $^{122}\text{Ag}$ . A discussion of the importance of these new results in terms of the systematics of neutron-rich Ag isotopes will be provided in Chapter 4.

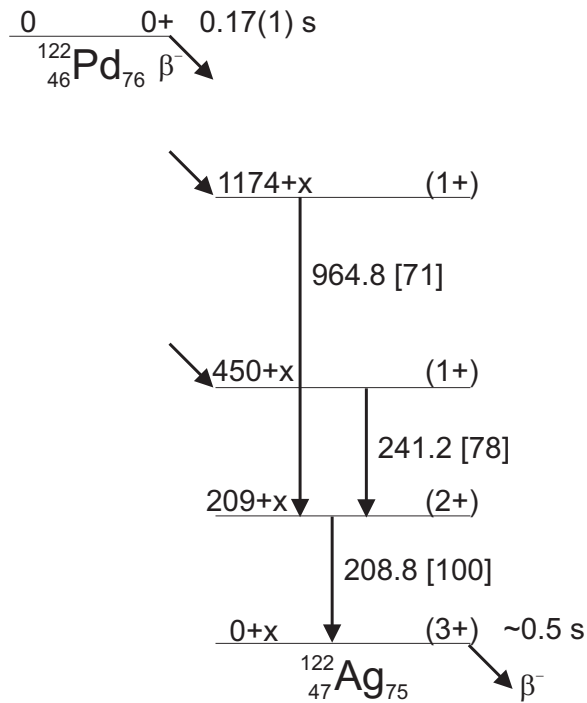


Figure 4.73: Decay scheme for the  $^{122}\text{Pd}$ . The quoted energies are in keV, and the relative intensities are in brackets.

### 4.3.5 $^{119}\text{Rh}$

Beta-decay data were obtained for  $^{119}\text{Rh}$ , which was identified within the Rh-A+1 PID region. The number of counts within the Rh-A+1 gate (total, implant-correlated, and decay-correlated) were given in Table 4.27. Approximately 61% of the Rh-A+1 fragments incident upon PIN01a were implanted in the DSSD, and 44% of the implanted Rh-A+1 fragments were correlated with beta-decay events.

The  $^{119}\text{Rh}$  beta-delayed gamma-ray spectrum is shown in Figure 4.74. Nine peaks were observed, and the deduced gamma-ray energies, peak areas, and relative intensities are displayed in Table 4.33. Coincidence relationships between the observed  $^{119}\text{Rh}$  delayed gamma rays were also investigated. The  $^{119}\text{Rh}$  fragment- $\beta\gamma\gamma$  coincidence spectra that were obtained in this work are shown in Figure 4.75.

Five gamma rays are tentatively assigned to the decay of  $^{119}\text{Rh}$ . Two gamma transitions following the beta decay of the daughter nuclide  $^{119}\text{Pd}$  were observed. Two  $^{116}\text{Rh}$  beta-delayed gamma rays were also observed, revealing that a portion of

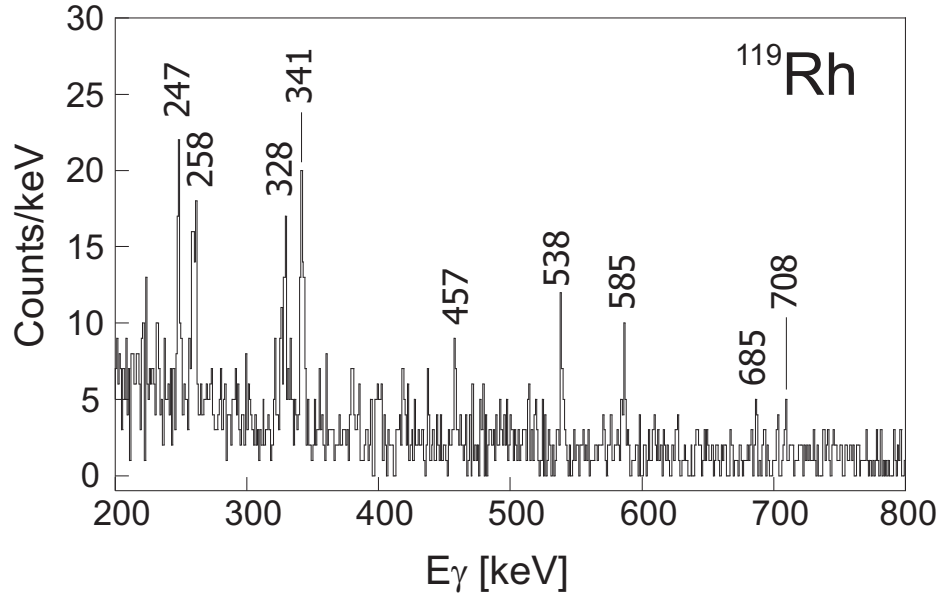


Figure 4.74: Beta-delayed gamma-ray spectrum for  $^{119}\text{Rh}$ .

Table 4.33: The  $^{119}\text{Rh}$  beta-delayed gamma-ray energies, integrated peak areas and relative intensities (normalized to 100 for the 247-keV  $\gamma$  ray).

Peak Energy [keV]	Fitted Peak Area	Relative Intensity	
		This Work	Literature
246.6(2)	38(8)	100(30)	-
258.2(4) $^{119}\text{Pd}$	72(19)	-	-
327.6(2) $^{119}\text{Pd}$	25(8)	-	-
340.5(2) $^{116}\text{Rh}$	59(10)	-	-
456.7(3)	19(5)	74(25)	-
537.4(3) $^{116}\text{Rh}$	33(7)	-	-
584.8(3)	19(5)	87(29)	-
685.3(3)	9(4)	45(22)	-
707.4(5)	10(4)	51(23)	-

the  $^{116}\text{Rh}^{44+}$  contaminant ions were implanted in the DSSD.

The  $^{119}\text{Rh}$  beta-decay curve is shown in Figure 4.76. Gamma-gated half-lives were also deduced in the present work. The fitted curves are shown in Figure 4.77. The the gamma-gated half-lives ranged in value between 0.24 s and 0.8 s. The sum of the individual curves was also fitted and yielded a half-life value of 0.35(2) s. The range of gamma-gated half-lives suggests that the presence of more than one beta-decaying state in  $^{119}\text{Rh}$  cannot be ruled out. Based on much better statistics, the fragment- $\beta$  gated half-life value of 0.19(1) s has been adopted as the  $^{119}\text{Rh}$  half-life in the present

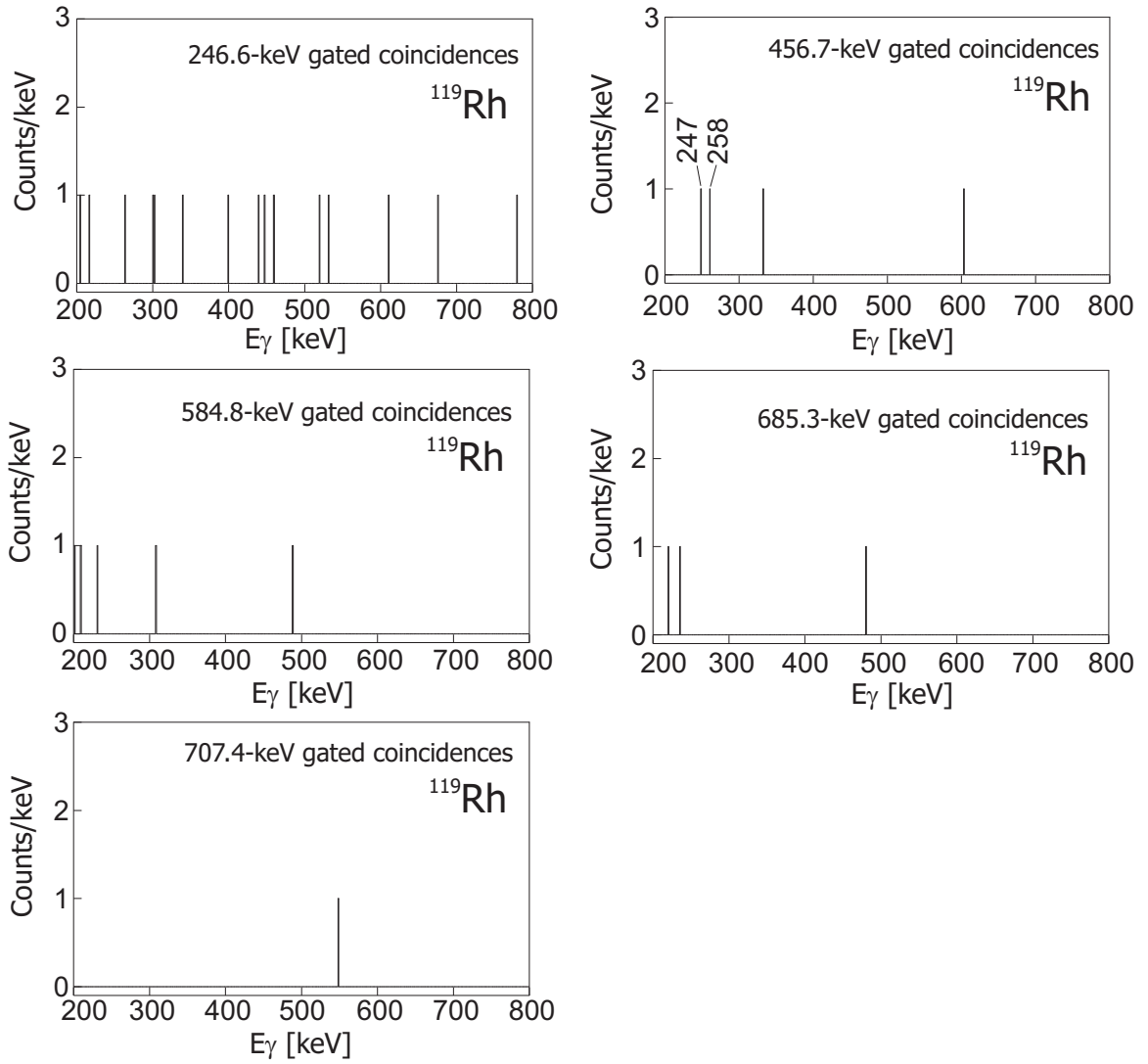


Figure 4.75: Fragment- $\beta\gamma\gamma$  coincidence spectra for the decay of  $^{119}\text{Rh}$ .

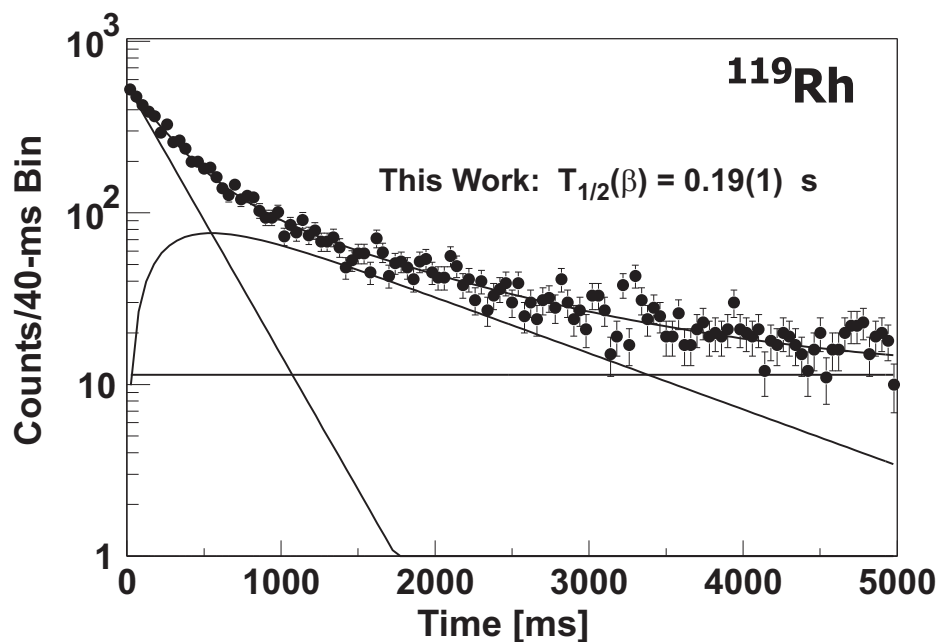


Figure 4.76: The fitted  $^{119}\text{Rh}$  beta-decay curve. The deduced half-life value is given in the inset. The daughter ( $^{119}\text{Pd}$ ) half-life was fixed at 0.92 s.

work.

The present work is the first report of the new nuclide  $^{119}\text{Rh}$ . Based on the systematics of lighter odd- $A$  Rh isotopes, it is speculated that the beta decay occurs out of a  $7/2^+$  ground state into  $5/2^+$ ,  $7/2^+$  or  $9/2^+$  levels in  $^{119}\text{Pd}$ . Fragment- $\beta\gamma\gamma$  coincidences were not sufficient to determine the relationships of the individual gamma rays. A decay scheme for  $^{119}\text{Rh}$  has not been proposed in the present work.

#### 4.3.6 $^{120}\text{Rh}$

Beta-decay data were obtained for  $^{120}\text{Rh}$ , which was identified within the Rh-A+2 PID region. The number of counts within the Rh-A+2 gate (total, implant-correlated, and decay-correlated) were given in Table 4.27. Approximately 21% of the Rh-A+2 fragments incident upon PIN01a were implanted in the DSSD, and 48% of the implanted Rh-A+2 fragments were correlated with beta-decay events.

The  $^{120}\text{Rh}$  beta-delayed gamma-ray spectrum is shown in Figure 4.79. Five peaks were observed, and the deduced gamma-ray energies, peak areas, and relative inten-

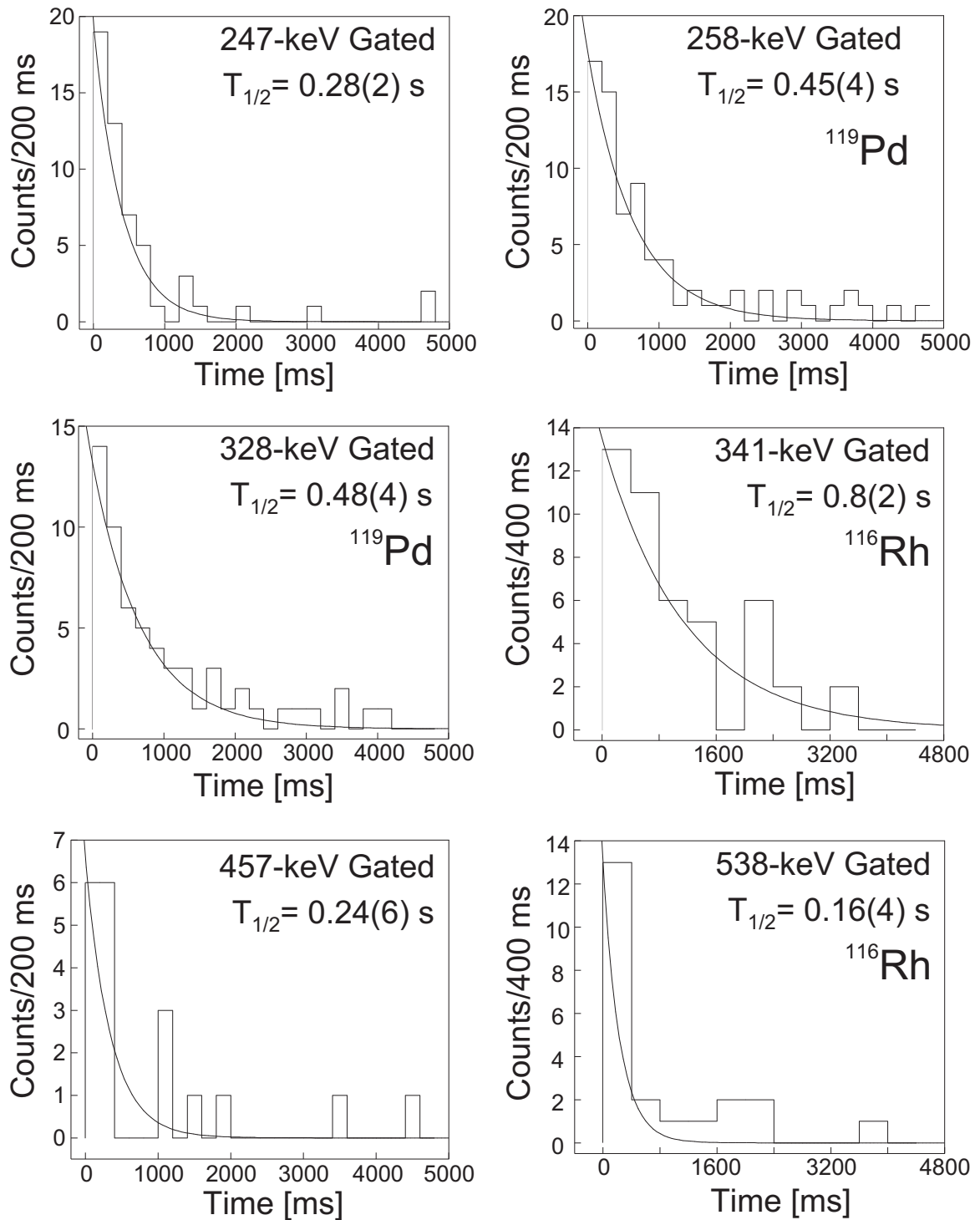


Figure 4.77: Gamma-ray gated  $^{119}\text{Rh}$  decay curves. The total gated decay curve is the sum of the individually gated decay curves, as denoted in the inset.

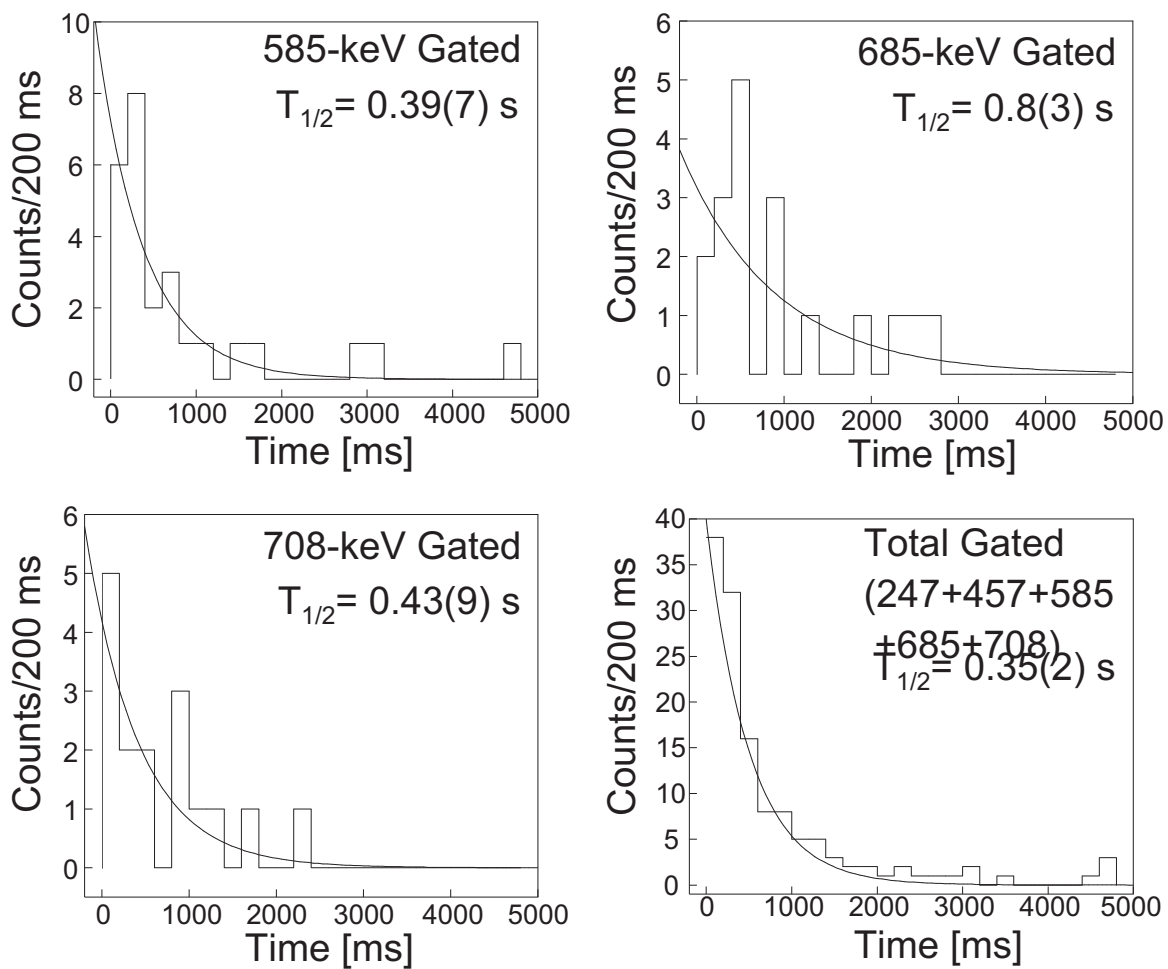


Figure 4.78: Gamma-ray gated  $^{119}\text{Rh}$  decay curves. The total gated decay curve is the sum of the individually gated decay curves, as denoted in the inset.

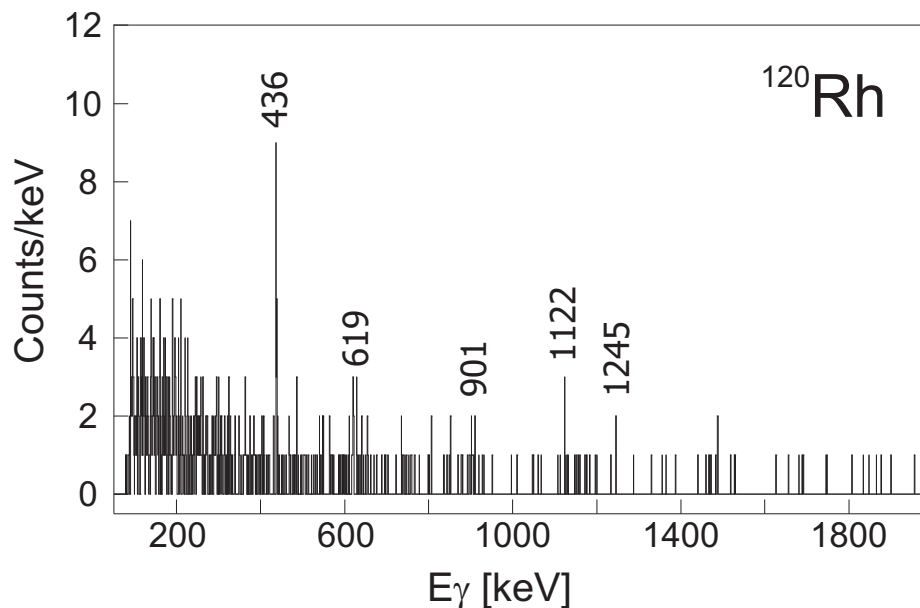


Figure 4.79: Beta-delayed gamma-ray spectrum for  $^{120}\text{Rh}$ .

Table 4.34: The  $^{120}\text{Rh}$  beta-delayed gamma-ray energies, integrated peak areas and relative intensities (normalized to 100 for the 436-keV  $\gamma$  ray).

Peak Energy [keV]	Fitted Peak Area	Relative Intensity
435.4(2)	13(4)	100(44)
618.6(2)	10(1)	96(31)
900.4(2)	3(2)	36(26)
1122.2(1)	2(1)	27(16)
1244.4(1)	3(1)	43(20)

sities are displayed in Table 4.34. Due to an improved gamma-energy calibration, the gamma-ray energies reported below differ slightly from the values that were published in Walters *et al.* [70], based on the same experimental data.

Five gamma rays are tentatively assigned to the decay of  $^{120}\text{Rh}$ . Coincidence relationships between the observed  $^{120}\text{Rh}$  delayed gamma rays were also investigated. No coincidences were observed due to the low statistics.

The fitted  $^{120}\text{Rh}$  beta-decay curve is shown in Figure 4.80. Gamma-gated half-lives were also deduced in the present work. The fitted curves are shown in Figure 4.81. Only the 436-keV gated decay curve had sufficient counts to determine a half-life. The deduced half-life is 0.16(2) seconds; the sum of the individual curves was also

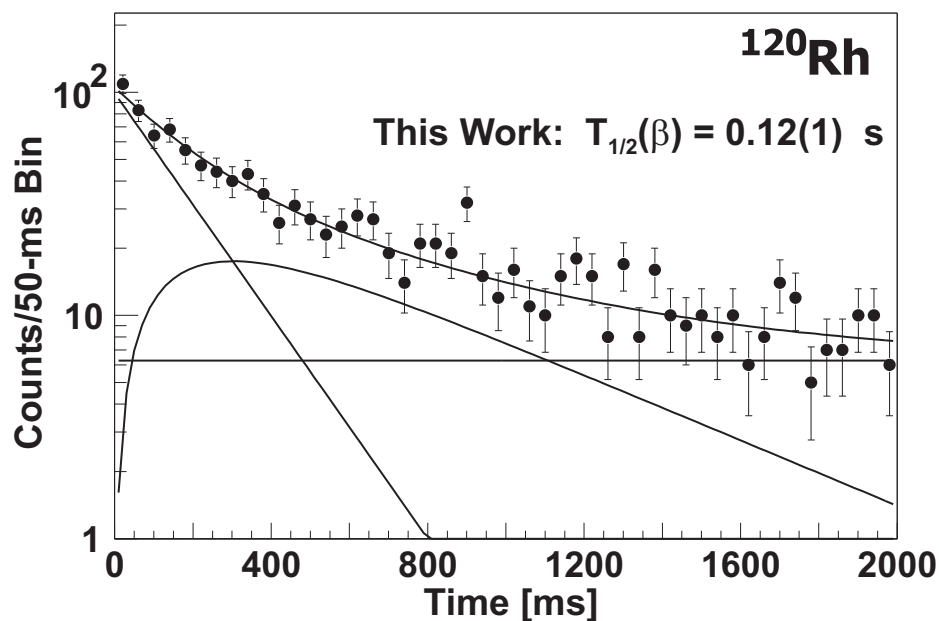


Figure 4.80: The fitted  $^{120}\text{Rh}$  beta-decay curve. The deduced half-life value is given in the inset.

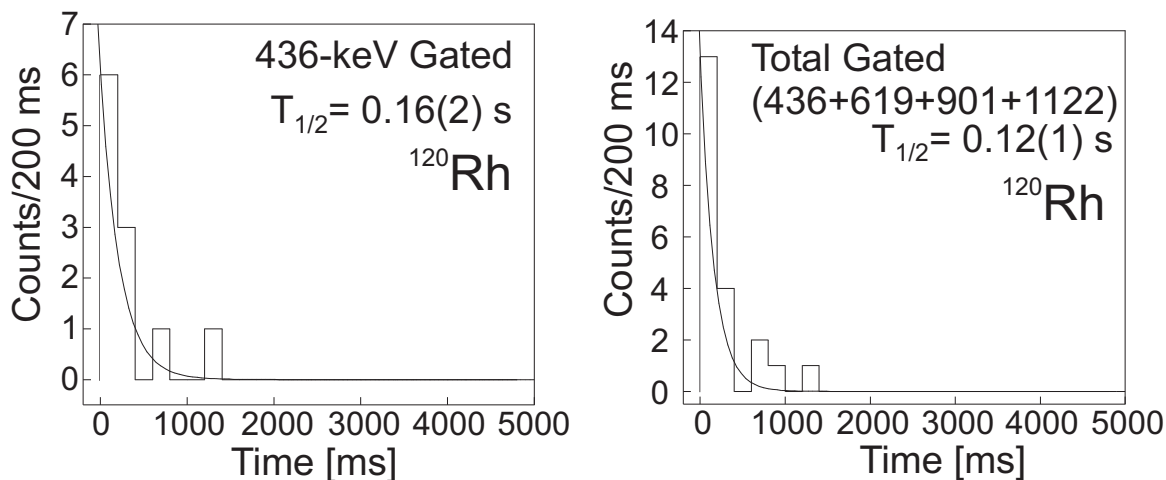


Figure 4.81: Gamma-ray gated  $^{120}\text{Rh}$  decay curves. The total gated decay curve is the sum of the individually gated decay curves.

fitted and yielded a half-life value of  $0.12(1)$  s, in agreement with the value obtained from the total decay curve. The value of  $0.12(1)$  s is adopted in this work.

Prior to this work, no observation of  $^{120}\text{Rh}$  had been reported in the literature. Five gamma rays have been tentatively assigned to the decay of  $^{120}\text{Rh}$ . The most intense gamma ray, 436 keV, has been assigned the  $2_1^+ \rightarrow 0^+$  transition, and the next most intense gamma ray, 619 keV, has been attributed to the  $4_1^+ \rightarrow 2_1^+$  transition. The

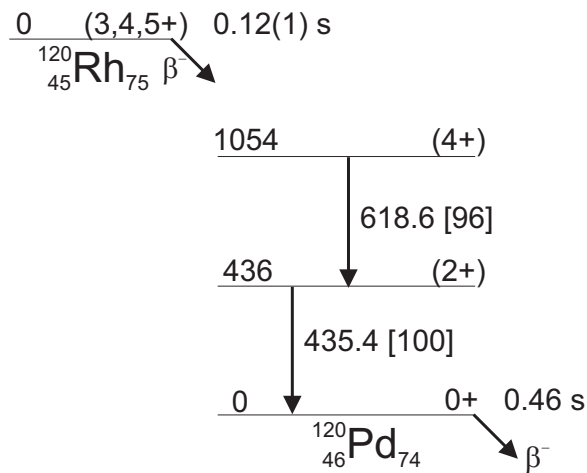


Figure 4.82: Decay scheme for the  ${}^{120}\text{Rh}$ . The quoted energies are in keV, and the relative intensities are indicated in brackets.

remaining three gamma rays have not been assigned. The proposed  ${}^{120}\text{Rh}$  beta-decay scheme is shown in Figure 4.82. Spin-parity assignments are based on the systematics of even-even nuclides. The nearly 100% relative intensity of the  $4_1^+ \rightarrow 2_1^+$  transition suggests that the  $4_1^+$  level is fed by beta decay more strongly than the  $2_1^+$  level. The spin-parity of the beta decaying level in  ${}^{120}\text{Rh}$ , as shown in Figure 4.82, is based on this assumption. The proposed energies of the  $2_1^+$  and  $4_1^+$  levels are well supported by theoretical calculations (430 and 1040 keV, respectively) made by Kim *et al.* [71] using the Interacting Boson Model-2 (IBM-2). A discussion of the importance of these new results for  ${}^{120}\text{Pd}$  in terms of the systematics of even-even Pd isotopes will be given in Chapter 4.

# Chapter 5

## Interpretation of Results

### 5.1 Shell Quenching Near $^{132}\text{Sn}$ ?

The present work, based on NSCL Experiment 01015, investigated the nuclear structure of several nuclides, from  $_{44}\text{Ru}$  to  $_{50}\text{Sn}$ , near  $N = 82$ . The quantum structures of these nuclides were studied using a combination of beta-gamma and isomer spectroscopies. The results of this work were presented in the previous chapter. The following sections will provide our interpretation of these results in the context of the  $N = 82$  shell closure. In particular, the new data for  $^{120}_{46}\text{Pd}$ ,  $^{123,125}_{47}\text{Ag}$ , and  $^{125-127}_{48}\text{Cd}$  reveal that the  $N = 82$  shell closure appears to be retained in these exotic nuclides below  $Z = 50$ .

Microscopically, neutron shell quenching is believed to arise from a combination of a weakening of the nucleon-nucleon potential at the nuclear surface and strong n-n and p-p pairing effects [57]. The monopole component of the p-n interaction is strongly involved in the shifting of single-particle energies of shell-model orbitals that not only gives rise to subshell gaps but also may reduce the well known major shell gaps [72]. Quenching of the  $N = 8, 20$  shells has been experimentally identified in some neutron-rich nuclides [1–3], but until very recently experimental access to exotic neutron-rich nuclides near the larger magic numbers  $N = 50, 82$  in nuclides

away from stability has been limited.

## 5.2 Systematics of Even-Even Pd Isotopes

The influence of a neutron shell closure, whether intact or weakened, is manifest in a number of nuclear structure observables, including the excitation energies of low-lying excited states. As described in Section 1.1.2, the excitation energies of  $2_1^+$  and  $4_1^+$  states in even-even nuclides in the vicinity of a neutron shell closure are expected to rise with increasing neutron number towards a maximum at the magic number.

Recent investigations of the structure of neutron-rich even-even  $_{46}\text{Pd}$  nuclides have shown a similarity with the comparable isotonic  $_{54}\text{Xe}$   $2_1^+$  energies over much of the known range of neutron numbers, including the expected rise in  $E(2_1^+)$  with increasing neutron number towards  $N = 82$ . Low-energy excited states in even-even  $_{46}\text{Pd}$  isotopes were studied theoretically by Kim *et al.* [71] using the IBM-2. The adjustable parameters of the modern IBM-2 calculation by Kim *et al.* were based on the microscopic mapping between the multinucleon and interacting boson systems [71]. The choice of the model space assumed regular  $Z = 50$  and  $N = 82$  closed shells. At the time of publication, predictions of low-energy excited state energies up to  $^{126}\text{Pd}_{80}$  were made, based on experimental values known only up to  $^{116}\text{Pd}_{70}$ . Subsequent study of the beta decay of  $^{118}\text{Rh}_{73}$  to levels of  $^{118}\text{Pd}_{72}$  revealed that the observed yrast energies up through the  $6^+$  level were within a few keV of the energies calculated by Kim *et al.* and were also within a few keV of the energies observed for isotonic  $^{126}\text{Xe}_{72}$  as shown in Table 5.1. The structure of  $^{142}\text{Xe}_{88}$ , established by Mowbray *et al.* [73], was found to satisfy the predictions of the IBM-2 under conditions where the counting of both neutron and proton bosons is well established.

In the present work, the systematics of  $E(2_1^+)$  and  $E(4_1^+)$  for the even-even Pd isotopes were extended to  $^{120}\text{Pd}_{74}$ . The proposed new values of  $E(2_1^+)$  and  $E(4_1^+)$  for this nuclide are given in Table 5.1, along with previously published  $2_1^+$  and  $4_1^+$

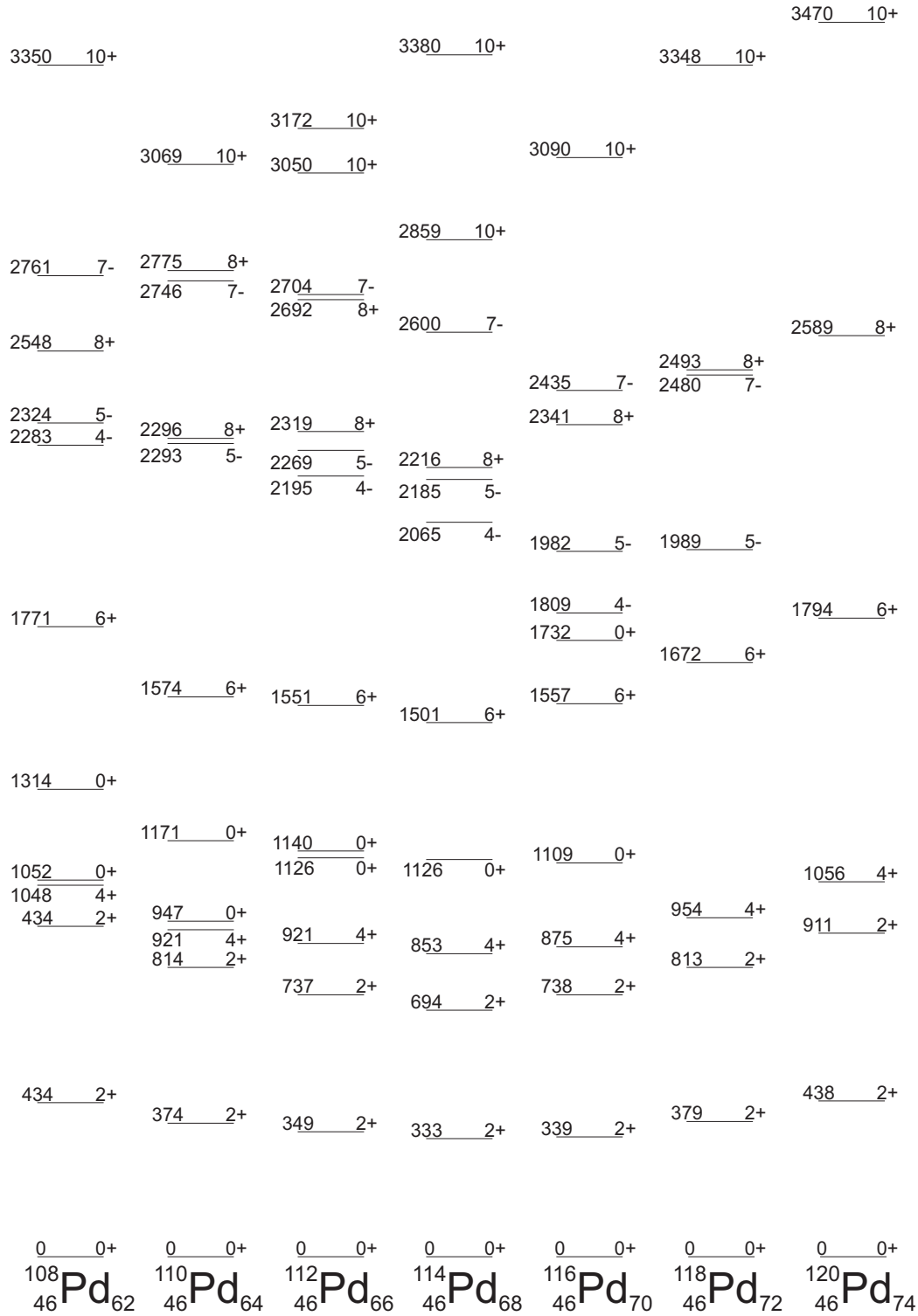


Figure 5.1: Partial level-scheme systematics for the even-even Pd isotopes  $A = 108 - 120$ . The additional states in  $^{120}\text{Pd}$  ( $2_2^+$ ,  $6^+$ ,  $8^+$ ,  $10^+$ ) have been determined by Stoyer [74] from mass-gated alpha-induced fission of  $^{238}\text{U}$ .

Table 5.1: Experimental  $2_1^+$  and  $4_1^+$  energies for  $_{46}\text{Pd}$  and  $_{54}\text{Xe}$  and the IBM-2 calculated energies for  $^{118,120}\text{Pd}$  [71].

Nuclide	$E(2_1^+)$ [keV]	IBM-2 [keV]	$E(4_1^+)$ [keV]	IBM-2 [keV]
$^{108}_{46}\text{Pd}_{62}$	434		1046	
$^{120}_{46}\text{Pd}_{74}$	436	430	1054	1040
$^{128}_{54}\text{Xe}_{74}$	443		1033	
$^{110}_{46}\text{Pd}_{64}$	374		921	
$^{118}_{46}\text{Pd}_{72}$	379	380	953	900
$^{126}_{54}\text{Xe}_{72}$	388		942	

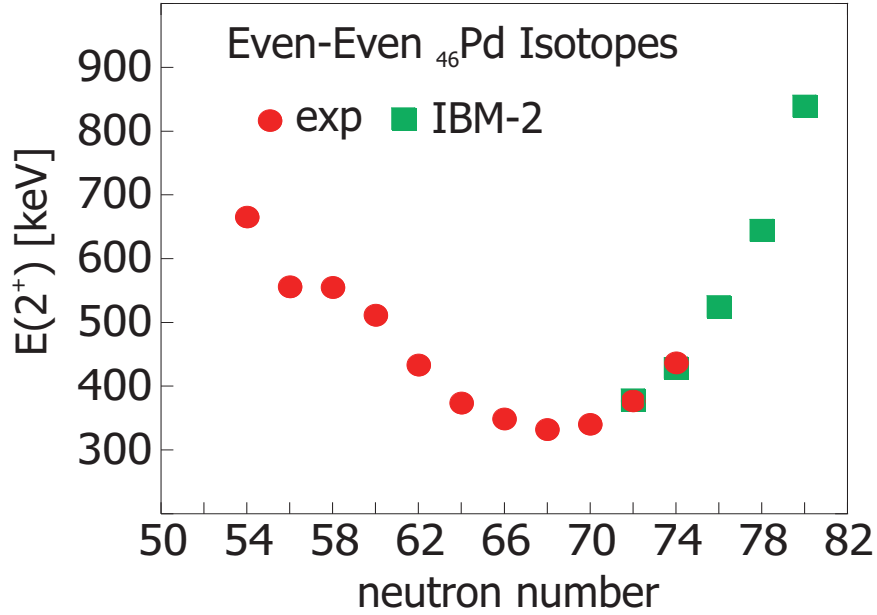


Figure 5.2: Energies for the first  $2^+$  levels in the even-even  $_{46}\text{Pd}$ .

energies for  $_{46}\text{Pd}$  and  $_{54}\text{Xe}$  nuclides and the IBM-2 predictions for  $^{118}\text{Pd}$  and  $^{120}\text{Pd}$ . The experimental  $E(2_1^+)$  values for even-even Pd isotopes, including the new value for  $^{120}\text{Pd}$ , are plotted as a function of neutron number in Figure 5.2 alongside the theoretical values. The predictions of Kim *et al.* agree remarkably well with the experimental energies of both  $^{118}\text{Pd}$  and  $^{120}\text{Pd}$ , and this agreement strongly suggests the persistence of the  $N = 82$  closed shell in these Pd isotopes.

In addition to comparisons with theoretical predictions, the  $2_1^+$  and  $4_1^+$  energies deduced in this work were also compared with isotopic and isotonic nuclides. Comparison of the energy values in the table reveal a distinct two-way isotopic symmetry, using nuclides on either side of the  $Z = 50$  shell (centered on  $^{114}\text{Pd}_{68}$ ) with  $^{110}\text{Pd}_{64}$

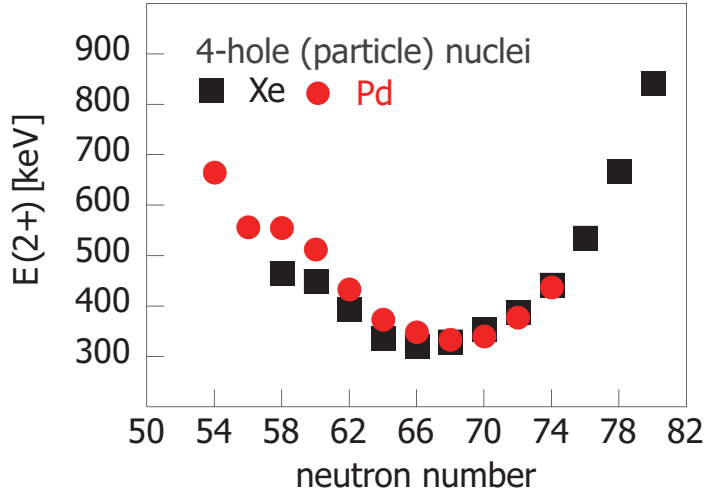


Figure 5.3: Energies for the first  $2^+$  levels in the 4-hole (particle) nuclides  $_{46}\text{Pd}$  and  $_{54}\text{Xe}$ .

and  $^{108}\text{Pd}_{62}$  and isotonic symmetry with  $^{126}\text{Xe}_{72}$  and  $^{128}\text{Xe}_{74}$ , respectively. The new  $E(2_1^+)$  value for  $^{120}\text{Pd}$  is also presented in the plot of Figure 5.3, which includes the even-even Xe isotope  $E(2_1^+)$  systematics.

Given the remarkable agreement of the new  $E(2_1^+)$  and  $E(4_1^+)$  values in  $^{120}\text{Pd}$  with the calculated energies, to isotopic  $^{110}\text{Pd}$ , and to isotonic  $^{128}\text{Xe}$ , it has been inferred that the protons and neutrons in  $^{120}\text{Pd}$  are subject to the same  $N = 82$  closed shell as is felt by  $^{128}\text{Xe}$ , as well as the same  $Z = 50$  proton closed shell. This inference is supported by recent mass measurements of neutron-rich Pd isotopes. On average, these experimental mass measurements are within one standard deviation of the theoretical values calculated with the Finite Range Droplet Model (FRDM) [75], which does not have shell quenching, providing added support for the regular neutron and proton shell closures influencing the low-energy structure of  $^{120}\text{Pd}$ . Thus, in conclusion, the evidence provided by the new  $2_1^+$  and  $4_1^+$  energies deduced in this work support the notion that neutron shell quenching is not observed in Pd isotopes with  $N \leq 74$ .

## 5.3 Neutron- and Proton-Hole Configurations in Odd-Even Ag Isotopes

The odd- $A$  Ag isotopes studied in the present work,  $^{123,125}\text{Ag}$ , demonstrate dominant single-particle characteristics, serving as evidence of the persistence of the  $N = 82$  shell closure in these nuclides. Comparison of the low-energy level structures of  $^{123,125}\text{Ag}$  with the level structures of the odd- $A$  In isotones,  $^{125}\text{In}$  and  $^{127}\text{In}$ , reveals a significant degree of similarity, as shown in Figure 5.5. The one proton-hole In nuclides have been well described by shell-model configurations based on proton and neutron holes in doubly-magic  $^{132}\text{Sn}$ . The  $9/2^+$  levels in the In and Ag nuclides, as well as the  $7/2^+$  levels in the Ag nuclides, are built on  $g_{9/2}$  proton-hole configurations. The odd- $A$  Ag systematics shown in Figure 5.4 reveal that three low-lying states,  $9/2^+$ ,  $7/2^+$  and  $1/2^-$ , become the ground state at different neutron numbers between  $N = 60 - 78$ . The  $9/2^+$  and  $1/2^-$  levels are possibly single-particle in nature and are attributed to a proton hole in the  $1g_{9/2}$  and  $2p_{1/2}$  orbitals, respectively. The  $7/2^+$  state has been described in terms of three-particle configurations— $\pi g_{9/2}^{-3}$ ,  $\pi g_{9/2}^{-3} \otimes \nu(h_{11/2}^{-2})_{2^+}$  and  $\pi g_{9/2}^1 \otimes \nu(h_{11/2}^{-2})_{2^+}$  [76, 77]. The lower-than-expected energy of this state may be explained by a significant decrease of pairing energy due to orbital blocking [76, 77]. In the current work it is speculated that the ground state of  $^{123}\text{Ag}_{76}$  is  $7/2^+$  and that of  $^{125}\text{Ag}_{78}$  is  $9/2^+$ . A similar change in ground-state spins has been observed at the other end of the  $N = 50 - 82$  shell. The ground-state spins of the odd- $A$  Ag isotopes from  $N = 50 - 54$  are  $9/2^+$  and for  $N = 56$  is  $7/2^+$ . The rise in the energy of the  $7/2^+$  state at both ends of the  $N = 50 - 82$  shell may be attributed to the higher excitation energies of the component neutron configurations. The  $11/2^+$  and  $13/2^+$  levels in both Ag and In may be ascribed to  $g_{9/2}$  proton-hole configurations coupled to  $h_{11/2}$  neutron holes. Thus, it is inferred that these two Ag isotopes, while more exotic (*i.e.* higher  $N/Z$  ratio) than their isotonic In counterparts, are structurally quite similar. Therefore, it is deduced that the low-energy structure

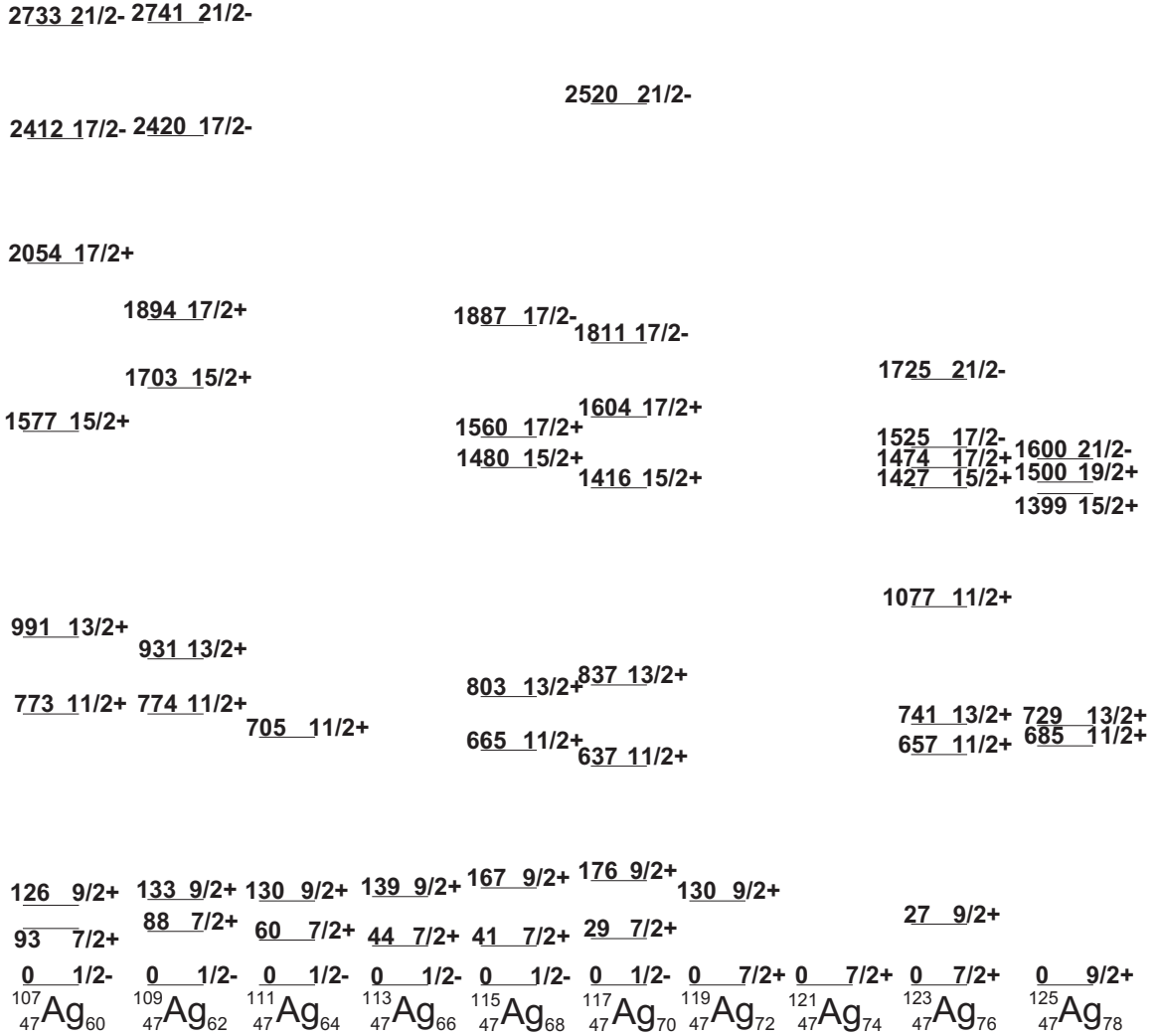


Figure 5.4: Partial level-scheme systematics for the odd- $A$  Ag isotopes  $A = 107 - 125$ .

of the odd- $A$  Ag isotopes,  $^{123,125}\text{Ag}$ , are governed by a small number of neutron holes and three proton holes in doubly-magic  $^{132}\text{Sn}$ .

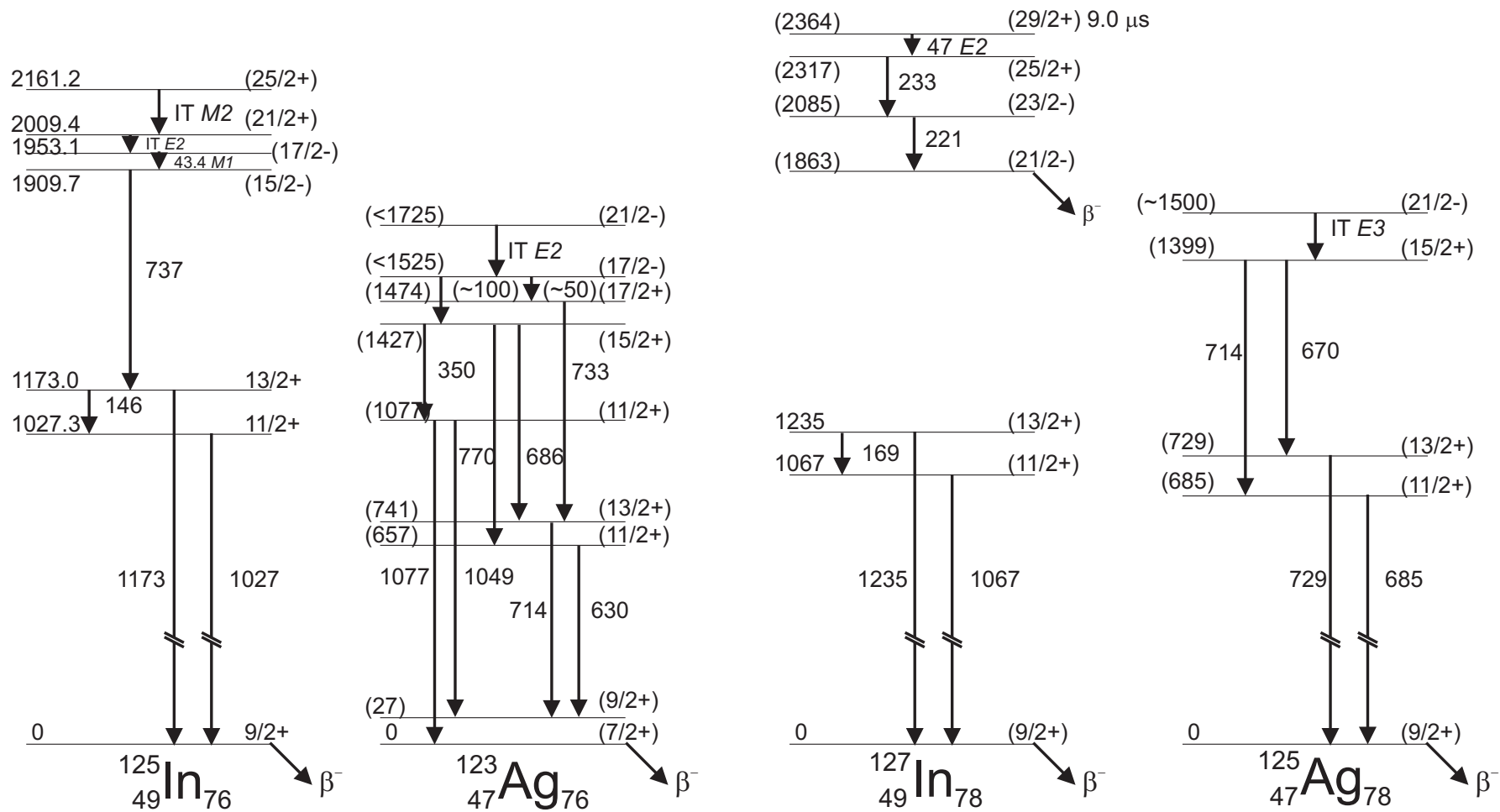


Figure 5.5: Comparisons of the partial level schemes of  $^{123,125}\text{Ag}$  and  $^{125,127}\text{In}$ .

## 5.4 Systematics of Cd Isotopes

The present work also provides evidence in support of the persistence of the  $N = 82$  shell closure in the Cd isotopes  $^{125,126,127}\text{Cd}$ . As has already been described, much of the speculation regarding the quenching of the  $N = 82$  shell is based upon experimental data for  $^{130}\text{Cd}$ . However, prior to this work very little was known about the Cd isotopes beyond  $A = 124$ . The new data obtained in this work for  $^{125,126,127}\text{Cd}$ , particularly the odd- $A$  isotopes each with a single odd neutron, provide insight into the neutron shell structure very close to  $N = 82$ .

Examination of the deduced  $^{126}_{48}\text{Cd}_{78} 2_1^+$  energy in the context of the even-even Cd systematics, as shown in Figure 5.6, seems to support the notion of a weakened  $N = 82$  shell closure. The Cd  $E(2_1^+)$  values appear to flatten out at  $N = 78, 80$ , possibly corresponding to a quenching of the  $N = 82$  shell gap in  $^{126}\text{Cd}_{78}$  and  $^{128}\text{Cd}_{80}$ , respectively. In a similar situation near the  $N = 126$  shell closure, the  $2_1^+$  energies of  $_{80}\text{Hg}$  (two holes in  $Z = 82$  proton closed shell), which are also plotted in Figure 5.6, exhibit flattened values just before the  $N = 126$  neutron-shell closure, much like that observed in  $_{48}\text{Cd}$  (two holes in  $Z = 50$ ). Also, a departure away from smooth parabolic  $E(2_1^+)$  systematics, as in the example of the even-even Pd isotopes in Figure 5.3, is evident for Cd isotopes near the  $N = 50$  shell closure. This same type of deviation is also observed in the even-even  $_{52}\text{Te}$  (two particles beyond  $Z = 50$ ) isotopes near  $N = 50$ . Neutron shell quenching, however, has not been proposed in either Te or Hg, and the unusual behavior of the  $E(2_1^+)$  systematics of these two elements is, instead, attributed to the dominance of shell-model, rather than collective, effects [70] in these three 2-hole (particle) elements.

Terasaki *et al.* have explained the anomalous behavior of the Te  $E(2_1^+)$  and  $B(E2)$  values near  $N = 82$  as arising from the single-particle properties, specifically a reduced neutron-neutron pairing interaction [78]. It is proposed in this work that the rather flat  $E(2_1^+)$  values of  $^{126}\text{Cd}$  and  $^{128}\text{Cd}$  are also a signature of the shell-model

nature of these Cd isotopes with reduced nucleon-nucleon interaction strengths and not the result of a diminished  $N = 82$  shell gap. This position is supported by the fact that the excited-state level structure of  $^{126}\text{Cd}$  has been reproduced by shell-model calculations, performed with the OXBASH code, using reduced nucleon-nucleon interaction strengths [79]. The theoretical  $^{126}\text{Cd}$  partial level scheme, shown in Figure 5.7, was deduced from a truncated OXBASH (OXBASHT) calculation using a proton space with the  $\pi f_{5/2}$  orbital included in the core. The total valence proton space incorporated the three orbitals  $2p_{3/2}$ ,  $2p_{1/2}$ , and  $1g_{9/2}$ . The total valence neutron space encompassed the  $1g_{7/2}$ ,  $2d_{5/2}$ ,  $2d_{3/2}$ ,  $3s_{1/2}$  and  $1h_{11/2}$  orbitals. This calculation used “normal” nucleon-nucleon interaction strengths [57]. Significant discrepancies between the the experimental level energies and the calculated level energies are observed, especially for the critical  $7^-$  level, the importance of which will be explained. Furthermore, the  $E(4_1^+)/E(2_1^+)$  ratio for  $^{126}\text{Cd}$ , as deduced in this work, has a value of 2.2, which indicates a low degree of collectivity. Thus, the anomalous Cd  $2_1^+$  energy systematics, which may appear to support the notion of  $N = 82$  shell quenching in  $^{126}\text{Cd}$ , is more likely a result of a reduced nucleon-nucleon interaction strength in the shell model potential. Such a reduced interaction may be explained by the mismatch of proton and neutron single-particle orbitals as two separate major shells are being filled for protons and neutrons, respectively.

Further insight into the structure of  $^{126}\text{Cd}$  was obtained from the observed isomer. An isomeric state, referred to as a seniority isomer, is typically observed in the highest-spin state (maximum seniority) of a  $|j^n; J\rangle$  configuration near a shell closure. In this context, seniority refers to the minimum number of unpaired particles in a  $|j^n; J\rangle$  configuration necessary to produce a total angular momentum  $J$  [80]. Short-range residual interactions (*e.g.*, the  $\delta(x)$  interaction) produce monotonically decreasing energy spacings between  $J$  and  $J+2$  levels in even-even nuclides, where  $J$  is even [81]. A seniority isomer occurs when the energy spacing between the  $J_{max}$  ( $= 2j - 1$ ) and  $J_{max} - 2$  ( $= 2j - 3$ ) levels is sufficiently small enough to produce a long-lived state

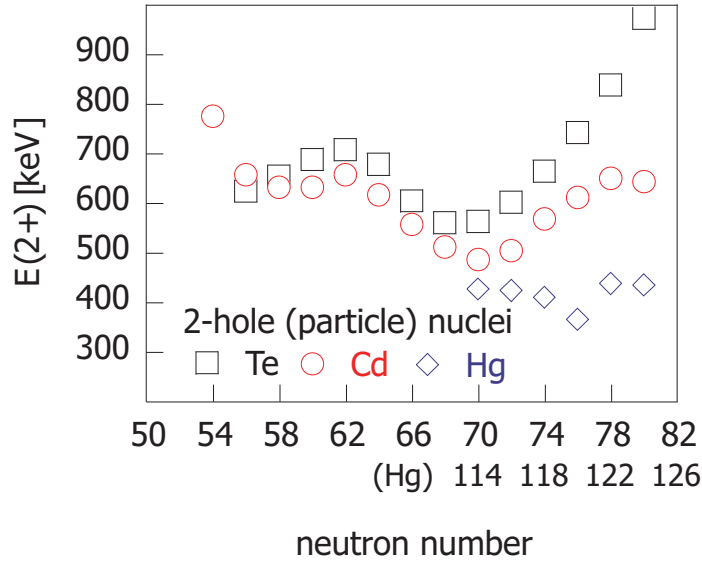


Figure 5.6: Energies for the first  $2^+$  levels in the 2-hole (particle) nuclides  $_{48}\text{Cd}$ ,  $_{52}\text{Te}$  and  $_{80}\text{Hg}$ .

that decays via  $E2$  gamma-ray emission or beta emission [81]. Ressler *et al.* have demonstrated that the seniority scheme gives way to a collective description very quickly as valence protons *and* neutrons are added [82].

Prior to the present work, no isomers had been observed in any even-even Cd isotopes. An  $8^+$  seniority isomer, arising from the pair of proton holes ( $g_{9/2}^{-2}$ ) in  $Z = 50$  was expected in even-even  $^{126}_{48}\text{Cd}_{78}$  [70]. Based on the present work it is postulated that the observed isomeric state is not the expected  $8^+$  level but is instead a  $12^+$  level. The absence of the seniority isomer suggests that  $^{126}\text{Cd}$  may be showing some degree of collectivity, which would be indicative of a weakened  $N = 82$  shell closure. However, it is argued here that the absence of the  $8^+$  isomer is due to the relatively large energy separation between the  $8_1^+$  and  $6_1^+$  levels, which may be attributed to a reduced nucleon-nucleon interaction strength. As stated in Section 4.2.5, the proposed  $12^+$  isomeric state is attributed to the four-particle  $(\pi g_{9/2}^{-1} p_{1/2}^{-1})_{5^-} \otimes (\nu h_{11/2}^{-1} d_{3/2}^{-1})_{7^-}$  configuration [57]. The excited-state systematics of the even-even Cd isotopes, as shown in Figure 5.8, reveal that the energy of the  $7^-$  decreases slowly up to  $^{124}\text{Cd}$  and then abruptly between  $^{124}\text{Cd}$  and  $^{126}\text{Cd}$ . In contrast the energy of the seniority-two  $\nu h_{11/2}^{-2} 10^+$  level remains essentially constant across the isotopic chain, giving rise

to the energy compression of the  $12^+$  and  $10^+$  levels and the isomeric nature of the former. The preceding explanation of the sudden appearance of the  $^{126}\text{Cd}$  isomer was based upon the evolution of the  $7^-$  and  $10^+$  levels, both of which are produced by pure two-neutron shell-model configurations.

Finally, the excited state level structures of the two odd-A Cd isotopes studied in this work,  $^{125}\text{Cd}$  and  $^{127}\text{Cd}$ , are well described in terms of shell-model states built upon doubly-magic  $^{132}\text{Sn}$ , as described in Sections 4.2.4 and 4.2.6. Just as the ratio  $E(4_1^+)/E(2_1^+)$  is used as an indicator of collectivity in even-even nuclides, the ratio  $R$ , given by

$$R = \frac{E_{19/2^-} - E_{11/2^-}}{E_{15/2^-} - E_{11/2^-}} \quad (5.1)$$

has been used as an indicator of collectivity in odd-A Cd isotopes [83, 84], where the indicated odd-parity states are the result of  $\nu h_{11/2}^n \otimes \text{core}$  configurations. A value of  $R \leq 2.0$  is indicative of a spherical nucleus [83], and hence stronger single-particle shell-model character. The systematics of  $R$  for odd-A Cd isotopes are illustrated in Figure 5.9. Based on the  $19/2^-$ ,  $15/2^-$ , and  $11/2^-$  excited-state energies proposed in the present work (see Figs. 4.21 and 4.31), the calculated  $R$  values for  $^{125}\text{Cd}$  and  $^{127}\text{Cd}$  are both 2.0. Thus, it is surmised that these Cd isotopes exhibit a low degree of collectivity, as anticipated for nuclides only a few particles away from a shell closure.

Furthermore, comparisons of  $^{125}\text{Cd}$  and  $^{127}\text{Cd}$  with their respective Sn isotones,  $^{127}\text{Sn}$  and  $^{129}\text{Sn}$ , support the attribution of single-particle characteristics to these Cd nuclides. As shown in Figure 5.10, the ground states and first few excited states of these Cd and Sn nuclides are quite similar. The proton-magic, odd-A Sn isotopes are good examples of single-particle nuclides. The first three states in each nuclide are dominated by the odd neutron occupying the nearly degenerate  $3s_{1/2}$ ,  $2d_{3/2}$ , and  $1h_{11/2}$  orbitals. The higher-spin odd-parity levels arise from three or more unpaired neutrons in the  $1h_{11/2}$  orbital—that is odd neutron holes in the doubly-magic  $^{132}\text{Sn}$ . Similar level structures are postulated in  $^{125}\text{Cd}$  and  $^{127}\text{Cd}$  and attributed to the same

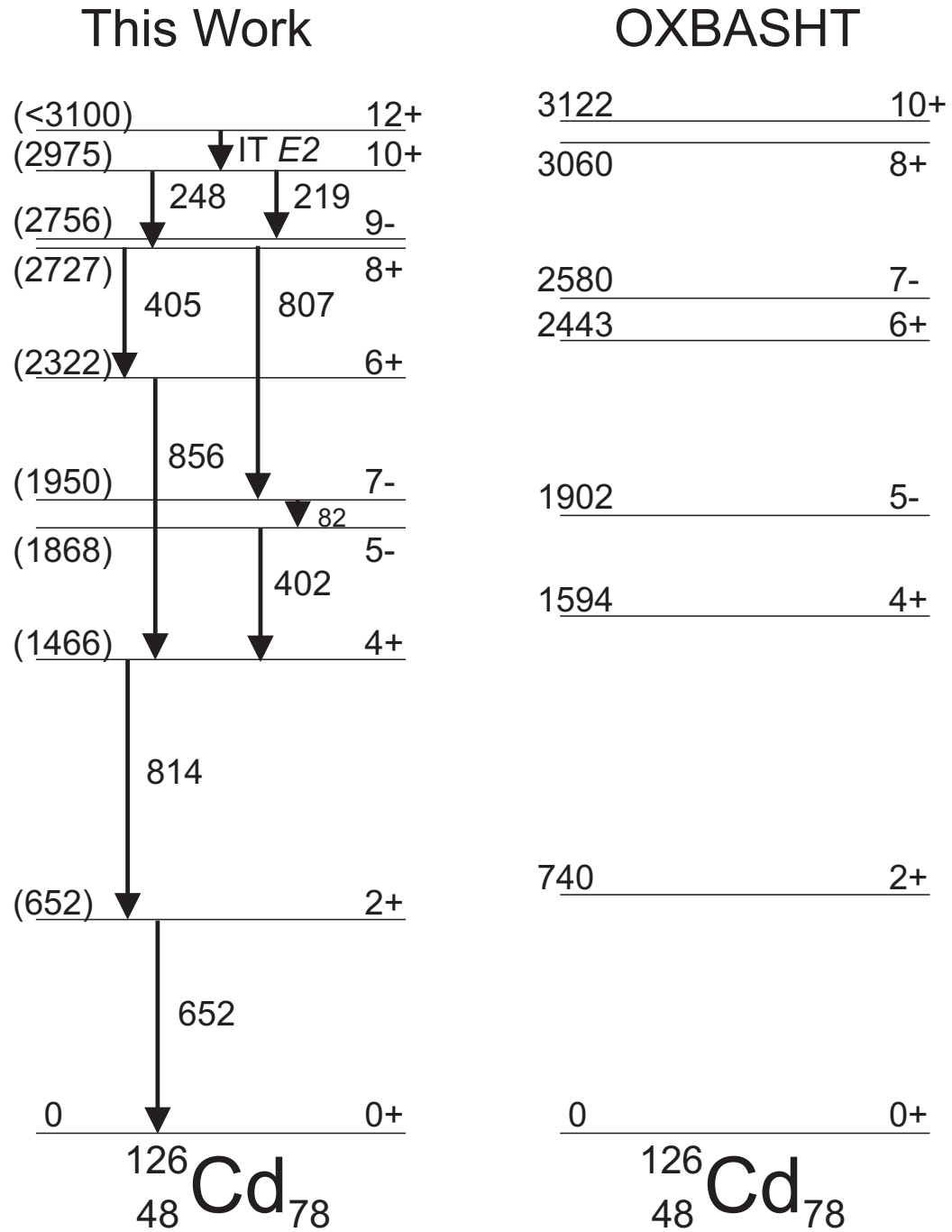


Figure 5.7: On the left is a proposed decay scheme for the  $^{126}\text{Cd}$  isomer from this work. On the right is the level order deduced from OXBASHT calculations (see text). The position of the  $12^+$  level was not calculated. The quoted energies are in keV.



shell-model valence neutron configurations. Thus, the appearance of single-particle level structures in  $^{125}\text{Cd}$  and  $^{127}\text{Cd}$ , along with the low collectivity indicated by the  $R$  values, suggests that  $N = 82$  remains a good shell closure in these nuclides.

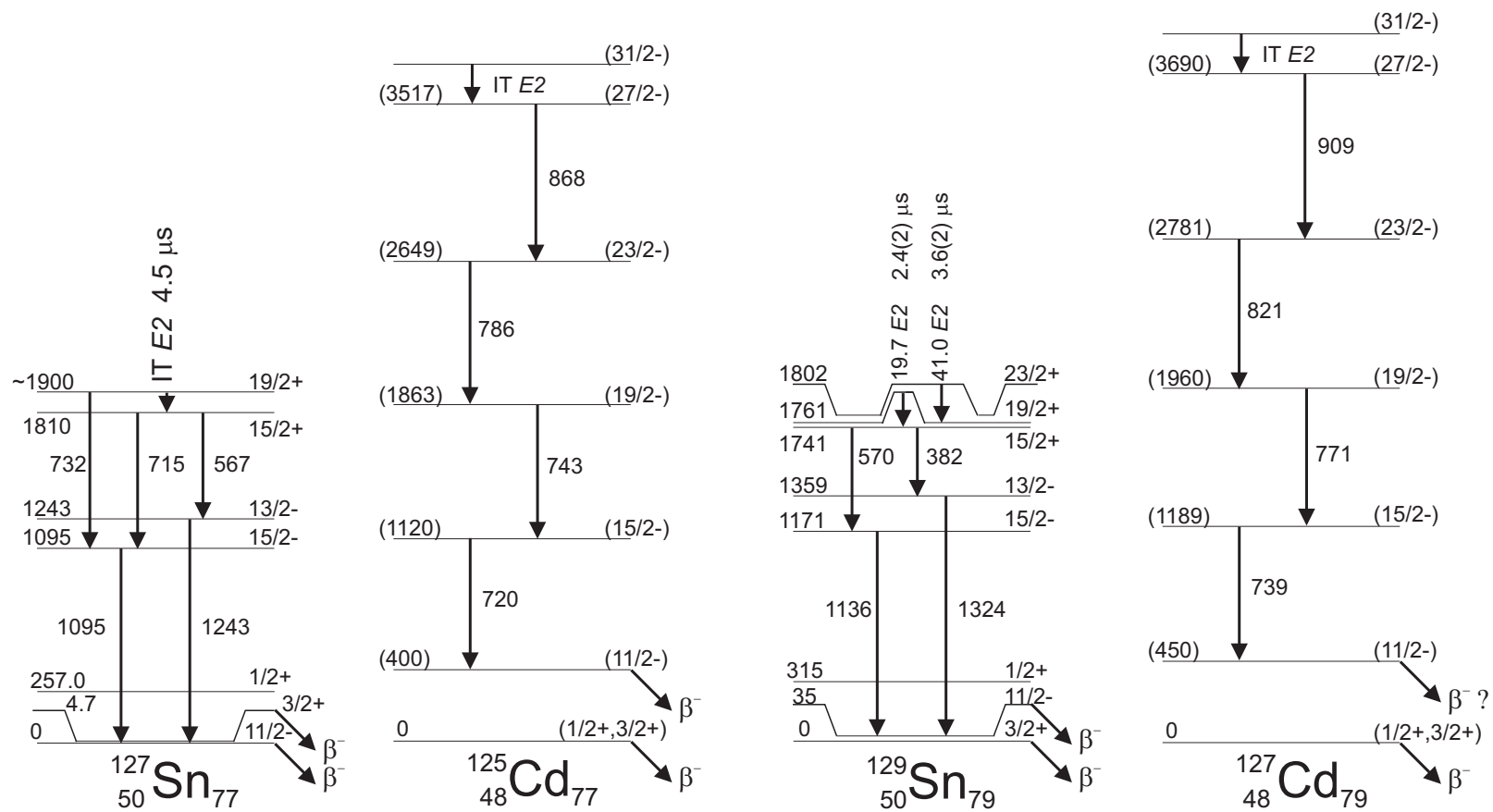


Figure 5.10: Comparisons of the partial level schemes of  $^{125,127}\text{Cd}$  and  $^{127,129}\text{Sn}$ .



50 and  $N = 82$  shell closures. Similar arguments were made for the new Ag isotopes,  $^{123}\text{Ag}$  and  $^{125}\text{Ag}$ , where level-scheme comparisons with isotonic In nuclides reveal analogous  $Z = 50$  proton-hole and  $N = 82$  neutron-hole configurations. Finally, the even-even nuclide  $^{126}_{48}\text{Cd}_{78}$  was studied, and a gamma-emitting isomer was identified. The isomeric level has been attributed to a compressed  $12^+$  intruder state, rather than the  $8^+$  seniority isomer anticipated near the neutron- and proton-shell closures. The deduced  $^{126}\text{Cd}$   $2_1^+$  energy was compared with the even-even Cd  $E(2_1^+)$  systematics. The systematics reveal an apparent flattening of  $2_1^+$  energies for  $N = 78, 80$ . It was argued in the present work that this is not a symptom of neutron-shell quenching but is an effect of reduced nucleon-nucleon interactions, as also observed in  $_{52}\text{Te}$ . The speculated appearance of reduced interactions strengths in nuclides in the region near  $N = 82$  and below  $Z = 50$  requires further study, however.

# Chapter 6

## Summary

We understand many things about the atomic nucleus in terms of the nuclear shell model, which is primarily based on the experimentally deduced properties of nuclides close to beta-decay stability. However, nuclear shell structure has been seen to evolve in regions away from stability, and the characteristics of stable and nearly stable nuclides should not be blindly extrapolated to nuclides with  $N/Z$  ratios that deviate significantly from unity.

With the advent of radioactive ion beam facilities in recent years, more exotic neutron-rich nuclides have been studied experimentally, allowing for more stringent tests of the classic nuclear shell model. In certain exotic nuclides the well-known neutron shell closures  $N = 8, 20$  have been observed to disappear. Much speculation exists regarding the possible reduction or disappearance of the larger neutron magic numbers  $N = 50, 82$ . Recent experimental evidence has suggested that the  $N = 82$  shell gap may be quenched in  ${}^{130}_{48}\text{Cd}_{82}$ .

The possibility of  $N = 82$  shell quenching in nuclides of  ${}_{48}\text{Cd}$ ,  ${}_{47}\text{Ag}$ , and  ${}_{46}\text{Pd}$  in the vicinity of doubly-magic  ${}^{132}_{50}\text{Sn}_{82}$  was investigated in Experiment 01015 at the National Superconducting Cyclotron Laboratory at Michigan State University. The neutron-rich transition metal nuclides of interest were produced via projectile fragmentation of  ${}^{136}\text{Xe}$  employing the Coupled-Cyclotron Facility and the A1900 fragment separator.

Table 6.1: A summary of new prompt  $\gamma$  rays and deduced  $T_{1/2}$  for nuclides observed in this work.

Nuclide	Gamma Rays [keV]	$T_{1/2}$ [ $\mu$ s]
$^{126}\text{In}$	244, 266, 279, 615 836, 864	5(7)
$^{125}\text{Cd}$	409, 720, 743, 786 868, 923	1.7(8)
$^{126}\text{Cd}$	220, 248, 402, 405 653, 807, 815, 857	2.0(7)
$^{127}\text{Cd}$	739, 771, 822, 909	1.9(6)
$^{123}\text{Ag}$	350, 384, 391, 630 686, 714, 733, 770 1049, 1077, 1134	0.32(3)
$^{124}\text{Ag}$	156, 1133	1.9(2)
$^{125}\text{Ag}$	670, 685, 714, 729	0.44(9)
$^{121}\text{Pd}$	135	0.70(5)
$^{120}\text{Rh}$	211	not determined
$^{117}\text{Ru}$	185	1.4(6)

Several experimental observables provide clues as to how shell structure evolves in increasingly exotic nuclides. In the present work the nature of  $N = 82$  was investigated by studying low-lying quantum states of specific nuclides that were populated by beta decay and isomeric gamma decay. Inferences regarding the energy, spin-parity, and ordering of nuclear excited states were based on the spectroscopy of beta-delayed and prompt gamma rays, combined with isotopic systematics.

New spectroscopic data were obtained for a number of nuclides with  $A \sim 120$  from  $^{44}\text{Ru}$  to  $^{48}\text{Cd}$ . Comparison of data obtained for several  $^{50}\text{Sn}$  and  $^{49}\text{In}$  nuclides with data reported in the literature for these nuclides was used to validate the methods of analysis that were employed. The partial excited-state level schemes deduced for  $^{120}\text{Pd}$ ,  $^{123,125}\text{Ag}$ , and  $^{125-127}\text{Cd}$  were interpreted with regard to the effects of the  $N = 82$  shell gap.

In the present work, the observation of several new isomers was reported. A summary of gamma-ray energies and deduced half-lives for all of the new isomers that were seen in Experiment 01015 is provided in Table 6.1.

Table 6.2: A summary of new  $\beta$ -delayed  $\gamma$  rays and adopted  $\beta$ -decay half-lives. The superscripts in the righthand column indicate the  $\gamma$  ray used for gating.

Nuclide	Gamma Rays [keV]	$T_{1/2}$ [s]	$\gamma$ -gated $T_{1/2}$ [s]
$^{122}\text{Ag}$	325, 570, 651, 668 760, 800, 849	0.29(5) <sup>[760]</sup> 0.8(2) <sup>[800]</sup>	
$^{121}\text{Pd}$	135, 358, 626, 682 709, 1023, 1027 1369	0.248(5)	
$^{122}\text{Pd}$	209, 241, 965	0.17(1)	0.40(3) <sup>[209]</sup> , 0.23(2) <sup>[965]</sup>
$^{119}\text{Rh}$	247, 457, 585, 685 708	0.19(1)	0.28(2) <sup>[247]</sup> , 0.24(6) <sup>[457]</sup> 0.39(7) <sup>[585]</sup> , 0.8(3) <sup>[685]</sup> 0.43(9) <sup>[708]</sup> , 0.39(2) <sup>[total]</sup>
$^{120}\text{Rh}$	436, 619, 901 1122, 1245	0.12(1)	0.16(2) <sup>[436]</sup> , 0.12(1) <sup>[total]</sup>
$^{116}\text{Ru}$	246	0.18(1)	
$^{117}\text{Ru}$	583, 1276	0.16(2)	

Also, the observation of the beta decay of several new neutron-rich nuclides was reported. A summary of delayed gamma-ray energies and deduced half-lives for all of the new nuclides that were seen in Experiment 01015 is provided in Table 6.2.

The neutron-rich nuclide  $^{120}\text{Pd}$  was investigated, and the new  $2_1^+$  energy of  $^{120}\text{Pd}$  was compared with the systematics of the lighter even-even Pd isotopes. The new  $E(2_1^+)$  value was found to continue the upward trend of  $2_1^+$  energies as a function of neutron number toward the anticipated neutron-shell closure at  $N = 82$ . Comparable  $2_1^+$  energies of  $^{120}\text{Pd}$  and isotonic  $^{128}\text{Xe}$  suggest a symmetry about  $Z = 50$ , which has been characterized as evidence that  $^{120}\text{Pd}$  feels the same  $Z = 50$  and  $N = 82$  shell closures as its stable isotonic partner  $^{128}\text{Xe}$ . Also, the  $E(2_1^+)$  values for Pd isotopes up to  $A = 120$  were found to be in good agreement with values calculated from the Interacting Boson Model (IBM-2). This well-vetted model assumes normal  $Z = 50$  and  $N = 82$  shell closures, and agreement with it has been interpreted as further support for the persistence of these shell closures in  $^{120}\text{Pd}$ .

Systematic comparisons of the studied Cd isotopes with neighboring Sn isotones, as well as analysis of empirical excitation energy ratios, provide support for the interpretation of the  $^{125,127}\text{Cd}$  excited-state spectra as being of the single-particle character

anticipated for a few holes in the  $Z = 50$  and  $N = 82$  shell closures. Similar arguments were made for the new Ag isotopes,  $^{123}\text{Ag}$  and  $^{125}\text{Ag}$ , where level-scheme comparisons with isotonic In nuclides reveal analogous  $Z = 50$  proton-hole and  $N = 82$  neutron-hole configurations.

Finally, the even-even nuclide  $^{126}_{48}\text{Cd}_{78}$  was studied, and a gamma-emitting isomer was identified. The isomeric level has been attributed to a compressed  $12^+$  intruder state, rather than the  $8^+$  seniority isomer anticipated near the neutron- and proton-shell closures. The deduced  $^{126}\text{Cd } 2^+$  energy was compared with the even-even Cd  $E(2^+)$  systematics. The systematics reveal an apparent flattening of  $2^+$  energies for  $N = 78, 80$ . It was argued in the present work that this is not a symptom of neutron-shell quenching but is an effect of reduced nucleon-nucleon interactions, as also observed in  $_{52}\text{Te}$ . The speculated appearance of reduced interactions strengths in nuclides in the region near  $N = 82$  and below  $Z = 50$  requires further study, however.

In summary, the persistence of the  $N = 82$  shell gap in the region below doubly-magic  $^{132}_{50}\text{Sn}_{82}$  has been called into question based on recent experimental studies of  $^{130}_{48}\text{Cd}_{82}$ . The thesis of the present work has been that in certain isotopes of  $_{46}\text{Pd}$ ,  $_{47}\text{Ag}$ , and  $_{48}\text{Cd}$  with neutron numbers between  $N = 74 - 78$  the signatures of normal  $N = 82$  and  $Z = 50$  shell closures—namely characteristic single-particle configurations—are observed. Nuclear structure is known to evolve rapidly, however, so the present conclusions should not be extrapolated to isotopes with larger neutron numbers. Quite obviously, further experimental investigations are needed to determine how the  $N = 82$  shell gap evolves below  $Z = 50$ .

# Bibliography

- [1] T. Motobayashi et al. *Phys. Lett. B*, **346**:9, 1995.
- [2] A. Navin et al. *Phys. Rev. Lett.*, **85**:266, 2000.
- [3] T. Glasmacher et al. *Phys. Lett. B*, **395**:163, 1997.
- [4] T. Tondeur. *Z. Phys. A*, **288**:97, 1978.
- [5] I. Dillmann et al. *Phys. Rev. Lett.*, **91**:162503, 2003.
- [6] T. Kautzsch and et al. *Eur. Phys. J. A*, **9**:201, 2000.
- [7] J. I. Prisciandaro, A. C. Morton, and P. F. Mantica. *Nucl. Instr. and Meth. A*, **505**:140, 2003.
- [8] G. Friedlander, J. W. Kennedy, E. S. Macias, and J. M. Miller. *Nuclear and Radiochemistry*, page 45. (Wiley, New York), 3rd edition, 1981.
- [9] M. G. Mayer. *Phys. Rev.*, **75**:1969, 1949.
- [10] O. Haxel, J. H. D. Jensen, and H. E. Suess. *Phys. Rev.*, **75**:1766, 1949.
- [11] B. A. Brown. *Prog. in Part. and Nucl. Phys.*, **47**:517, 2001.
- [12] K. S. Krane. *Introductory Nuclear Physics*, page 131. (Wiley, New York), 1988.
- [13] A. Poves et al. *Eur. Phys. J. A*, **20**:119, 2004.
- [14] S. S. M. Wong. *Introductory Nuclear Physics*, page 205. (Wiley, New York), 2nd edition, 1998.
- [15] R. F. Casten. *Nuclear Structure from a Simple Perspective*, pages 142–146. (Oxford University Press, New York), 1990.
- [16] A. Arima and F. Iachello. *Ann. Phys.*, **99**:253, 1976.
- [17] A. Arima and F. Iachello. *Ann. Phys.*, 1978.
- [18] A. Arima and F. Iachello. *Ann. Phys.*, **123**:468, 1979.
- [19] R. F. Casten. *Nuclear Structure from a Simple Perspective*, pages 198–199. (Oxford University Press, New York), 1990.

- [20] C. W. Reich and R. G. Helmer. *Nucl. Data Sheets*, **85**:171, 1998.
- [21] E. N. Shurshikov and N. V. Timofeeva. *Nucl. Data Sheets*, **67**:45, 1992.
- [22] L. Grodzins. *Phys. Rev.*, **2**:88, 1962.
- [23] F. S. Stephens et al. *Phys. Rev. Lett.*, **29**:438, 1972.
- [24] K.-L. Kratz et al. *Hyperfine Int.*, **129**:185, 2000.
- [25] J. Dobaczewski et al. *Phys. Rev. C*, **53**:2809, 1996.
- [26] P. Möller et al. *At. Data and Nucl. Data Tables*, **59**:185, 1995.
- [27] Y. Aboussir et al. *At. Data and Nucl. Data Tables*, **61**:127, 1995.
- [28] J. Duflo and A.P. Zuker. *Phys. Rev. C*, **52**:R23, 1995.
- [29] J. M. Pearson et al. *Phys. Lett. B*, **387**:455, 1996.
- [30] Atomic Mass Data Center. Program: PC-NUCLEUS, 2003.  
<http://csnwww.in2p3.fr/AMDC/web>.
- [31] G. Audi et al. *Nucl. Phys. A*, **624**:1, 1997.
- [32] J. M. Blatt and V. F. Weisskopf. *Theoretical Nuclear Physics*, page 627. (Wiley, New York), 1952.
- [33] K. S. Krane. *Introductory Nuclear Physics*, pages 331–333. (Wiley, New York), 1988.
- [34] D. J. Morrissey et al. *Nucl. Instr. and Meth. B*, **204**:90, 2003.
- [35] R. Pfaff et al. *Phys. Rev. C*, **53**:1753, 1996.
- [36] O. Tarasov et al. *Nucl. Phys. A*, **701**:661, 2002.
- [37] W. T. Milner. Oak Ridge National Laboratory, unpublished.
- [38] R. Fox, 2001. <http://docs.nscl.msu.edu/daq/spectcl>.
- [39] S. N. Liddick. *Beta-Decay Studies of Neutron-Rich Nuclides and the Possibility of an  $N=34$  Subshell Closure*. PhD thesis, Michigan State University, 2004.
- [40] P. F. Mantica et al. *Phys. Rev. C*, **67**:014311, 2003.
- [41] W. F. Mueller. *Nucl. Instr. and Meth. A*, **466**:492, 2001.
- [42] B. M. Coursey, D. D. Hoppes, and F. J. Schima. *Nucl. Instr. and Meth.*, **193**:1, 1982.
- [43] J. F. Briesmeister editor. *MCNP: A General Monte Carlo N-Particle Transport Code*, 2000.

- [44] B. Fogelberg et al. *Phys. Rev. Lett.*, **73**:2413, 1994.
- [45] J. Genevey et al. *Phys. Rev. C*, **65**:034322, 2002.
- [46] M. Hellström et al. In *Proceedings of the 3rd International Conference on Fission and Properties of Neutron-Rich Nuclei*. World Scientific, 2002.
- [47] H. Gausemel et al. *Phys. Rev. C*, **69**:054307, 2004.
- [48] R. B. Firestone. *Table of Isotopes*. John Wiley & Sons, New York, 1996.
- [49] R. H. Mayer et al. *Phys. Lett. B*, **336**:308, 1994.
- [50] J. A. Pinston et al. *Phys. Rev. C*, **61**:024312, 2000.
- [51] B. A. Brown, A. Etchegoyen, and W. D. H. Rae. Oxbash. Technical report, MSU-NSCL, 1985.
- [52] L.-E. De Geer and G. B. Holm. *Phys. Rev. C*, **22**:2163, 1980.
- [53] A. Scherillo et al. *Phys. Rev. C*, **70**:054318, 1998.
- [54] M.-G. Porquet et al. *Eur. Phys. J. A*, **20**:245, 2004.
- [55] J. Genevey et al. *Phys. Rev. C*, **67**:054312, 2003.
- [56] T. Kautzsch. *Gamma-Spektroskopie an Neutronenreichen Silber-Isotopen*. PhD thesis, Johannes-Gutenberg-Universität in Mainz, 2004.
- [57] W. B. Walters, 2005. Private communication.
- [58] L. Spanier et al. *Nucl. Phys. A*, **474**:359, 1987.
- [59] D. Fong et al. *Phys. Rev. C*, **72**:0143315, 2005.
- [60] W. Urban et al. *Eur. Phys. J. A*, **22**:157, 2004.
- [61] J. Kurpeta et al. *Eur. Phys. J. A*, **2**:241, 1998.
- [62] M. L. Gartner and John C. Hill. *Phys. Rev. C*, **18**:1463, 1978.
- [63] J. Katakura and K. Kitao. *Nucl. Data Sheets*, **97**:765, 2002.
- [64] N. V. Zamfir et al. *Phys. Rev. C*, **51**:98, 1995.
- [65] T. Tamura. *Nucl. Data Sheets*, **71**:461, 1994.
- [66] B. Fogelberg, A. Bäcklin, and T. Nagarajan. *Phys. Lett. B*, **36**:334, 1971.
- [67] L. L. Shih, John C. Hill, and S. A. Williams. *Phys. Rev. C*, **17**:1163, 1978.
- [68] J. R. McConnell and W. L. Talbert. *Nucl. Instr. and Meth.*, **128**:227, 1975.

- [69] A. Piotrowski, R. L. Gill, and D. C. McDonald. *Nucl. Instr. and Meth.*, **114**:1, 1984.
- [70] W. B. Walters et al. *Phys. Rev. C*, **70**:034314, 2004.
- [71] K.-H. Kim et al. *Nucl. Phys. A*, **604**:163, 1996.
- [72] R. F. Casten, D. S. Brenner, and P. E. Haustein. *Phys. Rev. Lett.*, **58**:658, 1987.
- [73] A. S. Mowbray et al. *Phys. Rev. C*, **42**:1126, 1990.
- [74] M. A. Stoyer, 2005. Private communication.
- [75] Yu. A. Litvinov et al. Gsi scientific report 2003. Technical report, GSI, 2004.
- [76] L. K. Peker, J. H. Hamilton, and P. G. Hansen. *Phys. Lett. B*, **167**:283, 1986.
- [77] K. Heyde and V. Paar. *Phys. Lett. B*, **179**:1, 1986.
- [78] J. Terasaki et al. *Phys. Rev. C*, **66**:054313, 2002.
- [79] B. A. Brown, 2005. Private communication.
- [80] R. F. Casten. *Nuclear Structure from a Simple Perspective*, page 115. (Oxford University Press, New York), 1990.
- [81] J. J. Ressler et al. *Phys. Rev. C*, **69**:034317, 2004.
- [82] J. J. Ressler et al. *J. Phys. G*, **31**:S1605, 2005.
- [83] J. K. Hwang et al. *J. Phys. G*, **28**:L9, 2002.
- [84] N. Fotiades et al. *Phys. Rev. C*, **61**:064326, 2000.